First Principles Based Multiscale Modeling of Single Crystal Plasticity: Application to BCC Tantalum

Thesis by

Guofeng Wang

In Partial Fulfillment of the Requirements

for the Degree of

Doctor of Philosophy

California Institute of Technology

Pasadena, California

2002

(Defended April 30, 2002)

Acknowledgement

I would like to thank all the people who helped me in my study, research, and life at Caltech. I appreciate their kindness and assistance. Especially, I would like to thank the following people for their contributions to this thesis.

First, I would like to thank my advisor, Prof. William A. Goddard III, for his support, encouragement and guidance in the last five years. Bill is a great scientist, who is knowledgeable, creative, and enthusiastic. He patiently educated and tutored me in scientific thinking and English writing and speaking. He sets a fine example for me to follow in my future career.

Second, I would like to thank Dr. Tahir Çağın and Dr. Alejandro Strachan. They are my project directors and good friends. We discussed research works deeply and thoroughly and I learned many techniques from them. Furthermore, they also gave me many suggestions on my life and career. It is an honor for me to acknowledge Prof. William L. Johnson, Prof. Brent Fultz, Prof. Zhen-Gang Wang and Prof. Sossina Haile for their attendance at both my candidacy exam and thesis defense. They are the best committee members. They gave me much advice on my work and personal development. During my stay at Caltech, I benefited a lot from collaboration with other current and former group members. I would like to thank everyone at MSC. In particularly, Ryan Martin, Yue Qi, Darryl Willick, Rick Muller, Peter Schultz (Sandia National Laboratory), Hyon-Jee Lee and Darren Segall (MIT).

Last but not least, I dedicate this thesis to my parents, my wife and my daughter. I would like to express my gratitude to my parents, who have been supporting my education both financially and emotionally. My wife, Fang Li, gives me love, support and encouragement. My daughter Eilleen Wang, who is definitely an angel, brings us happiness and makes us proud.

Abstract

In principle, the macroscopic plasticity properties of crystalline materials are derivable from the physical processes involving dislocations and interactions between dislocations with other defects. However, a quantitative theory of plasticity based on the dislocation mechanism requires crossing multiple length and time scales. To accommodate these requirements, we developed a multiscale approach for modeling crystalline solids. In this thesis, to establish the connections between simulations in different length and time scales, I mainly focus on identifying and determining the importance and influence of various unit processes involving the dislocations through atomic level simulations. These unit processes in turn play a major role in modeling the single crystal plasticity.

Key Results from Atomistic Simulations

Dislocation core structure and core energy: Using the first-principles qEAM force field (FF), we determine the core energy for 1/2a<111> screw dislocation and 1/2a<111> edge dislocation in bcc Ta. We find that the core energy of edge dislocation is 1.77 times higher than that of screw dislocation. This ratio (1.77) is a fundamental material property used as input to the macroscopic model. Furthermore, we find that the central 12 atoms closest to the 1/2a<111> screw dislocation line have distinguishably higher atomistic strain energy than the other atoms. Thus, we arrive at a physical definition of dislocation core.

Screw dislocation mobility: In this thesis, we proposed a new method to investigate dislocation mobility by analyzing the process of migration of a screw dislocation dipole. The new method is based on the energy distribution at the atomistic scale and is used to calculate

the Peierls potential barrier and Peierls stress for dislocation continuous motion. The calculated Peierls stress is in good agreement with results obtained using other method. Simulating dislocation motion at finite temperatures (from 20 K to 300 K), we find that the activation energy for dislocation motion is about 6 times lower than computed at 0.001 K. Our results suggest that the decrease in the correlation between neighboring segments in the dislocation line accounts for the decrease of activation energy. We observe that the formation of kink pair along the dislocation line enhances the dislocation mobility. This verifies the traditional belief that the screw dislocation in bcc metals moves by first kink pair nucleation and subsequently lateral movements of kinks along the dislocation.

Kinks in screw dislocations: To bridge the atomistic process of dislocation motion with continuum model, we accurately calculate the material properties, such as kink pair formation energy and effective kink pair length, using atomic level simulations. In detailed structural analysis, we discover the substructures of different kinks when the screw dislocation core is asymmetric. There are only two kinds of elementary kinks in the dislocation and the others are the composite kinks consisting of an elementary kink and one or two flips. Based on these findings, we further explain the observed trend of the formation energy and mobility of different classes of kinks. (Note: Similar trend and conclusion could have been found in earlier studies but not mentioned by the authors of those papers.)

In summary, we have used quantum mechanics based interaction potentials to investigate the unit processes that play important role in single crystal plasticity and verified the findings using the quantitative results obtained from the atomic level simulation in a macroscopic model for single crystal plasticity.

Table of Contents

Chapter 1 Introduction

1.1 Dislocations and plasticity

Dislocations[1,2,3] are line defects in the atomic arrangement of a crystalline material. Since dislocation is a disorder in the crystalline system, its presence in a material increases the internal energy, electrical conductivity, and hardness, and influences many other physical properties. Among all influences caused by dislocations, people are most interested in the role that dislocations play in the plastic deformation of materials. Many experimental and theoretical studies have established the belief that dislocations are the primary agents of plasticity, i.e., plastic deformation proceeds by the generation and movement of dislocations. It is also firmly established that the macroscopic plasticity properties of crystalline materials are derivable, at least in principle, from the behavior of dislocations and their interactions with other defects[4].

The following provides a brief introduction to dislocations. For a further reading, please consult the references (Refs. 5, 6 and 7).

(1) Dislocation type. There are two basic types of dislocation in the crystalline materials: edge dislocation and screw dislocation. Figure 1-1 shows the descriptive model of the basic geometry of an edge (Figure 1-1 (a)) and a screw (Figure 1-1 (b)) dislocation. In an edge dislocation, an extra plane of atoms is inserted in the crystal but not extending through all of the crystal by ending in the dislocation line as illustrated in Figure 1-1 (a). Figure 1-1 (b) shows a screw dislocation originates from a shift of one atom in the lattice with respect to a perfect arrangement and can be described as a single surface helicoid,

rather like a spiral staircase. In the most general case, the dislocation (called mixed dislocation) has a mixed edge and screw character.

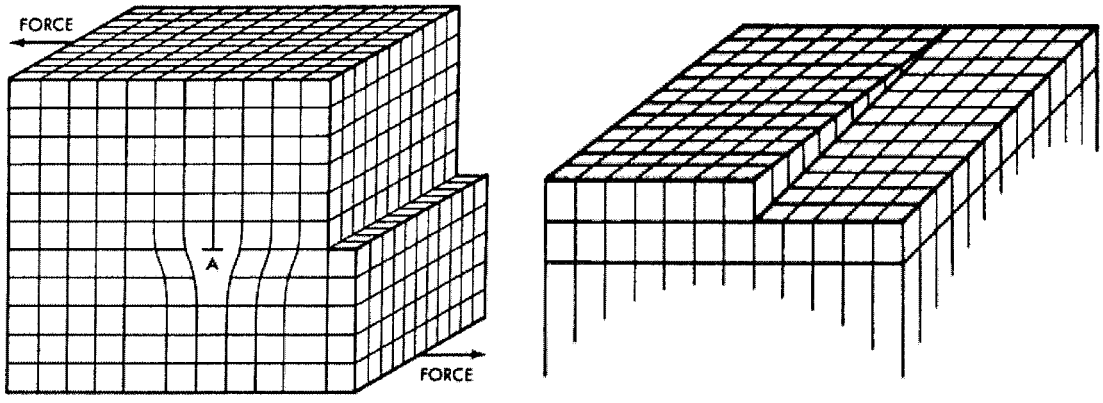

(a) (b)

Figure 1-1. Descriptive models of the edge dislocation and screw dislocation. (a) In an edge dislocation, an extra plane of atoms is present in the lattice structure of the crystal. In this case the extra plane is found adjacent to area A. (b) In a screw dislocation, a plane of atoms forms a step in the crystal surface. Other atoms can then line up against this step as the crystal grows.

(2) Burgers vector. Burgers vector **b** is the fundamental quantity defining an arbitrary dislocation. Its atomistic definition follows from a Burgers circuit around the dislocations in the real crystal, which is illustrated in Figure 1-2 for an edge dislocation. In Figure 1-2 (a), if making a closed circuit from lattice point to lattice point (or atom to atom) that encloses the dislocation, we obtain a closed chain of the base vectors defining the lattice. However, making exactly the same chain of base vectors in a perfect reference

lattice (Figure 1-2 (b)), we would obtain a chain not closed. The vector needed for closing the circuit in the reference crystal is the *Burgers vector* ***b***.

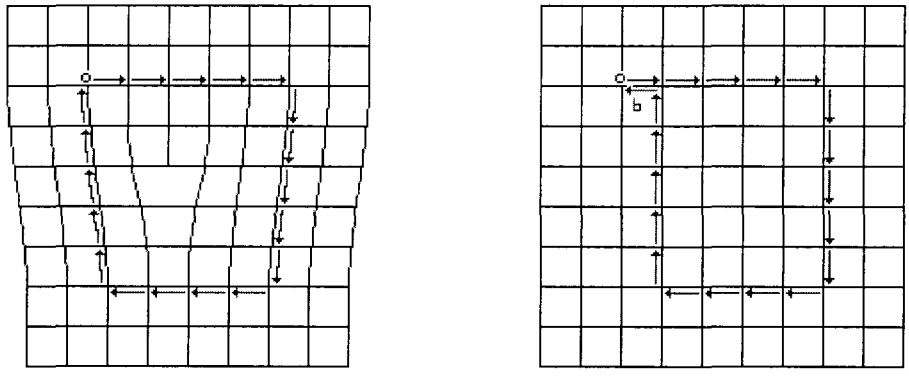

(a) (b)

Figure 1-2. (a) Burgers circuit around an edge dislocation, (b) the same circuit in a perfect reference crystal; the closure failure is the Burgers vector.

The following are two important rules for dislocation Burgers vector.

(a) *The Burgers vector of an edge dislocation is normal to the line of the dislocation.*

(b) The Burgers vector of a screw dislocation is parallel to the line of the dislocation.

For a mixed dislocation, the dislocation line may lie at an arbitrary angle to its Burgers vector. However, the Burgers vector of the dislocation is always the same and independent of the position of the dislocation.

(3) Slip and the Schmid law.

There are two basic types of dislocation movement: *glide* (or *conservative*) motion, in which the dislocation moves in the surface which contains both its line and

Burgers vector; and *climb* or (*non-conservative*) motion, in which the dislocation moves out of the glide surface normal to the Burgers vector. The concept of *slip*, providing a valuable understanding of the structure of the dislocation, is the most important manifestation of glide.

Plastic deformation in a crystal occurs by the sliding or successive displacement of one plane of atoms over another on the slip planes. Discrete blocks of crystal between two slip planes remain undistorted during the slip. Further deformation occurs either by more movement on existing slip planes or by the formation of new slip planes. The slip plane for a dislocation is normally the plane with the highest density of atoms and the direction in the slip is the direction of the slip plane in which atoms are most closely spaced. A slip plane and a slip direction in the plane constitute a *slip system.*

A characteristic shear stress is required for dislocation to slip. Arduous experiments on the relative orientation between the required shear stress and slip system for a dislocation lead to the famous Schmid law of the critical resolved shear stress (CRSS)[8]. The Schmid law states that the dislocation can slip in a slip system when the shear stress, resolved on the slip plane and in the slip direction, reaches the critical resolved shear stress (CRSS).

1.2 Features in plasticity of bcc metals

For body-centered cubic metals (e.g., iron, molybdenum, tantalum, vanadium, chromium, tungsten, niobium, sodium, and potassium), there are certain macroscopic

features common to the low temperature deformation behavior that distinguish the whole group from fcc and hcp metals and alloys[9].

These features include

- a rapid increase of the yield and flow stresses with decreasing temperature,
- a marked sensitivity of the stress to the imposed strain rate,
- a rather small and not very temperature sensitive work-hardening rate,
- a sensitivity to small amounts of impurity or solute, particularly, interstitial solutes,
- a tendency in many cases to brittle cleavage fracture at low temperatures,
- a complete breakdown of the Schmid law of critical resolved shear stress.

No doubt, associated to these features are the distinguished microscopic physical processes of dislocations in the bcc metals. The *in situ* high-voltage electron microscope study at low temperature finds for bcc metals the plastic deformation is characterized by the slow movement of long screw dislocations and fast movement of mixed dislocations[10]. This leads to the assertion that the mobility of screw dislocations governs the low temperature deformation behavior for bcc metals. Furthermore, the kink pair mechanism[11], assuming the screw dislocation in bcc metals moves by the kink pair nucleation and subsequently lateral motion of the component kinks, can successfully account for the rapid increase of flow stress with decreasing temperature[12-14]. The most interesting feature in bcc metal is the asymmetry of the slip, which contradicts the Schmid law. In bcc metals (for instances, iron and silicon-iron alloys[15,16], tungsten[17,18] niobium[19,20], tantalum[18,21], and molybdenum[21,22]), the shear stress to move a dislocation

lying in a slip plane in one direction is not the same as the shear stress required to move it in the opposite direction in the same plane.

To understand these nontrivial features of plastic deformation in bcc metals at low temperatures, we performed the accurate and systematic simulations for the 1/2a<111> screw dislocation in bcc Ta single crystal and summarized the results in this thesis.

1.3 Computer modeling of material plasticity

Following the postulations of dislocations in 1934[1-3], there have been several waves of activity in dislocation studies (see reviews 23, 24). The isotropic elastic field theories of dislocations and interactions among them were developed in the 1940s. Anisotropic elastic theory, pileup theory, direct observations of dislocations in transmission electron microscopy and work hardening theory were developed in the 1950s and 1960s. Extended dislocation arrays and the advent of atomistic computer simulations appeared in the 1960s and 1970s. And, since then, there has been the refinement in the details of dislocation interactions and core structures, extensive work on thin films, and computer simulations at several size scales.

With the fast development of the computer power and algorithms, the structures and behaviors of dislocations could be simulated using the physics and chemistry realistic models to attain a fundamental understanding of the elementary process of dislocation slip[25-30]. However, it is still prohibitive for us to quantitatively derive the macroscopic material plasticity based on the microscopic dislocation mechanism, because of the need to trace the evolution of a large number of interacting dislocations over long periods of

time. On the other hand, many equations of crystal plasticity used for continuum modeling have been developed to handle the multiplicity and complexity of describing the mechanisms of dislocation motion and interactions. However, most of these current continuum equations are phenomenological and largely disconnected from the physics of the underlying dislocation behavior.

To bridge the existing gap between dislocation physics and crystal plasticity, the strongly connected multiscale simulations, which are over multiple size scales and time scales, are necessary[31-39]. In an embedded (or hybrid) multiscale simulation, different regions are treated in different ways. The region of the greatest interest is simulated using quantum mechanics (QM) or molecular dynamics (MD), while the region, in which the atoms move collectively, can be simulated using finite element method (FEM) or field theory. Another model for the multiscale simulation is the hierarchical informed model. In this model, separate simulations are carried out at different size scales ranging from Ångstrom in QM regime to meters in continuum materials. At each size scale, some important physical parameters are extracted from detailed simulations and are input into the next level simulation with a larger size and time scale.

To better understand the concept of multiscale simulation, Figure 1-3 shows that the size and time scale of the physical processes could be studied by different simulation methods. Generally and roughly, the simulation methods are classified into four regimes.

(1) **Quantum Mechanics (QM) simulation**.

In quantum mechanics calculations, we regularly need to solve the Schrödinger equation for one or more particles (in most cases, electrons) to obtain the energy and

force of the system. The popular methods in this field are the Hartree-Fock (HF) method[40,41] and density functional theory (DFT) method[42,43]. The physical system can be efficiently treated with QM calculations are within the size no larger than tens of nanometers and over the period no longer than nanoseconds.

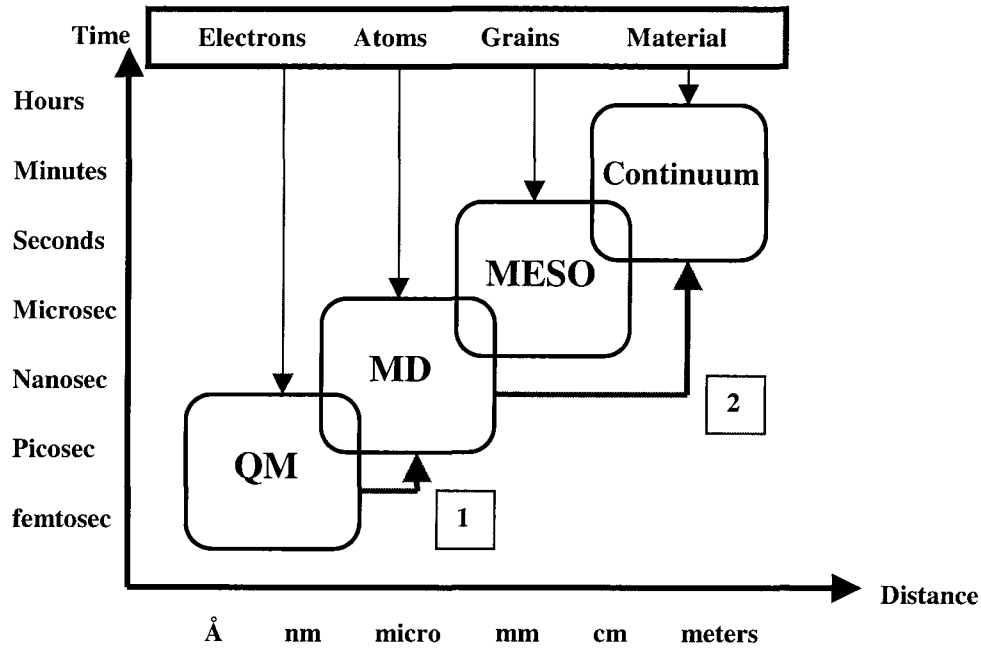

Figure 1-3. Model for the hierarchical informed multiscale simulation.

(2) **Molecular dynamics (MD) simulation.**

Systems of many interacting atoms or molecules can be studied classically by solving Newton's equations of motion in an MD simulation. The MD simulation consists essentially of integrating the equations of motion of the system numerically. Therefore it simulates the system as it develops over a period of time. In the simulation, the system moves in the phase space along its physical trajectory as determined by the equations of motion. Currently, a highly paralleled MD simulation can handle a system over millions

of atoms (or molecules) and over a period of time of microseconds. In Chapter 2, we will discuss MD simulation methods further.

(3) **MESO scale simulation.**

To study the subjects such as grain growth or dislocation pattern, the mesoscale simulation techniques ignoring the atomistic details of the system are desired. There are many ways to reduce the complexity of the system of interest. The Kinetic Monte Carlo (KMC) method[44] is widely used to simulate a large system over a rather long time based on the known mechanisms.

(4) **Continuum simulation.**

In this regime, the material is considered as a continuum media. The fully developed theories, such as statistical mechanics, kinetic mechanics, and continuum mechanics, are employed to investigate the material properties in much larger spatial and temporal scales (for example, Ref. 45).

In this study, we adopt the hierarchical informed model to simulate the single crystal plasticity for Ta. The red lines in Figure 1-3 show our approach to cross over the simulations of electrons (QM), atoms (MD), grains (MESO), and material (Continuum). Our multiscale approach for modeling Ta crystalline solids consists of three hierarchical parts.

(1) Derive the atomistic interaction potential for Ta based on the data obtained from the accurate quantum mechanics calculation,

(2) Predict the properties and behaviors of dislocations in the atomistic simulations using the derived first-principles potential,

(3) Describe the material plasticity in the kink pair mechanism based mesoscopic model with the input of the predicted atomistic-level dislocation properties.

This thesis (from Chapter 3 to Chapter 5) will focus on the work of simulating, identifying and predicting the physical processes of dislocations in atomistic level simulations, i.e., the part (2) of the whole multiscale simulation approach. The part (1) of the approach will be briefly described in Chapter 2. Chapter 6 reports the predicted results of the developed approach exercised to describe the mechanical response of high-purity Tantalum single crystals.

1.4 References

1. G. I. Taylor, Proc. R. Soc. Lond. A, **145**, 362 (1934).
2. E. Orowan, Z. Phys., **89**, 605 (1934).
3. M. Polanyi, Z. Phys., **89**, 660 (1934).
4. V. V. Bulatov, N. Tang and H. M. Zbib, MRS Bull., **26(3)**, 191 (2001).
5. D. Hull, *Introduction to Dislocations*, 2nd Ed., (Pergamon, Oxford, 1975).
6. J. P. Hirth and J. Lothe, *Theory of dislocations* (Wiley, New York, 1982).
7. Series of *Dislocation in Solids*, Edited by F. R. N. Nabarro, (North Holland Publishing Company, Armsterdam).
8. E. Schmid, Proc. Intl. Congr. Appl. Mech., Delft, 342 (1924).
9. J. W. Christian, Metall. Trans. A, **14A**, 1237 (1983).
10. F. Louchet and L. P. Kubin, Philos. Mag. A, **39**, 433 (1979).
11. A. Seeger and P. Schiller, *Physical Acoustics*, edited by W. P. Mason (Academics, New York 1966), Vol. 3A, p. 361.
12. M. S. Duesbery, Acta Metall., **31**, 1747 (1983).
13. M. S. Duesbery, Acta Metall., **31**, 1759 (1983).
14. M. S. Duesbery and Z. S. Basinski, Acta Metall. Mater., **41**, 643 (1993).
15. T. Taoka, S. Takeuchi, and E. Furubayashi, J. Phys. Soc. Japan, **19**, 701 (1964).
16. S. Sestak and N. Zarubova, Phys. Stat. Sol., **10**, 239 (1965).
17. A. S. Argon and S. R. Maloof, Acta Met., **14**, 1449 (1966).
18. D. Hull, J. F. Byron, and F. W. Noble, Can. J. Phys., **45**, 1091 (1967).
19. D. K. Bowen, J. W. Christian, and G. Taylor, Can. J. Phys., **45**, 903 (1967).

20. R. A. Foxall, M. S. Duesbery, and P. B. Hirsch, Can. J. Phys., **45**, 607 (1967).

21. P. J. Sherwood, F. Guiu, H. C. Kim, and P. L. Pratt, Can. J. Phys., **45**, 1075 (1967).

22. D. F. Stein, Can. J. Phys., **45**, 1063 (1967).

23. F. R. N. Nabarro, *Theory of Crystal Dislocations*, (Oxford University Press, Oxford, 1967).

24. J. P. Hirth, Metall. Trans., **16A**, 2085 (1985).

25. V. V. Bulatov, S. Yip and A. S. Argon, Philos. Mag. A, **72**, 453 (1995).

26. V. Vitek, Cryst. Lattice Defects, **5**, 1 (1974).

27. W. Xu and J. A. Moriarty, Phys. Rev. B, **54**, 6941 (1996).

28. L. H. Yang, P. Söderlind, and J. A. Moriarty, Philos. Mag. A, **81**, 1355 (2001).

29. S. Ismail-Beigi and T. A. Arias, Phys. Rev. Lett., **84**, 1499 (2000).

30. C. Woodward and S. I. Rao, Philos. Mag. A, **81**, 1305 (2001).

31. V. V. Bulatov *et al.*, Nature, **391**, 669 (1998).

32. J. A. Moriarty, W. Xu, P. Söderlind, J. Belak, L. H. Yang and J. Zhu, J. Eng. Mater. Tech., **121**, 120 (1999).

33. A. M. Cuitino, L. Stainier, G. Wang, A. Strachan, T. Çağın, W. A. Goddard, and M. Ortiz, *A Multiscale Approach for Modeling Crystalline Solids*, J. Comput.-Aided Mater. Design, to be published.

34. V. V. Bulatov and L. P. Kubin, Curr. Opin. Solid State Mater. Sci., **3 (6)**, 558 (1998).

35. R. Phillips, Curr. Opin. Solid State Mater. Sci., **3 (6)**, 526 (1998).

36. G. H. Campbell, S. M. Foiles, H. C. Huang, D. A. Hughes, W. E. King, D. H. Lassila, D. J. Nikkel, T. D. de la Rubia, J. Y. Shu, and V. P. Smyshlyaev, Mater. Sci. Eng. A, **251 (1-2)**, 1 (1998).

37. R. Phillips, D. Rodney, V. Shenoy, E. Tadmor, and M. Ortiz, Model. Simul. in Mater. Sci. Eng., **7 (5)**, 769 (1999).

38. M. I. Baskes, Curr. Opin. Solid State Mater. Sci., **4 (3)**, 273 (1999).

39. R. Phillips, *Crystals, Defects and Microstructures — Modeling Across Scales*, (Cambridge University Press, 2001).

40. D. R. Hartree, Proc. Camb. Phil. Soc., **24**, 89 (1928).

41. F. Fock, Z. Phys., **61**, 126 (1930).

42. P. Hohenberg and W. Kohn, Phys. Rev., **136**, B864 (1964).

43. W. Kohn and L. J. Sham, Phys. Rev., **140**, A1133 (1965).

44. V. V. Bulatov, J. F. Justo, W. Cai, S. Yip, A. S. Argon, T. Lenosky, M. de Koning, and T. D. de la Rubia, Philos. Mag. A, **81 (5)**, 1257 (2001).

45. A. M. Cuitino, L. Stainer and M. Ortiz, *Micromechanical modeling of hardening, rate sensitivity and thermal softening in bcc single crystals*, Journal of the Mechanics and Physics of Solids, 2001.

Chapter 2 Atomistic Simulation Methods

2.1 Overview

Computer simulations have been extensively used in the last several decades and become an indispensable part of scientific research. Providing detailed linkages between microscopic and macroscopic properties for the interested system, computer simulations help us to interpret and design experiments. We could simulate the response of a system and compare to the experimental observed values to understand the underlying physical processes. We also could simulate the system under conditions where experiments have not been performed or cannot be performed easily. Computer simulations in these cases are able to give the detailed microscopic information that is useful for designing better experiments. Among various simulation methods, molecular dynamics (MD) is one of the most widely used simulation methods for studying the properties of liquid, solids and molecules[1]. In MD simulation, the motion of individual particles (atoms or molecules) is modeled on the basis of either Newtonian deterministic dynamics or a Langevin-type stochastic dynamics, given their initial positions and velocities.

As the computer gets more powerful today and more accurate interatomic potentials were developed, modeling of more realistic and more complicated systems becomes possible. General materials always contain defects, such as grain boundary, dislocation, cracks, void, vacancy, impurities, etc. To study these materials requires to model ever-increasing system scale, at least millions of atoms. The massively parallel (MP) computing hardware got improved in the last 10 years, so did the parallel algorithms for MD simulations.

2.2 Molecular dynamics (MD) simulations

Molecular dynamics (MD) is a kind of computer simulation techniques solving the Newton's equations of motion with the time evolution for a collection of atoms interacting via a potential U. The equations of motion for all atoms in a system are integrated numerically by various finite differential methods at every time step. MD simulations could generate detailed phase space information for a system, such as atomic position and velocities at each time step. This information is also called the trajectory of the system. Further analysis of the trajectory from MD simulations provides the linkage between microscopic properties and average thermodynamic properties, such as pressure, temperature, internal energy, etc.

There are several different forms of molecular dynamics to simulate different ensembles. The original form of molecular dynamics generates the microcanonical ensemble, or constant volume and constant total energy dynamics (NVE). Nosé[2] added an extra degree of freedom to describe the thermal bath behavior, such that the temperature of the system will fluctuate with respect to the thermal bath temperature, this method can achieve canonical ensemble, or constant volume and constant temperature dynamics (NVT). Hoover[3] further developed the Nosé method to make the NVT calculation simpler. Andersen[4] developed a procedure to carry out isobaric-isoenthalpic ensemble, or constant pressure and constant enthalpy dynamics (HPN), by making volume a dynamical variable.

Parrinello and Rahman[5] generalized Andersen method to allow the changes in the size and shape of the simulation cell. They define a new matrix h by h=(**a**,**b**,**c**), where **a**, **b**

and **c** are the three vectors spanning the periodic repeating parallelepiped simulation cell. In Parrinello and Rahman's theory, h becomes a dynamical variable to describe the shape and size changes of simulation cell. The introduction of h into MD simulations makes it possible to give a full description of the elastic properties of the system. Thus, one can define the strain and stress tensor to be a new pair of extensive and intensive variables as V and P for a thermodynamics system, which lead to constant thermodynamic tension and constant enthalpy dynamics (HtN), or isobaric-isoenthalpic ensemble. The introduction of h also clarified that the original NVE dynamics is actually NhE, and original Nosé constant NVT MD is actually NhT form of molecular dynamics, in which the simulation box is kept unchanged not only in size but also in shape.

Ray and Rahman[6] have presented a detailed form of TtN dynamics, which combines Nosé constant-temperature theory with Parrinello-Rahman variable shape-size form of molecular dynamics. One can also combine Nosé's theory and Andersen's changing volume dynamics to achieve constant TPN dynamics. The TPN dynamics is suitable for isotropic liquid and gas phases, while the TtN dynamics can simulate elastic deformation of solid state.

In the remainder of this section, we discuss MD simulation methods for four ensembles (EhN, ThN, HtN and TtN). The Ray and Rahman's single Hamiltonian formulation is used to cover all of these different forms of MD.

The Hamiltonian for the TtN form of MD has the form

$$H(s,\pi,h,\Pi,f,P)=\sum_i \frac{\tilde{\pi}_i G^{-1}\pi_i}{2m_i f^2}+U+\frac{Tr(\tilde{\Pi}\Pi)}{2W}+V_0 Tr(t\varepsilon)+\frac{P^2}{2M}+(3N+1)K_B T_0 \ln(f),(1)$$

where (s_i, π_i) are the scaled coordinates and conjugate momentums of particle *i*, (h,Π) are the coordinates and momentums of the simulation cell, and (*f*, *P*) are the Nosé mass scaling variable and its conjugate momentum. U is the potential energy, which is a function of the position of atoms. The constants W ("piston mass") and M ("thermal inertia") are parameters to make *h* and *f* satisfy dynamical equations. The tilde indicates matrix transpose. T_0 is the thermal reservoir temperature, ε is the strain matrix which is given by

$$\varepsilon = (\tilde{h}_0^{-1} G h_0^{-1} - 1)/2, \tag{2}$$

where G is the metric tensor, $G = \tilde{h}h$, and h_0 is the reference state of the cell matrix *h* at zero tension. V_0 is the reference volume, calculated from $V_0=\det(h_0)$.

The usage of h matrix maps the simulation cell with any shape into a unit cell. Thus the position and momentum (r_i, p_i) of physical particles are related to the scaled particle variables (s_i, π_i) by $r_i = hs_i$ and $p_i = \tilde{h}^{-1}\pi_i / f$, and s_i range from 0~1. Therefore, the particle kinetic energy is represented by the first term in Hamiltonian (if we define the physical momentum of the particle as $p_i = m_i f h \dot{s}_i$, then $KE = \sum_i p_i^2 / 2m_i$), and the first two terms in Eq. (1) are the Hamiltonian for N particles in the simulation system.

The elastic energy of the system given in the 4th term in Eq. (1), and the 3rd term in Eq. (1) is similarly to the kinetic energy with the momentum of the *h* matrix. The last two terms are a similar kinetic term and the potential term for *f* (the mass scale variable to achieve constant temperature dynamics).

The equations of motion derived from Hamiltonian in Eq. (1) has the form of

$$m_i f^2 \ddot{s}_{i\alpha} = -\sum_{j \neq i} \frac{(\partial U / \partial r_{ij}) s_{ij\alpha}}{r_{ij}} - m_i (f^2 G^{-1} \dot{G} + 2 f \dot{f}) s_{i\alpha}, \tag{3a}$$

$$W \ddot{h}_{\alpha\beta} = P_{\alpha\beta} V \tilde{h}^{-1} - h V_0 h_0^{-1} t \tilde{h}_0^{-1}, \tag{3b}$$

$$M \ddot{f} = \frac{2KE}{f} - \frac{(3N+1) k_B T_0}{f}, \tag{3c}$$

where $P_{\alpha\beta}$ is the microscopic stress tensor and the second term in Eq. (3b) is related to the applied tension to the system. It is the difference of the system tension and applied tension that causes the fluctuation of h matrix.

With no constraints, TtN dynamics requires the solutions of 3N+9+1 equation of motions. (N is the number of movable particles with 3 degrees of translation freedom, h matrix has 9 independent components, and one more degree of motion of f). We can get the equations of motion for the other three dynamics from TtN dynamics by exerting constraints. If the Nosé variable f satisfies $\dot{f} = 0, f = 1$, then only the Eqs. (3a) and (3b) are needed to be solved. This way, we reduce the constant TtN MD to the constant HtN dynamics. Similarly, constraints on h as $\dot{h} = 0$, h=constant lead to the equations of motion reduced to the combination of Eqs. (3a) and (3c), such that a constant ThN dynamics is achieved. If f and h satisfy that $\dot{f} = 0, f = 1$ and $\dot{h} = 0, h$=constant, the only equation of motion is Eq. (3a), which gives the constant EhN dynamics.

2.3 Embedded atoms model (EAM) force fields (FF)

2.3.1 Physical foundation

The embedded-atom method (EAM) force field is a many-body potential for computing the total energy of metallic systems, in which coordinate-dependent (or many-body) interactions are prominent[7]. In contrast, much simpler pair potentials always lead to elastic constants $C_{12}=C_{44}$ (Cauchy relation) in cubic solids and the ratio of the vacancy formation energy to cohesive energy as unity, which strongly deviate from the fundamental properties of metallic solids[8].

Daw and Baskes[9,10] first proposed the EAM potential. They view the energy of the metal as the energy obtained by embedding an atom into the local electron density provided by the other atoms of the system. In addition, there is an electrostatic interaction. The formula they used is

$$E_{coh} = \sum_i G_i\left(\sum_{j=i} \rho_j^a(R_{ij})\right) + \frac{1}{2}\sum_{i,j(i\neq j)} U_{ij}(R_{ij}), \tag{4}$$

where G is the embedding energy defined as the interaction of the atom with the background electron gas. The background electron density for each atom in the equation is determined by evaluating at its nucleus the superposition of atomic-density tails from other atoms. ρ^a is the spherically averaged atomic electron density and U is an electrostatic, two-atom interaction. A particular appealing aspect of the above EAM is its

physical picture of metallic bonding, i.e., each atom is embedded in a host electron gas created by its neighboring atoms.

Next, I will show how to derive the approximate expression as Eq. (4) for the cohesive energy of a metallic system that is an explicit function of the positions of the atoms.

The density functional expression for the cohesive energy of a solid is as follows[11]

$$E_{coh} = G[\rho] + \frac{1}{2}\sum_{i,j}{}' \frac{Z_i Z_j}{R_{ij}} - \sum_i \int \frac{Z_i \rho(\vec{r})}{|\vec{r} - \vec{R}_i|} d\vec{r} + \frac{1}{2}\iint \frac{\rho(\vec{r}_1)\rho(\vec{r}_2)}{r_{12}} d\vec{r}_1 d\vec{r}_2 - E_{atoms}, \quad (5)$$

where the sums over i and j are over the nuclei of the solid, the primed sum indicates the omission of the i=j term, Z_i and $\vec{R}_i$ are the charge and position of the ith nucleus, the integrals are over $\vec{r}$ (or $\vec{r}_1$ and $\vec{r}_2$), and $r_{12}=|\vec{r}_1 - \vec{r}_2|$. E_{atoms} is the collective energy of the isolated atoms. G[ρ] is the kinetic, exchange, and correlation energy functional.

To go from Eq. (5) to Eq. (4), the following two assumptions are made.

(a) G[ρ] can be described by $G[\rho] = \int g(\rho(\vec{r}), \nabla\rho(\vec{r}), \nabla^2\rho(\vec{r}), ...) d\vec{r}$, where g is the density and is assumed to be a function of the local electron density and its lower derivatives,

(b) The electron density of the solid can be described as a linear superposition of the densities of the individual atoms $\rho_s(\vec{r}) = \sum_i \rho_i^a(\vec{r} - \vec{R}_i)$.

The first approximation is motivated by studies of the response function of the nearly uniform electron gas. The second approximation is justified by the observation that, in many metals, the electron distribution in the solid is closely represented by a superposition of atomic densities. In addition, due to the variational nature of the energy functional, errors in the assumed density should only affect the energy to second order. It is also useful to define the embedding energy for an atom in an electron gas of some constant density $\overline{\rho}$ (neutralized by a positive background):

$G_i[\overline{\rho}_i] = G[\rho_i^a + \overline{\rho}_i] - G[\rho_i^a] - G[\overline{\rho}_i]$. Using the above assumptions and the definition for the embedding energy, the Eq. (6) can be obtained.

$$E_{coh} = \sum_i G_i\left(\sum_{j\neq i} \rho_j^a(R_{ij})\right) + \frac{1}{2}\sum_{i,j(i\neq j)} U_{ij}(R_{ij}) + E_{err} \quad , \tag{6}$$

The error (E_{err}) is a function of the background density $\overline{\rho}_i$. Setting the error to zero gives an equation for the optimal background density. The solution to E_{err}=0 is discussed in detail by Daw[12].

The EAM method has been applied successfully to study bulk and interface problems, such as phonons[13], thermodynamics functions and melting point[14,15], liquid metals[16], defects[17-19], grain boundary structure[21-25], alloys[18,19,26,27], segregation to grain boundaries[27-29], interdiffusion in alloys[30,31], and fracture and mechanical properties[32-38]. The EAM has been also applied to problems in surface structure[17-19,39-42], adsorbate phase diagrams[43-47], segregation to surfaces[48-54], surface structural order-disorder transitions[40], surface ordered alloys[41,53], surface phonons[55,56], and clusters on surfaces[57,58].

Despite much success, EAM method will not work as well in the following two cases: (1) where directional bonding is important, such as semiconductors and elements from the middle of the transition series[59] and (2) where the Fermi-surface or band-structure effects are important.

2.3.2 The qEAM FF

We develop and use the qEAM many-body Embedded-Atom-Model (EAM) type force field (FF) for Ta. This FF is based on *ab initio* QM calculations and has been used previously for molecular dynamics (MD) studies of the melting temperature of Ta as a function of pressure[60], where it predicts values in excellent agreement with experiment. It has also been used to characterize the nature of spall failure[61].

The qEAM FF uses a functional form similar to that proposed by Chantasiriwan and Milstein[62]. The total energy of system with atomic positions $\{\mathbf{r}_i\}$ is given by

$$E = \sum_i F(\rho_i) + \sum_{i<j} \phi(r_{ij}), \tag{7}$$

with

$$\rho_i = \sum_{i \neq j} f(r_{ij}), \tag{8}$$

where $F(\rho)$ is the embedding energy, ρ_i is the total "electronic density" at site i, $f(r_{ij})$ is the electron density function, $\phi(r_{ij})$ is the pair potential function, and r_{ij} is the distance between atoms i and j.

The electronic density is given by

$$f(r) = \frac{[1 + a_1 \cos(\alpha r / V^{\frac{1}{3}}) + a_2 \sin(\alpha r / V^{\frac{1}{3}})}{r^{\beta}}, \quad (9)$$

where V is the volume per atom, a_1=0.07293238, a_2=0.15781672, α(1/Å)=21.79609053, and β=7.79329426.

The pair potential $\phi(r)$ is taken to be a polynomial function,

$$\phi(r) = (r - r_m)^4 [b_0 + b_1 r + b_2 r^2 + b_3 r^3 + b_4 r^4 + b_5 r^5 + b_6 r^6 + b_7 r^7], \quad (10)$$

where r_m(Å)=4.81253968 is the cutoff radius. The parameters b_i have the units of eV/Å$^{(4+i)}$ with b_0 = 6.50281587, b_1 = -11.26455130, b_2 = 8.01451544, b_3 = -2.97299223, b_4 = 0.60004206, b_5= -0.06222106, b_6 = 0.00258801, and b_7 = -0.00000504.

The embedding function $F(\rho)$ is determined from the Rose universal equation of state[63],

$$F(\rho) = E_{EOS}(a^*) - \frac{1}{2}\sum \phi(r), \quad (11a)$$

where

$$E_{EOS}(a^*) = -E_{coh}(1 + a^* + k a^{*3} + f_4 a^{*4}) e^{-a^*}, \quad (11b)$$

with

$$a^* = \frac{a - a_0}{a_0 \lambda}, \quad (11c)$$

The parameters entering the definition of the embedding energy are a_0(Å)=3.32389219, E_{coh}(eV)=8.154204, λ=0.207828, k=-0.00717801, and f_4= -0.00000504.

2.3.3 Validation of the qEAM FF[60]

As input data to fit the qEAM FF, we use the following results from the linearized augmented plane wave (LAPW) method with the generalized gradient approximation (GGA) QM calculations.

(1) The zero temperature equation of state (EOS) of Ta for bcc, fcc, and hcp crystal structures for pressures up to ~ 500 GPa,

(2) the elastic constants,

(3) the volume relaxed vacancy formation energy also as a function of pressure,

(4) the equation of state for the A15 structure of Ta,

(5) the (100) surface energy in the bcc Ta,

(6) the energies for shear twinning of the bcc Ta.

To describe the properties of dislocation in bcc Ta accurately, the qEAM FF must reproduce the quantum calculation results for important quantities, such as equation of state, elastic constants and energetics of homogeneously shear for bcc Ta crystal. In the following we show a detailed comparison between the qEAM FF and the data it was fitted to.

A. Equation of state (EOS) for bcc Ta

Figure 2-1 shows the energy [in Figure 2-1(a)] and pressure [in Figure 2-1(b)] as a function of volume for bcc Ta at T=0 K. The circles denote the LAPW GGA results and the lines the qEAM FF calculations. The QM and the qEAM FF results agree to each other. We also calculate the T=330 K EOS for bcc Ta with the qEAM FF using

isothermal-isobaric (NPT) MD with a Hoover[3] thermostat and Rahman-Parrinello[64] barostat.

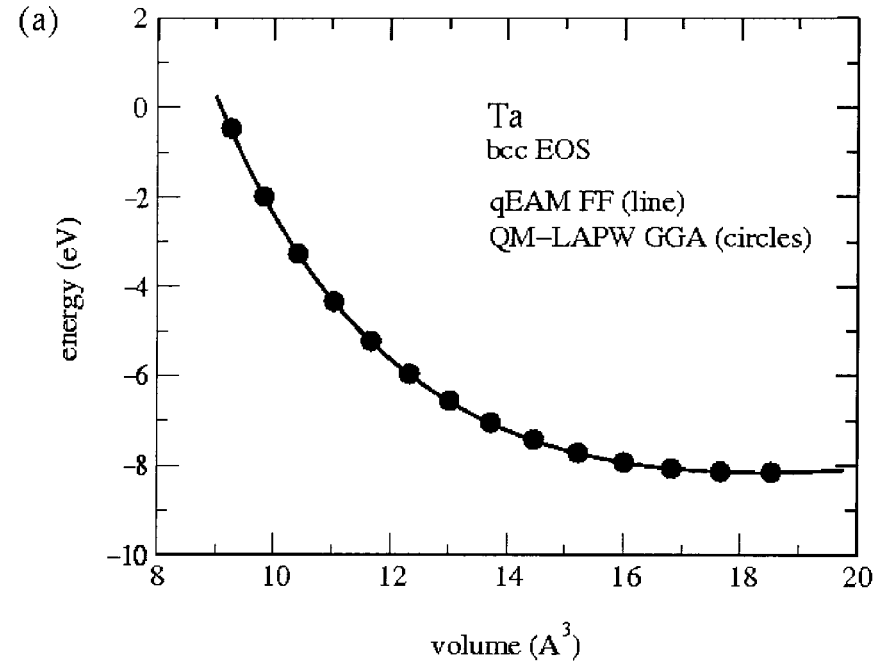

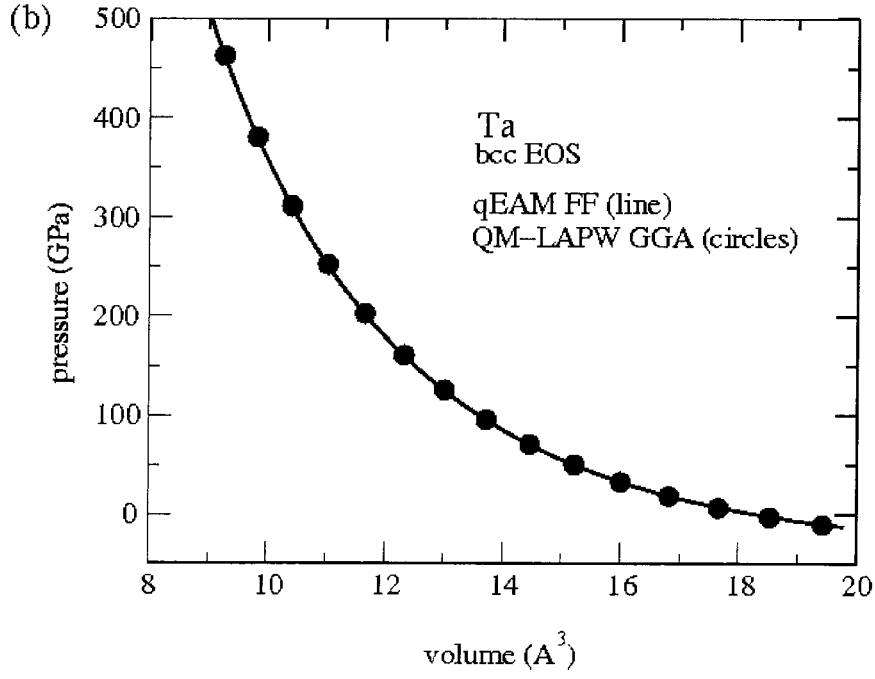

Figure 2-1. Zero temperature EOS for bcc Ta, LAPW GGA and qEAM FF results: energy [Figure 2-1(a)] and pressure [Figure 2-1(b)] as a function of volume. Circles denote LAPW GGA results and lines show qEAM FF results.

In Table 2-1 we show the zero pressure volume, bulk modulus and its first derivative with respect to volume for bcc Ta at T=0K and 300K; we also show recent compressibility data[65] obtained in a diamond-anvil cell at room temperature. It is clear that the qEAM FF reproduces the EOS for bcc Ta very well.

Table 2-1. EOS parameters for bcc Tantalum.

	V_0 (Å^3)	B_T (GPa)	B_T'	C_{11} (GPa)	C_{12} (GPa)	C_{44} (GPa)
T=0 K						
LAPW-GGA	18.33	188.27	4.08	245.18	159.8	67.58
qEAM FF	18.36	183.04	4.16	272.54	137.57	69.63
FP LMTO GGA SC [a]	17.68	203	-	281	163	93
T=300 K						
qEAM FF	18.4	176	4.9	-	-	-
Experiment [b]	18.04	194.7±4.8	3.4	264	159.7	82.2

[a] Reference 66.

[b] Reference 65.

B. Elastic constants

By fitting our energy-volume data [Figure 2-1(a)] to Rose's universal equation of state, we obtained zero pressure volume (V_0), zero temperature bulk modulus (B_T), and its derivative with respect to pressure (B_T') and, furthermore, the bulk modulus at different pressures.

Static elastic constants [$C_s = (C_{11}-C_{12})/2$ and C_{44}] were obtained from strain energies by straining the bcc cell with volume conserving tetragonal and orthorhombic. We calculate C_s using tetragonal strain of the cubic bcc lattice:

$$\vec{a} = a(1+\varepsilon,0,0),$$

$$\vec{b} = a(0,1+\varepsilon,0),$$

$$\vec{c} = a(0,0,1/(1+\varepsilon)^2), \tag{12}$$

where a is the cubic lattice constant of the system, $\vec{a}$, $\vec{b}$ and $\vec{c}$ are the lattice vectors and ε is the strain. C_s is related to the quadratic term of the strain energy

$$E(\varepsilon) = E_0 + 6V_0C_s\varepsilon^2 + O(\varepsilon^3), \tag{13}$$

where E_0 is the energy of the unstrained system and V_0 is its volume.

Similarly C_{44} is obtained from the orthorhombic strain:

$$\vec{a} = a(1,\varepsilon,0),$$

$$\vec{b} = a(\varepsilon,1,0),$$

$$\vec{c} = a(0,0,1/(1-\varepsilon^2)), \tag{14}$$

the shear constant C_{44} is obtained from

$$E(\varepsilon) = E_0 + 2V_0C_{44}\varepsilon^2 + O(\varepsilon^3), \tag{15}$$

Table 2-1 reported the obtained bulk modulus and elastic constants (C_{11}, C_{12} and C_{44}) at 0 K and 300 K for bcc Ta using the qEAM FF and QM calculations. Figure 2-2 shows the elastic constants [bulk modulus $B_T=(C_{11}+2C_{12})/3$, $C_s=(C_{11}-C_{12})/2$ and C_{44}] as a function of pressure obtained with the qEAM FF (filled circles and full lines) and the LAPW results. While the agreement in B_T is excellent and that for C_s is good, the qEAM FF greatly underestimates C_{44} for high pressures.

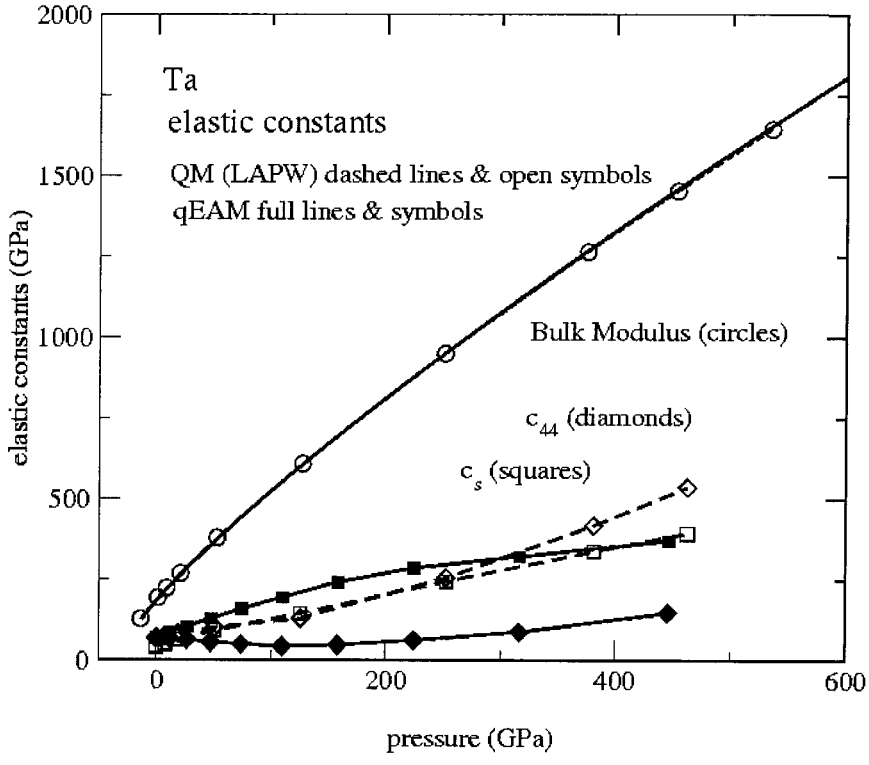

Figure 2-2. Zero temperature elastic constants for Ta, LAPW GGA and qEAM FF results. Circles show bulk modulus [$(C_{11} + 2C_{12})/3$]; diamonds show C_{44} and squares represent C_s = $(C_{11}-C_{12})/2$. qEAM FF results are shown with filled symbols and full lines and *ab initio* LAPW results with open symbols and dashed lines.

C. Energetics of homogeneously sheared bcc crystal

The ideal shear strength is defined to be the stress separating elastic and plastic deformation when a homogeneous shear is applied to a perfect crystal. It gives an upper bound for the shear strength of the material. The shear transformation is in the direction of the observed twining mode and deforms the crystal into itself[66, 67]. For bcc crystal we use the following transformation of the cell vectors[66, 67]

$$\vec{a} = \frac{1}{2}[\bar{1}\,1\,1] + \frac{s}{\sqrt{18}}[\bar{1}\,\bar{1}\,1],$$

$$\vec{b} = \frac{1}{2}[1\,\bar{1}\,1] + \frac{s}{\sqrt{18}}[\bar{1}\,\bar{1}\,1],$$

$$\vec{c} = \frac{1}{2}[1\,1\,\bar{1}], \qquad (16)$$

when the shear variable s is equal to the twinning shear $s = s_{tw} = 2^{-1/2}$ the lattice vectors [a = 1/3 [$\bar{2}$12], b=1/3 [1$\bar{2}$2] and c = [11$\bar{1}$]] form a bcc structure, twin of the initial one.

In this way one can calculate the energy along the shear path,

$$W(s) = e(V, s) - e(V, s = 0), \qquad (17)$$

where e(V, s) is the energy per atom of the deformed system and e(V, s = 0) is the perfect crystal energy. The energy barrier associated with this transformation is W_{max} = W (s = 0.5). The corresponding stress is defined as:

$$\tau(s) = \frac{1}{V}\frac{dW(s)}{ds}, \qquad (18)$$

The ideal shear strength (τ_{max}) is defined as the maximum stress along the path. Figure 2-3 shows energy and stress as a function of shear using the qEAM FF for zero pressure volume.

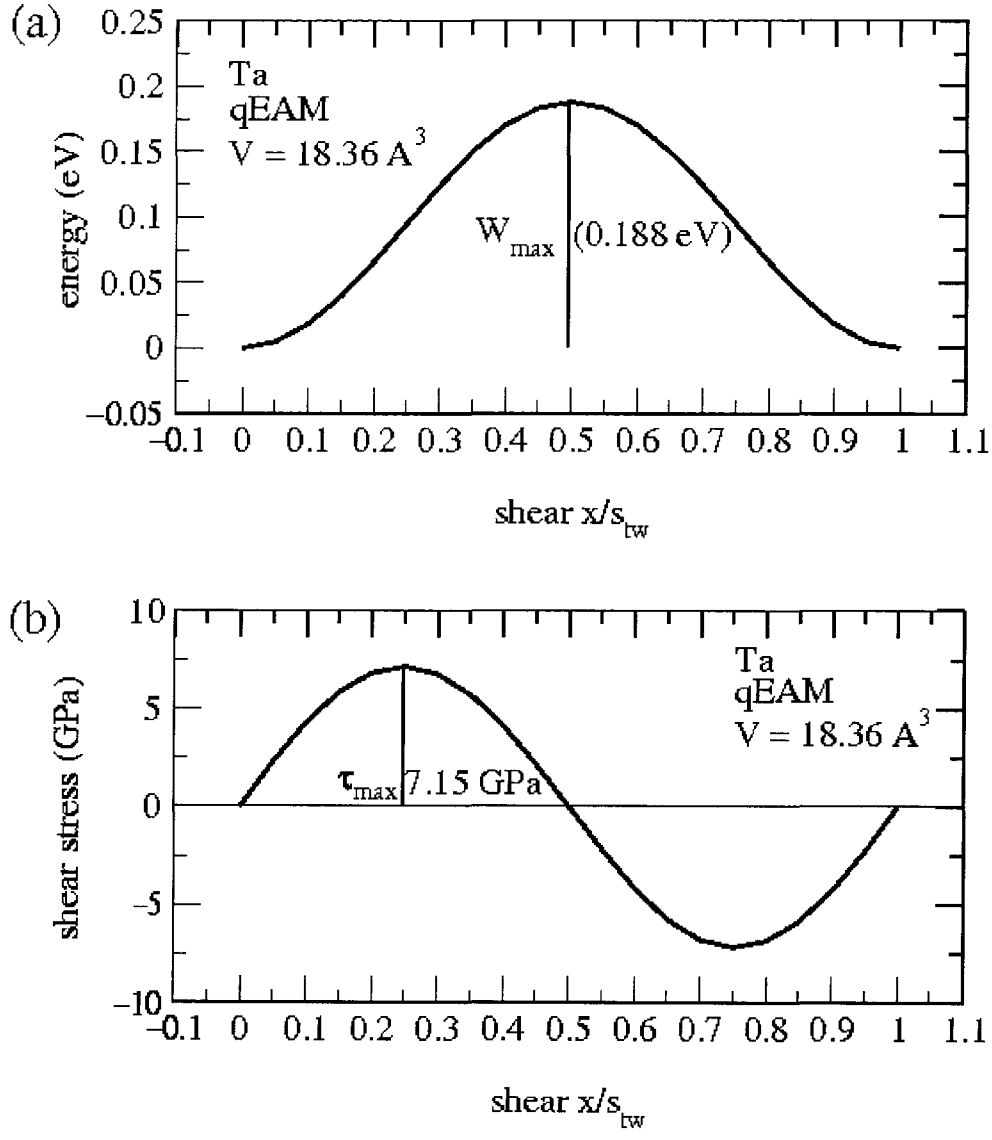

Figure 2-3. Ideal shear strength of Ta using qEAM FF at zero temperature and volume V=18.36 $Å^3$. We show energy W(s) [Figure 2-3(a)] and stress τ(s) [Figure 2-3(b)] as a function of shear.

Söderlind and Moriarty calculated W(s) and τ(s) for Ta at different volumes, from first principles. In developing the qEAM FF we used W_{max} for V=17.6186 $Å^3$ and V=10.909 $Å^3$ as part of the training set. In Table 2-2 we show a comparison between the

first principles results and the ones obtained using the qEAM FF. We can see that the qEAM results[66] are in very good agreement with the *ab initio* calculations.

Table 2-2. Shear deformation in the observed twinning mode in Ta.

Volume ($Å^3$)	W_{max} (eV)	τ_{max} (GPa)	W_{max} (eV)	τ_{max} (GPa)
	qEAM FF		FP LMTO GGA SC [a]	
18.360000	0.188	7.14	-	-
17.618602	0.2	8.0	0.194	7.37
15.143996	0.26	12.05	0.276	12.4
10.9090116	0.43	28.2	0.566	36.2

[a] Reference 66.

2.4 References

1. M. P. Allen and D. T. Tildesley, *Computer Simulation of Liquids*, (Oxford, 1987).
2. S. Nosé, J. Chem. Phys., **81**, 511 (1984).
3. W. G. Hoover, Phys. Rev. A, **31**, 1695 (1985).
4. H. C. Andersen, J. Chem. Phys., **72**, 2384 (1980).
5. M. Parrinello and A. Rahman, Phys. Rev. Lett., **45**, 1196 (1980).
6. J. R. Ray and A. Rahman, J. Chem. Phys., **82**, 4243 (1985).
7. M. S. Daw, S. M. Foiles and M. I. Baskes, Mater. Sci. Rep., **9**, 251 (1993).
8. F. Ercolessi, M. Parrinello and E. Tosatti, Philos. Mag. A, **58**, 213 (1988).
9. M. S. Daw and M. I. Baskes, Phys. Rev. Lett., **50**, 1285 (1983).
10. M. S. Daw and M. I. Baskes, Phys. Rev. B, **29**, 6443 (1984).
11. P. Hohenberg and W. Kohn, Phys. Rev. B, **37**, 10411 (1964).
12. M. S. Daw, Phys. Rev. B, **39**, 7441 (1989).
13. M. S. Daw and R. D. Hatcher, Solid State Commun., **56**, 697 (1985).
14. S. M. Foiles and M. S. Daw, Phys. Rev. B, **38**, 12643 (1988).
15. S. M. Foiles and J. B. Admas, Phys. Rev. B, **40**, 5909 (1989).
16. S. M. Foiles, Phys. Rev. B, **32**, 3409 (1985).
17. M. S. Daw and M. I. Baskes, Phys. Rev. B, **29**, 6443 (1984).
18. S. M. Foiles, M. I. Baskes and M. S. Daw, Phys. Rev. B, **33**, 7983 (1986).
19. S. M. Foiles, M. I. Baskes and M. S. Daw, Phys. Rev. B, **37**, 10387 (1988).

20. S. M. Foiles, M. I. Baskes and M. S. Daw, in *Interfacial Structure, Properties and Design*, eds. M. H. Yoo, W. A. T. Clark and C. L. Briant, (Materials Research Society, Pittsburgh, PA, 1988).

21. S. M. Foiles, Acta Metall., **37**, 2815 (1989).

22. M. J. Mills, G. J. Thomas, M. S. Daw and F. Cosandey, Mater. Res. Soc. Symp. Proc., **159**, 365 (1989).

23. U. Dahmen, C. J. D. Hetherington, M. A. O'Keefe, K. H. Westmaccott, M. J. Mills, M. S. Daw and V. Vitek, Philos. Mag. Lett., **62**, 327 (1990).

24. M. J. Mills and M. S. Daw, Mater. Res. Soc. Proc., **183**, 15 (1990).

25. M. J. Mills, M. S. Daw, G. J. Thomas and F. Cosandey, Ultramicroscopy, **40**, 247 (1992).

26. S. M. Foiles and M. S. Daw, J. Met., **39**, 39 (1987).

27. S. M. Foiles, in *High-Temperature Ordered Intermetallic Alloys*, Vol. **2**, eds. N.S. Stoloff, C. C. Koch, C. T. Liu and O. Izumi (Materials Research Society, Pittsburgh, PA, 1987).

28. S. M. Foiles, Phys. Rev. B, **40**, 11502 (1989).

29. A. Seki, D. N. Seidman, Y. Oh and S. M. Foiles, Acta Metall., **39**, 3167 (1991).

30. J. B. Admas, S. M. Foiles and W. G. Wolfer, J. Mater. Res., **4**, 102 (1989).

31. J. B. Admas, S. M. Foiles and W. G. Wolfer, in *Atomistic Simulation of Materials*, eds. D. Srolovitz and V. Vitek, (Plenum Press, New York, 1989).

32. M. I. Baskes, S. M. Foiles and M. S. Daw, J. Phys., **C5**, 483 (1988).

33. M. S. Daw, M. I. Baskes, C. L. Bisson and W. G. Wolfer, in *Modeling Environmental Effects on Crack Growth Processes*, Metallurgical Society Fall Meeting, Toronto, Canada (1985), eds. R. H. Jones and W. W. Gerberich.

34. M. S. Daw and M. I. Baskes, in *NATO Advanced Workshop on Physics and Chemistry of Fracture*, Bad Reichenhall, Weat Germany, eds. R. M. Latanision and R. H. Jones (Nijhoff, Dordrecht, 1986).

35. M. I. Baskes and M. S. Daw, in *Fourth International Conference on the Effect of Hydrogen on the Behavior of Materials*, Jackson Lake Lodge, Moran, WY, eds. N. Moody and A. Thompson (The Minerals, Metals, and Materials Society, Warrendale, PA, 1989).

36. R. G. Hoagland, M. I. Baskes, M. S. Daw and S. M. Foiles, J. Mater. Res., **5**, 313 (1990).

37. R. G. Hoagland, M. S. Daw, S. M. Foiles and M. I. Baskes, in *Atomic Scale Calculations of Structure in Materials,* eds. M. S. Daw and M. A. Schluter (Materials Research Society, Pittsburgh, PA, 1990).

38. R. G. Hoagland, M. S. Daw and J. P Hirth, J. Mater. Res., **6**, 2565 (1991).

39. S. M. Foiles, Surface Sci., **191**, L779 (1987).

40. M. S. Daw and S. M. Foiles, Phys. Rev. Lett., **59**, 2756 (1987).

41. M. S. Daw and S. M. Foiles, in 2^{nd} *International Conference on the Structure of Surfaces*, Amsterdam, The Netherlands, eds. J. F. van der Veen and M. A. Van Hove, (Springer, Berlin, 1987).

42. M. S. Daw and S. M. Foiles, J. Vacuum Sci. Technol. A, **4**, 1412 (1986).

43. S. M. Foiles and M. S. Daw, J. Vacuum Sci. Technol. A, **3**, 1565 (1985).

44. M. S. Daw and S. M. Foiles, in *1st International Conference on the Structure of Surfaces*, Berkeley, CA, eds. M. A. Van Hove and S. Y. Tong (Springer, Berlin, 1985).

45. T. E. Felter, S. M. Foiles, M. S. Daw and R. H. Stulen, Surface Sci., **171**, L379 (1986).

46. M. S. Daw and S. M. Foiles, Phys. Rev. B, **35**, 2128 (1987).

47. T. L. Einstein, M. S. Daw and S. M. Foiles, Surface Sci., **227**, 114 (1990).

48. S. M. Foiles, Phys. Rev. B, **32**, 7685 (1985).

49. S. M. Foiles, J. Vacuum Sci. Technol. A, **4**, 761 (1986).

50. S. M. Foiles, in *Computer-Based Microscopic Description of the Structure and Properties of Materials*, eds. J. Broughton, W. Krakow and S. T. Pantelides (Materials Research Society, Pittsburgh, PA, 1986).

51. S. M. Foiles, in Physical and Chemical Properties of Thin Metal Overlayers and Alloy Surfaces, eds. D. M. Zehner and D. W. Goodman, (Materials Research Society, Pittsburgh, PA, 1987).

52. S. M. Foiles, J. Vacuum Sci. Technol. A, **5**, 889 (1987).

53. S. M. Foiles, Surface Sci., **191**, 329 (1987).

54. S. M. Foiles, in *Surface Segregation and Related Phenomena*, eds. P. A. Dowben and A. Miller (CRC Press, Boca Rotan, 1990).

55. J. S. Nelson, M. S. Daw and E. C. Sowa, Phys. Rev. B, **40**, 1465 (1989).

56. J. S. Nelson, E. C. Sowa and M. S. Daw, Phys. Rev. Lett., **61**, 1977 (1988).

57. P. Schwoebel, S. M. Foiles and G. Kellogg, Phys. Rev. B, **40**, 10639 (1989).

58. A. F. Wright, M. S. Daw and C. Y. Fong, Phys. Rev. B, **42**, 9409 (1990).

59. A. E. Carlsson, in *Solid State Physics: Advances in Research and Applications*, eds. H. Ehrenreich and D. Turnbull, (Academic Press, Boston, 1990), Vol **43**, P1.

60. A. Strachan, T. Çağın, O. Gülseren, S. Mukherjee, R. E. Cohen, and W. A. Goddard, *First Principles Force Field for Metallic Tantalum*, Phys. Rev. B, submitted.

61. A. Strachan, T. Çağın and W. A. Goddard, Phys. Rev. B, **63**, 060103 (2001).

62. S. Chantasiriwan and F. Milstein, Phys. Rev. B, **53**, 14080 (1996).

63. J. H. Rose, J. Ferrante, and J. R. Smith, Phys. Rev. Lett., **47**, 675 (1981).

64. M. Parinello and A. Rahman, J. Appl. Phys. **52**, 7182 (1981).

65. H. Cynn and C. Yoo, Phys. Rev. B, **59**, 8526 (1999).

66. P. Söderlind and J. A. Moriarty, Phys. Rev. B, **57**, 10340 (1998).

67. A. T. Paxton, P. Gumbsch and M. Methfessel, Philos. Mag. Lett., **63**, 267 (1991).

Chapter 3 Core structure and core energy of 1/2a<111> screw dislocation

3.1 Overview

The core energy of an isolated dislocation is an essential parameter in modern plasticity theory[1]. Xu *et al.*[2], Beigi and Arias[3], and Yang *et al.*[4] have computed the core energy of the a/2<111> screw dislocation for Mo and Ta by applying anisotropic elastic theory. There are two important parameters in their calculations.

1. **Anisotropic shear modulus.** It can be derived directly from the elastic constants of the perfect crystal[5] or extracted from the atomistic simulations of the dislocation energy as a function of cell size (as will be shown below). A good agreement between the results from two approaches indicates a quantitative correspondence between the elasticity theory and atomistic simulations.

2. **Dislocation core radius**. In previous studies[2,3], an approximate value 2b was obtained by fitting the strain energy for cylinders containing a dislocation with various radii to anisotropic elastic theory. Since the computed core energy depends strongly on the core radius, a physically based definition of the dislocation core radius is necessary.

To provide an increased atomistic insight into the nature of the dislocation core, we computed the dislocation core energy using two approaches (an atomistic model and a continuum model). By comparing and contrasting these two approaches, we obtained a consistent core energy and core radius of the a/2<111> screw dislocation in Ta.

3.2 Dislocation core structure

3.2.1 Construction of the dislocation quadrupole

To investigate the core structure and determine the core energy of 1/2a<111> screw dislocations in Ta, we use a quadrupole arrangement of dislocations in a periodic simulation cell. Thus, two of the dislocations have Burgers vector **b**=a/2[111] and the other two have **b**=a/2[-1-1-1]. This arrangement (Figure 3-1) leads to little positional misfit of atoms across the cell boundary due to the effect of periodic images.

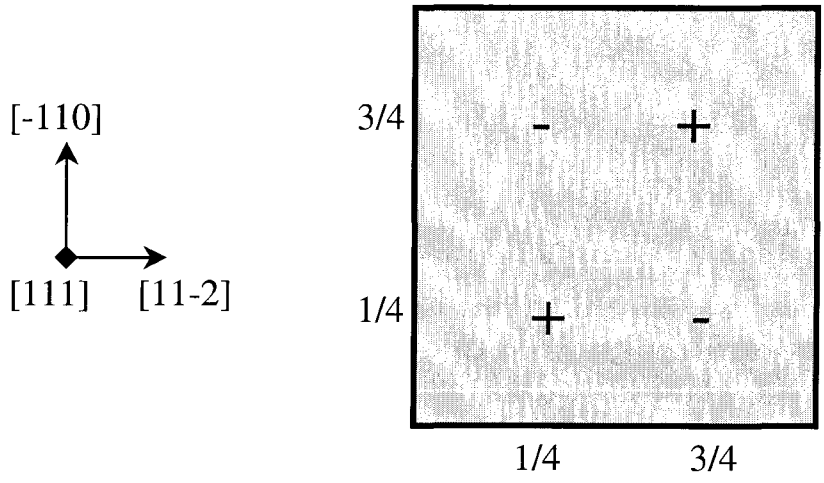

Figure 3-1. The geometrical arrangement of the dislocation quadrupole simulation cell. The [111], [-110] and [11-2] boundaries of simulation cells are periodic boundaries.

The initial configuration of the dislocation quadrupole was constructed using isotropic elastic theory. The displacement of each atom along the [111] direction is given by

$$\Delta d_{[111]}(r_j) = \sum_I \frac{\varphi_I(r_j)}{2\pi} b_I \ , \qquad (1)$$

where the sum runs over all dislocations on the (111) plane. Here, φ_I is the counterclockwise angle on the (111) plane from the [11-2] direction to the vector joining the center of dislocation I to the atom j, while $\boldsymbol{b}_I$ is the Burgers vector of dislocation I and b_I is equal to |a/2<111>|=2.88 Å.

The dislocations are initially located at the geometric centers of a triangle surrounded with three [111] columns of atoms. For the bcc structure, there are two kinds of dislocation core configurations that can be transformed to each other by reversing the Burgers vector; they are called "*easy core*" [Figure 3-2(c)] and "*hard core*" [Figure 3-2(b)][2]. The easy core is the low energy form and the only one we find from minimizations. Indeed, the dynamical simulations (Chapter 4) show that the dislocation moves from one easy form to an adjacent one avoiding the high-energy hard core.

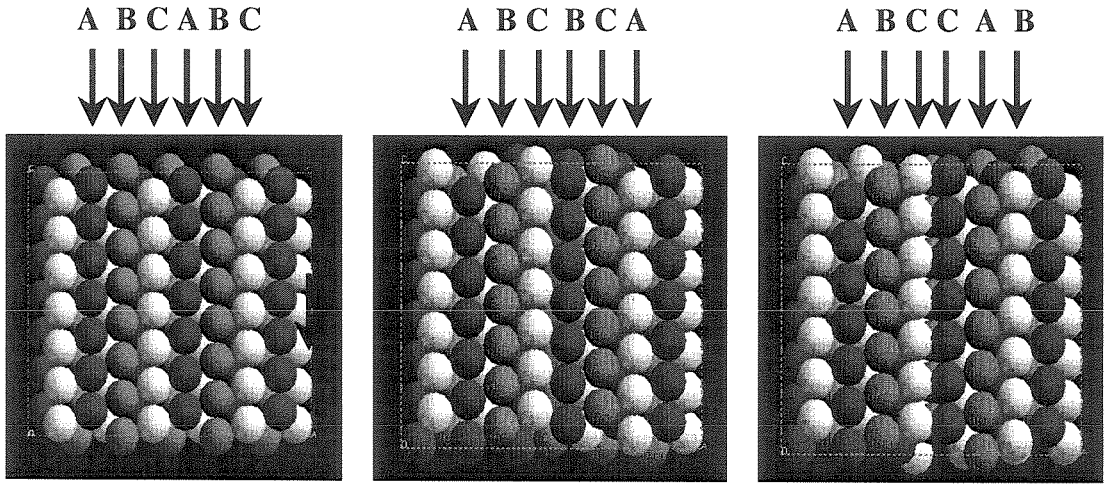

(a) (b) (c)

Figure 3-2. The [-110] view of the a/2<111> screw dislocation in Ta. The stacking sequence of {110} planes on both sides of the dislocation is shown as (a) 'ABCABC' in

bulk bcc crystal, (b) 'ABCBCA' in the "hard core" screw dislocation and (c) 'ABCCAB' in the "easy core" screw dislocation.

3.2.2 The differential displacement (DD) map

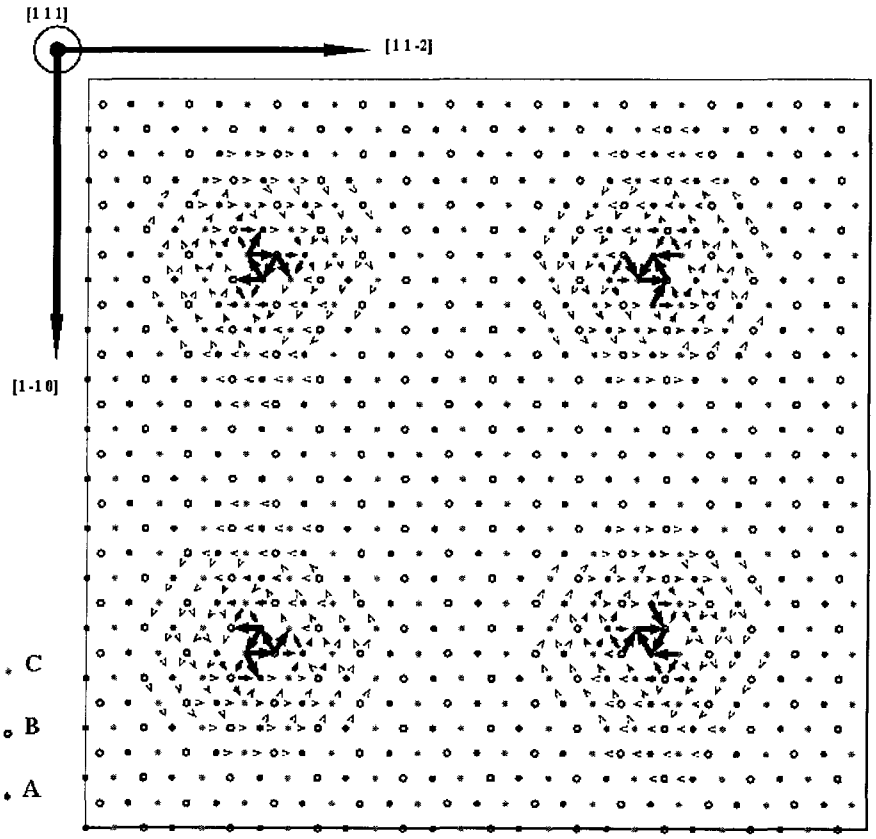

Figure 3-3. Differential displacement (DD) map for the equilibrated dislocation quadrupole in which there are 5670 atoms and each dislocation is 7 b long.

Some important features of dislocation cores can be visualized using differential displacement (DD) maps[6]. Figure 3-3 shows the DD map for a quadrupolar arrangement of dislocations after relaxing the atomic positions (using the qEAM FF). In this map, the atoms are represented by circles and projected on a (111) plane of the bcc lattice. The

arrows in the DD map indicate the relative displacements of neighboring atoms in the [111] direction with respect to their positions in the perfect bcc crystal. The direction of the arrow represents the sign of the displacement and the magnitude of the arrow is proportional to the relative displacement between the corresponding atoms. When an arrow spans the full distance between two atoms, the relative displacement is b/3.

Figure 3-3 shows that the equilibrium dislocation cores have threefold symmetry and spread out in three <112> directions on {110} planes in the DD map. There are 6 equivalent <112> directions on the (111) plane, so there are two kinds of "easy core" configurations, each with the threefold symmetry. The dislocations with different core configurations are energetically degenerate both in terms of core energy and in terms of elastic energy. In a dislocation quadrupole, changing the dislocation core configuration does not affect the equilibrium energy of the simulation cell.

3.2.3 Polarization of the dislocation

In addition to the relative displacement of neighboring atoms in the [111] direction, we computed the difference between the atomistic relaxation and the predictions of isotropic elasticity theory [Eq. (1)] for the atomic displacements parallel to the Burgers vector. We find that except for the 6 columns of atoms closest to the dislocation line, elastic theory and the atomistic relaxation lead to atomic displacement differences within (-0.05 Å, 0.05 Å). This shows that the continuum theory accurately describes the elastic displacement field of a screw dislocation, failing only for the innermost 6 columns of atoms within the dislocation core.

An interesting feature from the atomistic simulations is that after relaxation the three central columns of atoms of the dislocation translate simultaneously by 0.267 Å (~0.09 b) either in the [111] direction or the [-1-1-1] direction. This phenomenon is called *dislocation polarization*[7]. Dislocation polarization can be quantified by the simultaneous displacement in the [111] direction of the central three atoms at the dislocation core[4]. The [111] polarization leads to the dislocation core spreading along the [-1 -1 2], [-1 2 -1], and [2 -1 -1] directions in DD map. For the opposite polarization (in the [-1-1-1] direction) the dislocation cores spread out along the [1 1 -2], [1 -2 1], and [-2 -1 -1] directions in DD map. The two dislocations on the left of Figure 3-3 have [-1-1-1] polarization while the two dislocations on the right have [111] polarization. The above relationship between the dislocation polarization and the directions in which the dislocation core spreads is independent of the orientation of the Burgers vector.

Figure 3-4 shows differential displacement maps and relaxation maps for the four types of 1/2a<111> screw dislocations: N_+ (polarized in the [-1-1-1] direction and with **b**=1/2a[111]) dislocation, P_+ (polarized in the [111] direction and with **b**=1/2a[111]) dislocation; N- (polarized in the [-1-1-1] direction and with **b**=1/2a[-1-1-1]) dislocation, and P- (polarized in the [111] direction and with **b**=1/2a[-1-1-1]) dislocation.

(a) N_+

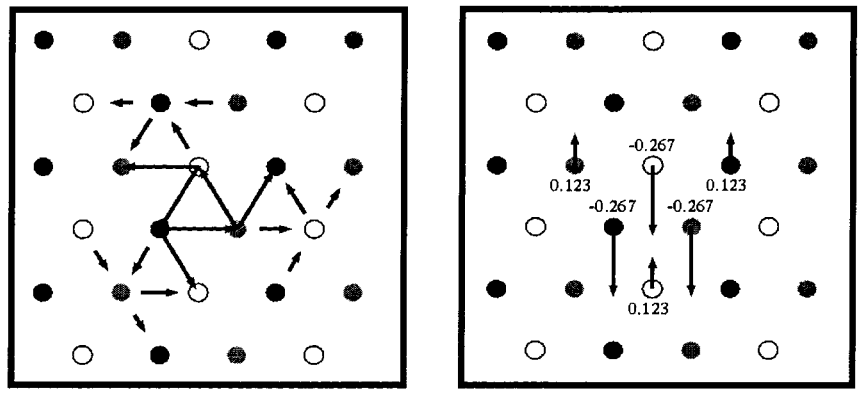
-0.267
0.123
0.123
-0.267
-0.267
0.123

(b) P_+

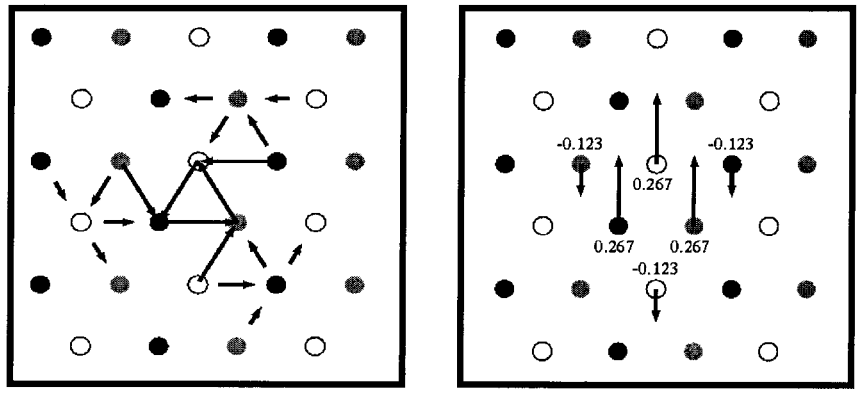
-0.123
-0.123
0.267
0.267
0.267
-0.123

(c) N-

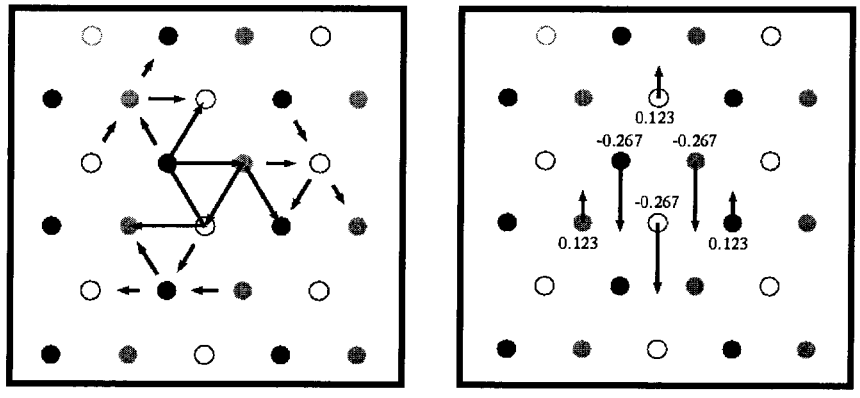
0.123
-0.267
-0.267
-0.267
0.123
0.123

(d) P-

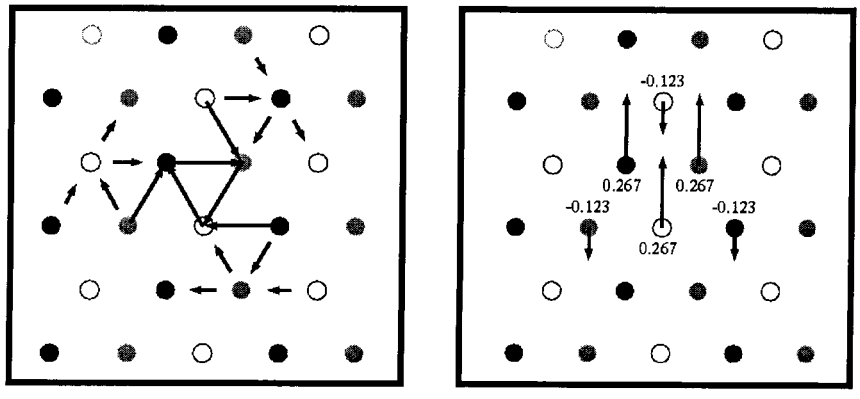
-0.123
0.267
0.267
-0.123
-0.123
0.267

Figure 3-4. The equilibrated dislocation core configurations for the 1/2a<111> screw dislocation in Ta. The circles represent the projected atoms in the (111) plane. The open, shaded or black circles indicate that the atoms are in three consecutive (111) layers of bcc lattice. However, the arrows in two columns of figures have different meanings. The left column shows the **differential displacement map**, in which the arrow indicates the displacement in [111] direction (perpendicular to the map) of the neighboring atoms *relative to their positions in the perfect bcc crystal*. The direction of the arrow represents the sign of the displacement and the magnitude is proportional to the relative displacement between corresponding atoms. When the arrow touches the two atoms, the relative displacement between these two atoms is 1/3 b. For clarity, the relative displacements less than 1/12 b are not shown in the figure. The right column shows the **relaxation map**, in which the arrow from each atom indicates the relaxation (parallel to the dislocation line) *relative to the displacement field predicted by isotropic elastic theory*. The magnitudes of such relaxation (in ångstrom) for the central six columns of atoms (the relaxation for the other atoms is less than 0.05Å) are printed next to the corresponding atom. Four types of energy degenerate dislocation core configurations are distinguished in terms of the relaxation direction of the three central columns of atoms (downward denoted as "N" and upward denoted as "P") and Burgers vector (a/2[111] denoted as "+" and -a/2[111] denoted as "-").

3.2.4 Comparison to other calculations

Using the qEAM FF, we find a polarization of the dislocation core in which the relative displacement field has the threefold symmetry, rather than the sixfold symmetry of (111) planes of the bcc lattice. However, we must be cautious about these results. Previous studies for bcc metals have led to both asymmetric (threefold symmetric) and symmetric (sixfold symmetric) core structures for the a/2<111> screw dislocation.

- Xu and Moriarty *et al.*[2,8,9] obtained an *asymmetric* core structure for bcc Mo using the multi-ion interatomic potentials from the model generalized pseudopotential theory (MGPT).
- Vitek arrived at an *asymmetric* core structure for bcc crystal employing pair-wise interatomic potentials from Ref. 6.
- Experimentally, Sigle investigated the dissociation of the a/2<111> screw dislocation in Mo using high-resolution transmission electron microscopy (HRTEM), obtaining a broken symmetry consistent with an *asymmetric* dislocation core configuration[10].
- Duesbery and Vitek[11] found a *symmetric* core for group VB metals (V, Nb, and Ta) but an *asymmetric* core for group VIB metals (Cr, Mo, and W) using Finnis-Sinclair (F-S) type central-force many body potentials.
- *Ab initio* density functional theory calculations for both Mo and Ta led to a *symmetric* dislocation core both with periodic boundary conditions[3] and lattice Green's function boundary conditions[12].

- Yang *et al.*[4] showed the core structure of the screw dislocation for Ta is very sensitive to the mechanical conditions and varies dramatically from *symmetric to asymmetric* with increasing pressure.

Summarizing, the weight of evidence is in favor of a symmetric dislocation core, but the evidence remains inconclusive.

The main difference between asymmetric [DD map in Figure 3-5(b)] and symmetric [DD map in Figure 3-5(a)] core is the polarization. The symmetric core does not have polarization. The extent of polarization for an asymmetric core is [-b/6,0) and (0, b/6].

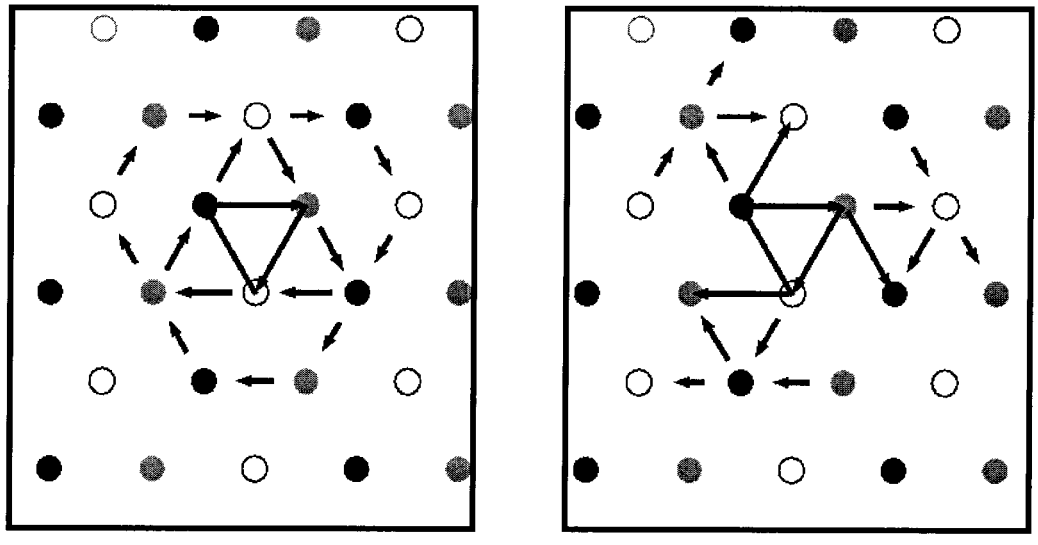

(a) (b)

Figure 3-5. The DD maps for the equilibrium dislocation core structures. (a) The dislocation polarization p is equal to 0.00 b and the corresponding core is symmetric, while (b) the dislocation polarization p is equal to 0.09 b and the corresponding dislocation core is asymmetric, spreading along three <112> directions on the (110) planes.

Starting from the asymmetric core structure, we constructed a symmetric dislocation core by translating the central six columns of atoms along the [111] direction and then relaxing the full unit cell while fixing the positions of central six columns of atoms in the [111] direction. The resultant symmetric core has atomic displacements similar to those in the literature[3,11,12]. We calculate using the qEAM FF that the dislocation core energy per Burgers vector b for symmetric core is 1.440 eV, which is 0.040 eV higher (2.9 %) than the relaxed asymmetric core.

3.3 Dislocation core energy

3.3.1 Atomistic approach

We define the strain energy associated with each atom as in Eq. (2):

$$E_i = F(\rho_i) + \frac{1}{2}\sum_{j \neq i} \phi(r_{ij}) - E^{coh}, \tag{2}$$

where E^{coh} is the atomic cohesive energy in perfect crystal.

The atomic strain energies calculated using Eq. (2) for the relaxed dislocation quadrupole with 5670 atoms (with cell size: **X**=9<112>a, **Y**=15<110>a, and **Z**=7/2<111>a) are displayed in Figure 3-6(a). Here each atom is projected on the (111) plane and drawn as a circle whose radius is proportional to its atomic strain energy. Most atoms have very small strain energy; only 12 atoms close to the dislocation line have significant strain energies. Figure 3-6(b) shows the atomic strain energy distribution per dislocation per b for the same dislocation quadrupole cell. Here we see that the atomic strain energy of the six atoms close to the dislocation line is 0.15 eV to 0.17 eV, while

another 6 atoms have atomic strain energies ranging from 0.06 eV to 0.08 eV. These 12 atoms near the center of the dislocation in Figure 3-6(a) are denoted as A, B, C and D in Figure 3-6(b), in decreasing atomic strain energy order. Except for these 12 atoms, all other atoms have atomic strain energies less than 0.05 eV. Based on these observations, we define *the core of the dislocation to be formed by the 12 atoms with higher strain energy per Burgers vector.* This leads to the dislocation core energy of E_c=1.400 eV per Burgers vector b.

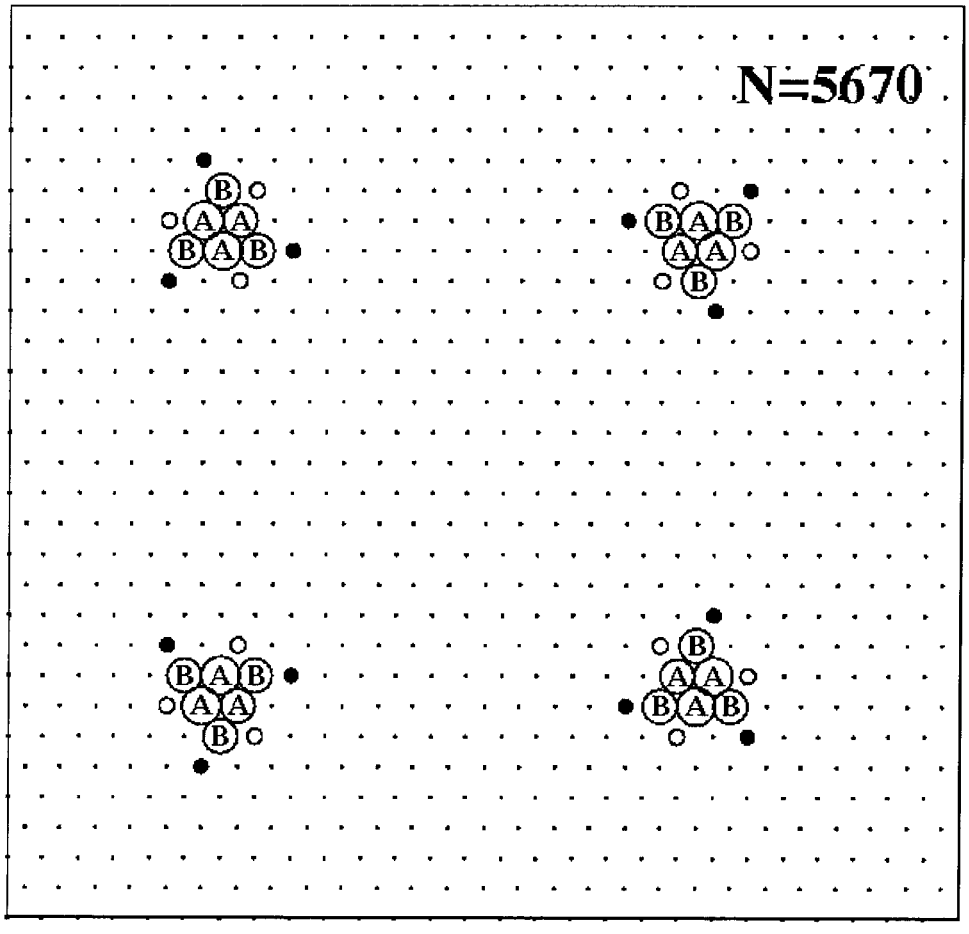

(a)

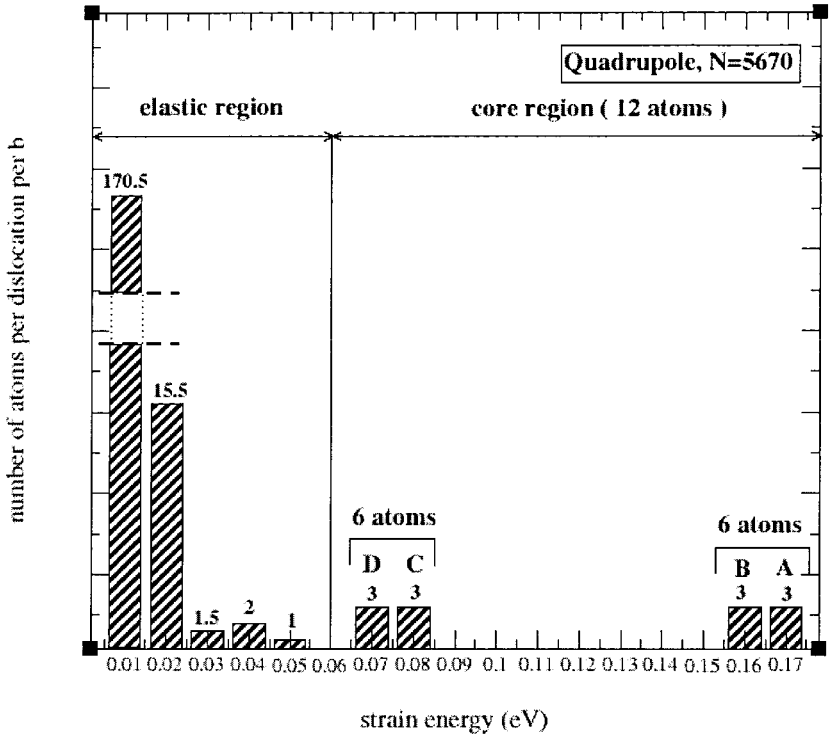

(b)

Figure 3-6. (a). The <111> projection of atomic strain energy distribution for a 1b thick slab in an equilibrated dislocation quadrupole in which there are 5670 atoms and each dislocation is 7b long. Atoms are represented as circles and the radius of circle is proportional to the strain energy of the atom. (b). Histogram of atomic strain energy distribution for a 1b segment of the dislocation obtained from the same quadrupole simulation. The number of atoms in each energy bin is shown on the top of the corresponding bar.

In Figures 3-6 (a) and (b), the atoms with atomic strain energy ranging from 0.165 eV to 0.170 eV are denoted as 'A' and atoms denoted as 'B' have atomic strain energy ranging from 0.156 eV to 0.157 eV. Atoms 'C' in Figure 3-6(b) are represented as black

circles in Figure 3-6(a), while atoms 'D' in Figure 3-6(b) are represented as white circles in Figure 3-6(a). The atoms labeled by 'C' have higher strain energy than the atoms 'D'.

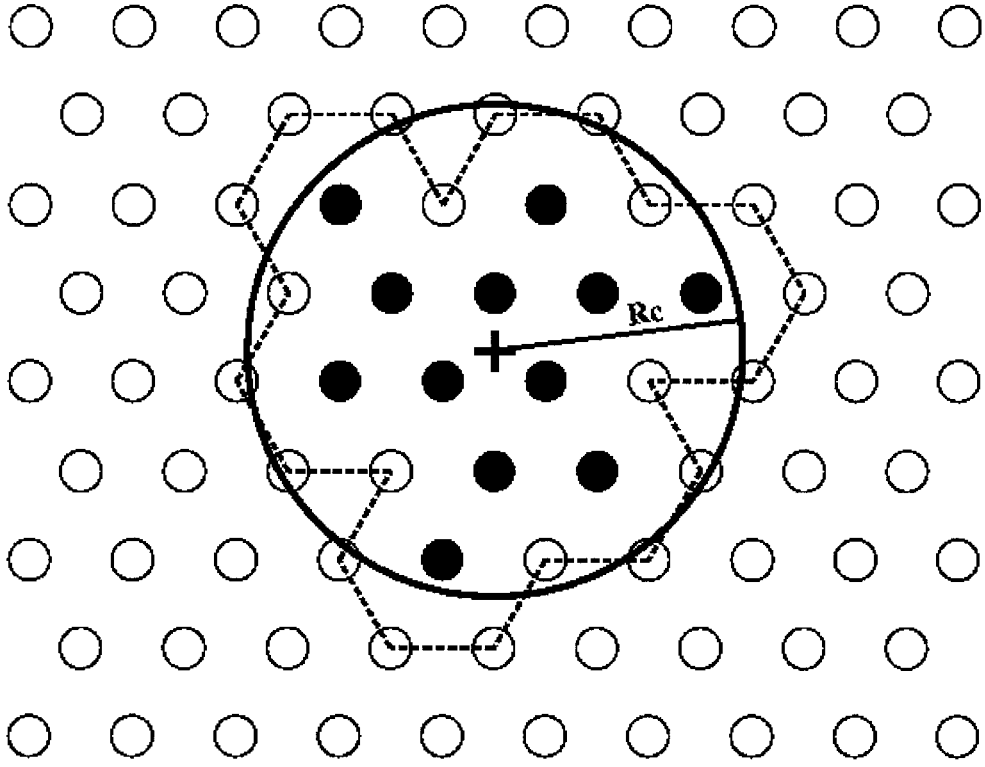

Figure 3-7. Schematic drawings for a dislocation core in the atomistic model and in the continuum model. Atoms are projected in (111) plane and represented by circles. The black circles indicate the atoms constituting the dislocation core according to the atomistic model, the other atoms are in the elastic region and drawn as white circles. The dotted line connects the non-core atoms that most closely encircle the dislocation core providing a cutoff boundary for the atomistic model. The solid circle whose radius is the average distance from the dislocation center to the atomistic cutoff boundary (2.287 b) is the dislocation core radius for the continuum model.

Corresponding to this definition, we define the core radius as the average distance from the dislocation center to the closest non-core atoms encircling the core region. This is shown in Figure 3-7 as the dotted line. This leads to a core radius of r_c=2.287 b. Note in Figure 3-7 that the 12 atoms of the core are *not* the 12 closest atoms to the dislocation center.

Summarizing, the atomic strain energy distribution provides a criterion for distinguishing which atoms are inside and outside the core region of the dislocation. This leads to a core energy of E_c=1.400 eV/b and a core radius of r_c=2.287 b for the 1/2<111> screw dislocation in Ta.

3.3.2 Continuum approach

The presence of dislocations leads to strain in the crystal. The total strain energy can be considered as the summation of the dislocation core energy and the elastic energy outside the dislocation core. The latter, including the dislocation self-energy and interaction energy, can be calculated using elasticity theory. Inside the dislocation cores the strains are too large for elasticity theory to apply.

The total strain energy per Burgers vector for two parallel straight dislocations with equal and opposite Burgers vectors at a separation d is

$$E = 2E_c(r_c) + 2Kb^3 \ln(\frac{d}{r_c}), \tag{3}$$

where r_c is the core radius of the dislocation and the elastic modulus K can be expressed as[5]

$$K = \frac{\{S_{11}/[S_{44}(S_{11}S_{44} - S_{15}^2)]\}^{\frac{1}{2}}}{4\pi}, \quad (4)$$

S_{11}, S_{44}, and S_{15} are the modified elastic compliance constants. The details of determining them from standard elastic constants of the cubic crystal can be found in Ref.5.

Summing the pair interactions in Eq. (3) leads to the total energy per dislocation per b in a dislocation quadrupole cell as in Eq. (5) [3]

$$E = E_c(r_c) + Kb^3[\ln(\frac{d_1}{r_c}) + A(\frac{d_1}{d_2})], \quad (5)$$

where d_1 and d_2 are the distances between the dislocations along the [-110] and [11-2] directions, $A(d_1/d_2)$ is a convergent summation of all pair interaction effects and is related to the geometry of the simulation cell. In Eq. (5), the core energy $E_c(r_c)$ and effective elastic parameter Kb^3 are constants, leading to a total strain energy that varies linearly with the scaled elastic energy $[ln(d_1/r_c)+A(d_1/d_2)]$, as the size of simulation cell is changed. Plotting the total strain energy versus the scaled elastic energy, we determine the effective elastic modulus K from the slope and the core energy $E_c(r_c)$ from the intercept. Obviously, the core energy $E_c(r_c)$ obtained in this way depends on the choice of r_c, while K does not.

To determine $E_c(r_c)$ and K using Eq. (5), we simulated quadrupole arrays of dislocations for various system sizes ranging from 1890 atoms (40.71Å by 42.31Å by 20.15Å) to 51,030 atoms (219.8Å by 211.5Å by 20.15Å) and optimized the atomic

coordinates by minimizing the energy. The geometrical parameters of simulation cells, numbers of the atoms and the obtained strain energies are shown in Table 3-1.

Table 3-1. Table of size of simulation cells, number of atoms per simulation cell and strain energy per dislocation per Burgers vector. **X**, **Y** and **Z** are the cell parameters for the simulation cells. **X** is in the unit of a[11-2], **Y** is in the unit of a[-110] and **Z** is in the unit of a/2[111]. |**X**|, |**Y**| and |**Z**| are the size of simulation cells in unit of Å.

	X	**Y**	**Z**	|**X**| (Å)	|**Y**| (Å)	|**Z**| (Å)	N (/cell)	E (eV/b)
1	5	9	7	40.71	42.31	20.15	1890	1.833
2	5	11	7	40.71	51.71	20.15	2310	1.891
3	7	9	7	56.99	42.31	20.15	2646	1.927
4	7	11	7	56.99	51.71	20.15	3234	2.039
5	9	11	7	73.28	51.71	20.15	4158	2.095
6	9	15	7	73.28	70.51	20.15	5670	2.265
7	21	33	7	171.0	155.1	20.15	29106	2.912
8	27	45	7	219.8	211.5	20.15	51030	3.150

In Figure 3-8, we show that the total strain energy for various simulation cells as a function of the scaled elastic energy $[ln(d_1/r_c)+A(d_1/d_2)]$. Our results show the linear dependence expected from Eq. (5). Taking the core radius as 2.287 b obtained from the atomistic method and using the linear fit of our data in Figure 3-8, we determine the "easy core" dislocation to have the core energy of 1.404 eV/b. This is in excellent agreement with the dislocation core energy of 1.400 eV/b calculated directly using the atomistic model. This linear fit leads to an elastic modulus of $K = 3.3497 \times 10^{-2}$ eV/Å^3. Alternatively using the computed elastic constants for the bcc crystal from the qEAM FF,

we obtain the K = 3.3492 × 10^{-2} eV/Å^3, which is within 0.02% of the value derived from fitting Eq. (5) in Figure 3-8.

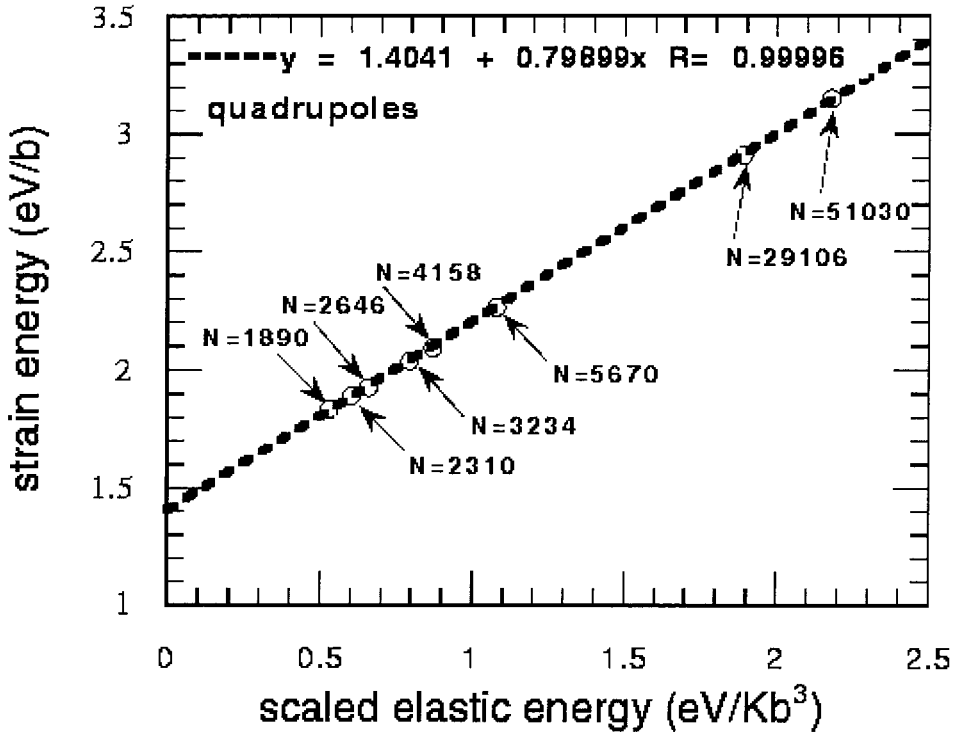

Figure 3-8. The strain energy (*E/b*) as a function of the scaled elastic energy ($ln[d_1/r_c]+A(d_1/d_2)$) obtained from the simulations of different sized dislocation quadrupoles. The dotted line represents the linear fitting

$E/b=1.4041+0.79899[ln(d_1/r_c)+A(d_1/d_2)]$ with r_c=2.287 b leading to a dislocation core energy of 1.4041 eV/b. The number of atoms in each simulation cell is specified in the figure.

Beigi and Arias[3] calculated the core energy of 1/2a <111> screw dislocation in Ta from *ab initio* methods. They used r_c = 2b which led to E_c = 0.86 eV/b. Using our force fields, with the same core radius, we compute the core energy to be E_c = 1.297 eV/b.

Thus, the dislocation core energy based on *ab initio* QM is 34% lower than our calculation.

In the MGPT calculations on Ta [4], a value of r_c = 1.75 b was used, leading to E_c = 0.60 eV/b. This can be compared to the value of E_c =1.190 eV/b that our results in Figure 3-8 would lead to for r_c = 1.75 b. Thus, the dislocation core energy based on the MGPT force field is 50% lower than our calculation.

Table 3-2 compares the predicted lattice parameter and elastic constants for bcc Ta from the *ab initio* calculations[3,4,12,14], MGPT [4], and qEAM computations as well as the experiments[13]. Predicted elastic constants differ by tens of a percent, especially for C_{44}. It is likely that the predicted dislocation core energies from different computations would have at least the same magnitude of diversity. However, even with such energy differences, we expect that the character and properties of dislocations can be understood properly from the simulations.

Table 3-2. Experimental and theoretical values of lattice parameter a (Å), elastic constants C_{11} (GPa), C_{12} (GPa) and C_{44} (GPa). Errors with respect to the experimental values for different *ab initio* pseudopotentials, MGPT and qEAM force field calculations are shown.

		a (Å)	C_{11} (GPa)	C_{12} (GPa)	C_{44} (GPa)
Exp. [a]		3.30	266	158	87.4
Ab Initio [b]	Value	3.25	304	182	66
(Beigi *et al.*)	Error	-1.5 %	14 %	15 %	-25 %
Ab Initio [c]	Value	3.30	265	155	91.3
(Söderlind *et al.*)	Error	0 %	-0.4 %	-1.9 %	4.5 %
Ab Initio [d]	Value	3.23	291	175	52.9
(Woodward *et al.*)	Error	-2.1 %	9.4 %	11 %	-39 %
Ab Initio [e]	Value	3.36	244	160	66.3
(Gülseren *et al.*)	Error	1.8 %	-8 %	1.3 %	-24 %
MGPT FF [f]	Value	3.30	266	161	82.5
(Yang *et al.*)	Error	0 %	0 %	1.9 %	-5.6 %
qEAM FF	Value	3.32	273	138	69.6
(present work)	Error	0.6 %	2.6 %	-13 %	-20 %

[a] Reference 13.

[b] Reference 3. The total-energy plane-wave density-functional pseudopotential calculation.

[c] Reference 4. The full-potential (FP) linear muffin-tin orbital (LMTO) calculation.

[d] Reference 12. Using ultrasoft (US) pseudopotential and Vienna *Ab-initio* Simulation Package (VASP).

[e] Reference 14. Using the linearized augmented plane wave and mixed-basis pseudopotential methods.

[f] Reference 4.

3.4 Dislocation core structure revisited

3.4.1 Dislocation core energy variations with its polarization

In Section 3.2.4, we pointed out that the main difference between the asymmetric and symmetric cores is their polarizations. The symmetric core does not have polarization, while an asymmetric core has. In the previous *ab initio* calculations[3,12], the observed equilibrium screw dislocation has a symmetric core. However, our qEAM FF predicted an equilibrium asymmetric screw dislocation core. To understand the difference between the *ab initio* and the qEAM FF calculations in predicting dislocation core structures, we calculated the dislocation core energy variation with its polarization both using *ab initio* method and the qEAM FF.

We constructed a dislocation core with a particular polarization by translating the central six columns of atoms along the [111] direction. The starting structure is the asymmetric core (p=0.094 b) obtained using the qEAM FF. The final positions of those six central columns of atoms are determined by scaling their displacement with the dislocation polarization. To make the quantum calculations feasible, we choose the parameters of simulation cells as **X**=3a[11-2], **Y**=5a[1-10] and **Z**=a[111], which lead to 90 atoms per simulation cell in total. We further relax the quadrupole dislocation cells while fixing the Z ([111]) positions of the central six columns of atoms for every dislocation.

We also compared the resultant dislocation quadrupoles with the previous *ab initio* calculation[3,15] using the same simulation size. In that *ab initio* study, the

equilibrium dislocation with a symmetric core was obtained by minimization. We define the averaged atomic deviation from the *ab initio* structure (denoted as "AI-structure") for each simulation cell (contains 90 atoms) as Eq. (6).

$$\Delta\xi = \frac{\sqrt{\sum_{i=1}^{N}(\xi_i^{FF} - \xi_i^{AI})^2}}{N}, \tag{6}$$

here, ξ_i^{FF} is the x, y or z component of the position for an atom in the simulation cell predicted by the qEAM FF, while ξ_i^{AI} is the x, y or z component of the position for the corresponding atom in the "AI-structure." The N stands for the number of the atoms in the simulation cell and is 90 in our case. Note that the "AI-structure" has been scaled to have the same equilibrium lattice parameter as those from the qEAM FF calculations.

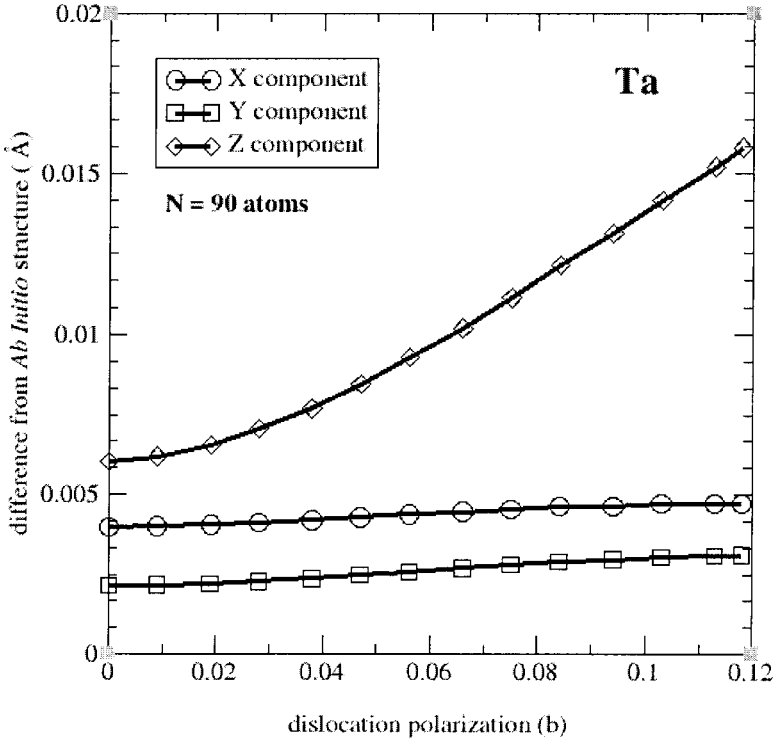

Figure 3-9. The averaged deviation of the atomic positions (x, y and z component) between the 90-atom equilibrium dislocation quadrupoles from the qEAM FF and the "AI-structure" from the *ab initio* (Ref. 3) calculations. In each equilibrium dislocation quadrupole from the qEAM FF calculation, the dislocations have the same and specified polarization. The "AI-structure" (from Ref. 3) contains four dislocations whose cores are symmetric and zero polarized.

Figure 3-9 shows the averaged x, y and z component differences between the qEAM FF predicted dislocation quadrupole with different polarizations and the "AI-structure." When polarization p = 0, the averaged atomic deviation between our resultant structure and the "AI-structure" is small ($\Delta x = 0.004$ Å, $\Delta y = 0.002$ Å, and $\Delta z = 0.006$ Å). It means that our resultant symmetric core structure is very close to the "AI-structure" directly predicted using *ab initio* method. When the dislocation polarization increases, the averaged atomic deviations of x and y components of position increase very little. Δx changes from 0.004 Å for the dislocations with symmetric core to 0.005 Å for the dislocations with fully polarized core; Δy changes from 0.002 Å for the dislocations with symmetric core to 0.003 Å for the dislocations with fully polarized core. On the contrary, the z component of atomic deviation increases from 0.006 Å to 0.016 Å (increases by 167%) when the polarization of the dislocations in the simulation cell changes from 0 b (symmetric core) to 0.118 b (fully polarized core). These results are consistent with our previous claim that the difference between the symmetric core and the asymmetric core for a screw dislocation is mainly the dislocation polarization in the [111] (z) direction.

For each simulation cell, which contains a quadrupole of dislocations with the particular polarization, we performed the one-energy evaluation using both the qEAM FF and the DFT-LDA calculations[16]. Choosing the core energy of the symmetric core as the reference point, we plot in Figure 3-10 the dislocation core energy variations with its polarization.

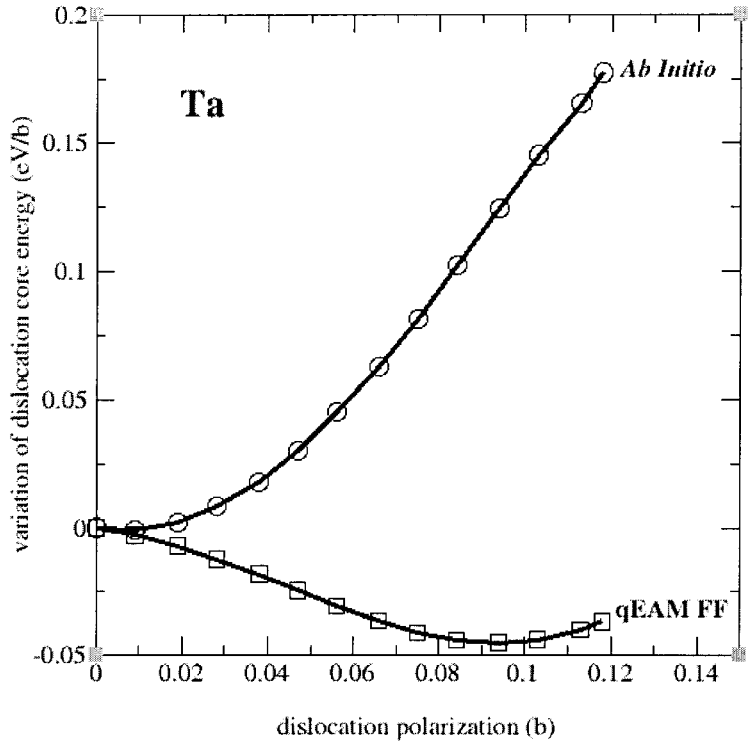

Figure 3-10. The calculated dislocation core energy variations with its polarization using the qEAM FF and *ab initio* methods.

Figure 3-10 shows that the dislocation core energy has a minimum (0.045 eV/b less than the symmetric core) at p = 0.094 b, leading to an equilibrium asymmetric dislocation core structure in the qEAM FF calculations. While the *ab initio* computation predicts that the symmetric or very close to symmetric dislocation core is energy

favorable, because the core energy is much higher when dislocation polarization is large. Figure 3-10 gives us an explanation why the qEAM FF produces a different dislocation core structure from the *ab initio* calculation. Though the *ab initio* methods are the most rigorous way to evaluate the system energy, we still should bear in mind that the employed 90-atom simulation cell is pretty small such that dislocation cores are contacting with each other. The plot in Figure 3-10 might change if a much larger simulation cell were used. At this moment, we consider our qEAM FF has its limitation and need re-parameterizing to reproduce the *ab initio* results in Figure 3-10.

3.4.2 Force field re-parameterization

There are 19 tunable parameters in our EAM model force field. Our original force field (denoted as "qEAM1") was originally trained to optimally fit the following quantum results[17].

(1) The zero temperature equation of state (EOS) of Ta for bcc, fcc, and hcp crystal structures for pressures up to ~ 500 GPa,

(2) the elastic constants,

(3) the volume relaxed vacancy formation energy also as a function of pressure,

(4) the equation of state for the A15 structure of Ta,

(5) the (100) surface energy in the bcc Ta,

(6) the energies for shear twinning of the bcc Ta.

To investigate the possibility whether the EAM model force field can predict the same dislocation core structure as the *ab initio* calculations or not, we re-parameterized the

force field to fit the above quantum results as well as the quantum results of dislocation core energy variations with its polarization.

During the force field re-parameterization process, we obtained another three versions of the qEAM force fields and denoted them as "qEAM2," "qEAM3," and "qEAM4." Table 3-3 gives the calculated lattice parameters a (Å) and elastic constants (C_{11}, C_{12} and C_{44} in unit of GPa) for bcc Ta model crystal.

Table 3-3. Experimental and theoretical values of lattice parameter a (Å), elastic constants C_{11} (GPa), C_{12} (GPa) and C_{44} (GPa).

	a (Å)	C_{11} (GPa)	C_{12} (GPa)	C_{44} (GPa)
qEAM1 FF	3.32	273	138	69.6
qEAM2 FF	3.35	255	148	60.2
qEAM3 FF	3.32	257	148	77.3
qEAM4 FF	3.33	254	155	67.4
Ab Initio [a]	3.36	244	160	66.3
Exp. [b]	3.30	266	158	87.4

[a] Reference 14. Using the linearized augmented plane wave and mixed-basis pseudopotential methods. They are the inputs for force field fitting.

[b] Reference 13.

The results in Table 3-3 show that the force fields (qEAM1, qEAM2, qEAM3, and qEAM4) all describe the bcc Ta crystal well, however, Figure 3-11 shows that these force fields lead to different behaviors of the dislocation core energy variation with its polarization. The qEAM1 FF predicted an equilibrium asymmetric dislocation core

structure and an energy minimum when the dislocation polarization p is 0.094 b. The qEAM2, qEAM3 and qEAM4 force fields predict that the dislocation core energy would increase with the increase of the dislocation polarization. The qEAM3 FF describes a large rate of increase and best fit to the *ab initio* results, the qEAM4 FF describes a very small increase rate, and the qEAM2 FF leads to an intermediate increase rate. Regardless of the difference in the increase rate of the dislocation core energy with its polarization, these three force fields all predict an equilibrium symmetric dislocation core for the 1/2a<111> screw dislocation in Ta. The polarizations of the resultant dislocation core are less than 1×10^{-4} b, which is at the same magnitude but smaller than the 7×10^{-4} b from the MGPT FF calculation[4].

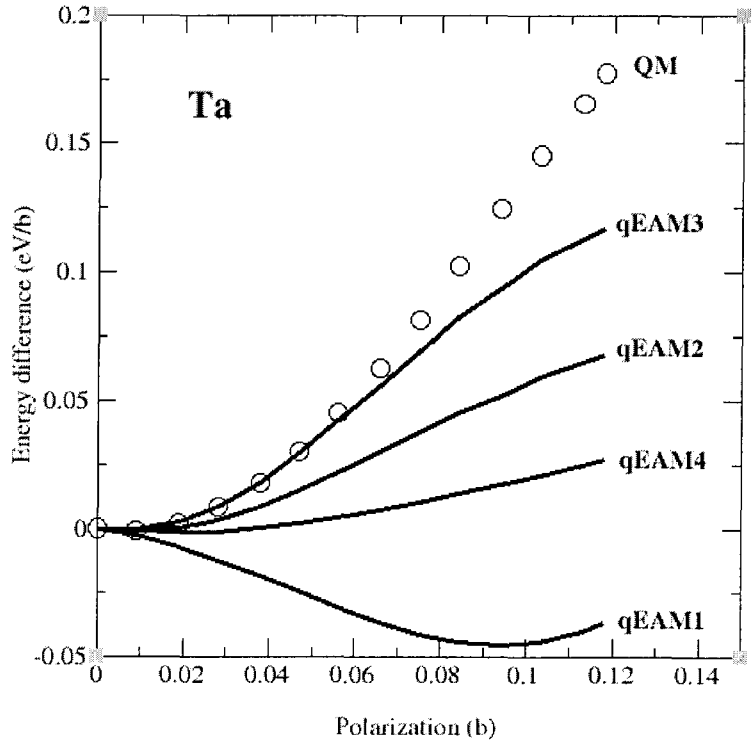

Figure 3-11. The calculated dislocation core energy variations with its polarization using the qEAM force fields (qEAM1, qEAM2, qEAM3, and qEAM4) and *ab initio* methods.

We conclude here that the EAM model force field can predict the same symmetric dislocation core structure as the *ab initio* method even though it does not completely reproduce the quantum results (such as the qEAM4 FF). The above findings pose two fundamental questions. (1) What is the reason for different force fields predict different equilibrium dislocation core structures? (2) What is the affect of this difference to the study of plasticity of bcc Ta? In Section 3.4.3, we will report our preliminary results on the first issue. The Question (2) is still under investigation. It should be noticed that the reported calculation results in the following chapters are obtained in simulations using the original qEAM FF unless specified.

3.4.3 Generalized stacking-fault energy (γ) surface

The generalized stacking-fault energy (γ) surface is an energy profile of two semi-infinite half crystals first displaced relative to each other by a vector **v** on a crystallographic plane, then relaxed only in the direction perpendicular to the plane[6]. The γ surfaces are the major input parameters to the well-developed generalized Peierls-Nabarro model[18], which is a continuum model for describing dislocation properties. The generalized Peierls-Nabarro model informed with γ surfaces calculated using the *ab initio* electron theory has been used to study the <001> dislocations in bcc metal Mo and Nb[19], super-dislocations in Ni_3Al[20] and NiAl[21], and dislocations in fcc metal Al[22,23]. The γ surfaces are also considered very important for accurately modeling bcc screw dislocation behavior. Duesbery and Vitek[11] used the <111> cross section of the {110} plane γ surface in tantalum and molybdenum to explain the observed screw dislocation

core structure difference. They found for the 1/2a<111> screw dislocation a symmetric core in Ta but an asymmetric core in Mo.

We calculated the <110> and <111> cross sections of the {112} γ surfaces and the <111> cross section of the {110} γ surface using the force fields qEAM1, qEAM2, qEAM3, and qEAM4. These results are displayed in Figure 3-12 comparing with *the ab initio* calculations[4]. In our force field calculations, two parallel equivalent generalized stacking-fault surfaces were introduced in a periodic bcc Ta crystal cell. The distances between two stacking-fault surfaces are 96 atomic planes for the {112} surface and 32 atomic planes for the {110} surface, which are two times larger than the previous MGPT FF calculations[4]. After constructing the initial surfaces, we relaxed atoms in the direction normal to the specified surface to the full convergence that the force on each atom is no more than 3.5×10^{-4} eV/Å. The *ab initio* result in Figure 3-12 is from Ref. 4. These results are obtained by relaxing 12-plane supercell using the pseudopotential (PP) techniques, then evaluating energies for the defined geometries using the full-potential linear muffin-tin orbital (FP-LMTO) method.

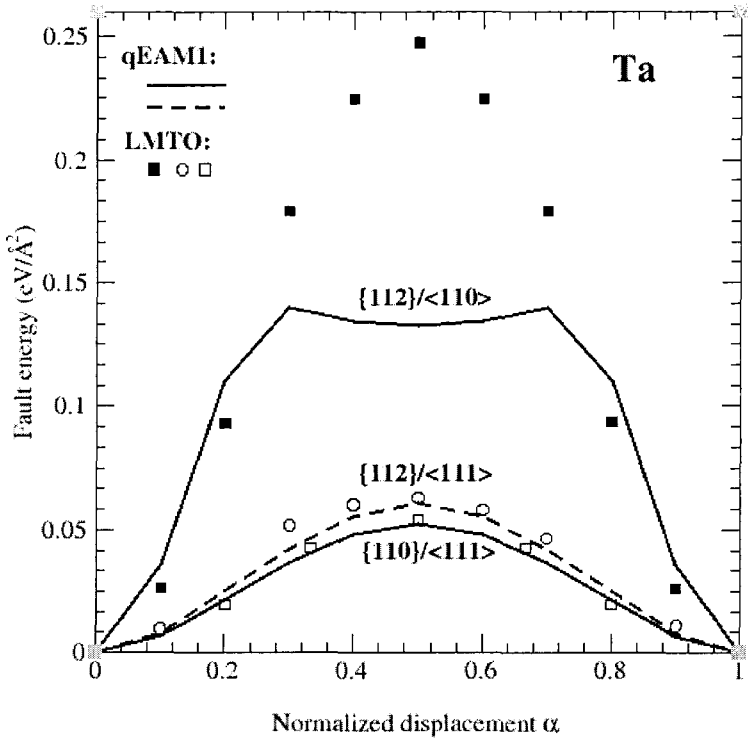
qEAM1:
LMTO:
Ta
{112}/<110>
{112}/<111>
{110}/<111>
Fault energy (eV/Å²)
Normalized displacement α
0
0.05
0.1
0.15
0.2
0.25
0.2
0.4
0.6
0.8
1

(a)

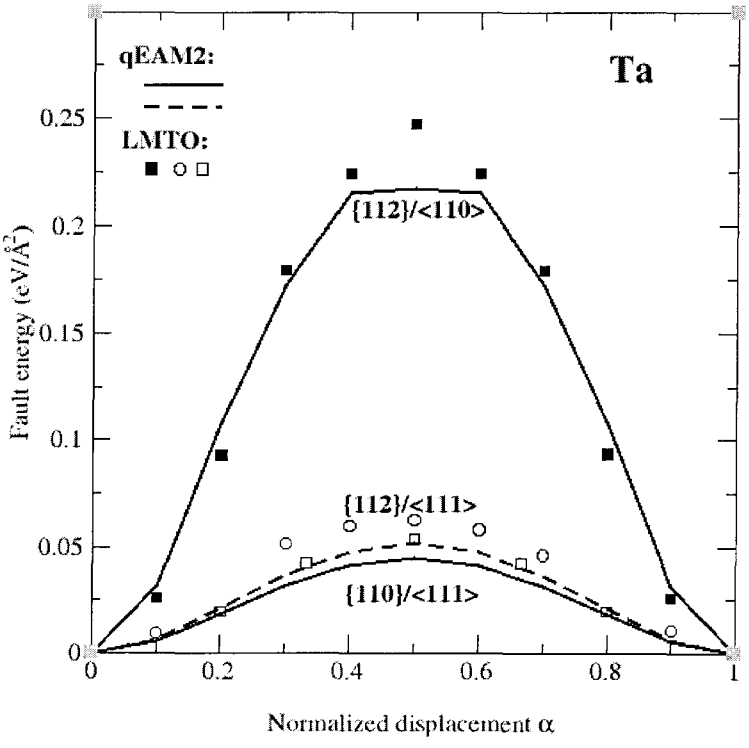
qEAM2:
LMTO:
Ta
{112}/<110>
{112}/<111>
{110}/<111>
Fault energy (eV/Å²)
Normalized displacement α
0
0.05
0.1
0.15
0.2
0.25
0.2
0.4
0.6
0.8
1

(b)

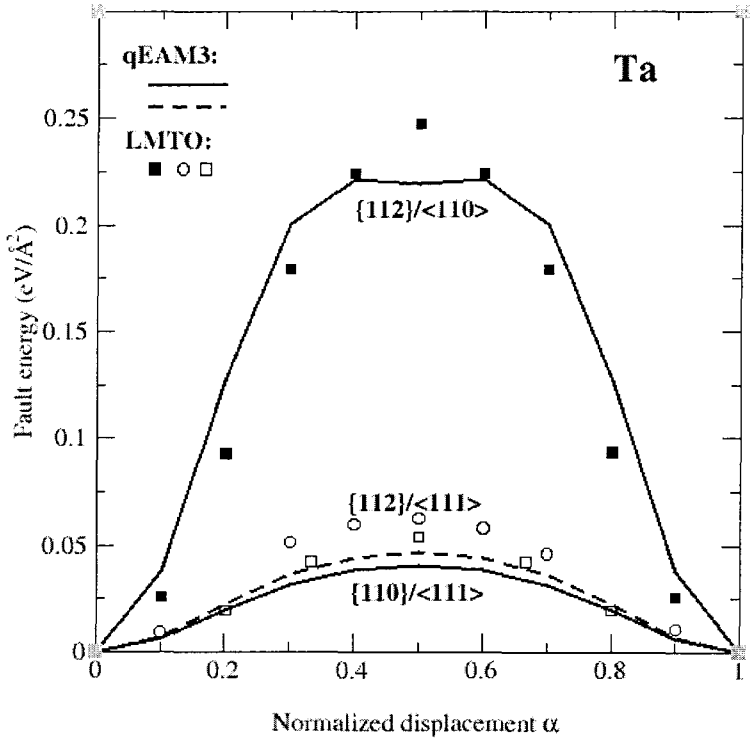
qEAM3:
LMTO:
Ta
{112}/<110>
{112}/<111>
{110}/<111>
Fault energy (eV/Å²)
Normalized displacement α
0
0.05
0.1
0.15
0.2
0.25
0.2
0.4
0.6
0.8
1

(c)

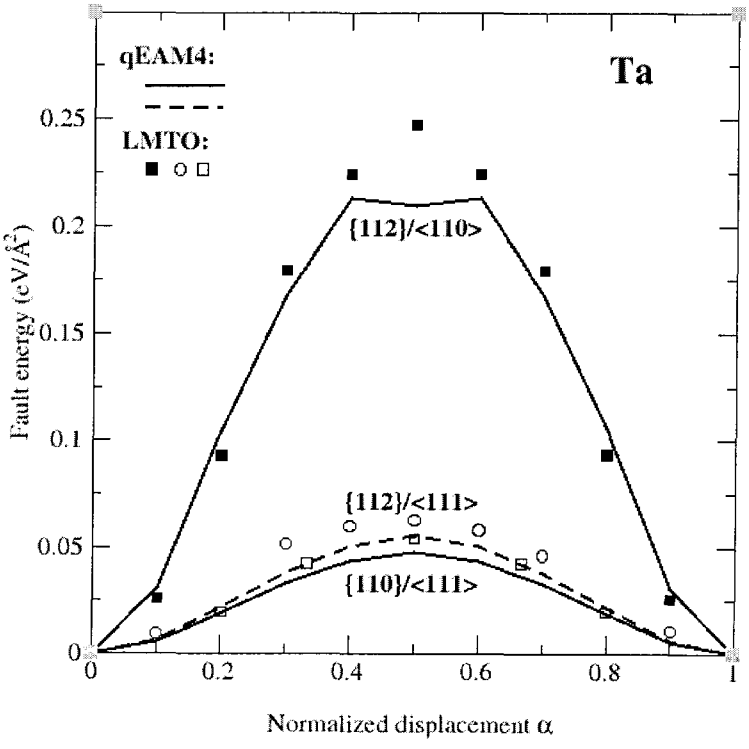
qEAM4:
LMTO:
Ta
{112}/<110>
{112}/<111>
{110}/<111>
Fault energy (eV/Å²)
Normalized displacement α
0
0.05
0.1
0.15
0.2
0.25
0.2
0.4
0.6
0.8
1

(d)

Figure 3-12. High-symmetry lines in the {112} and {110} γ surfaces for bcc Ta, as calculated with the ab initio FP-LMTO electronic structure method and with the force fields (a) qEAM1, (b) qEAM2, (c) qEAM3, and (d) qEAM4.

Figure 3-12(a) shows that the <111> cross section of both the {112} and the {110} γ surface from our original qEAM1 FF quantitatively agree with the FP-LMTO results but the γ surface {112}/<110> deviate severely from the *ab initio* results when the normalized displacement is in the range of $0.3 \le \alpha \le 0.7$. On the other hand, Figure 3-12(b), (c) and (d) shows that the γ surfaces {112}/<111> and {110}/<111> calculated using the qEAM2, qEAM3 and qEAM4 FF are lower than the *ab initio* results by almost the same amount. More interestingly, the MGPT FF in Ref. 4 also made the same amount of error. The γ surfaces {112}/<110> calculated using the above three force fields agree with the *ab initio* calculations except at α=0.5.

The qEAM1 FF predicts an asymmetric core for screw dislocation, while the qEAM2, qEAM3 and qEAM4 force fields predict symmetric cores for screw dislocation. We find that the calculated γ surfaces using these two groups of force fields show some different features. This suggests that there is a possible relationship between the γ surfaces and the equilibrium dislocation core structure.

3.5 Conclusion

In this chapter, we first obtained the equilibrium dislocation core structure using our qEAM FF. The qEAM FF leads to a polarized and asymmetric dislocation core, spreading along three <112> directions in {110} planes. We calculated the equilibrium

dislocation core energy both in atomistic model and continuum model. These two models yield consistent results, 1.400 eV/b in atomistic model and 1.404 eV/b in continuum model. Furthermore, we obtained an insight to the dislocation core structure from an energetic point of view. We are going to apply this insight to determine the dislocation mobility in Chapter 4. By re-parameterizing the qEAM force field, we further show that the EAM model force field is able to lead to an equilibrium symmetric dislocation core as the *ab initio* calculations. Our calculated high-symmetry lines (<110> and <111>) in the {112} and {110} γ surfaces for bcc Ta using different groups (predicting asymmetric or symmetric dislocation core) of force fields show different features. This suggests the possible connection between the calculated γ surfaces and the resultant dislocation core structure.

3.6 References

1. A. M. Cuitino, L. Stainier, G. Wang, A. Strachan, T. Çağın, W. A. Goddard, and M. Ortiz, *A Multiscale Approach for Modeling Crystalline Solids*, J. Comput.-Aided Mater. Design, to be published.W. Xu and J. A. Moriarty, Phys. Rev. B, **54**, 6941 (1996).
2. W. Xu and J. A. Moriarty, Phys. Rev. B, **54**, 6941 (1996).
3. S. Ismail-Beigi and T. A. Arias, Phys. Rev. Lett., **84**, 1499 (2000).
4. L. H. Yang, P. Söderlind, and J. A. Moriarty, Philos. Mag. A, **81**, 1355 (2001).
5. J. P. Hirth and J. Lothe, *Theory of dislocations* (Wiley, New York, 1982), p.465.
6. V. Vitek, Cryst. Lattice Defects, **5**, 1 (1974).
7. A. Seeger and C. Wuthrich, Nuovo Cimento, **33B**, 38 (1976).
8. W. Xu and J. A. Moriarty, Comput. Mat. Sci., **9**, 348 (1998).
9. J. A. Moriarty, W. Xu, P. Söderlind, J. Belak, L. H. Yang and J. Zhu, J. Eng. Mater. Tech., **121**, 120 (1999).
10. W. Sigle, Philos. Mag. A, **79**, 1009 (1999).
11. M. S. Duesbery and V. Vitek, Acta Mater., **46**, 1481 (1998).
12. C. Woodward and S. I. Rao, Philos. Mag. A, **81**, 1305 (2001).
13. *Single Crystal Elastic Constants and Calculated Aggregate Properties: A Handbook*, edited by G. Simmons and H. Wang (MIT Press, Cambridge, MA, 1971).
14. O. Gülseren and R. E. Cohen, Phys. Rev. B, 65, 064103 (2002).
15. S. Ismail-Beigi, D. E. Segall and T. A. Arias, private communication.

16. Using the program *seqQuest* and LDA pseudopotential for Ta developed by P. A. Schultz.

17. A. Strachan, T. Çağın, O. Gülseren, S. Mukherjee, R. E. Cohen, and W. A. Goddard, *First Principles Force Field for Metallic Tantalum*, Phys. Rev. B, submitted.

18. G. Schoeck, Philos. Mag. A, 69, 1085 (1994).

19. G. Schoeck, Philos. Mag. Lett., 76, 15 (1997).

20. G. Schoeck, S. Kohlhammer and M. Fähnle, Philos. Mag. Lett., 79, 849 (1999).

21. G. Schoeck, Acta Mater., 49, 1179 (2001).

22. G. Lu, N. Kioussis, V. V. Bulatov and E. Kaxiras, Phys. Rev. B, 62, 3099 (2000).

23. G. Schoeck, Philos. Mag. A, 81, 1161 (2001).

Chapter 4 Peierls energy barrier and Peierls stress of 1/2a<111> screw dislocation

4.1 Overview

To understand plasticity of crystals, it is critical to understand the mobility of dislocations and the role of the dislocation core in the slip process. The Peierls-Nabarro model provides an analytical strategy to compute the required stress to move a dislocation in an otherwise perfect crystal from the misfit energy. This model suggests that during the translation of a dislocation, the entire variation in the potential is associated with the changes in the shear misfit energy between two half-crystals and with no variation in the elastic field of the dislocation[1]. The Peierls-Nabarro model applies even though the dislocation core reconfigures during the motion[2]. In previous atomistic simulations[3,4], the Peierls stress was determined by increasing the applied shear stress incrementally and fully relaxing the simulation cell (containing a dislocation) until the dislocation glides. In the following, we present an alternative approach to obtain Peierls energy barrier and Peierls stress directly from the analysis of a moving dislocation, which we achieve by simulating a dislocation dipole migration process at extremely low temperature (0.001 K).

As pointed out in Ref. 5, the twinning and anti-twinning slip asymmetry (details see Section 4.4) of shear on {112} planes is an intrinsic factor in the observed violation of the Schmid law for plastic behavior of bcc metals. Owing to this asymmetry, the required shear stresses along [111] and [-1-1-1] in {112} planes for the same dislocation to glide are not equivalent. By measuring the dislocation core energy as a continuous

function of position in the lattice, we observe this twinning and anti-twinning slip asymmetry of the Peierls energy surface and dislocation motion trajectory. In this chapter, we also report our studies on dislocation motion at finite temperatures and via kink pair mechanism.

4.2 Dislocation dipole migration and annihilation process

We construct a dislocation dipole (two dislocations with opposite Burgers vectors) using elastic theory from the perfect crystal with periodic boundary conditions. The simulation cell contains 5670 atoms with lattice vectors **X**=9a[11-2], **Y**=15a[-110] and **Z**=7a/2[111]. In the simulation cell, the dislocations with b=a/2[111] and b=a/2[-1-1-1] are positioned at (1/2**X**, 3/4**Y**) and (1/2**X**, 1/4**Y**) in the (111) plane, respectively. This is denoted as the [1-10] dislocation dipole. Keeping the lattice parameters fixed to the perfect crystal values, the introduction of this [1-10] dislocation dipole causes stresses of σ_{xz} = -1080 MPa, σ_{xx} = 410 MPa, σ_{yy} = 530 MPa, σ_{zz} = 250 MPa and σ_{xy} = 0, σ_{yz} = 0. The large *xz* shear stress is due to the misfit of atomic positions in the (1-12) cell boundary (see Appendix). Since the non-glide stresses could have effect on the computed Peierls stress[3,4,6], we first relaxed the stress of the simulation cell using NPT MD simulations (with the Rahman-Parrinello barostat[7] and the Hoover thermostat[8] at T = 0.001 K) to reach a zero stress [1-10] dislocation dipole. The final lattice parameters are given in Table 4-1. The volume increase for a dislocation per Burgers vector from the bulk lattice cell to the zero-stress cell is 4.29 Å^3.

Table 4-1. The lattice parameters and volumes for simulation cells (containing the [1-10] dislocation dipole) with zero stress, bulk lattice parameters and different pure shear stresses. α denotes the angle between axes **Y** and **Z**; β denotes the angle between axes **Z** and **X**; while γ denotes the angle between axes **X** and **Y**.

	|**X**| (Å)	|**Y**| (Å)	|**Z**| (Å)	α	β	γ	Volume (Å^3)
σ_{xz} = 500 MPa	73.38	70.54	20.13	90.00	91.59	90.00	104178
σ_{xz} = 300 MPa	73.37	70.54	20.13	90.00	91.39	90.00	104172
σ_{xz} = 0 MPa	73.36	70.55	20.13	90.00	91.12	90.00	104170
σ_{xz} = -300 MPa	73.35	70.56	20.13	90.00	90.84	90.00	104168
σ_{xz} = -500 MPa	73.34	70.56	20.13	90.00	90.67	90.00	104167
σ_{xz} = -1100 MPa	73.34	70.57	20.13	90.00	90.13	90.00	104174
bulk lattice parameters	73.27	70.51	20.15	90.00	90.00	90.00	104110

In order to study dislocation migration, we applied an external shear stress to our simulation cell (in the twinning and anti-twinning directions). In a [1-10] dislocation dipole, both dislocations are sheared in the (1-12) plane in the twinning sense under the shear stress along the [111] direction ($\sigma_{xz} > 0$) and in the anti-twinning sense when the shear stress is in the [-1-1-1] direction ($\sigma_{xz} < 0$). In these two cases ($\sigma_{xz} > 0$ and $\sigma_{xz} < 0$), we start from zero stress and then increase (twinning) or decrease (anti-twinning) the applied shear stress σ_{xz} on the simulation cell in steps of 100 MPa until the dislocations begin to move. For each stress state, we performed 10 ps of NPT MD simulation followed by 25 ps of NVT MD simulation at 0.001 K. We find that the dislocation dipole

starts to move under twinning shear of σ_{xz} = 500 MPa and anti-twinning shear of σ_{xz} = -1100 MPa.

Once the dislocation dipole starts to move under the applied shear stress, we continued the NVT MD simulation up to 125 ps. In the course of simulation, dislocations move continuously until the annihilation occurs. The solid lines of Figure 4-1(a) (twinning) and Figure 4-1(b) (anti-twinning) show the time evolution of the total strain energy (the sum of the atomic strain energies calculated using Eq. (2) in Chapter 3 with reference to perfect crystal) per dislocation per Burgers vector during the dislocation migration and annihilation process. The total strain energy decreases as the dislocations approach each other. The rapid drop of the total strain energy at the end indicates dislocation annihilation. Figure 4-1(a) for the twinning shear (σ_{xz} = 500 MPa) shows a residual total strain energy of 0.2 eV (per dislocation per b) after dislocation annihilation. This is because the initially set cell parameters are different from the final dislocation free crystal cell lattice parameters (*cf.* Table 4-1). However, there is little residual strain energy in Figure 4-1(b) for the anti-twinning shear (σ_{xz} = -1100 MPa), because the lattice parameters of the simulation cell under σ_{xz} = -1100 MPa are very close to those of perfect crystal as shown in Table 4-1. This is reasonable because building the [1-10] dislocation dipole into crystal using the lattice parameter of the perfect crystal leads to a shear stress of σ_{xz} = -1080 MPa.

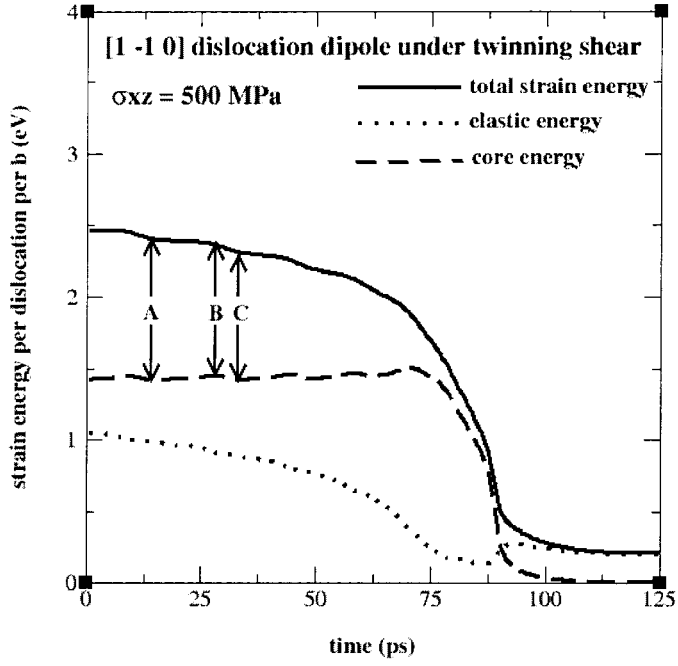
[1 -1 0] dislocation dipole under twinning shear
σxz = 500 MPa
total strain energy
elastic energy
core energy
A
B
C
strain energy per dislocation per b (eV)
time (ps)
0
1
2
3
4
0
25
50
75
100
125

(a)

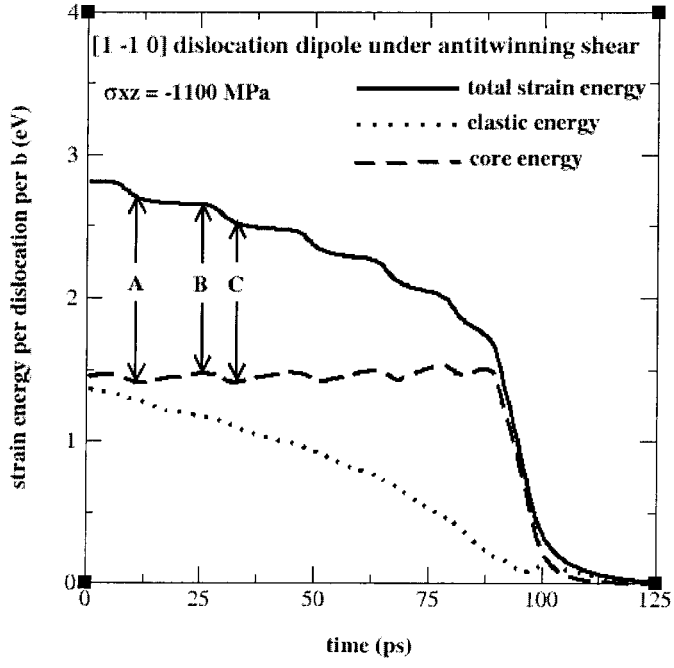
[1 -1 0] dislocation dipole under antitwinning shear
σxz = -1100 MPa
total strain energy
elastic energy
core energy
A
B
C
strain energy per dislocation per b (eV)
time (ps)
0
1
2
3
4
0
25
50
75
100
125

(b)

Figure 4-1. The variation of the total strain energy, elastic energy, and core energy with time in the NVT MD simulations at T=0.001 K. These simulations simulate the migration and annihilation of the [-110] dislocation dipole under the smallest shear stress required for dislocation migration. (a) Twinning shear (σ_{xz} = 500 MPa) and (b) Anti-twinning shear (σ_{xz} = -1100 MPa). There are 5670 atoms in the periodic simulation cell. The states A and C correspond to the minimum core energy configurations, while state B corresponds to the maximum core energy configuration as shown in Figure 4-3. The detailed structures for these states are shown in Figure 4-2 using the corresponding DD maps.

The dynamics in Figure 4-1 show that the total strain energies exhibit bumps on top of the generally monotonic decrease as the dislocations in the dipole migration. To understand the origin of these bumps, Figure 4-2 shows the DD maps of the dislocation dipole for the points labeled as A, B, and C in Figure 4-1. Panels (A) and (C) in Figure 4-2(a) and Figure 4-2(b) show that the valleys of the energy bumps have configurations in which the dislocations are in equilibrium positions. In contrast, panel (B) shows that the peak of the energy bump corresponds to a configuration in which the dislocation is halfway between two equilibrium positions. Thus, the bumps in total strain energy relate to the dislocation motion through a periodic Peierls energy barrier of lattice resistance. Figure 4-2 also shows that during each step the dislocation moves by a/3<112> on {110} planes regardless of the sense (twinning or anti-twinning) of shear. This leads to a zigzag path for dislocation motion as shown by the dotted lines in panel (D).

(a) Twinning (σ_{xz} = 500 MPa)

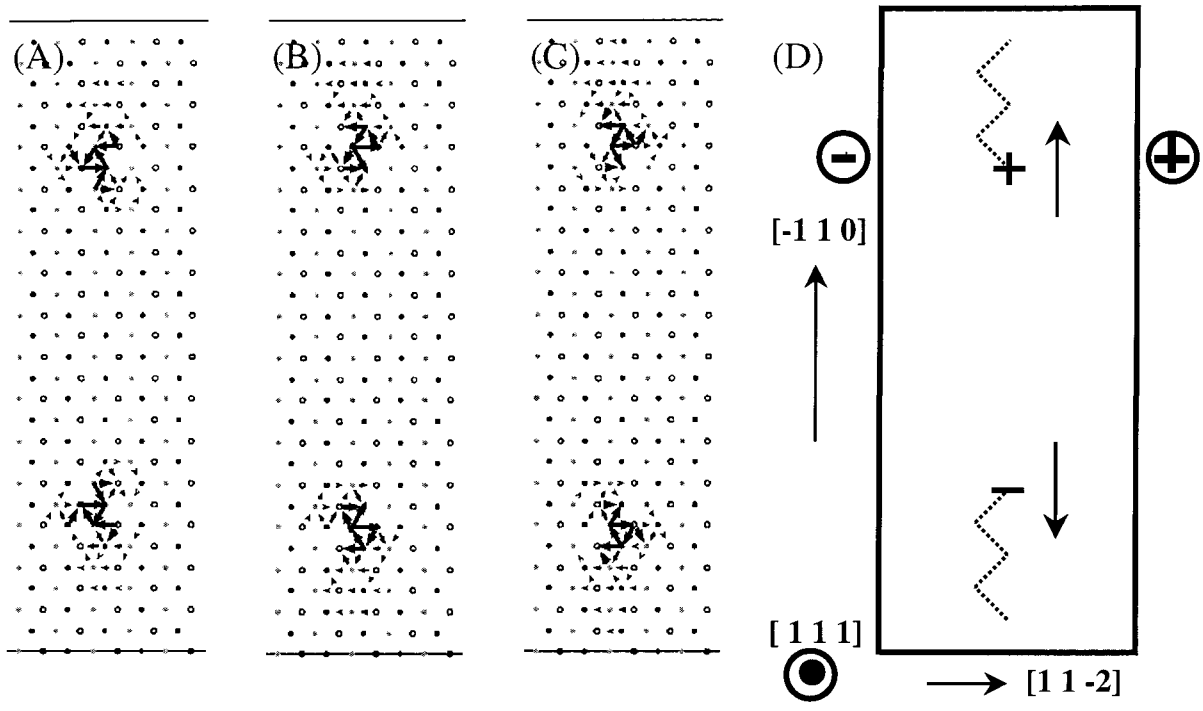

(b) Antitwinning (σ_{xz} = -1100 MPa)

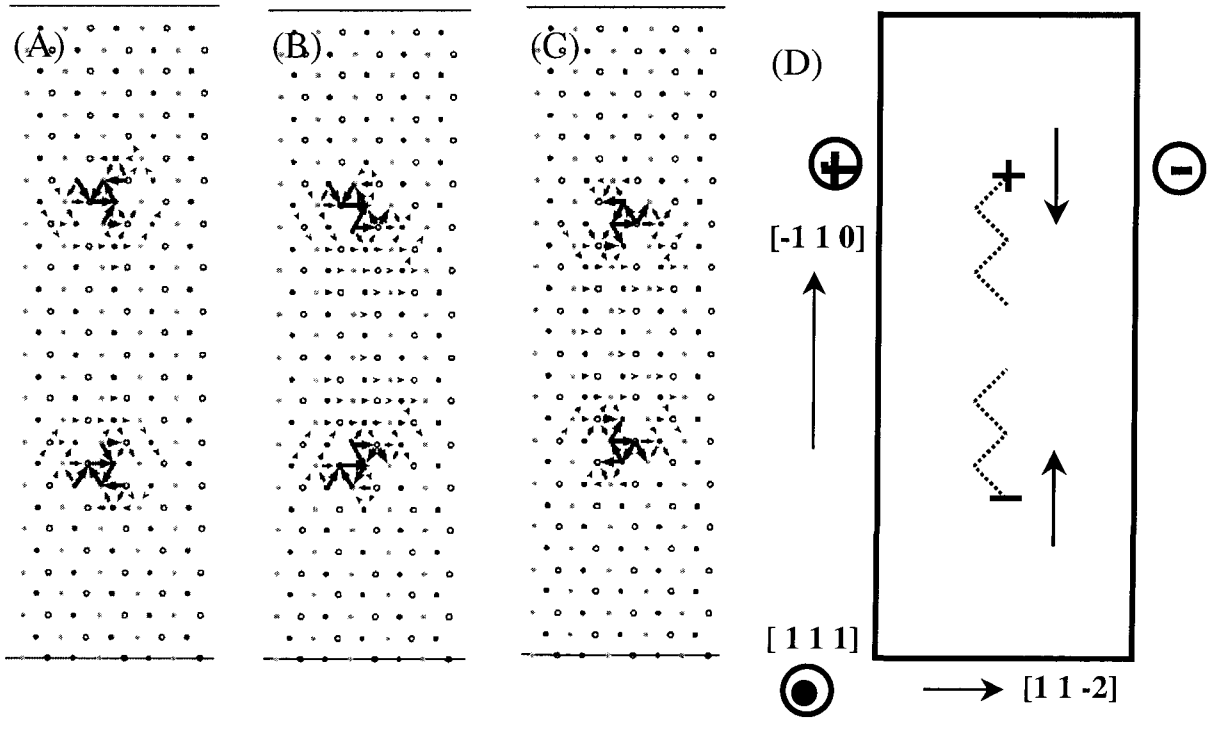

Figure 4-2. DD maps of the states of system during the dynamical process of dislocation dipole migration and annihilation under (a) twinning and (b) anti-twinning shear. Panels (A) and (C) show the dislocation dipoles at equilibrated states, while (B) show the dislocation dipoles translating halfway between two equilibrium states. These maps show only the central region of the simulation cell containing 5670 atoms. Panels (D) show the [111] projections of dislocation dipole. The dotted line in (D) plots the dislocation slip, which is in a zigzag style along <112> directions in {110} planes, in the simulation. The arrow beside dislocations (drawn as plus sign and minus sign) in panel (D) indicates the direction of the Peach-Koehler force for that dislocation introduced by the applied shear stress. The directions of the shear stresses σ_{xz} are represented by the plus sign ([111]) and minus sign ([-1-1-1]) in the circles in panel (D).

In Section 3.3.1 we defined the dislocation core as the twelve atoms with highest strain energy per Burgers vector for the equilibrium dislocation. We now apply this definition to any configuration of a dislocation during its motion. In this way, the total strain energy of our system can be partitioned into two parts: core energy and elastic energy. The dashed lines in Figure 4-1 show the time evolution of the core energy and the dotted lines show the similar curve for the elastic energy. The core energy is rather constant throughout the dislocation migration process, showing bumps at the same places as the total strain energy. The core energy rapidly drops to zero as the dislocation pair is annihilated. This clear-cut definition of elastic energy leads to desirable smooth monotonic decrease with no bumps as the two dislocations move towards each other. These results support the validity of our definition of dislocation core energy.

4.3 Peierls energy barrier and Peierls stress from dislocation dipole migration

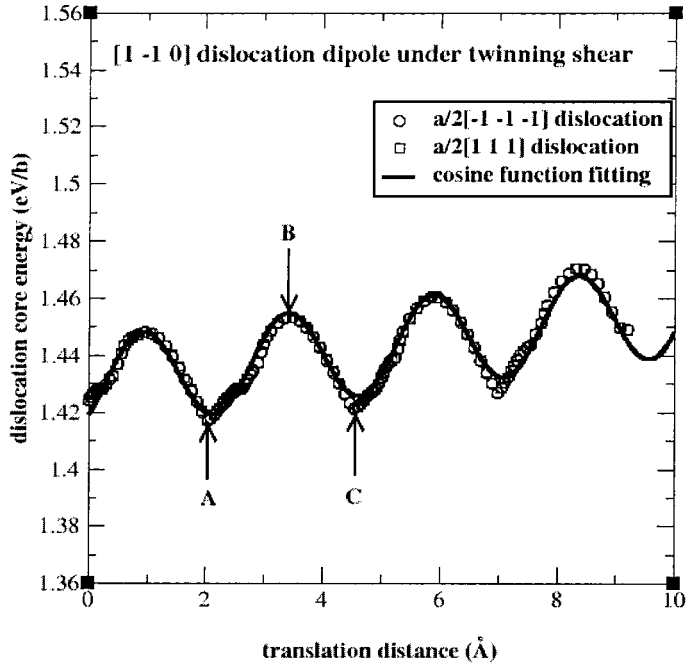

(a)

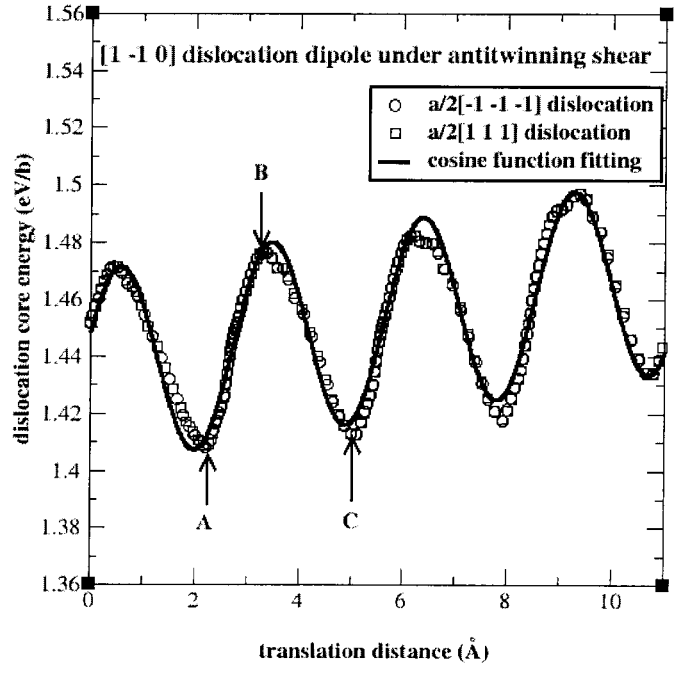

(b)

Figure 4-3. Dislocation core energy as a function of distance traveled by the dislocation under (a) twinning and (b) anti-twinning shear. The solid line shows the cosine function [Eq. (1)] fit to the atomistic data. Table 4-2 gives the parameters from optimal fitting. The states, denoted as A, B and C, correspond to those shown in Figure 4-2.

We define the dislocation *position* as the strain-energy weighted geometric center of the 12 atoms forming the dislocation core per Burgers vector. Figure 4-3(a) shows the variation of dislocation core energy with the dislocation translation distance for the case of twinning shear and Figure 4-3(b) shows the similar plots for the case of anti-twinning shear. Both core energy variation curves fit well the following cosine function in Eq. (1).

$$E_c(x) = \frac{E_p}{2}[1-\cos(\frac{2\pi x}{L}+\varphi)] + k \cdot x + E_c, \quad (1)$$

Here x is the distance traveled by the dislocation and $E_c(x)$ is the dislocation core energy at translation position x. The parameter E_p is the Peierls energy barrier, L is the translation distance for a single dislocation jump, and E_c is the dislocation core energy at its equilibrium position. A phase shift φ and linear term $k \cdot x$ are also introduced to better describe our data. Table 4-2 gives the fitting parameters for dislocation motion under twinning and anti-twinning shears. The Peierls energy barriers are determined to be E_p(twinning)=0.032 eV/b and E_p(anti-twinning)=0.068 eV/b. The anti-twinning to twinning ratio of Peierls energy barrier is E_p(anti-twinning)/E_p(twinning) = 2.125.

Table 4-2. The parameters obtained from fitting the dislocation (1b long) core energy to a cosine function [Eq. (1)] of its translation distance under twinning and anti-twinning shears. The parameters include the Peierls energy barrier E_p in eV, periodic translation

distance L in Å, dislocation core energy E_c in eV, phase shift φ, and the slope k of linear term.

	E_p (eV)	L (Å) [a]	E_c (eV) [b]	φ	k (eV/Å)
Twinning	0.032	2.48	1.414	0.83	0.003
Antitwinning	0.068	2.90	1.401	1.93	0.003

[a] Compare with |a/3<112>| = 2.72 Å in perfect crystal.

[b] Compare with the equilibrium dislocation core energy E_c (eq.) = 1.400 eV.

In the Peierls-Nabarro model, the stress $\tau(x)$ felt by the dislocation during its motion is the derivative of the core energy with respect to the distance it traveled[1].

$$\tau(x) = \frac{1}{b^2}\frac{dE_c(x)}{dx}, \tag{2}$$

Substituting only the cosine term in Eq. (1) to Eq. (2) leads to the Peierls stress [the maximum stress from Eq. (2)] in Eq. (3).

$$\tau_p = \frac{1}{b^2}\frac{\pi \cdot E_p}{L}, \tag{3}$$

Using the E_p and L obtained above (Table 4-2) and the Burgers vector b=2.88 Å, we determine Peierls stresses of

τ_p(twinning)=790 MPa or τ_p(twinning)/μ = 0.013,

τ_p(anti-twinning)=1430 MPa or τ_p(anti-twinning)/μ = 0.024,

τ_p(anti-twinning)/τ_p(twinning) = 1.80.

Here, the calculated shear modulus for the perfect crystal of μ=62.3 GPa [9].

An alternative approach for calculating the Peierls stress [also called the critical resolved shear stress (CRSS)] is to shear an infinite cylinder containing a dislocation. Using the same qEAM FF the calculated CRSS=740 MPa [10] is in good agreement with the 790 MPa derived above for twinning shear with periodic boundary conditions.

Table 4-3. The computed Peierls stresses τ_p in unit of MPa for twinning and anti-twinning shears for 1/2a<111> screw dislocation in Ta.

Force Fields	F-S [a] (Ito *et al.*)	MGPT [b] (Yang *et al.*)	qEAM (present work)
Dislocation Polarization (b)	0	0.0007	0.09
τ_p (twinning)	4120	600	790
τ_p (anti-twinning)	14800	1380	1430
Anti-twinning / Twinning ratio	3.59	2.29	1.80

[a] Reference 4. The reported τ_p is 0.05 C_{44} for twinning shear and 0.18 C_{44} for anti-twinning shear. To calculate τ_p in MPa, we used C_{44} = 82.4 GPa from Ref. 5.

[b] Reference 3. The reported τ_p is 0.0096 G for twinning shear and 0.022 G for anti-twinning shear. The shear modulus G is 62.5 GPa.

Table 4-3 compares our results for Peierls stresses with previous calculations using other force fields. The recent calculations using the MGPT potential[3] lead to 600 MPa for twinning (24% less than ours) and 1380 MPa for anti-twinning (3% less). Calculations using the simple Finnis-Sinclair (F-S) potential[4] lead to a nonpolarized dislocation and much different values (4120 MPa for twinning and 14800 MPa for anti-

twinning). Thus, even though qEAM FF leads to a larger dislocation polarization than MGPT FF, the two force fields lead to a similar description of dislocation mobility.

Our best estimate of the Peierls stress (790 MPa) at 0.001 K is still larger by a factor of two than the best extrapolation to 0 K (~300 MPa [11]) from experiments at finite temperatures. A possible reason for this disagreement is that dynamic kink-like processes might lower the Peierls stress at the experimental temperatures (>73 K). Our simulation at 0.001 K would not include such processes (due to the short length of the periodic cell in the [111] direction). Section 4.5 considers simulations of the dislocation motion at finite temperatures, where we find Peierls stresses in reasonable agreement with experiment.

4.4 Twinning/Anti-twinning asymmetry

In bcc crystal, there is the inherent twinning and anti-twinning asymmetry in {112} planes[5,12]. The stacking sequence of {112} planes has a six-layer repetition ...ABCDEF.... A displacement a/6[111] on (-1-12) plane produces a stacking sequence of ...ABCDCDEFAB..., which corresponds to a monolayer twin and it is natural to regard this as a possible single layer fault (twinning fault). However, the displacement in the opposite sense (-a/6[111]) would produce a stacking ...ABCDABCDEF..., which is different from the former one and does not correspond to a monolayer twin and thus the fault created is different from the above "twinning" fault. It is called the "anti-twinning" fault.

Our results show clearly the twinning and anti-twinning asymmetry of shear for 1/2a<111> screw dislocation in bcc Ta. We find an anti-twinning/twinning ratio of 2.125 for Peierls energy barriers and 1.80 for Peierls stresses. Table 4-2 also shows that the derived dislocation core energy E_c(twinning) = 1.414 eV/b is 1% higher than E_c(anti-twinning) = 1.401 eV/b. Both agree quite well with the dislocation core energy E_c(eq.) = 1.400 eV/b obtained by summing the atomic strain energies for the 12 atoms in the equilibrium dislocation core. The difference between the periodic translation distance for twinning shear (2.48 Å) and anti-twinning shear (2.90 Å) suggests that dislocations move differently in these two cases.

Figure 4-4 shows the trajectories for dislocations with b=a/2[-1-1-1] [Figure 4-4(a)] or b=a/2[111] [Figure 4-4(b)] under twinning and anti-twinning shears. The dislocation position in the figures is determined as the strain-energy-weighted geometric center of the 12 atoms constituting dislocation core. The origin of the plot is the initial position for the dislocation. Figure 4-4 shows that dislocations with b=a/2[-1-1-1] and b=a/2[111] behave similarly under the same sense (twinning or anti-twinning) of shear, while a dislocation moves along completely different trajectories under different senses of shear. Under anti-twinning shear, the dislocation moves along a path at an angle of 29.5° with the [-110] direction. This angle is close to the 30° for the observed slip system (<112> directions on {110} planes) from DD maps. Because the dislocation trajectory is not a straight line, the periodic translation distance 2.90 Å of this path is larger than |a/3<112>|=2.72 Å. However, for twinning shear the path of the dislocation makes an angle of only 8.5° with the [-110] direction, leading to a shorter periodic translation distance (2.48 Å).

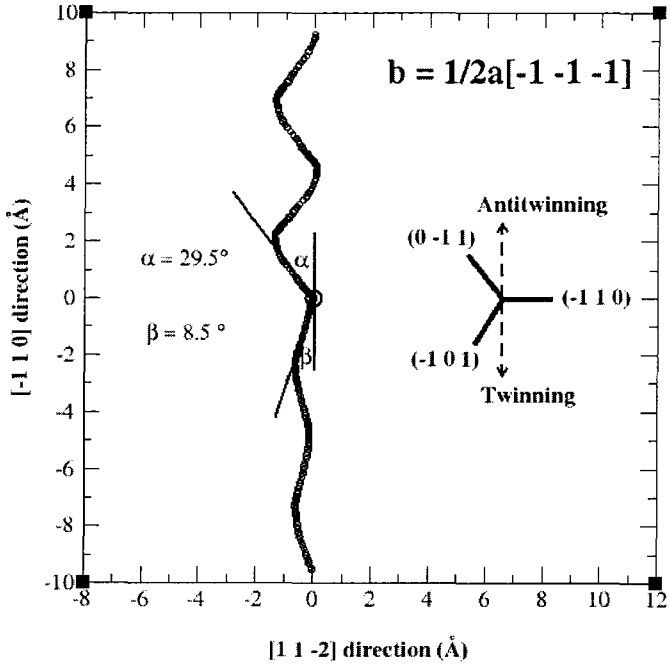
b = 1/2a[-1 -1 -1]
α = 29.5°
β = 8.5 °
α
β
Antitwinning
(0 -1 1)
(-1 1 0)
(-1 0 1)
Twinning
[-1 1 0] direction (Å)
[1 1 -2] direction (Å)

(a)

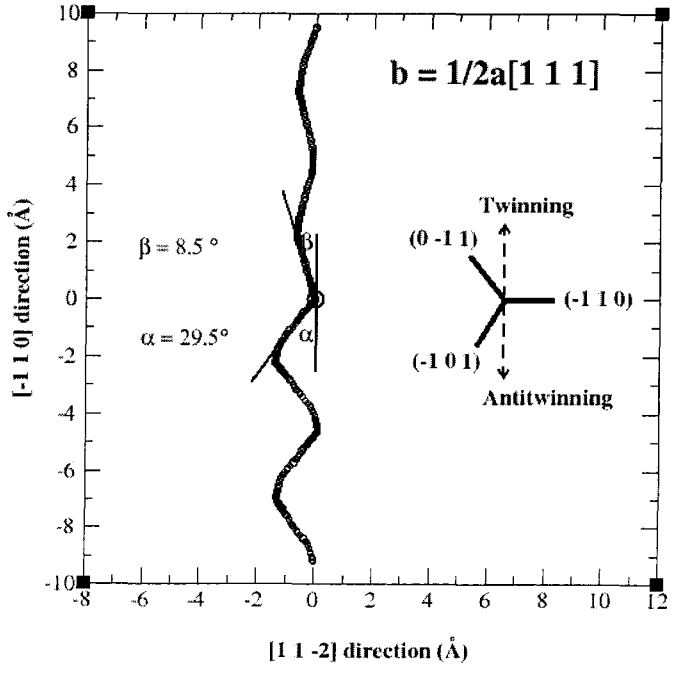
b = 1/2a[1 1 1]
β = 8.5 °
α = 29.5°
β
α
Twinning
(0 -1 1)
(-1 1 0)
(-1 0 1)
Antitwinning
[-1 1 0] direction (Å)
[1 1 -2] direction (Å)

(b)

Figure 4-4. The <111> projection of the motion trajectory for a dislocation with (a) b=a/2[-1-1-1] and (b) b=a/2[111] under twinning and anti-twinning shears. The origin represents the position of the initial equilibrium dislocation. The schematic map on the right shows the crystal geometry and the twinning or anti-twinning direction of shears. The path which dislocation follows under anti-twinning shear makes an angle of α=29.5° with the [-110] direction while the path which dislocation follows under twinning shear makes an angle of β=8.5° with the [-110] direction.

Table 4-3 shows that the qEAM FF calculations (screw dislocation with a polarization of 0.09 b) lead to τ_p(anti-twinning)/τ_p(twinning) = 1.80, whereas the MGPT FF calculations[3] (screw dislocation only slightly polarized 0.0007 b) lead to τ_p(anti-twinning)/τ_p(twinning) = 2.29 and the F-S FF calculations[4] (screw dislocation with a fully isotropic core, zero polarization) lead to τ_p(anti-twinning)/τ_p(twinning) = 3.59. Thus, the τ_p(anti-twinning)/τ_p(twinning) is larger than one and seems to increase as the polarization decreases.

4.5 Dislocation motion at finite temperatures

The previous section used the Peierls-Nabarro model to analyze the dislocation motion at T=0.001 K. However, at high temperatures, the thermal energy fluctuations are too large for this atomistic-energy-based analysis to be useful. Hence, we now use constant temperature and pressure (NPT) MD simulations to study the dynamic processes of dislocation motion at finite temperatures. This study employed a larger simulation cell

containing 22,680 atoms and performed the simulations at temperatures (20K, 50K, 100K, and 300K) and under zero pressure.

For the cases of T = 20K and T = 50K, we find that dislocations always move in <112> directions on (110) planes (the same slip system found in the simulations at T=0.001K). However, dislocations do not always move towards each other, sometimes they take steps perpendicular to the dipole direction.

At 100K, the dislocations still move in the same slip system but the thermal energy is large enough for the polarizations to occasionally change the sign without jumping. Such processes were not observed in lower temperature simulations (T=0.001K, 20K and 50K). Figure 4-5(a)-(d) shows the DD maps for the motion of one dislocation at T=100 K and time t=1.6 ps, 2.4 ps, 3.2 ps, and 4.4 ps. We observe that from t=1.6 ps to t=2.4 ps the dislocation moves in the [-1-12] direction (left) [Figures 4-5(a) and Figure 4-5(b)] and changes its polarization after the hop/jump. From t=2.4 ps to t=3.2 ps [Figures 4-5(b) and Figure 4-5(c)], the dislocation changes its polarization but it stays at the same position. Finally, at t=4.4 ps [Figure 4-5(d)], the dislocation moves forward to the next equilibrium position along the [-12-1] direction and again changes polarization in the jump. Figure 4-5(e) summarizes schematically the motion of this dislocation from t=1.6 ps to 4.4 ps.

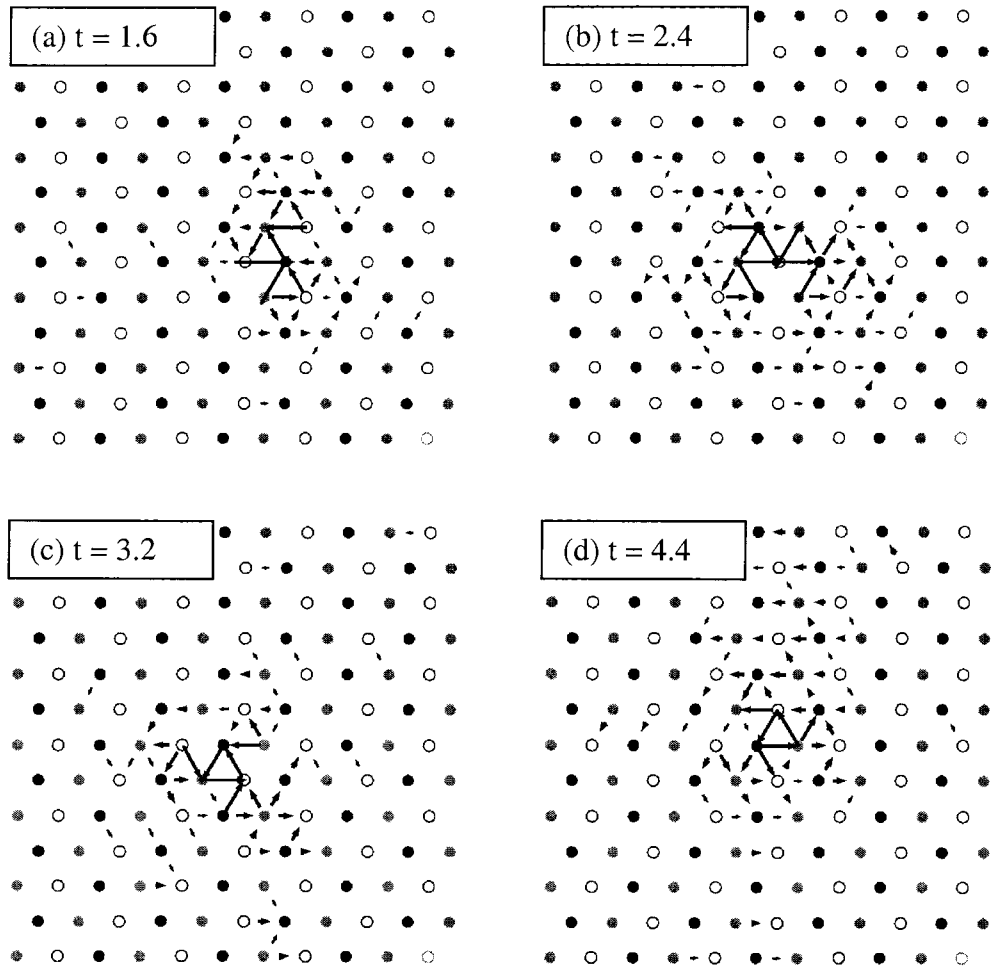

(e) Dislocation motion at T=100 K

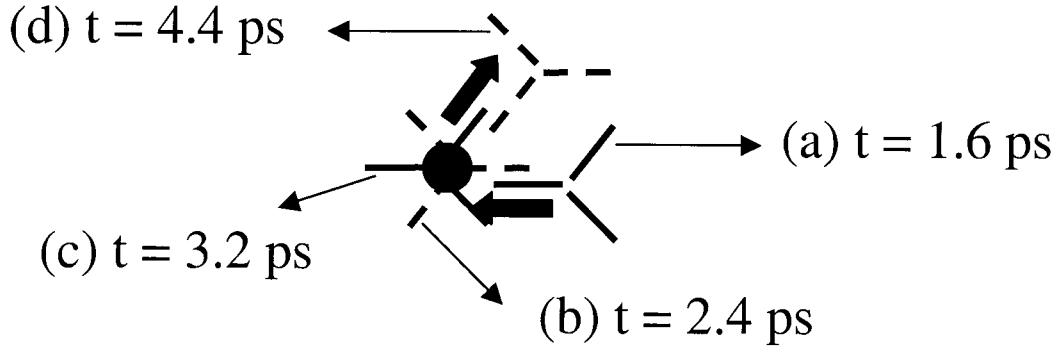

Figure 4-5. Dislocation dipole dynamics process for a system containing 22,600 atoms at T=100 K simulated with NPT MD. Snapshots at different times [(a) t=1.6 ps; (b) t=2.4 ps; (c) t=3.2 ps and (d) t=4.4 ps] are shown using DD maps. Only the 30x30 $Å^2$ region of interest is shown. In the figure, the dislocation moves one step towards the right from 1.6 ps to 2.4 ps and changes polarization while staying in the same equilibrium position at 3.2 ps. This change of polarization allows the dislocation to move to the position shown in figure (d). (e), The schematic representation of the dislocation motions from figure (a) to (d).

The simulation at T=300 K also sometimes shows dislocation polarization changes without a dislocation jump. Thus, Figures 4-6 (a)-(f) show the DD maps for a dislocation at T=300 K. We observe that the dislocation changes its polarization from t=2 ps [Figure 4-6(d)] to t=2.5 ps [Figure 4-6(e)]. The process for this motion is sketched in Figure 4-6(g).

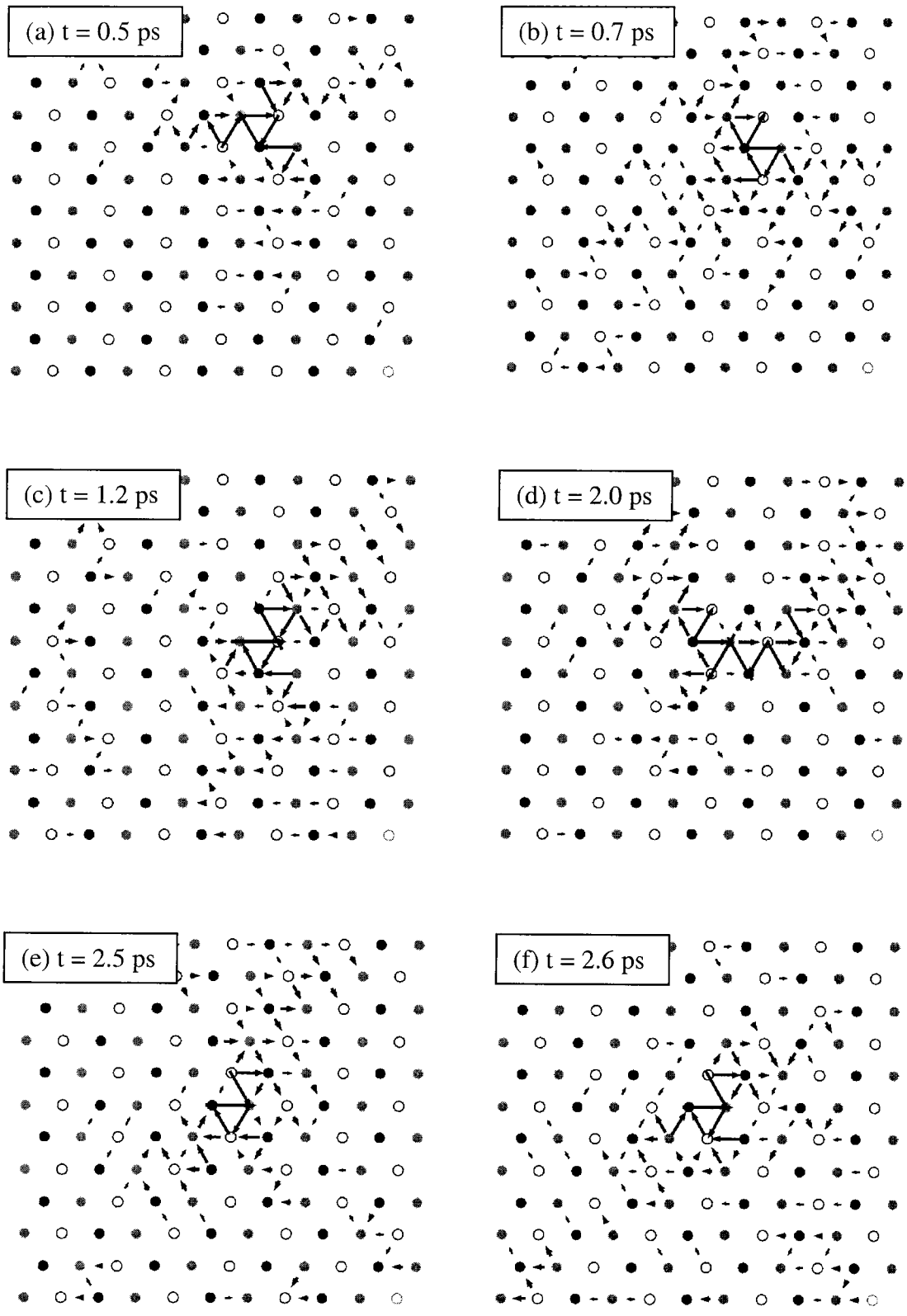
(a) t = 0.5 ps
(b) t = 0.7 ps
(c) t = 1.2 ps
(d) t = 2.0 ps
(e) t = 2.5 ps
(f) t = 2.6 ps

(g)

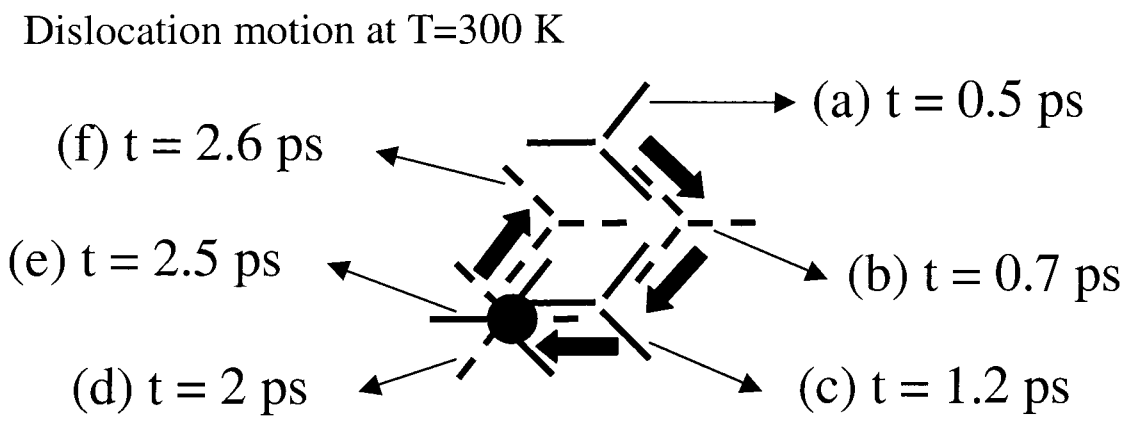

Figure 4-6. Dislocation dipole dynamics process for a system containing 22,600 atoms at T=300 K simulated with NPT MD. Snapshots at different times [(a) t=0.5 ps; (b) t=0.7 ps; (c) t=1.2 ps; (d) t=2.0 ps; (e) t=2.5 ps and (f) t=2.6 ps] are shown using DD maps. Only the 30x30 $Å^2$ region of interest is shown. A process of changing polarization of dislocation can be seen in figure (d) and (e). (g), The schematic representation of the dislocation motions from figure (a) to (f).

For the finite temperature simulations of dislocation dipole dynamics, we compute the hopping rate (η) of dislocations as a function of temperature. We calculated the hopping time as the average duration for the first 8 jumps for each dislocation and then took the reciprocal to obtain the hopping rate. Figure 4-7 shows that the hopping rate follows an Arrhenius behavior with temperature, yielding activation energy of 0.0053 eV/b for dislocation hopping. This activation energy is 6 times lower than the Peierls energy barrier 0.032 eV/b obtained at 0.001 K for twinning motion.

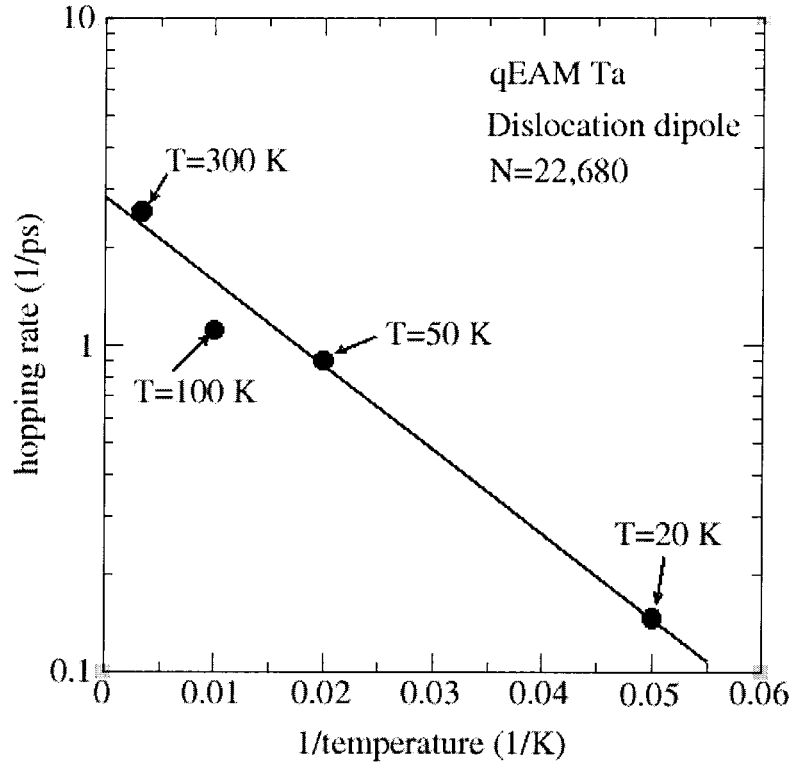

Figure 4-7. The Arrhenius plot of logarithm of dislocation hopping rate with reciprocal of simulation temperature. The dislocation hopping time is defined to be the average dislocation jumping duration for the first 8 jumps. The dislocation dipole containing N=22,600 atoms was simulated with NPT MD at 20 K, 50 K, 100 K and 300 K, respectively. This leads to activation energy for dislocation hopping of 0.0053 eV.

To estimate the Peierls stress at high temperatures, we assume that the Peierls stress is proportional to the height of the energy barrier. This leads to an average Peierls stress of τ_p = 700×(0.0053/0.031) = 120 MPa for temperature in the range of 20K to 300K. This estimated average stress from the dynamical simulations agrees well with the empirical average flow stress[11] (~110 MPa) in the same temperature region (170 MPa at 73 K and 50 MPa at 273 K).

The dramatic drop of the activation energy for dislocation motion from 0.032 eV/b at 0.001K to 0.0053 eV/b for the range of 20K to 300K implies a change in the nature of the dislocation dynamics between these temperature regions. At 0.001K, we find that the dislocation moves collectively as a whole with every part of the dislocation overcoming the same Peierls energy barrier. However, at finite temperatures, thermal fluctuations cause different segments of the dislocation to move in a less correlated way (but without creating a dislocation kink).

To study the effect of temperature on the dislocation topology, we heated the dislocation quadrupole (5670 atoms) at temperature increments of 25K. At each simulation temperature, we carried out 10 ps NPT MD (the pressure is 0 GPa) to allow the volume to change and followed by 25 ps of NVT MD. At this heating rate, we find that the dislocations fluctuate thermally about their centers but do not migrate. We analyzed the dislocation polarization at different temperatures and found that the average polarization of the dislocation does not change with temperature. However, as shown in Figure 4-8(a), the standard deviation of the dislocation polarization fluctuation increases with temperature and is about 8 times larger at 300K than at 1K. Figure 4-8(b) shows the correlation coefficients for the polarization fluctuation between two nearest neighboring one Burgers vector long dislocation pieces at different temperatures. These results indicate that the correlation coefficient between the neighboring pieces of a dislocation decreases with increasing temperature. Apparently, this decreased correlation may decrease the effective energy barrier for dislocation motion.

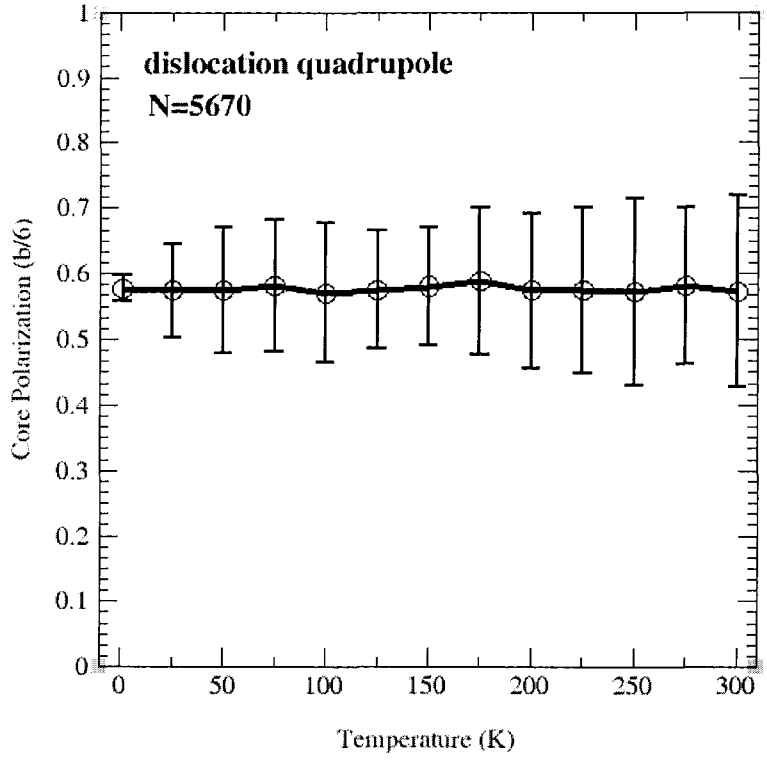
dislocation quadrupole
N=5670
Core Polarization (b/6)
Temperature (K)
0
0.1
0.2
0.3
0.4
0.5
0.6
0.7
0.8
0.9
1
0
50
100
150
200
250
300

(a)

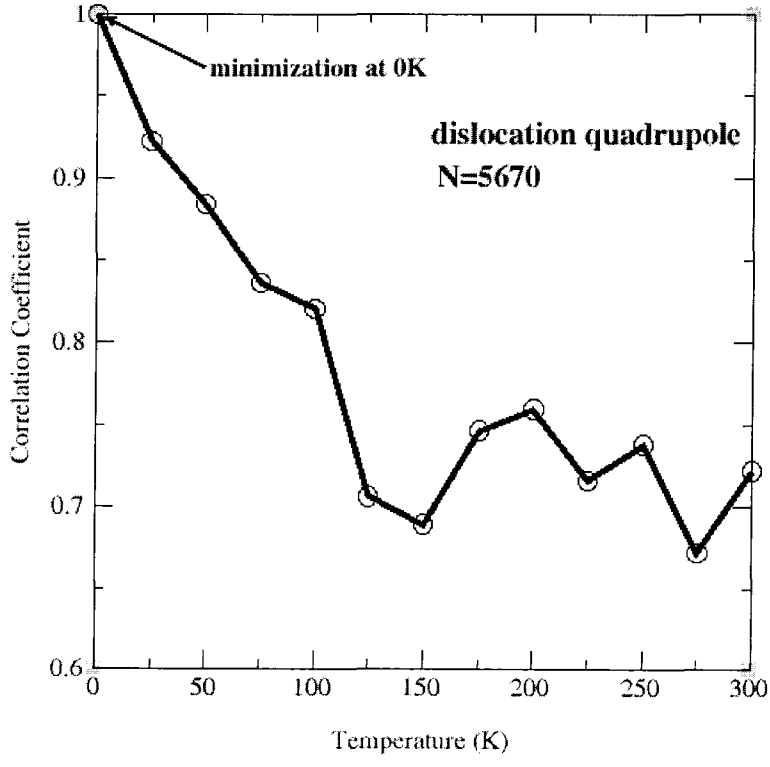
minimization at 0K
dislocation quadrupole
N=5670
Correlation Coefficient
Temperature (K)
0.6
0.7
0.8
0.9
1
0
50
100
150
200
250
300

(b)

Figure 4-8. (a) The average polarization of the dislocation core as a function of temperature. The error bars in the figure indicate the standard deviation of the dislocation polarization. (b) The correlation coefficients of the dislocation core polarization between the first nearest neighboring dislocation segments as a function of temperature. The data at 0K is derived from a minimization simulation and the others are computed by analyzing the last 15 ps simulation trajectory from a total 25 ps TVN MD simulation.

4.6 Dislocation motion by nucleating kinks

In previous sections, we studied the dislocation motion in the cases that it moves as a whole line. We are also interested not only in the case that the dislocation moves via kink pair mechanism, i.e., nucleation of kink pairs and propagation of kinks along the dislocation. The process of kink pair nucleation is hard to study in atomistic scale because the relatively short lengths of dislocations (~ hundreds of Burgers vectors) and short times (~ hundreds of picoseconds) make the kink pair nucleation along a dislocation very unlikely to happen during the course of a MD simulation. To remedy it, we studied the process of dislocation migration and annihilation for a [1-10] oriented dipole of screw dislocations via MD at T=0.001K and provided a nucleation center for the kink pair by introducing a vacancy in the path of a dislocation (denote as D_v). The other dislocation (D_f) sees a defect-free environment. We used a relatively long simulation cell (N=56,700 atoms) whose lattice parameters are **X**=9a[1-12] (73.356 Å), **Y**=15a[1-10] (70.548 Å) and **Z**=70a/2[111] (201.5 Å). We find that dislocations and vacancies attract each other. For Ta, the vacancy formation energy in the core of a screw dislocation is 2.45 eV, while the vacancy formation energy in the perfect bcc crystal is 2.95 eV.

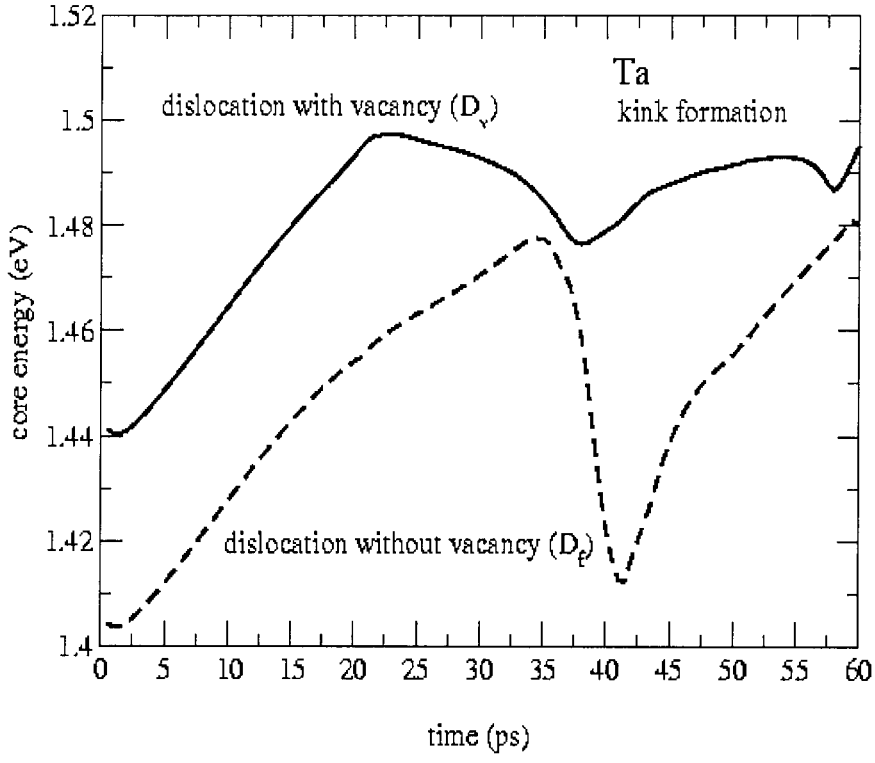

Figure 4-9. Dislocation core energy as a function of time for dislocation dipole migration. The full line shows the dislocation with a vacancy in its path will nucleate a kink pair to reduce the activation energy for a jump.

From our MD simulations of dipole migration, we find that the vacancy helps the dislocation nucleate a kink pair that propagates making the dislocation advance. In Figure 4-9, we show the core energy per Burgers vector as a function of time for two dislocations (D_v and D_f). The core energy is defined as the strain energy of the 12 atoms with higher atomic strain energy per dislocation, per Burgers vector. The dislocation without the vacancy (D_f) shows the same motion behavior we found in smaller (7b long) cells[13], shown as the dashed line in Figure 4-9. It moves as a rigid straight line with an activation barrier of 0.07 eV/b. On the other hand, the dislocation with the vacancy in its

way (D_v) moves faster and experiences a lower energy barrier. The activation energy for the first jump of D_v (0.06eV/b) is very similar to the one corresponding to a rigid dislocation but after the maximum, the energy does not go down to the initial relaxed value. As explained below, this is because of the presence of a kink pair.

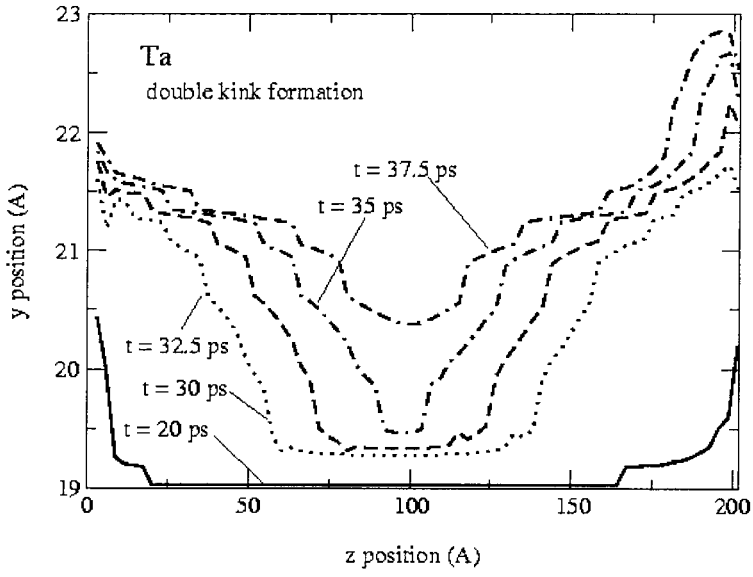

(a)

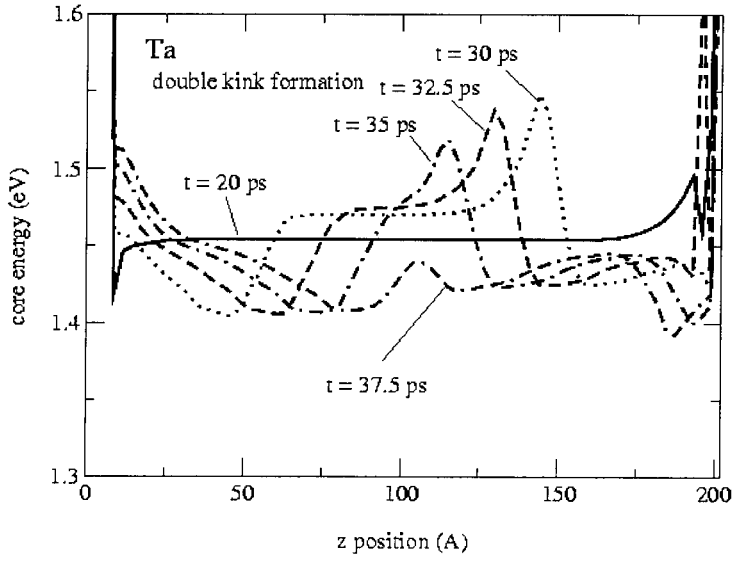

(b)

Figure 4-10. (a) Profile of dislocation D_v (y position of the dislocation along the dislocation line) at different times form 20 to 37.5 ps. (b) Core energy along the dislocation line for the same times.

In Figure 4-10(a), we show the position profile of dislocation D_v (z and y represent the position of the dislocation in [111] and [11-2] directions in the plot) from 20 ps to 37.5 ps in the MD simulation. Figure 4-10(b) shows the core energy along the dislocation line at the same times. We can see that at t = 20 ps the dislocation is almost perfectly straight and the core energy is constant along the dislocation line. Note that the position of the dislocation and core energy are affected by the presence of the vacancy with a z position only close to zero. At time t = 30 ps a kink pair can be clearly seen both from the dislocation profile and core energy plot (note that we have periodic boundary conditions). Part of the dislocation line has advanced to the next equilibrium position while the middle part of D_v (from $z \approx 60$Å to $z \approx 125$Å) is still climbing the Peierls potential barrier. From Figure 4-10(b) we see that the core energy is lower for the portions of the dislocation that advanced and is still higher in the middle part of our simulation cell. The asymmetry in the energy plots comes from the fact that the kink pair contains two different kinds of kinks (will be explained in the next chapter).

4.7 Conclusion

Using the first principles based qEAM force field, we studied the mobility of the a/2<111> screw dislocation in Ta. Applying the definition that the core of the 1/2a<111> screw dislocation is formed by the 12 atoms with higher strain energy per Burgers vector,

we examined the variations of the core energy as the dislocation migrates. This leads to a novel way of calculating the Peierls energy barrier and stress from MD simulations that provides detailed information about the mobility of dislocations. This method gives a Peierls energy barrier of E_P = 0.032 eV/b for twinning shear and E_P = 0.068 eV/b for anti-twinning shear. The predicted Peierls stress at 0K is τ_p=790 MPa for twinning shear and τ_p=1430 MPa for anti-twinning shear. These values are about 7% larger than the Critical Resolved Shear Stress (CRSS) calculated (using the same force field) by shearing a large cylinder containing a dislocation. As in experiments and earlier simulations, we find a clear non-Schmid behavior. The analysis of atomic strain energy distribution also allows us to follow the path of dislocation migration under both twinning and anti-twinning shear. We find that both in the twinning and anti-twinning motion, the dislocations move in <112> directions on {110} planes, but the actual path taken by the dislocations differ due to the twinning/anti-twinning asymmetry of the energy landscape.

Our simulations at temperatures T = 20K, 50K, 100K, and 300K have shown a marked difference from those performed at T=0.001K revealing the importance of temperature effect on dislocation mobility. At high temperatures, thermal fluctuations lead to incoherent motions of the segments within the dislocation apparently aiding the migration. This leads to activation energy of 0.0053 eV/b. Based on this activation energy, we estimate that the Peierls flow stress for temperatures in the range 20K-300K is ~ 120 MPa. This is in good agreement with experimental results[11], 170 MPa at T=73K to 50 MPa at T =273K. Furthermore, in Section 4.6, our preliminary simulation on the kink migration process in screw dislocations clearly shows that the screw dislocation may decrease the energy barrier that impede its motion by forming a kink pair along its line. A

detailed study on the kink formation energy, structure and relations will be given in Chapter 5.

4.8 Appendix: Periodic boundary for the simulation cell containing a screw dislocation dipole

Our computations simulate the system as a crystal with periodic boundary conditions, since this removes questions of the boundary surfaces and simplifies the calculations. We construct the periodic cells containing a dipole of screw dislocations by starting with a perfect periodic crystal and applying isotropic elastic theory. This causes a partial stacking fault along the periodic boundary for the crystal cell unless the lattice parameters for the crystal cell are optimized.

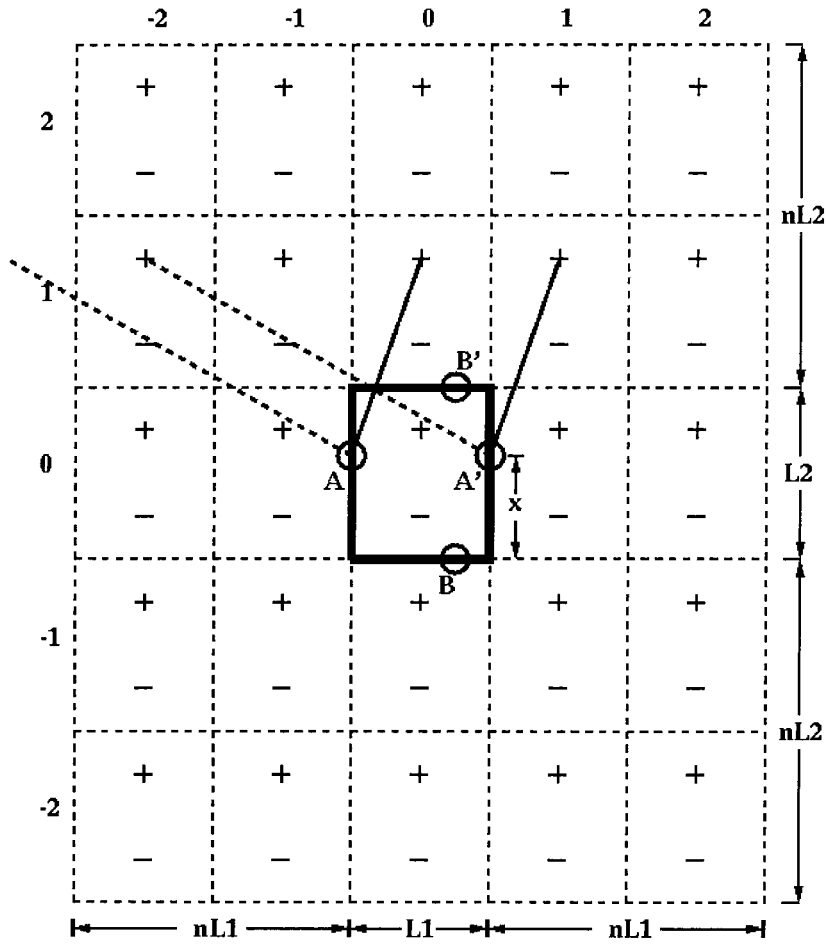

Figure 4-11. The 2-D Schematic map of an atomistic simulation cell (solid primary rectangle cell) containing a screw dislocation dipole and its n (n=2) layers of image cells. The lattice parameters of the simulation cell are L_1 and L_2. The Burger vectors of the screw dislocation are normal to the plane. In the cells, the dislocation with Burgers vector **b** (represented by a plus sign) is at the fractional coordinate (1/2, 3/4) but the dislocation with Burgers vector -**b** (represented by a minus sign) is at the fractional coordinate (1/2, 1/4). The atom A and A' are on the boundaries parallel to the dislocation dipole and equivalent in the periodic perfect crystal. While the atom B and B' are on the boundaries perpendicular to the dislocation dipole and also equivalent in the perfect crystal.

Figure 4-11 shows the scheme we used to compute the atomic displacements for a periodic screw dislocation dipole from isotropic elastic theory. The rectangular primary dipole cell (in the center of Figure 4-11) is surrounded with n layers of its periodic image cells. The Burgers vectors of the screw dislocations in the dipole are normal to the plane, leading to atomic displacements only along the direction normal to the plane. Each cell contains the dislocation dipole, where the dislocation with positive (pointing out) Burgers vector has fractional coordinates of (1/2, 3/4) and the dislocation with negative (pointing inside) Burgers vector is at (1/2, 1/4). The displacements for the atoms in the primary cell are calculated by summing the contributions from all dislocations in the supercell, which includes the primary cell and image cells. The calculated atomic displacements approach their converged values as the number of image cells is increased.

We will consider next the issue of periodic boundaries in the calculations. Consider two cases:

- Equivalent atoms A and A' are on the boundaries parallel to the dislocation dipole in the crystal cell before the introduction of the screw dislocation dipole.
- Equivalent atoms B and B' are on the boundaries perpendicular to the dislocation dipole.

We will now evaluate the displacement difference between these pairs of atoms caused by the periodic screw dislocation dipole.

Figure 4-11 shows that the displacement of the atom A caused by the positive dislocation in the image cell (1, 0) is same as the displacement of the atom A' caused by the dislocation with the same Burgers vector in the image cell (1, 1). This is because the

lines (solid) connecting the atoms to the dislocations are parallel. However, there is no dislocation in the supercell causes the same amount of displacement to the atom A as the dislocation in the leftmost column of the image cells displaces the atom A' (as indicated by the dashed lines). Thus the displacement difference between the atom A and A' is the displacement of the atom A caused by the dislocations in the rightmost image cells less the displacement of the atom A' caused by the dislocations in the leftmost column of the image cells, as given in Eq. (4).

$$\Delta d_{A-A'} = \frac{b}{\pi}\left(\sum_{i=0}^{n}\left\{\tan^{-1}\left[\frac{(i+\frac{3}{4})L_2 - x}{(n+\frac{1}{2})L_1}\right] - \tan^{-1}\left[\frac{(i+\frac{1}{4})L_2 - x}{(n+\frac{1}{2})L_1}\right]\right\} + \right.$$
$$\left.\sum_{i=0}^{n-1}\left\{\tan^{-1}\left[\frac{(i+\frac{3}{4})L_2 + x}{(n+\frac{1}{2})L_1}\right] - \tan^{-1}\left[\frac{(i+\frac{1}{4})L_2 + x}{(n+\frac{1}{2})L_1}\right]\right\}\right), \quad (4)$$

Here L_1 and L_2 are the lattice parameters of the primary cell, x is the distance from the atom A (or A') to the bottom of the primary cell and n is the number of layers of the image cells.

A similar procedure leads to the displacement between atoms B and B' given in Eq. (5).

$$\Delta d_{B-B'} = \frac{b}{\pi}\left(\sum_{i=0}^{n}\left\{\tan^{-1}\left[\frac{(i+\frac{1}{2})L_1 - x}{(n+\frac{1}{4})L_2}\right] - \tan^{-1}\left[\frac{(i+\frac{1}{2})L_1 - x}{(n+\frac{3}{4})L_2}\right]\right\} + \right.$$
$$\left.\sum_{i=0}^{n-1}\left\{\tan^{-1}\left[\frac{(i+\frac{1}{2})L_1 + x}{(n+\frac{3}{4})L_2}\right] - \tan^{-1}\left[\frac{(i+\frac{1}{2})L_1 + x}{(n+\frac{1}{4})L_1}\right]\right\}\right), \quad (5)$$

Here x is the distance from the atom B (or B') to the left boundary of the primary cell.

As n goes to infinity, we find that

$$\Delta d_{A-A'} = \frac{b}{\pi}\tan^{-1}[\frac{L_2}{L_1}], \quad \text{for all } x \in [0, L_2] \tag{6}$$

$$\Delta d_{B-B'} = 0, \quad \text{for all } x \in [0, L_1] \tag{7}$$

Eq. (6) implies that for finite values of L_1 and L_2, introducing the periodic screw dislocation dipole makes atoms A and A' *nonequivalent*. As a result, a partial stacking fault along the boundary parallel to the dislocation dipole is formed in the crystal cell with the magnitude of this stacking fault determined by the ratio of lattice parameters. This stacking fault disappears only when $L_2 << L_1$, which corresponds to dislocation dipole annihilation when L_1 is finite.

On the other hand, Eq. (7) shows that the screw dislocation dipole does not cause a stacking fault along the boundary perpendicular to the dislocation dipole in the crystal cell.

4.9 References

1. J. P. Hirth and J. Lothe, *Theory of dislocations* (Wiley, New York, 1982), p.241
2. G. Schoeck, Philos. Mag. A, **79**, 2629 (1999).
3. L. H. Yang, P. Söderlind, and J. A. Moriarty, Philos. Mag. A, **81**, 1355 (2001).
4. K. Ito and V. Vitek, Philos. Mag. A, 81, 1387 (2001).
5. M. S. Duesbery and V. Vitek, Acta Mater., **46**, 1481 (1998).
6. M. S. Duesbery, Proc. R. Soc. Lond. A, **392**, 175 (1984).
7. M. Parrinello and A. Rahman, J. Appl. Phys., **52**, 7182 (1981).
8. W. G. Hoover, Phys. Rev. A, **31**, 1695 (1985).
9. A. Strachan, T. Çağın, O. Gülseren, S. Mukherjee, R. E. Cohen, and W. A. Goddard, *First Principles Force Field for Metallic Tantalum*, Phys. Rev. B, submitted.
10. D. E. Segall, T. A. Arias, A. Strachan, and W. A. Goddard, *Accurate Calculations of the Peierls Stress in Small Periodic Cells*, J. Comput.-Aided Mater. Design, to be published.
11. R. Lachenmann and H. Schultz, Scripta Met., **4**, 709 (1970).
12. V. Vitek, Cryst. Lattice Defects, **5**, 1 (1974).
13. G. Wang, A. Strachan, T. Cagin and W. A. Goddard, Journal of Material Engineering and Science A, **309-310**, 133 (2001).

Chapter 5 Flips and kinks on 1/2a<111> screw dislocation in Ta

5.1 Overview

The plasticity of metals and semiconductors is controlled by the properties of dislocations and the interactions between dislocations with other defects in crystals. Hence, knowledge of the structure, self-energy, and evolution pattern of dislocations is essential to arrive at a good understanding of plastic deformation of materials and to obtain a mesoscopic model of deformation processes[1-4]. Much information on dislocations can be obtained from such high-resolution experimental techniques as HRTEM and STM. However, many details of the structural and energetic properties of dislocations are beyond the resolution of current experimental methods. Computer simulations at the atomistic level provide the best way to attain deeper insight about dislocations[5,6].

In bcc metals (e.g., K, α-Fe, Mo, and Ta) at low temperatures, the crystal lattice resists the motion of screw dislocations more strongly than the motion of edge dislocations[7]. Therefore, the mobility of screw dislocations governs the plastic deformation behavior of these materials at low temperatures. From atomistic simulations at 0 K, the screw dislocation is thought to move in a rigid, collective fashion leading to a minimal external Peierls stress of about 10^{-2} μ (μ is the shear modulus of the crystal)[8-11]. However, the observed rapid decrease of the Peierls stress with increasing temperature implies that at finite temperatures the screw dislocations move by formation and subsequent migration of kinks rather than by translation of the straight dislocation[12].

The concept of kinks in dislocations and using kinks in describing plastic flow behavior of crystal were mathematically treated in the framework of elasticity theory by Seeger and Schiller[13] in 1966. These ideas are still applicable. The first direct observation of the dislocation kinks was made by Kolar *et al.*[14] using atomic resolution transmission electron microscopy (TEM) on partial dislocations in Si. Many modern mesoscale plasticity theories (for instance, Ref. 4) use the kink-pair mechanism to describe the motions of dislocations. These theoretical models can benefit from the accurate atomistic descriptions of dislocation kinks provided in this thesis.

Using an atomistic simulation, Seeger *et al.*[15] proposed that the asymmetric dislocation cores for the 1/2a<111> screw dislocation in α-Fe were polarized, and then explained the multiplicity of kinks and the existence of flips (antiphase defect[5]) in dislocations. In two classical papers[16,17], Duesbery studied the detailed structure, Peierls stress, and formation energy of the isolated kinks in the 1/2a<111> screw dislocation in K and α-Fe. Duesbery and Basinski[18] showed that atomistic computer simulations of kink pair generation and migration agreed with the experimental flow stress of Potassium (K). Recently, the formation energies of kinks in screw dislocation in Ta [9] and Mo [19] have been determined much more accurately in simulations with Green's function boundary.

In this chapter, we use a simulation model with periodic/ fixed boundaries to

(1) determine the formation energies of 1/3a<112> kinks in the 1/2a<111> screw dislocation in Ta,

(2) estimate the lateral motion energy barriers of those kinks,

(3) analyze the configurations and structures of thosekinks,

(4) investigate the inherent relationship between different types of kinks.

The remainder of this chapter is organized as follows. Section 5.2 describes of the details the periodic/fixed boundary simulation models. Section 5.3 describes the core configurations of the 1/2a<111> screw dislocation and outline the types of the dislocation defect (flip and kink). Section 5.4 reports our results on formation energies of the isolated kinks and kink pairs, while Section 5.5 estimates the migration energies of kinks without using an applied stress. Section 5.6 describes our analysis of the flip and kink structures and the inherent relationship between different kinks. In this section, we also summarize and explain the trend of the kink formation energy and mobility from present work and literature[19]. Finally, our conclusions are given in Section 5.7.

5.2 Simulation model

5.2.1 Construction of simulation model

To study kinks in dislocations, we use the model crystal shown schematically in Figure 5-1, which is orthorhombic and oriented by the [11-2], [1-10] and [111] crystal directions. This cell consists of three distinct construction regions (region A, region B and region C) in the [111] direction.

The construction region A and region C contain four a/2<111> screw dislocations arranged as a quadrupole, in which a pair of dislocations has Burgers vector b = a/2[111] and the other pair of dislocations has Burgers vector b = a/2[-1-1-1]. In region A and C, the initial dislocation was constructed based on elasticity theory and it was subsequently

relaxed to reach its equilibrated configuration under 3-D periodic boundary conditions. The positions of the dislocations in the region A and region C differ by a vector $\vec{v}$ from the equilibrium dislocation center in the region A pointing to the equilibrium dislocation center in the region C as indicated in Figure 5-1.

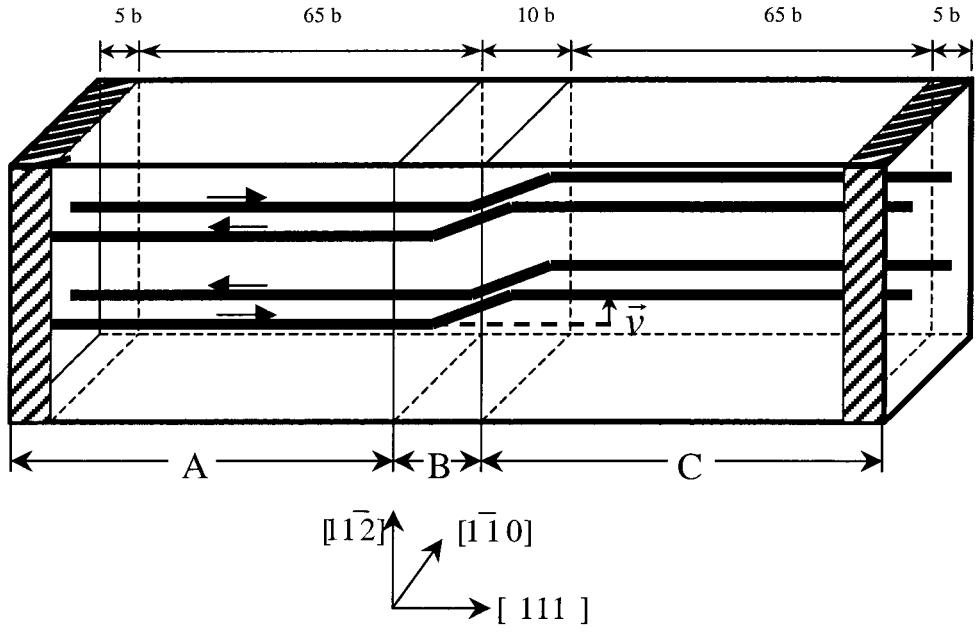

Figure 5-1. The schematic plot of the simulation model. In this model, region A and region C contain the equilibrated dislocation quadruples. Region B is constructed based on elastic theory to smooth the configuration misfit. The vector $\vec{v}$ starts from the center of the dislocation in region A and points to the dislocation in the region C. In our simulations, $\vec{v}$ can only be 0 (flips), 1/3a[11-2] (right kinks) or 1/3a[-1-12] (left kinks). The shaded regions indicate the fixed boundaries, which are 5 b thick, in the simulation. The cell parameters are 5a[11-2] (=40.7Å), 9a[1-10] (=42.3Å), and 150a/2[111] (=431.8Å).

The central region B is designed to smooth the interfacial misfit between the region A and region C. The initial atomic displacement relative to the perfect crystal for each atom in the region B is obtained from elastic theory by the following equations.

$$\Delta d^{B}_{[111]}(\vec{r}) = (1-\alpha)\cdot \Delta d^{A}_{[111]}(\vec{r}) + \alpha \cdot \Delta d^{C}_{[111]}(\vec{r}), \quad (1)$$

with

$$\alpha = \frac{\vec{r}\cdot[111]}{h_B}, \quad (2)$$

where $\Delta d^{A}_{[111]}(\vec{r})$ and $\Delta d^{C}_{[111]}(\vec{r})$ are the displacements determined by elastic theory for the atom positioned at $\vec{r}$ caused by the periodic dislocation quadruples in the region A and the region C, respectively. The h_B is the height of the region B in the [111] direction.

5.2.2. Boundary conditions of simulation model

We employed the qEAM many-body force field (FF)[20] to describe the atomic interaction potentials for Ta. This embedded-atom-model force field was derived from accurate quantum mechanics (QM) calculations. It describes with good accuracy the bcc, fcc and A15 phases of Ta for pressure from ~ -10 GPa to ~ 500 GPa, and also the vacancy formation energy, surface energy and shear twinning energy for bcc Ta crystal. The qEAM FF has previously used to study the melting temperature of Ta as a function of pressure[20], spall failure[21] and properties of straight dislocations[22].

The simulations impose periodic boundary conditions in the [11-2] and [1-10] directions of the model crystal. The quadruple arrangement of the 1/2a<111> screw dislocation in the (111) plane eliminates the misfit of atoms on the periodic boundaries due to dislocation images. On both ends of the simulation cell along the [111] direction,

there are fixed regions that are 5 b (~ 14.4 Å) [larger than the cut-off radius (9 Å) of the qEAM FF] thick. In this way, a 3-D simulation model is formed without introducing misfit or free surface. The movable atoms interacting with the fixed boundaries in the simulation effectively interact with an infinite equilibrium dislocation quadrupole and do not "feel" the existence of free surface.

It is appropriate for us to discuss the effects of the boundary conditions and the size of the simulation cell on the resultant kink at this point.

1) First, the 2-D periodic boundary of the model makes the simulation easy to implement. However, it introduces arrays of the dislocations with the kinks in the (111) plane. Also there is interaction energy between the kinks on different dislocations. This kink-kink interaction energy must be taken into account when we calculate the formation energy of the isolated kinks. Section 5.4 uses isotropic elasticity theory to estimate the kink-kink interaction energy raised by the 2-D periodic boundary and corrects to obtain the formation energy of the isolated kink.

2) Second, the fixed boundary in the [111] direction might cause an atomic misfit near the boundary if proper caution is not exercised. We computed the final kink width (details see Section 5.6.4) and kink formation energy of a NRP kink (definition see Section 5.3) using simulation cells with different lengths in the [111] direction. The results (from line 1 to line 4) in Table 5-1 demonstrate that the kink formation energy as well as the kink structure is well converged when the simulation cells are more than 100 b long. The equilibrium kink width obtained from the strain energy distribution converges to 18 b, while the geometric kink width converges to 10.7 b. In

a simulation cell of length 38 b, incomplete relaxation causes the calculated kink with a 22% wider strain energy peak and 12% larger kink formation energy.

3) The third issue is the height of the region B in Figure 5-1. The optimal choice is the width of the kink of interest. However this information is not available before the simulation. The analysis in Section 5.6 shows that 10 b is a good approximation for all kind of kinks. In fact, our results (line 4, 5 and 6 in Table 5-1) show that the choice of this height has no affect on the kink structure and the kink formation energy.

Table 5-1. The determined final kink width and kink formation energy (before the correction of the kink-kink interaction) for a NRP kink (definition see Section 5.3) in different simulation cells. All simulation cells are 40.7 Å long in the [11-2] direction and 42.3 Å long in the [1-10] direction. In the table, the total length of the simulation cell and the length of the region A, B and C as indicated in Figure 5-1 are given in the unit of Burgers vector b, which is 2.88 Å.

Length in the [111] direction (b)				Final kink width (b)		Formation energy (eV)
Total	Region A	Region B	Region C	Method I	Method II	
38	14	10	14	9.9	221	0.696
94	42	10	42	10.7	22	0.625
136	63	10	63	10.7	18	0.624
150	70	10	70	10.7	18	0.624
150	63	24	63	10.8	18	0.624
150	56	38	56	10.7	18	0.624

With the above considerations, we employed the simulation cell whose geometry was 5a[1-12] (=40.7 Å), 9a[1-10] (=42.3 Å) and 150a/2[111] (=431.8 Å) in our study. As indicated in Figure 5-1, the length of the region A, region B and region C is 70 b (=201.6 Å), 10 b (=28.8 Å) and 70 b (=201.6 Å), respectively. Our cell contains 40,500 atoms (37,800 movable) in the simulation cell.

5.3 Multiplicity of flips and kinks

5.3.1 Equilibrium dislocation core structure

A. Differential displacement map

We used elasticity theory to construct the initial simulation cell with screw dislocation quadrupole. Then, we used the qEAM FF to minimize the total strain energy of the quadruple, obtaining the equilibrium dislocation configuration.

The differential displacement (DD) map[23] in Figure 5-2 (left column) shows the local strain field around the dislocation center. The interpretation of these DD maps is given in the figure caption. Figures 5-2 (a) and (b) show two equilibrium dislocation cores for the dislocation with **b** is equal to 1/2a[111] while Figures 5-2 (c) and (d) show the dislocation cores when **b** is 1/2a[-1-1-1]. These figures show that the equilibrium dislocation core has threefold symmetry and spreads out in three <112> directions on the {110} planes in the DD map. There are 6 equivalent <112> directions on the (111) plane, so there exist two kinds of core configurations both for the dislocation with Burgers vector 1/2a[111] and for the dislocation with Burgers vector 1/2a[-1-1-1]. Despite the

difference in core configurations, all four dislocations have the same energy both in terms of self-energy (including core energy and elastic energy) and in terms of elastic interaction energy. Note that the quadrupole has four dislocations and each of which has one of two possible core configurations. This causes 16 combinations of the quadrupole, but we find that all have identical energies.

B. Relaxation map

The displacement of each atom along the [111] direction from the atomistic relaxation as compared to that calculated from continuum elasticity theory is shown in the relaxation maps (the right column of Figure 5-2). The magnitude of this difference for all atoms, except the 6 columns of atoms closest to the dislocation line, is less than 0.05 Å (0.017 b). These atoms are at distance more than 1.44 b (4.15 Å) from the center of dislocation. This demonstrates that elasticity theory describes the elastic field of screw dislocation quite well and fails only near the core region of the dislocation (within 1.09 b = 3.31 Å). The direction and magnitude of the displacement difference for the central 6 columns of atoms are presented in the relaxation maps. The most important result in these maps is that three central atoms of the dislocation relax simultaneously 0.267 Å (=0.09 b) either in the [111] direction in a P (Positive) type dislocation or in the [-1-1-1] direction in an N (Negative) type dislocation. This phenomenon is called the polarization of dislocation[15]. Regardless of the orientation of Burgers vector b, the P type dislocation core spreads along the [-1 -1 2], [-1 2 -1], and [2 -1 -1] directions in the DD map. While, the N type dislocation cores spread out along the [1 1 -2], [1 -2 1], and [-2 -1 -1] directions.

(a) N_+

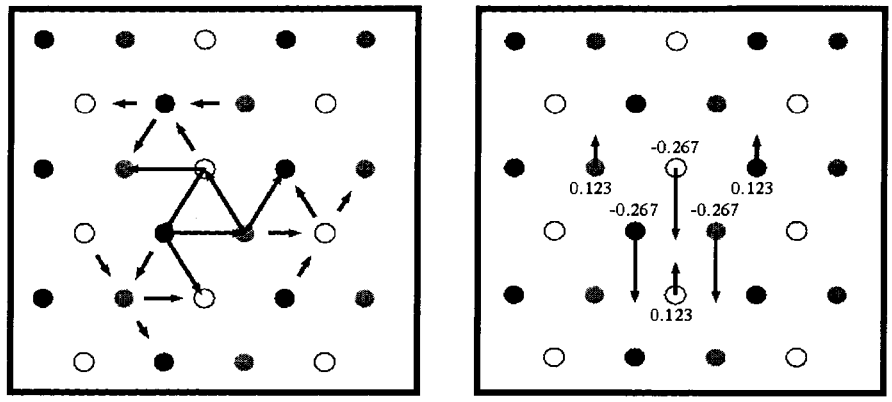
-0.267
0.123
0.123
-0.267
-0.267
0.123

(b) P_+

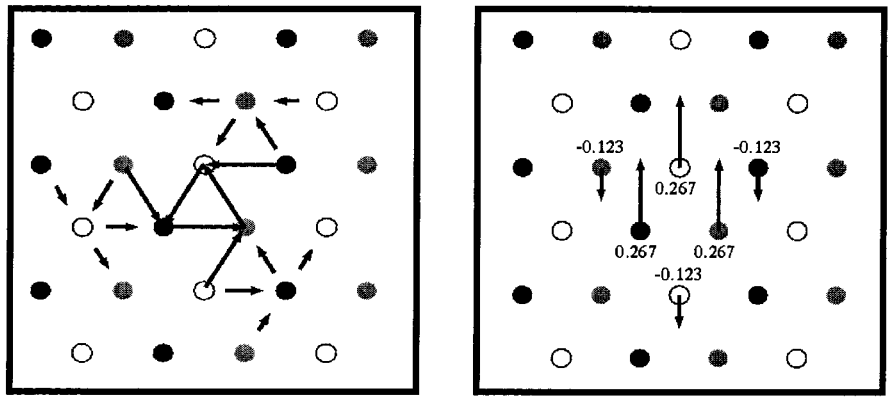
-0.123
-0.123
0.267
0.267
0.267
-0.123

(c) N-

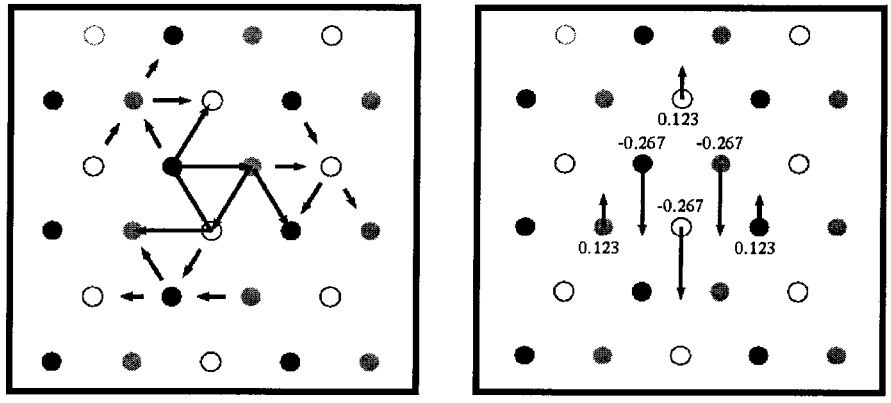
0.123
-0.267
-0.267
-0.267
0.123
0.123

(d) P-

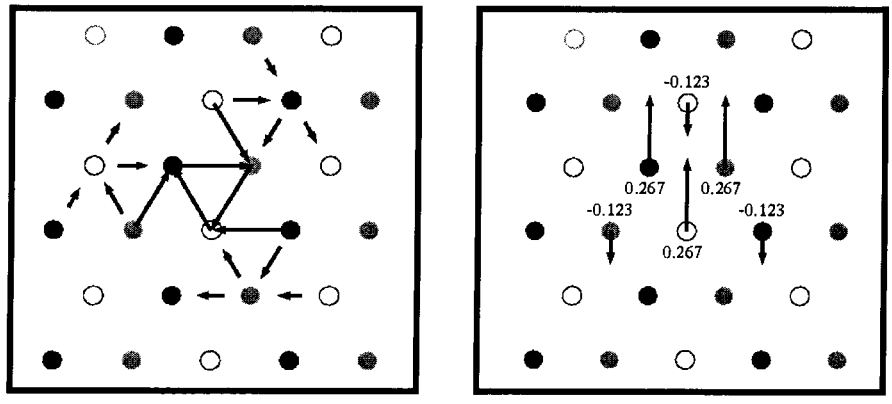
-0.123
0.267
0.267
-0.123
-0.123
0.267

Figure 5-2. The equilibrated dislocation core configurations for the 1/2a<111> screw dislocation in Ta. The circles represent the projected atoms in the (111) plane. The open, shaded or black circles indicate that the atoms are in three consecutive (111) layers of bcc lattice. However, the arrows in two columns of figures have different meanings.

The left column shows the **differential displacement map**, in which the arrow indicates the displacement in [111] direction (perpendicular to the map) of the neighboring atoms *relative to their positions in the perfect bcc crystal.* The direction of the arrow represents the sign of the displacement and the magnitude is proportional to the relative displacement between corresponding atoms. When the arrow touches the two atoms, the relative displacement between these two atoms is 1/3 b. For clarity, the relative displacements less than 1/12 b are not shown in the figure.

The right column shows the **relaxation map**, in which the arrow from each atom indicates the relaxation (parallel to the dislocation line) *relative to the displacement field predicted by isotropic elastic theory.* The magnitudes of such relaxation (in ångstrom) for the central 6 columns of atoms (the relaxation for the other atoms is less than 0.05Å) are printed next to the corresponding atom. Four types of energy degenerate dislocation core configurations are distinguished in terms of the relaxation direction of the three central columns of atoms (downward denoted as "N" and upward denoted as "P") and Burgers vector (a/2[111] denoted as "+" and -a/2[111] denoted as "-").

5.3.2 Flips

By definition, the flip[24] (or antiphase defect) is a defect where a core configuration changes to the other one along the screw dislocation line. Two kinds of the 1/2a<111> screw dislocation (N-type and P-type) lead to two possible configurations of flips (from P to N and from N to P) as schematically shown in Figure 5-3(a). We find the formation energy of a P-N flip is 0.005 eV suggesting this flip could occur thermally along the dislocation. The nucleation energy of the N-P flip is 0.572 eV, which is higher than the energy fluctuations. The P-N and N-P are two distinct flip configurations in 1/2a<111> screw dislocation.

5.3.3 Isolated kinks

The kink refers to the region in which one segment of the dislocation in an energy minimum connects with another segment that lies in a neighboring position. In this study, we focused our interest on the kinks where the dislocation segments are separated by either 1/3a[11-2] (called the **R**ight kinks) or -1/3a[11-2] (called the **L**eft kinks). Figure 5-3(b) shows that in each category (**R**ight or **L**eft) of the kinks there are four combinations of the dislocation core configurations. We thus have 8 possible kinks: NRP, NRN, PRP, PRN, NLP, NLN, PLP and PLN. Among these kinks, the NRN and PRP are energy degenerate and related by symmetry operations, so are the NLN and PLP.

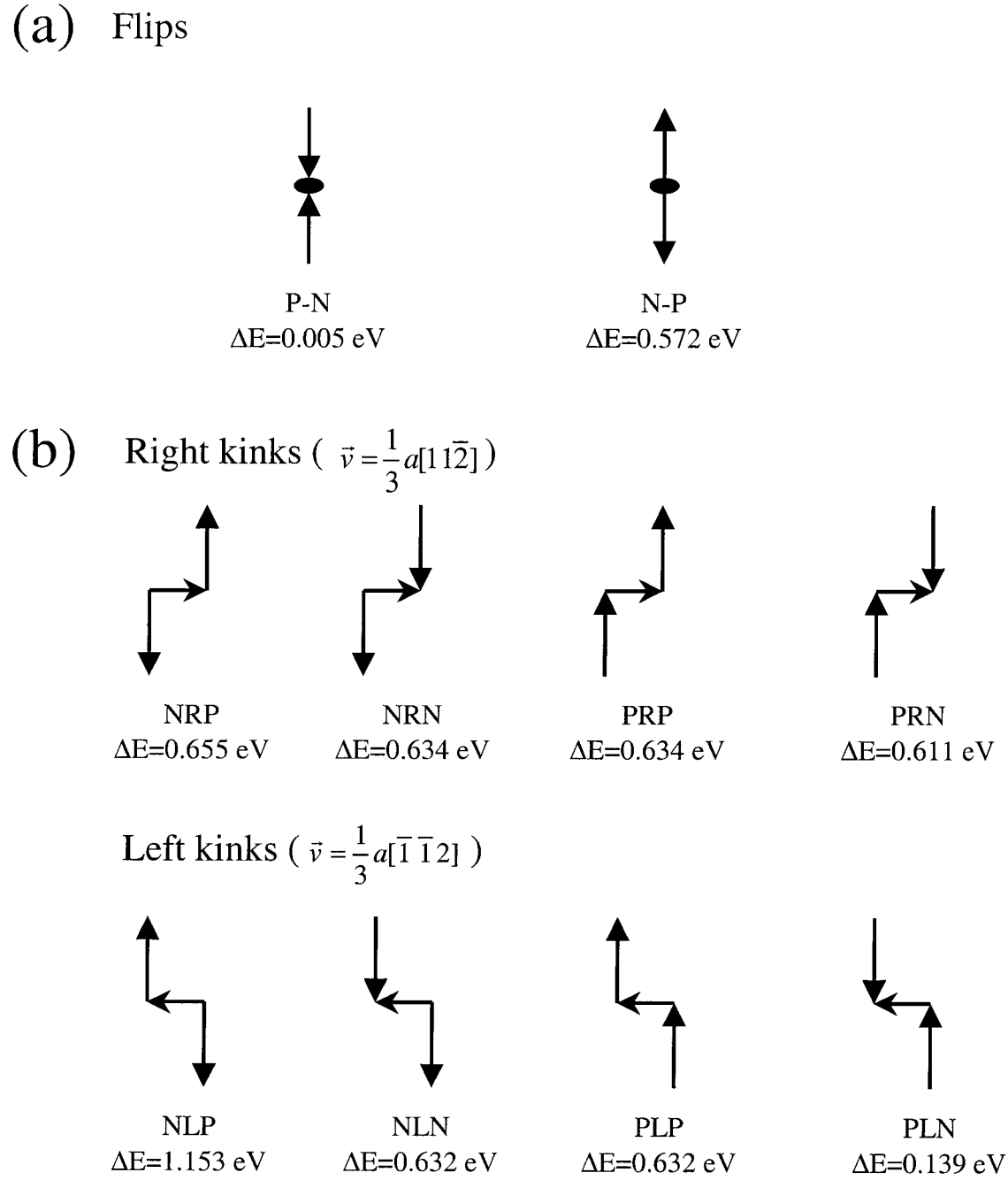

Figure 5-3. The schematic drawing, nomenclature and calculated formation energy of the defect (flip and kink) in 1/2a<111> screw dislocation. In figures, the arrow (▲) represents P type dislocation and (▼) represents N type dislocation. (a) Two kinds of flips exist in screw dislocation. The core configuration along a straight dislocation line can flip either

from P to N (denoted as P-N) or from N to P (denoted as N-P). The formation energy of N-P (0.572 eV) is larger than that of P-N (0.005 eV). (b) There are 4 kinds of right kinks (NRP, NRN, PRP, and PRN) and 4 kinds of left kinks (NLP, NLN, PLP, and PLN). The defect vector ν (indicated in Figure 5-1) is 1/3a[11-2] for right kinks and 1/3a[-1-12] for left kinks.

5.4 Kink formation energy calculations

5.4.1 Formation energy of the isolated kink

With the knowledge of the dislocation core configurations, the dislocation polarization and the multiplicity of flip and kink in the 1/2a<111> screw dislocation, it is feasible to construct a dislocation quadruple such that all dislocations in it have the same type of defects (flip or kink). We constructed and relaxed the quadrupole of the dislocations with the defect in the way described in Section 5.2. After obtaining the equilibrated dislocations with the defect, we calculated the total energy of the relaxed cell [$E_d(cell)$] by summing the atomistic energy for all movable atoms in the simulation. This energy includes the self-energies of the dislocations with the defect [$E_d(self)$] and the interaction energy between the dislocations with the defect [$E_d(inter)$].

On the other hand, the total energy [$E_p(cell)$] of a quadrupole with the same geometry but containing four equilibrium straight 1/2a<111> screw dislocations can also be calculated with simple 3-D periodic boundary simulation (the fixed boundaries in Figure 5-1 are removed). Similarly, the $E_p(cell)$ can be expressed as the self-energies of

the dislocations without the defect [$E_p(self)$] plus the interaction energy between the perfect dislocations [$E_p(inter)$].

The formation energy of the defect (flip or kink) is the self-energy difference between an isolated dislocation with the defect and the dislocation without that defect[25]. Thus the intrinsic formation energy of a defect (ΔE_f) is expressed as

$$\Delta E_f = \frac{1}{4}[E_d(cell) - E_p(cell)] - \frac{1}{4}[E_d(inter) - E_p(inter)], \quad (3)$$

In Eq. (3), the first term $\frac{1}{4}[E_d(cell) - E_p(cell)]$ (called the differential cell energy) is obtained directly from the simulations while the second term $-\frac{1}{4}[E_d(inter) - E_p(inter)]$ (called the interaction correction) is obtained from elasticity theory.

In elastic theory, the flip in the dislocation is considered as a dimensionless point defect and has no effect on the interaction energy between dislocations. Thus the second term is Eq. (3) is 0 when calculating the flip formation energy. However, this term does not vanish in the case of kink, which is a dislocation defect with finite dimension. The interaction energy between two kinked dislocations and the interaction energy between two straight dislocations can be calculated by summing the contributions from all piecewise straight segments[26]. This approach has been used to derive the elastic energy of the kink pair in the same dislocation[25]. Furthermore, the converged value of the second term in Eq. (3) can be obtained by summing the pair interactions in the 2-D periodic quadrupole of the kinked dislocations and the straight dislocations.

We consider two simple models for the description of kinks.

- The perpendicular model assumes the kink is a pure edge segment, which is 2.71 Å (|1/3a<112>|) long in the <112> direction. For every kind of kink in the 1/2a<111> screw dislocation, isotropic elastic theory comes to 0.030 eV for the second term of Eq. (3).
- The inclined model. In fact, the equilibrated kink is not a line segment perpendicular to the dislocation line but a region whose height is about 2.71 Å in the <112> direction and whose width is around 10 b (~28.8 Å) along the [111] direction (see Figure 5-14). The inclined model assumes the kink is a dislocation line segment spanning a width w along the dislocation line and a height h normal to the dislocation (the values of w and h of the kink are given in Table 5-5 of Section 5.6.4). Assuming isotropic Ta, The energy difference between a pair of kinked dislocations and a pair of straight dislocations, denoted as $W(L_1, L_2)$, is calculated using the following equations.

$$R_0(L_1, L_2) = 2\sqrt{L_1^2 + L_2^2} - \sqrt{L_1^2 + (L_2 - h)^2} - \sqrt{L_1^2 + (L_2 + h)^2}\,, \tag{4a}$$

$$R_w(L_1, L_2) = 2\sqrt{L_1^2 + L_2^2} - \sqrt{w^2 + L_1^2 + (L_2 - h)^2} - \sqrt{w^2 + L_1^2 + (L_2 + h)^2}\,, \tag{4b}$$

$$\begin{aligned} I(L_1, L_2) = R_w(L_1, L_2) - \frac{2hL_2}{\sqrt{w^2 + h^2}} \ln[\sqrt{L_1^2 + L_2^2} + \frac{hL_2}{\sqrt{w^2 + h^2}}] + \\ \frac{hL_2 + w^2 + h^2}{\sqrt{w^2 + h^2}} \ln[\sqrt{w^2 + L_1^2 + (L_2 + h)^2} + \frac{hL_2 + w^2 + h^2}{\sqrt{w^2 + h^2}}] + \\ \frac{hL_2 - w^2 - h^2}{\sqrt{w^2 + h^2}} \ln[\sqrt{w^2 + L_1^2 + (L_2 - h)^2} + \frac{hL_2 - w^2 - h^2}{\sqrt{w^2 + h^2}}] \end{aligned}\,, \tag{4c}$$

$$W(L_1,L_2)=\frac{\mu b_1 b_2}{4\pi}[R_0(L_1,L_2)+\frac{w^2}{w^2+h^2}I(L_1,L_2)]+$$
$$\frac{\mu b_1 b_2}{4\pi(1-\nu)}[\frac{h^2L_1^2\cdot[I(L_1,L_2)+R_w(L_1,L_2)]}{h^2L_1^2+w^2(L_1^2+L_2^2)}+\frac{h^2w^2L_2^2\cdot I(L_1,L_2)}{(w^2+h^2)[h^2L_1^2+w^2(L_1^2+L_2^2)]}] \quad (4d)$$

In the above equations, L_1 and L_2 are the separation distances between dislocations in the [11-2] and [1-10] directions; w and h are the kink width and height; b_1 and b_2 are the Burgers vectors of two dislocations. The shear modulus μ is equal to C_{44} and the Poisson ratio $\nu = 2C_{12}/(C_{11}+C_{12})$. In the calculations, we adopted the elastic moduli (C_{11}=272.54 GPa, C_{12}=137.57 GPa and C_{44}=69.63 GPa) of the perfect bcc Ta crystal at 0 K determined by the qEAM FF[20].

Table 5-2 gives the calculated results for the differential cell energy [first term of Eq. (3)] from the simulation and the interaction correction [the second term of Eq. (3)] from the inclined model calculation, which we used to calculate the formation energies for various flips and kinks. The values of the interaction correction from the inclined model deviate by at most 0.003 eV from the 0.030 eV obtained assuming the kink perpendicular model. This implies that ignoring the real geometry of the kink causes only a marginal error in determining the formation energy (e.g., 0.1 % for the NRP kink and 2 % for the PLN kink). Thus the calculated kink formation energy is insensitive to the uncertainty of the kink geometry.

Table 5-2. The differential cell energies (eV) from the qEAM FF simulations, interaction corrections (eV) from continuum theory using the inclined model [Eq. (4)], and the

intrinsic formation energies (eV) of the defects (flips and single isolated kinks) in the 1/2a<111> screw dislocation in Ta.

configuration	Differential cell energy [a] $1/4[E_d(cell)-E_p(cell)]$	Interaction correction [b] $-1/4[E_d(inter)-E_p(inter)]$	Intrinsic formation energy ΔE_f
N-P (flip)	0.572	0	0.572
P-N (flip)	0.005	0	0.005
NRP (right kink)	0.624	0.031	0.655
NRN (right kink)	0.604	0.030	0.634
PRP (right kink)	0.604	0.030	0.634
PRN (right kink)	0.582	0.029	0.611
NLP (left kink)	1.122	0.031	1.153
NLN (left kink)	0.601	0.031	0.632
PLP (left kink)	0.601	0.031	0.632
PLN (left kink)	0.106	0.033	0.139

[a] The perpendicular model gives 0.030 eV.

[b] see Eq. (3).

5.4.2 Formation energy of kink pairs

In addition to a single kink at which the dislocation line crosses a Peierls energy hill, there are also kink pairs consisting of a left kink and a right kink. These kink pairs can be formed by thermal fluctuation in the crystal and their nucleation and subsequent motion are thought to be important in low temperature deformation processes of bcc metals. If the separation between the left and right kink is sufficiently large, the formation

energy of a kink pair is just the sum of the formation energies of the two component kinks. Since there are 4 kinds of left kinks and 4 kinds of right kinks, there are 16 ways to combine a pair of the kinks in the 1/2a<111> screw dislocation in Ta. In some cases, one or two flips are required to fulfill the requirement of the dislocation core configuration when the kink pair nucleates from a perfect dislocation.

The whole spectrum of the configurations and the formation energies of all possible kink pairs are given in Table 5-3. The calculated formation energies of the kink pairs range from 0.794eV to 1.894 eV. We find that the PLN-NRP kink pair has the lowest formation energy, which is 0.794 eV. This formation energy is close to the value of 0.81 eV for the zero shear stress activation enthalpy of the 1/2a<111> screw dislocation in Ta determined by Tang *et al.*[27] by fitting the empirical data to the Kocks model. Our calculated range covers the available experimental measurements (0.92 eV by Funk[28],1.24 eV by Rodrian *et al.*[29], 0.98 eV by Werner[30], and 0.97 eV by Mizubayashi *et al.*[31]) of the formation enthalpy of the double-kink on the 1/2a<111> screw dislocation in the Ta single crystal. Our calculated kink pair formation energy compare favorable with of 0.88eV to 1.50 eV calculated by Yang *et al.*[9] using the multi-ion interatomic potential from the model generalized pseudopotential theory (MGPT) for Ta. This agreement is somewhat surprising. In our study, the three columns of the atoms closest to the dislocation core shift 0.09 b along the dislocation line causing an asymmetric dislocation core. In the MGPT FF calculations these atoms only translate 0.0007 b in the [111] direction leading to a symmetric core. The agreement between these two calculations suggests that the symmetry of the 1/2a<111> screw dislocation core does not play an important role in the study of screw dislocation kinks.

Table 5-3. Calculated formation energies of all kink pairs in 1/2a<111> screw dislocation in Ta. The total formation energy of kink pair is the summation of the formation energies of the component single kinks and the flips required. Note that the kink pair PLN-NRP has the lowest formation energy, which is 0.472 eV lower than the second lowest kink pair formation energy.

configuration				
Initial flip	Right kink	Internal flip	Left kink	Formation energy (eV)
	NRP		PLN	0.794
	NRN		NLN	1.266
	PRP		PLP	1.266
	NRP	P-N	NLN	1.292
P-N	NRP		PLP	1.292
N-P	PRP		PLN	1.345
	NRN	N-P	PLN	1.345
	PRN		NLP	1.764
	PRP	P-N	NLP	1.792
P-N	NRN		NLP	1.792
N-P	PRN		NLN	1.815
	PRN	N-P	PLP	1.815
P-N	NRP	P-N	NLP	1.818
N-P	PRP	P-N	NLN	1.834
P-N	NRN	N-P	PLP	1.834
N-P	PRN	N-P	PLN	1.894

5.5 Kink migration energy calculations

5.5.1 Kink migration energy

Once the kink pair nucleates, the component kinks would move laterally driven by an applied resolved shear stress. During the lateral motion, the kink would experience periodic energy barriers from crystal lattice. If the required kink migration energy were comparable with the kink formation energy, both kink pair formation and migration processes would govern the mobility of the dislocation. Hence, it is also important to quantify the kink migration energy. In this section, we propose a way to estimate the magnitude of the kink migration energy and demonstrate the difference of motion for various kinds of kinks.

In the simulation cell containing the equilibrated dislocations, the position of each atom differs from its position in perfect bcc crystal by an amount of $\Delta\vec{r}$, which is the atomistic displacement. If there is no kink in the dislocation, the atoms in the same column in the [111] direction will have the exactly same atomistic displacement. However, the existence of the kink in the dislocation destroys such regularity. The atoms in the kink region have different atomistic displacements from those atoms far away from the kink region even though they are in the same [111] column. When the kink migrates along the dislocation line one step, the strain field of the whole simulation model will migrate along the [111] direction by 1b, as will the atomistic displacements. In the current study, we translate the strain field rigidly and estimate the energy barrier during the kink moves along the dislocation. Suppose two consecutively neighboring atoms, atom i and atom j, are in a [111] column and the corresponding atomistic displacements

are $\Delta\vec{r}_i^{\,0}$ and $\Delta\vec{r}_j^{\,0}$ in an equilibrium dislocation with a kink. After the kink moves a distance d in the direction from the atom i to the atom j, the atomistic displacement of the atom i is determined with the following equation.

$$\Delta\vec{r}_i^{\,h} = (1-\frac{d}{b})\cdot\Delta\vec{r}_i^{\,0} + \frac{d}{b}\cdot\Delta\vec{r}_j^{\,0}, \tag{5}$$

A new configuration representing the moving kink is obtained by updating the atomistic displacements for all atoms in the model crystal.

We calculated the potential energy for every configuration and determined the potential energy barrier as the kink moves one Burgers vector along the dislocation line. The $\Delta\vec{r}_i^{\,h}$ in Eq. (5) keeps unchanged for a perfect dislocation because $\Delta\vec{r}_i^{\,0}$ is equal to $\Delta\vec{r}_j^{\,0}$, so the perfect dislocation segments do not cause any variation in the potential energy. Therefore, the calculated energy barrier must be the kink lateral migration energy. The kink migration energy of a NRP kink is estimated to be 2.5×10^{-4} eV (0.04% of its formation energy 0.655 eV) and the PLN kink migration energy is 3.5×10^{-4} eV (0.3% of its formation energy 0.139 eV). The NLP kink was found to have the largest migration energy 1.9×10^{-3} eV, which is only 0.2% of its formation energy 1.153 eV. In our calculation the kink moves in a rigid and collective way, which makes our result an overestimate of the kink migration energy. It applies only in the limit of low stress deformation. Since the kink migration energy is about two magnitudes smaller than the corresponding kink formation energy, it is evident that at low stress conditions the mobility of the 1/2a<111> screw dislocation in Ta is controlled by the kink pair formation energy rather than kink migration energy. The same conclusion has also been drawn from MGPT FF simulations[9]. Because the kink migration energy is much less

significant than the kink formation energy, we do not think an accurate determination of the kink migration energy is a priority.

5.5.2 Relative mobility of kinks

In section 5.3 and section 5.4, we studied the multiplicity of kinks and computed the formation energies of different kinks. It is also interesting to investigate the kink migration mobility for different kink configurations. The method described in subsection 5.5.1 can be used to estimate the kink migration energy barrier well. However, this method does not emphasize the role of the kink configuration in the migration process because atoms in the kink region and in regions far from the kink are translated simultaneously. In the following, we propose a way to compare the migration mobility of kinks.

Analyzing the atomic motions during kink migration, we found that atoms in the kink region move much more than atoms far from this region. Hence, we can partition the atoms in the simulation cell into two groups (group A and group B) using a cutoff parameter γ. When kink migrates by 1 b along the dislocation, the atoms in group A translate more than γ while the atoms in group B move less than or equal to γ. Using this grouping strategy, we constructed the dislocation configurations describing the kink migration process as follows: the atoms in group B are positioned as they were in the equilibrium kink configuration while the positions of the atoms in group A are computed by Eq. (5). In fact, we believe that this trajectory is close to what occurs to the kink when it moves rapidly under a high stress.

We carried out one-point potential energy evaluations for the different configurations of kink motion. The equilibrium configuration of the kink has the lowest potential energy and the potential energy of the system increases during the kink migration. The energy increase, called the elastic relaxation energy, indicates the far field of a kink (composed of the atoms in the group B) resists the migration of the core region of kink. Using a cutoff parameter γ as 0.05 Å, Figure 5-5 shows the elastic relaxation energies for different kink configurations [all right kinks in 5-5(a) and all left kinks in 5-5(b)]. The internal friction between the atoms in the group A and those in the group B causes the elastic relaxation energy increasing quadratically. The elastic relaxation energy after the kink moves 1 b can be used to infer the mobility of the kink (assuming that a higher elastic relaxation energy implies it is much harder to move the core region of the kink along the dislocation line).

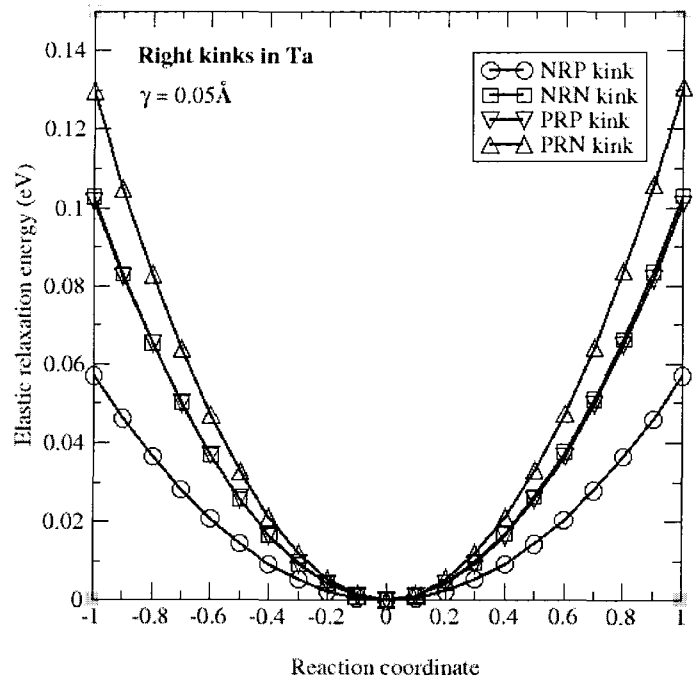
Right kinks in Ta
γ = 0.05Å
NRP kink
NRN kink
PRP kink
PRN kink
Elastic relaxation energy (eV)
Reaction coordinate
0.14
0.12
0.1
0.08
0.06
0.04
0.02
0
-1
-0.8
-0.6
-0.4
-0.2
0
0.2
0.4
0.6
0.8
1

(a)

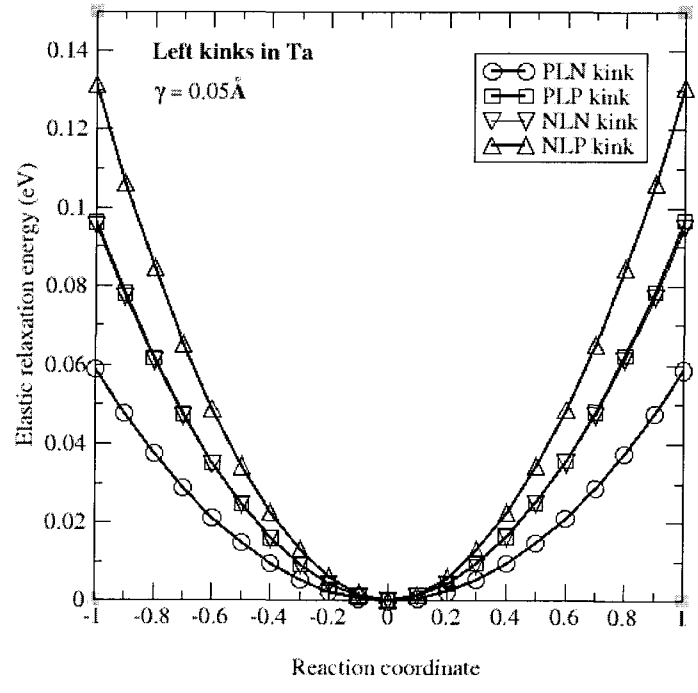
Left kinks in Ta
γ = 0.05Å
PLN kink
PLP kink
NLN kink
NLP kink
Elastic relaxation energy (eV)
Reaction coordinate
0.14
0.12
0.1
0.08
0.06
0.04
0.02
0
-1
-0.8
-0.6
-0.4
-0.2
0
0.2
0.4
0.6
0.8
1

(b)

Figure 5-5. The elastic relaxation energy associated with the kink lateral migration by +/- b. Atoms that move less than or equal to 0.05Å between the initial and final equilibrium configurations are kept fixed as their initial positions. While the atoms, which move more than 0.05 Å between two equilibrated configurations, are moved rigidly by 0.1 b at each step by linear extrapolation. In our computation, there are 14 such atoms per NRP kink, 30 atoms per NRN or PRP kink, 43 atoms per PRN kink, 15 atoms per PLN kink, 25 atoms per PLP or NLN kink and 36 atoms per NLP kink. (a) Right kinks and (b) Left kinks. The results show that the NRP kink and the PLN kink have the lowest elastic relaxation energy when kink move 1 b such that they have the highest migration mobility among the right and the left kinks, respectively.

For the various kinds of kinks, we plot in Figure 5-6 [all right kinks in Figure 5-6(a) and all left kinks in Figure 5-6(b)] the elastic relaxation energy after the kink moves 1 b. In these figures, we show the calculated elastic relaxation energy under various cut-off parameter γ. The results indicate that the mobility of kinks differ appreciatively when $\gamma > 0.01$ Å but are close when $\gamma < 0.01$ Å. Therefore, we expect to observe a mobility difference between kinks in high-stress conditions but similar migration behavior for the kinks under low stress. For $\gamma = 0.05$ Å, the calculated the elastic relaxation energies when kinks moved 1 b are about 0.1 eV. This hints that the kink migration energy would play an important part under high stress conditions. These computations show that the migration mobility of kinks is in the order of:

For right kinks, NRP > NRN (=PRP) > PRN, (6a)

For left kinks, PLN > NLN (=PLN) > NLP, (6b)

An explanation of the relations in (6) will be given in the next section.

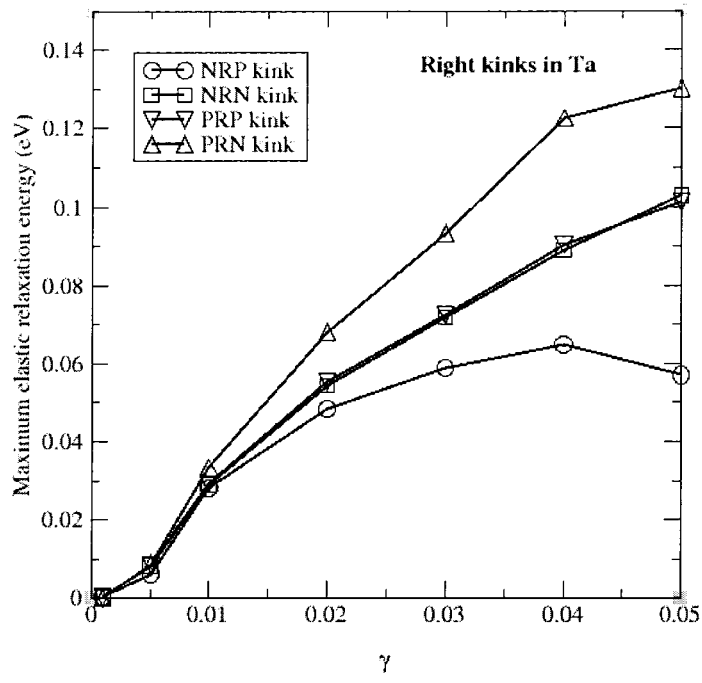
Right kinks in Ta
NRP kink
NRN kink
PRP kink
PRN kink
Maximum elastic relaxation energy (eV)
0.14
0.12
0.1
0.08
0.06
0.04
0.02
0
0
0.01
0.02
0.03
0.04
0.05
γ

(a)

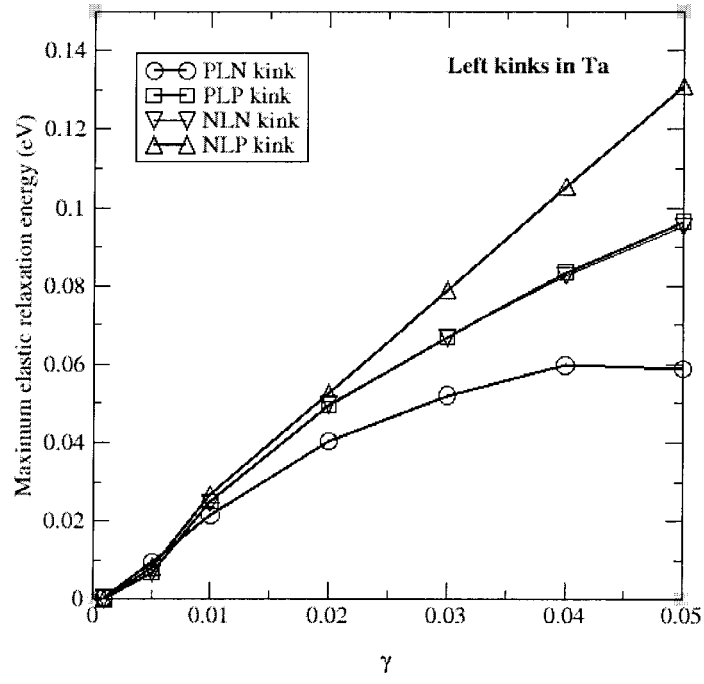
Left kinks in Ta
PLN kink
PLP kink
NLN kink
NLP kink
Maximum elastic relaxation energy (eV)
0.14
0.12
0.1
0.08
0.06
0.04
0.02
0
0
0.01
0.02
0.03
0.04
0.05
γ

(b)

Figure 5-6. The maximum elastic relaxation energy (when kink moved 1 b) associated to the kink lateral migration. The calculations same as reported in Figure 5-5 have been carried out for the different γ (from 0.001 to 0.05 Å). (a) Right kinks and (b) Left kinks.

The above results allow us to conclude that among all possible kink pairs the PLN-NRP kink pair has not only the lowest formation energy but also the lowest migration energy barrier.

5.6 Structural analysis

5.6.1 Overview

In this section, we present a detailed structural analysis of dislocation defects (flip and kink). The study aims to elucidate the reasons for the following:

(1) Why do N-P and P-N flip have different formation energies?

(2) Why does formation energy of the NRP, NRN (or PRP) and PRN kinks decrease and differ by ~0.02 eV while the formation energies of the NLP, NLN (or PLP) and PLN kinks decrease but differ by ~0.50 eV?

(3) Why does the mobility of kinks follow the rule: NRP > NRN (=PRP) > PRN and PLN > NLN (=PLN) > NLP?

We also carried out structural analyses on kinks to determine the geometrical parameters of the isolated kink (kink width w and kink height h) and to estimate the minimum stable separation between a pair of kinks.

5.6.2 Structural analysis of flips

A. Relative displacement between neighboring columns (DD map)

There are two kinds of flips for the a/2<111> screw dislocation in Ta. They are the P-N flip, whose formation energy is 0.005 eV, and the N-P flip, whose formation energy is 0.572 eV. Figure 5-7(a) and Figure 5-7(b) show the strain energy distribution of the relaxed quadrupole of dislocations containing the P-N flips or the N-P flips along the dislocation line. The strain energy is computed by summing the atomistic strain energies (the atomistic energy for each atom in the simulation cell less the atomistic cohesive energy in the perfect bcc Ta crystal) for all atoms in a 1b thick slice region. For the sake of comparison, the strain energy distribution of a perfect dislocation quadrupole in the same size simulation cell is also plotted. Figure 5-7(a) and Figure 5-7(b) show that the strain energy of the dislocations with flips deviates from that of the perfect dislocations only in the flip formation region (30 b long for P-N and 50 b long for N-P). It is interesting that the middle 10 b (Z from 70 b to 80 b) of a dislocation with P-N flip [Figure 5-7(a)] has less strain energy than the perfect dislocation while one with N-P flip in Figure 5-7(b) has a strain energy maximum. The DD maps for both flips in Figure 5-7(c) show the atomistic configurations of the dislocation core at various positions marked in Figure 5-7(a) and Figure 5-7(b). The DD maps for the P-N and N-P flip at the center of flip [figure B and E of Figure 5-7(c)] are extremely similar. At the flip center, the dislocation core is symmetric with zero polarization, quite different from the equilibrated dislocation cores [shown in the figure A, C, D, and F of Figure 5-7(c)].

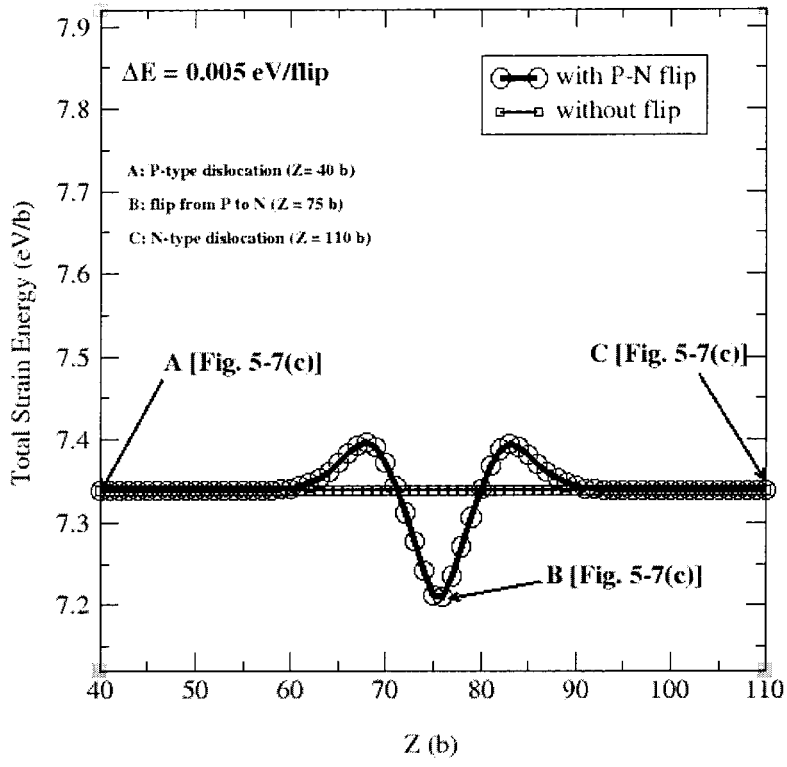
ΔE = 0.005 eV/flip
with P-N flip
without flip
A: P-type dislocation (Z= 40 b)
B: flip from P to N (Z = 75 b)
C: N-type dislocation (Z = 110 b)
A [Fig. 5-7(c)]
C [Fig. 5-7(c)]
B [Fig. 5-7(c)]
Total Strain Energy (eV/b)
Z (b)
7.9
7.8
7.7
7.6
7.5
7.4
7.3
7.2
40
50
60
70
80
90
100
110

(a)

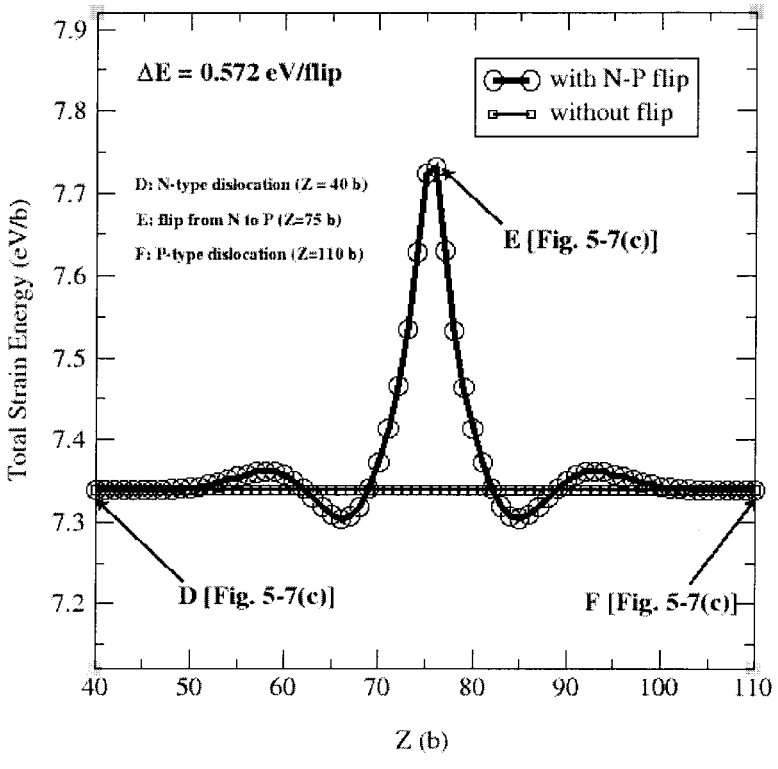
ΔE = 0.572 eV/flip
with N-P flip
without flip
D: N-type dislocation (Z = 40 b)
E: flip from N to P (Z=75 b)
F: P-type dislocation (Z=110 b)
E [Fig. 5-7(c)]
D [Fig. 5-7(c)]
F [Fig. 5-7(c)]
Total Strain Energy (eV/b)
Z (b)
7.9
7.8
7.7
7.6
7.5
7.4
7.3
7.2
40
50
60
70
80
90
100
110

(b)

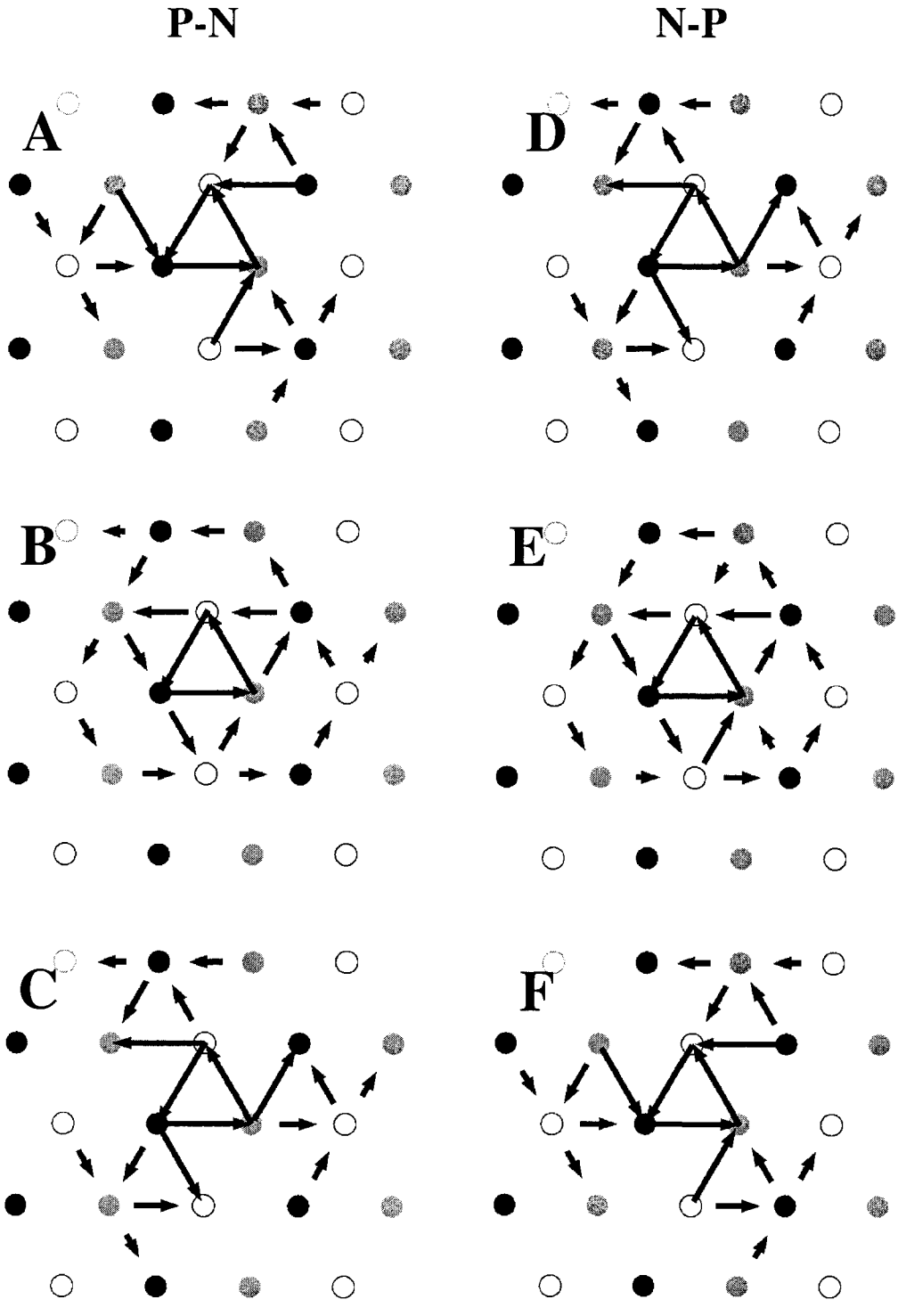

(c)

Figure 5-7. The strain energy distribution for the dislocation quadrupole with (a) P-N flip (formation energy is 0.005 eV) and (b) N-P flip (formation energy is 0.572 eV). (c) The differential displacement maps show different core configurations along the dislocation line (Z=40 b, 75 b and 100 b). Note: Although the dislocation with the P-N flip has a lower strain energy than the perfect dislocation in the P-N flip formation region, the total strain energy of the dislocation with a P-N flip is still 0.005 eV higher than the total strain energy of perfect dislocation.

B. Relative displacement within a column

The DD maps in Figure 5-7(c) show the relative displacements in the [111] direction between the neighboring atoms in a (111) plane in the dislocation core region. They do not contain information on the relative displacements in the [111] direction between the neighboring atoms in the same [111] column. In a perfect bcc crystal or a crystal with a straight 1/2a<1111> screw dislocation, the distance between two neighboring atoms in the same [111] column is 1 b (|1/2a<111>|). However, because of the change of the polarization along the dislocation, this regular atomic separation is expected to change when a flip is formed in the 1/2a<111> screw dislocation. For each individual column of atoms in the dislocation core, we calculated the distances between two consecutively neighboring atoms in the [111] direction. Figure 5-8 shows the atomic arrangement in a dislocation core. In this figure, the circle in the (111) plane represents a [111] column of atoms and the cross mark indicates the center of the dislocation. The atoms in the columns marked with the same letter are energetically and geometrically equivalent by symmetry.

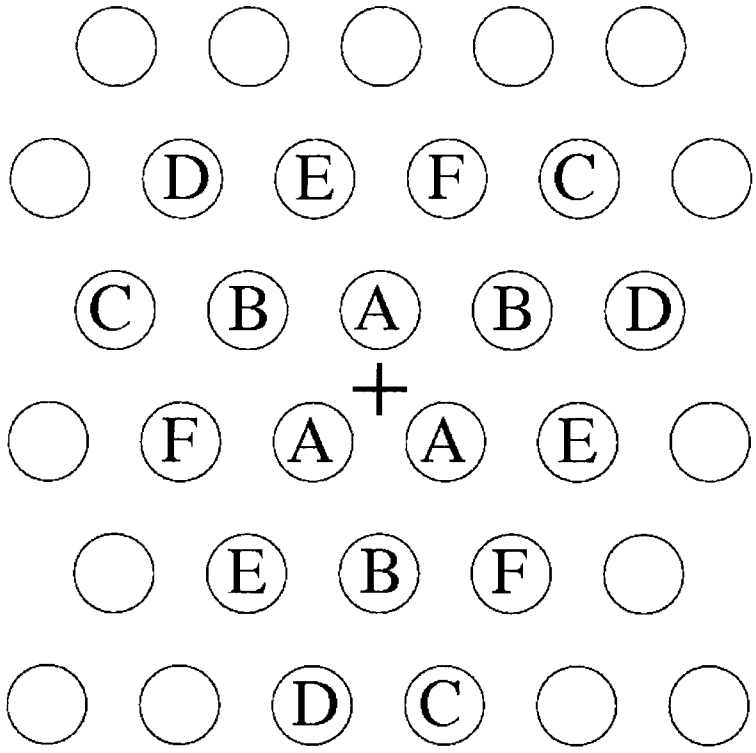

Figure 5-8. The (111) projection of atom arrangements around an a/2[111] screw dislocation. The cross indicates the center of the dislocation. The atoms marked with the same letters are energetically equivalent and related by symmetry. For the P type dislocation core configuration, the atomistic strain energies are in the order of the A>B>C>E>D>F; while for the N type dislocation core configuration, the order is A>B>D>F>C>E.

Figure 5-9(a) shows for the P-N flip the distance in the [111] direction between consecutive atoms in the same [111] column varies along the dislocation and Figure 5-9(b) shows the same plot for the N-P flip. In both cases, the distance between neighboring atoms in the [111] direction is equal to 1 b when far from the flip formation region but deviates significantly within the flip formation region. Figure 5-9(a) shows that for the P-N flip the distance between "A" atoms is compressed to 0.976 b (2.81 Å)

while Figure 5-9(b) shows that for N-P flip it is stretched to 1.032 b (2.97 Å). In comparison, for the P-N flip the "B" atoms are in tension (the maximal distance is 1.010b) while for the N-P flip they are in compression (the minimal distance is 0.996 b). The atoms "C", "D", "E", and "F" also have different mechanical states but with smaller magnitudes.

C. Energy distribution along the dislocation line

Figure 5-9(c) shows for the P-N flip the atomistic strain energy for each atom along the dislocation while Figure 5-9(d) shows the same for the N-P flip. Obviously, the change of the distance between neighboring atoms in the [111] direction affects the atomistic energy for atom in the flip formation region. Summarizing the atomistic strain energies for the 18 marked atoms comes to the core energy [shown in the insets of Figure 5-9(c) and 5-9(d)]. The elastic energy for each flip is computed by subtracting the core strain energy contribution from the total strain energy of a dislocation containing a flip. Figures 5-9(e) and 5-9(f) show the calculated elastic energy distribution along the dislocation with P-N or N-P flip.

The middle 10 b at the center of a P-N flip has higher elastic strain than the perfect dislocation energy but lower core energy. In comparison, the N-P flip has lower elastic energy in the middle 10 b but a higher core energy than the perfect dislocation. The energy field of a flip is the region where the energy (elastic or core energy) deviates from that of a perfect dislocation. The elastic energy field for a flip of 30 b for P-N flip and 50 b for N-P flip is much longer than its core energy field (20 b for P-N flip and 15 b for N-P flip). For a P-N flip (formation energy is 0.005 eV), the core strain energy part is

-0.275 eV while the elastic energy part is 0.280 eV. Similarly, the formation energy of the N-P flip (0.572 eV) can be partitioned in to 0.773 eV core energy and -0.201 eV elastic energy.

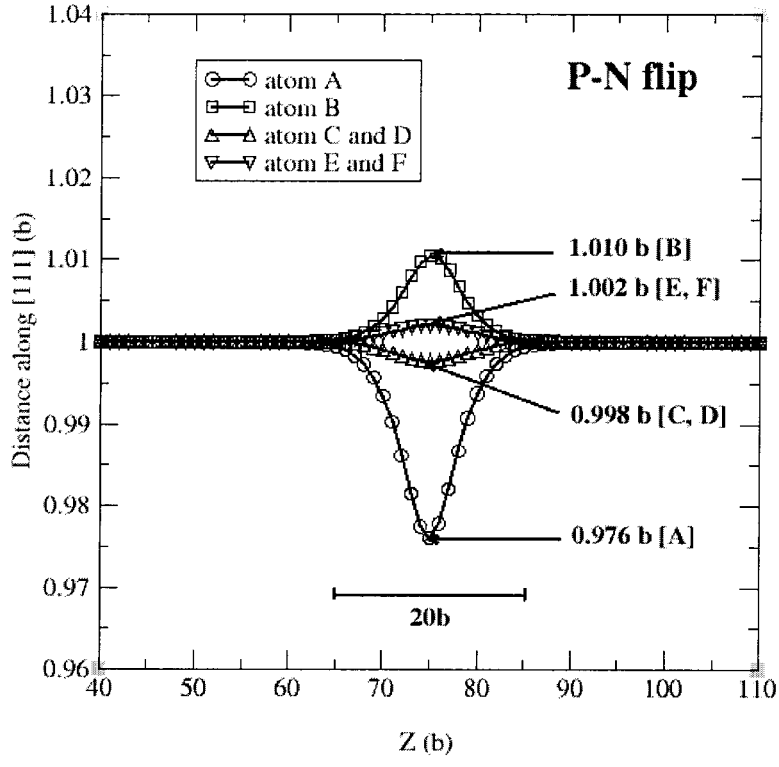

(a)

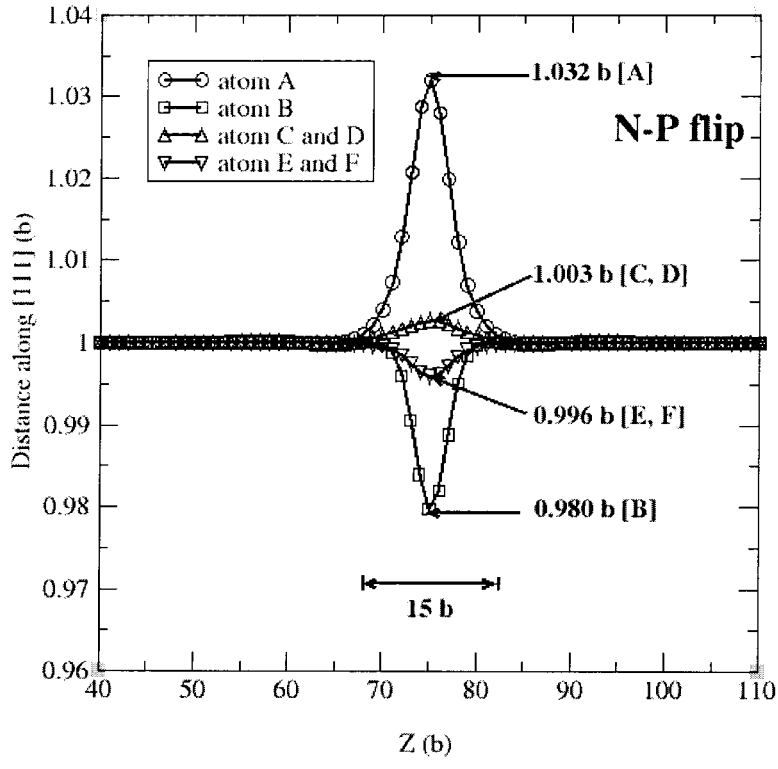
atom A
atom B
atom C and D
atom E and F
1.032 b [A]
N-P flip
1.003 b [C, D]
0.996 b [E, F]
0.980 b [B]
15 b
Distance along [111] (b)
Z (b)

(b)

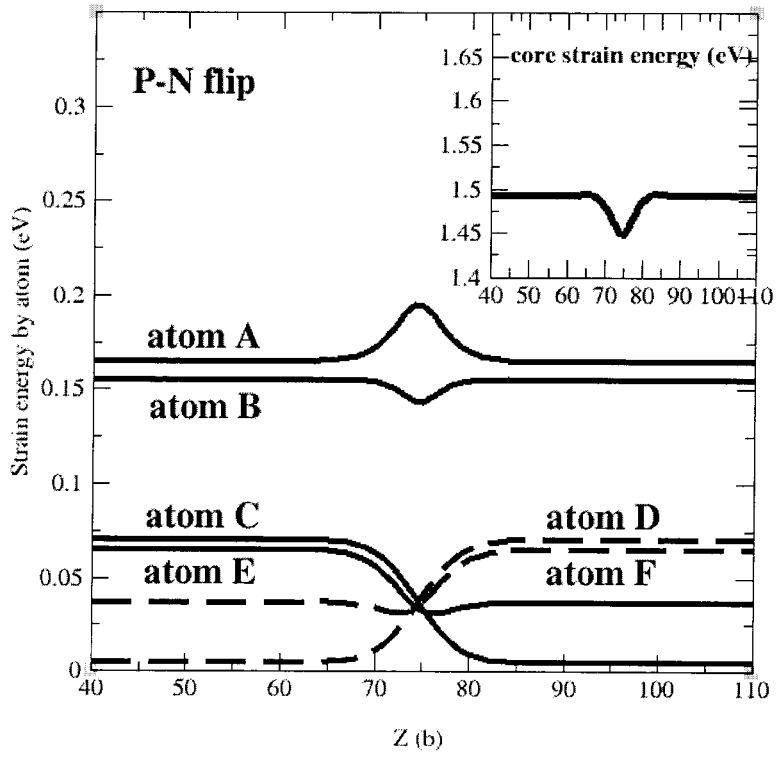
P-N flip
core strain energy (eV)
atom A
atom B
atom C
atom D
atom E
atom F
Strain energy by atom (eV)
Z (b)

(c)

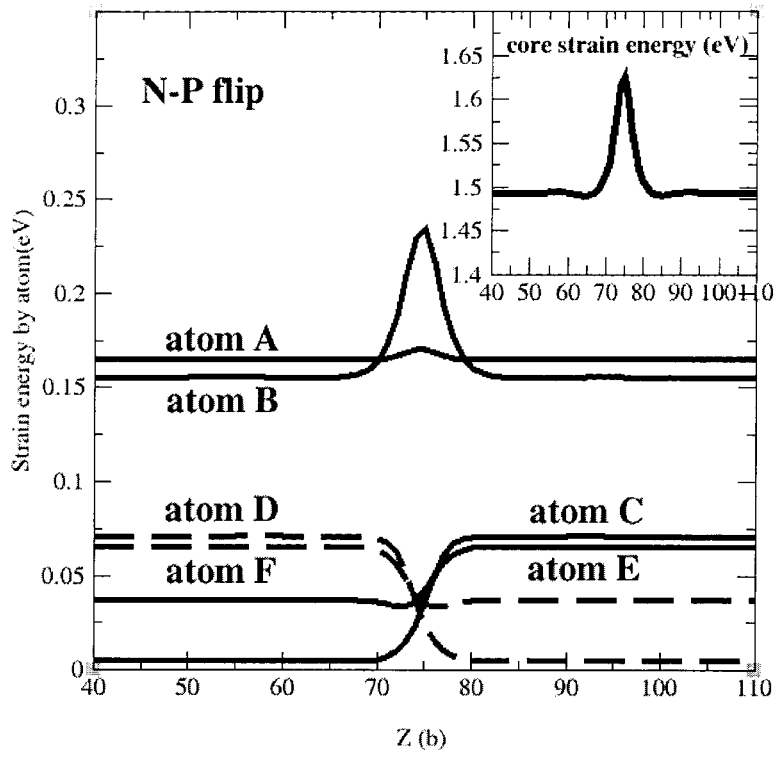
N-P flip
core strain energy (eV)
atom A
atom B
atom D
atom C
atom F
atom E
Strain energy by atom(eV)
Z (b)

(d)

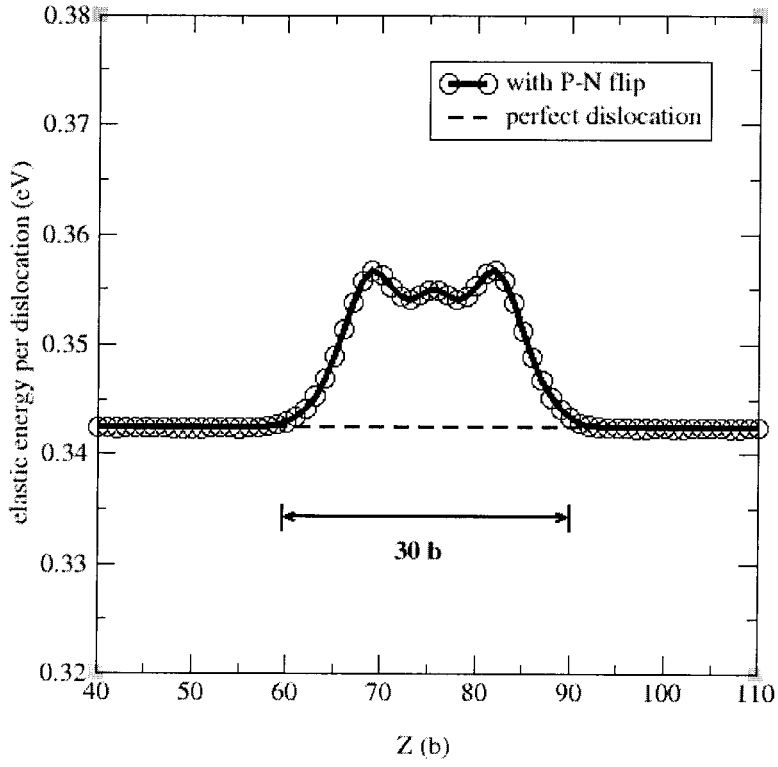
with P-N flip
perfect dislocation
30 b
elastic energy per dislocation (eV)
Z (b)

(e)

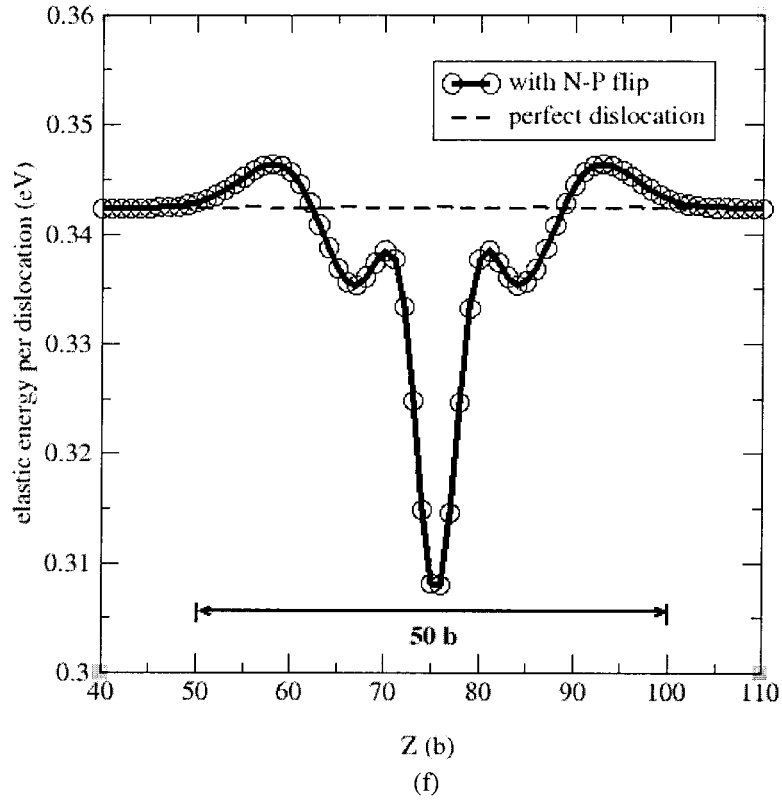

Figure 5-9. (a) The distance between neighboring atoms in the same [111] column around an a/2<111> screw dislocation with a P-N flip. (b) The same plot as (a) for an N-P flip. (c) The strain energy by atom around the 1/2a<111> screw dislocation with a P-N flip. (d) The same plot as (c) for an N-P flip. The positions of the atoms relative to the dislocation center are shown in Figure 5-8 using the same letters. The insets in (c) and (d) plot the summation of atomistic strain energy for individual atoms. Note that the obtained core energy for the equilibrium dislocation is different from calculations in Ref. 22, where the core energy is defined as the summation of 12 atoms with highest atomistic strain energy. To study the strain energy change in the flip region, we include 18 atoms in this computation. (e) The elastic energy [one-fourth of total energy in (a) less core strain energy in (c)] along a dislocation with P-N flip. (f) The same plot for a dislocation with N-P flip.

D. Discussion

The different ways to flip the polarization of dislocation cause that the same atom is at different mechanical states (compression or tension) in the [111] direction and has the different atomistic strain energy. This is the reason why the formation energy of P-N flip is different from that of N-P flip.

The calculated formation energy of N-P flip is 0.23 eV in Ref. 9, 0.20 eV in Ref. 19 and 0.572 eV in the present work. While the formation energy of P-N flip is 0.03 eV in Ref. 9, 0.00 eV in Ref. 19 and 0.005 eV in the present work. Our analysis shows that the atoms B (see Figure 5-8) in the different mechanical states are the principle cause that the formation energy of the N-P flip is higher that that of the P-N flip. The atoms B are stretched along the [111] direction and contribute -0.183 eV to the P-N flip formation energy. However, these atoms are compressed in the [111] direction and give 1.242 eV to the N-P flip formation energy in our study.

It is also accountable that the formation energies of two kinds of flips in 1/2a<111> screw dislocation will differ with a less magnitude (0.20 eV in Ref. 9 compared to 0.567 eV in our study) when the dislocation cores are only slightly polarized. The smaller polarization difference of different types of dislocations implies less compression or tension in the [111] direction for atoms.

5.6.3 Structural analysis of kinks

A. Relation of kinks

The formation energies of kinks given in Figure 5-3 clearly show the following trends. For right kinks, the formation energies decrease in the order of NRP, NRN (=PRP), and PRN with differences of ~0.02 eV. For left kinks, the formation energies increase in the order of PLN, NLN (=PLP), and NLP with differences of ~0.5 eV. We carried the structural analysis of these kinks to understand the origin of these trends.

Figure 5-10 shows the strain energy distribution maps for various right kinks. These figures show that

(1) The NRP kink [Figure 5-10(a)] has only a strain energy maximum at its formation region,

(2) the NRN kink [Figure 5-10(b)] has a strain energy maximum at the formation region and a strain energy minimum above its formation region,

(3) the PRP kink [Figure 5-10(c)] has a strain energy maximum at the kink formation region and a strain energy minimum below the formation region,

(4) the PRN kink [Figure 5-10(d)] has a strain energy maximum at the kink formation region and two strain energy minima on both sides of the formation region.

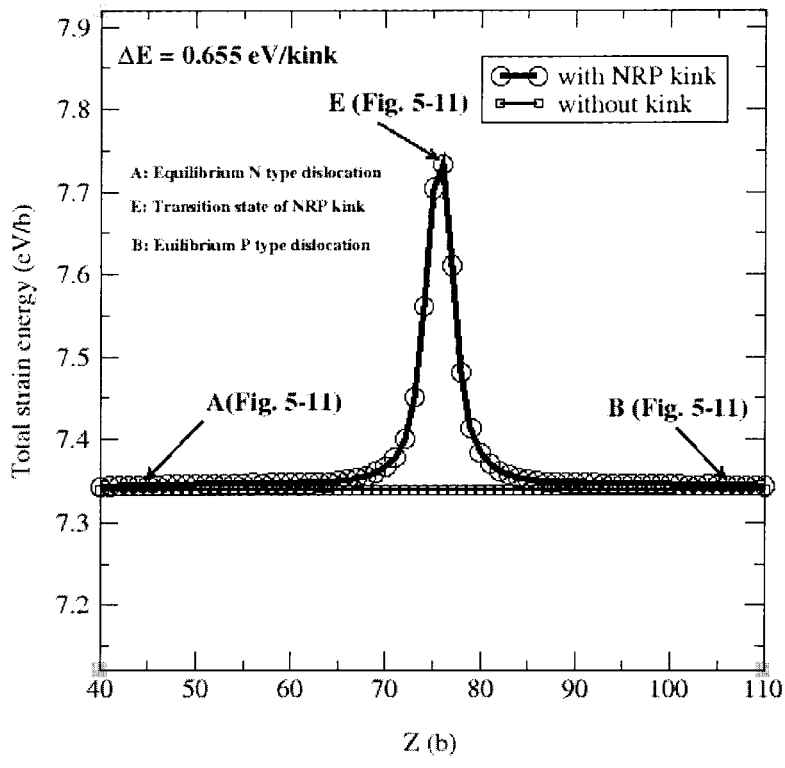
ΔE = 0.655 eV/kink
with NRP kink
without kink
E (Fig. 5-11)
A: Equilibrium N type dislocation
E: Transition state of NRP kink
B: Euilibrium P type dislocation
A(Fig. 5-11)
B (Fig. 5-11)
Total strain energy (eV/b)
Z (b)
7.9
7.8
7.7
7.6
7.5
7.4
7.3
7.2
40
50
60
70
80
90
100
110

(a)

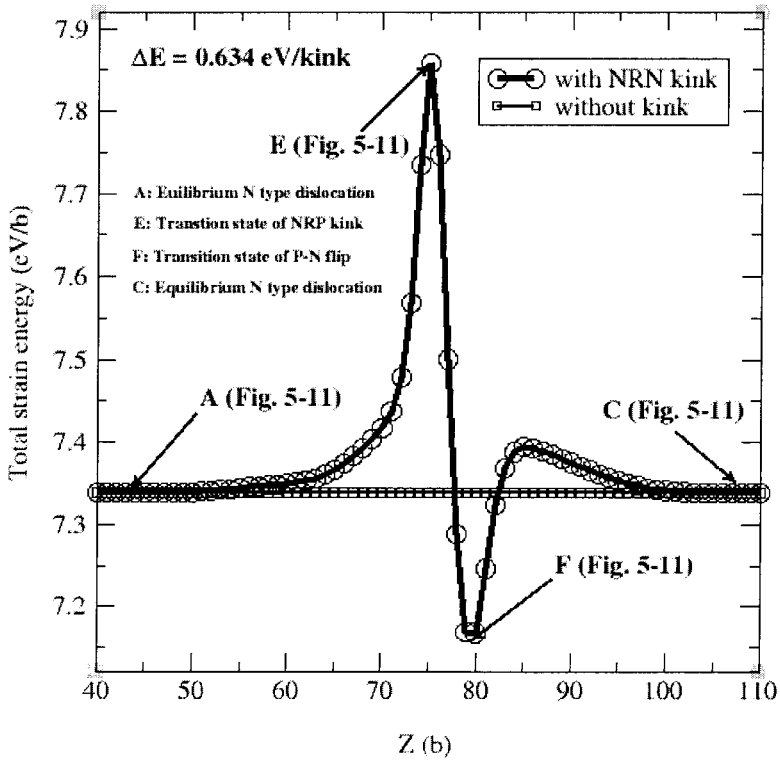
ΔE = 0.634 eV/kink
with NRN kink
without kink
E (Fig. 5-11)
A: Euilibrium N type dislocation
E: Transtion state of NRP kink
F: Transition state of P-N flip
C: Equilibrium N type dislocation
A (Fig. 5-11)
C (Fig. 5-11)
F (Fig. 5-11)
Total strain energy (eV/b)
Z (b)
7.9
7.8
7.7
7.6
7.5
7.4
7.3
7.2
40
50
60
70
80
90
100
110

(b)

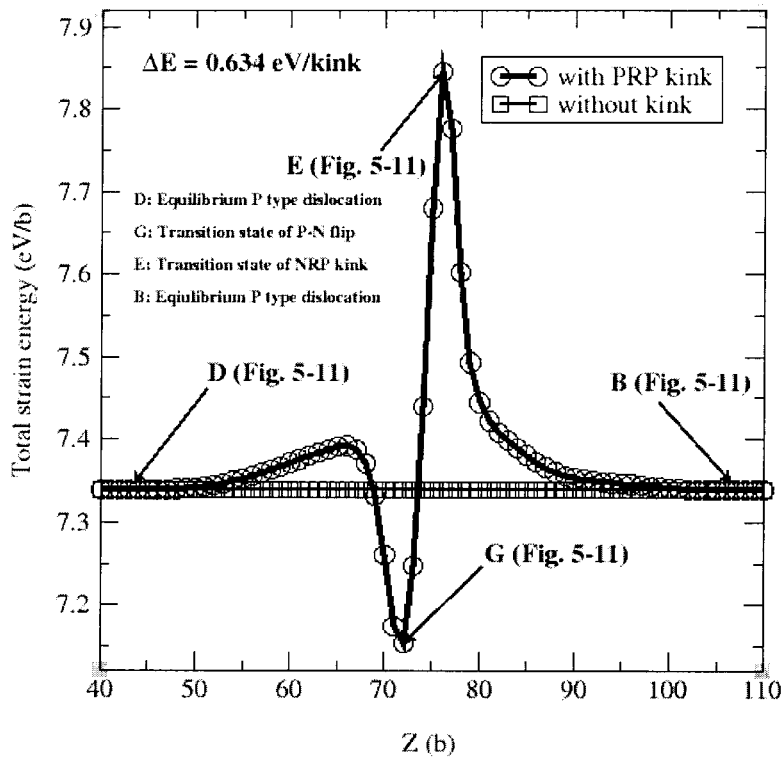
ΔE = 0.634 eV/kink
with PRP kink
without kink
E (Fig. 5-11)
D: Equilibrium P type dislocation
G: Transition state of P-N flip
E: Transition state of NRP kink
B: Equilibrium P type dislocation
D (Fig. 5-11)
B (Fig. 5-11)
G (Fig. 5-11)
Total strain energy (eV/b)
Z (b)

(c)

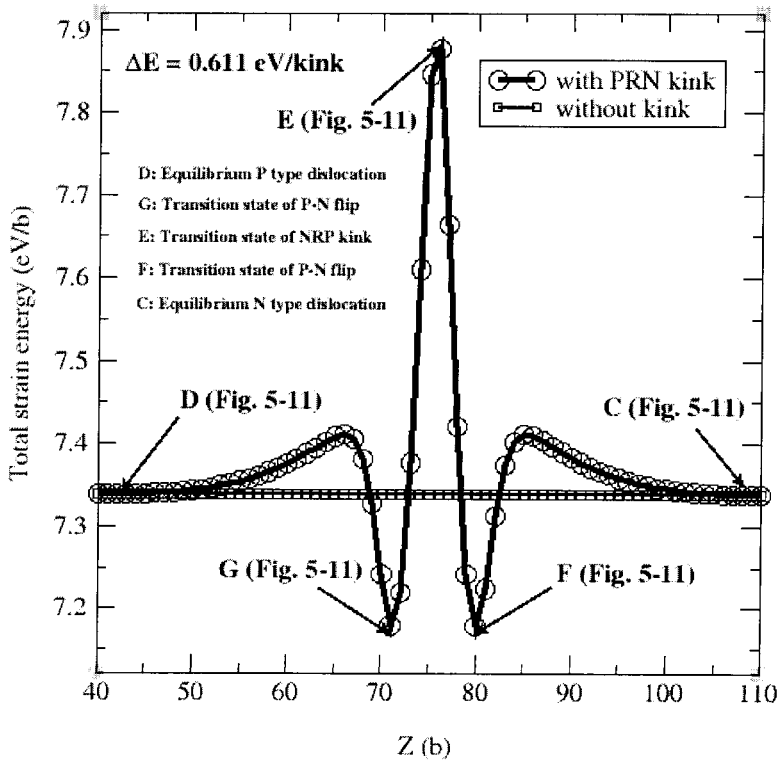
ΔE = 0.611 eV/kink
with PRN kink
without kink
E (Fig. 5-11)
D: Equilibrium P type dislocation
G: Transition state of P-N flip
E: Transition state of NRP kink
F: Transition state of P-N flip
C: Equilibrium N type dislocation
D (Fig. 5-11)
C (Fig. 5-11)
G (Fig. 5-11)
F (Fig. 5-11)
Total strain energy (eV/b)
Z (b)

(d)

Figure 5-10. The strain energy distribution for dislocation quadruples with right kinks. (a) the kink, (b) the NRN kink, (c) the PRP kink, and (d) the PRN kink. The letters in the figures indicate the regions with characteristic features along the dislocation. The dislocation core configurations of these regions are shown in Figure 5-11.

Figure 5-11 shows the DD maps corresponding to these critical states. The panels (A), (B), (C), and (D) in Figure 5-11 show the dislocation core configurations at regions far from the kink formation region. These maps are same as those of the equilibrated dislocation cores. The configurations of dislocation core in the region where the strain energy is a maximum in all four right kinks have the same differential displacement pattern as shown in Figure 5-11(E), which clearly indicates that the whole dislocation evenly splits into two parts in the neighboring equilibrium positions. We find that Figure 5-11(F) and (G) resemble the DD map of the flip in the panel C of Figure 5-5(c) such that the strain energy minima in Figure 5-10 correspond to the flips in screw dislocation.

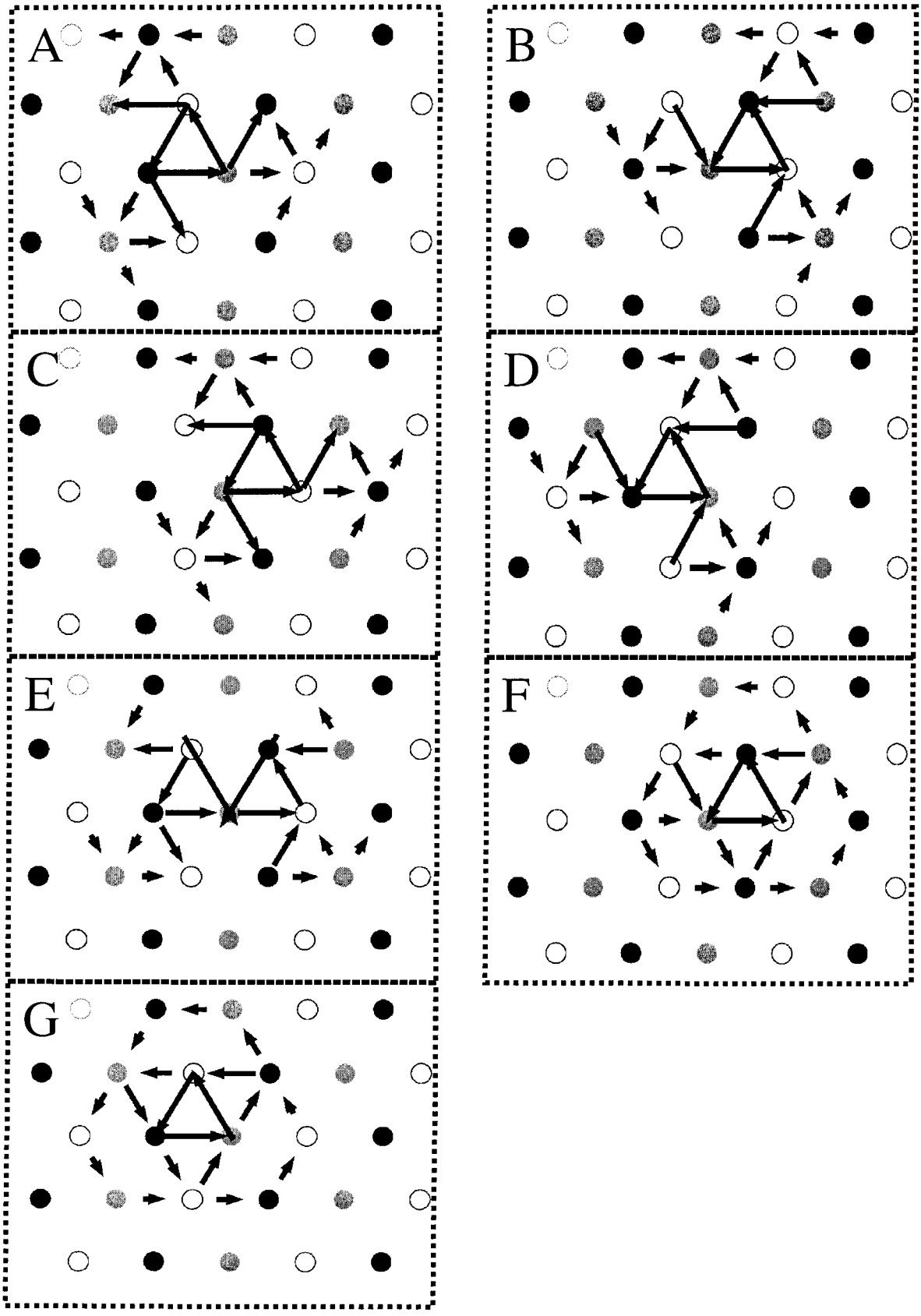
A
B
C
D
E
F
G

Figure 5-11. The differential displacement maps of dislocation core at different regions marked in Figure 5-10 along the 1/2a[111] screw dislocation. The figures (A), (B), (C), and (D) show the equilibrium dislocation cores; the figure (E) shows the atomic relative displacements at the center of the kink formation region; while the figures (F) and (G) indicate the flips in the kink formation region.

On the above analysis, the relation of the right kinks in the 1/2a<111> screw dislocation can be expressed as the following equations.

$$NRN = NRP + P\text{-}N, \tag{7a}$$

$$PRP = P\text{-}N + NRP, \tag{7b}$$

$$PRN = P\text{-}N + NRP + P\text{-}N, \tag{7c}$$

These equations indicate that the NRP kink is the elementary right kink and all other right kinks are composites consisting of the NRP kink and one or two P-N flips. The NRP kink and the P-N flips are only separated by 3 b in the composite kinks. The formation energy of an isolated P-N flip is 0.005 eV, but the close distance between the NRP kink and the P-N flip may decrease the total strain energy and leads to a -0.02 eV contribution for each P-N flip in the composite kink. Thus, Eq. (7) also explains why the formation energy of the NRP kink is 0.021 eV higher than that of the NRN (or PRP) kink and 0.044 eV higher than that of the PRN kink.

A similar analysis for the left kinks is presented in Figure 5-12 and Figure 5-13. Figure 5-12 shows the strain energy distributions along the dislocation with the different left kink.

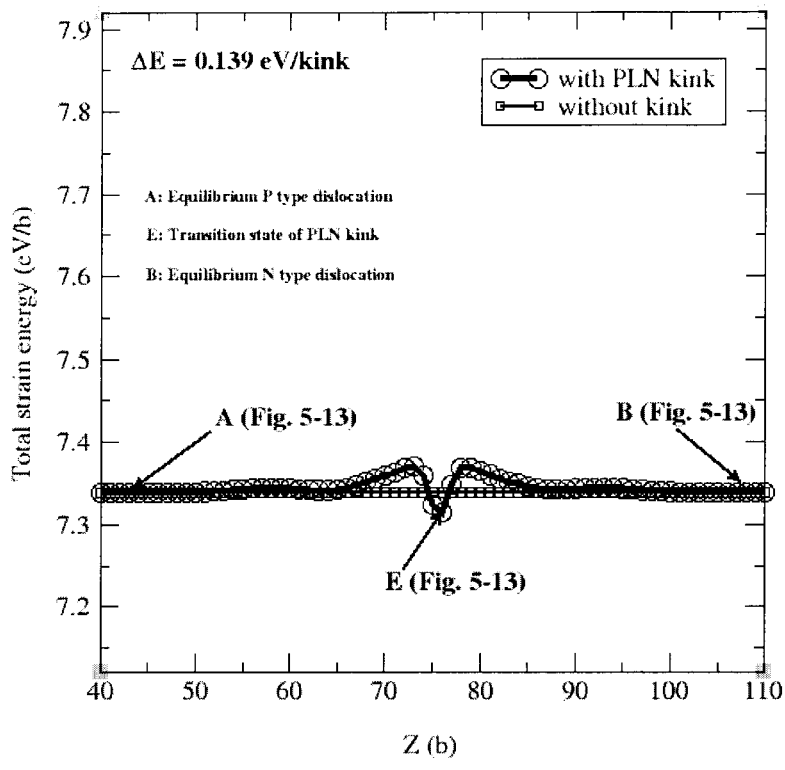
ΔE = 0.139 eV/kink
with PLN kink
without kink
A: Equilibrium P type dislocation
E: Transition state of PLN kink
B: Equilibrium N type dislocation
A (Fig. 5-13)
B (Fig. 5-13)
E (Fig. 5-13)
Total strain energy (eV/b)
Z (b)
7.9
7.8
7.7
7.6
7.5
7.4
7.3
7.2
40
50
60
70
80
90
100
110

(a)

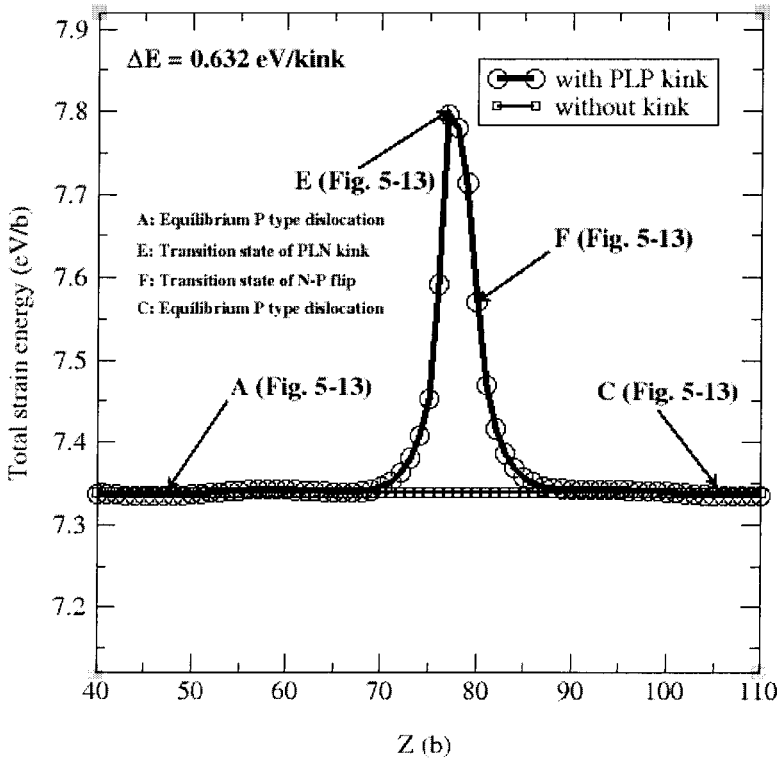
ΔE = 0.632 eV/kink
with PLP kink
without kink
E (Fig. 5-13)
F (Fig. 5-13)
A: Equilibrium P type dislocation
E: Transition state of PLN kink
F: Transition state of N-P flip
C: Equilibrium P type dislocation
A (Fig. 5-13)
C (Fig. 5-13)
Total strain energy (eV/b)
Z (b)
7.9
7.8
7.7
7.6
7.5
7.4
7.3
7.2
40
50
60
70
80
90
100
110

(b)

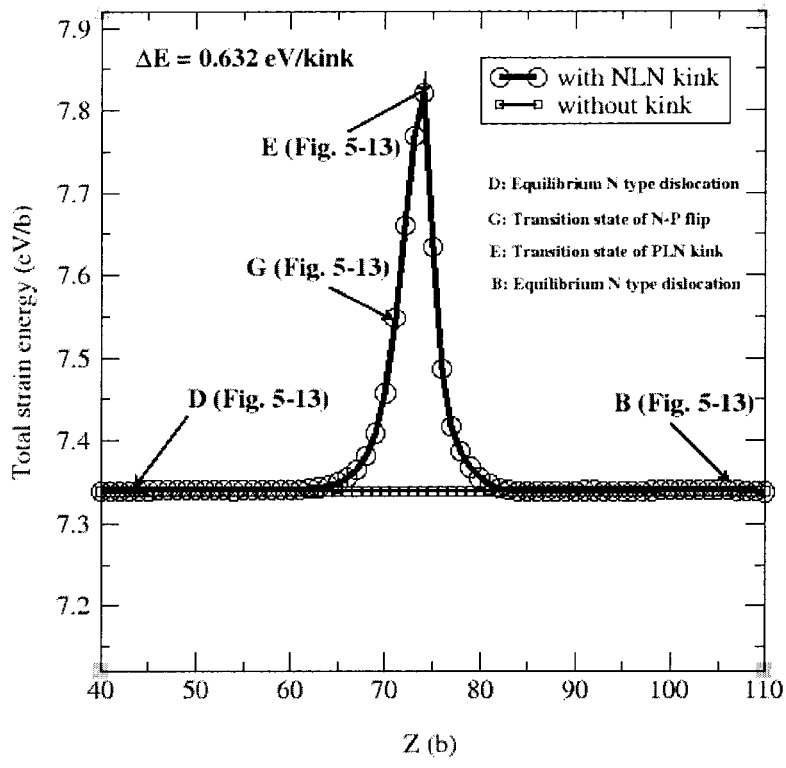
ΔE = 0.632 eV/kink
with NLN kink
without kink
E (Fig. 5-13)
D: Equilibrium N type dislocation
G: Transition state of N-P flip
E: Transition state of PLN kink
B: Equilibrium N type dislocation
G (Fig. 5-13)
D (Fig. 5-13)
B (Fig. 5-13)
Total strain energy (eV/b)
Z (b)

(c)

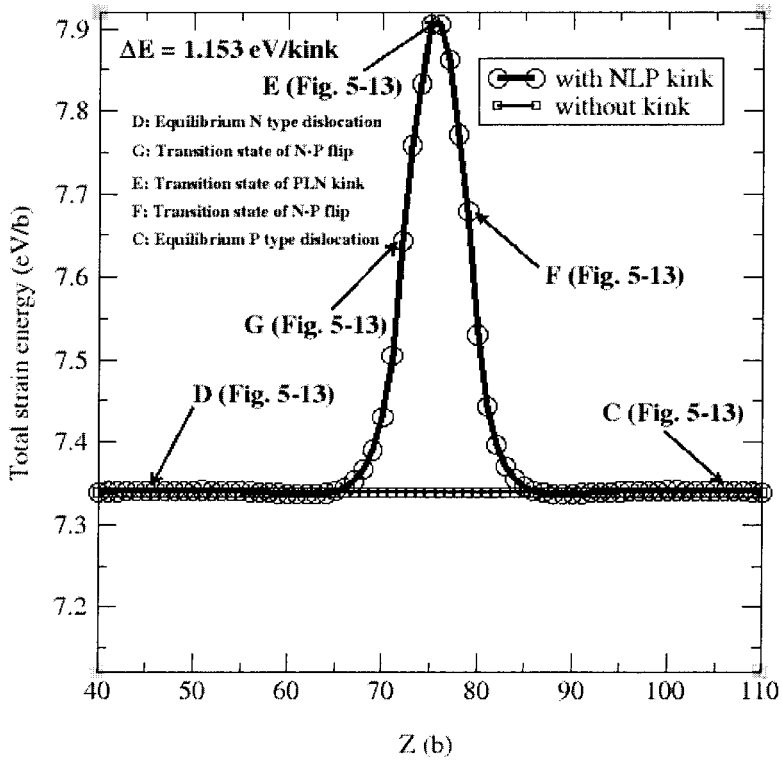
ΔE = 1.153 eV/kink
E (Fig. 5-13)
with NLP kink
without kink
D: Equilibrium N type dislocation
G: Transition state of N-P flip
E: Transition state of PLN kink
F: Transition state of N-P flip
C: Equilibrium P type dislocation
F (Fig. 5-13)
G (Fig. 5-13)
D (Fig. 5-13)
C (Fig. 5-13)
Total strain energy (eV/b)
Z (b)

(d)

Figure 5-12. The strain energy distribution for the dislocation quadruples with left kinks. (a) the PLN kink, (b) the PLP kink, (c) the NLN kink, and (d) the NLP kink. The letters in the figures indicate the regions with characteristic features along the dislocation. The dislocation core configurations of these regions are shown in Figure 5-13.

In these figures, we see a strain energy minimum at the PLN kink formation region and a superficial resemblance of the strain energy distribution, in which there is only a strain energy maximum at the kink formation region, for the NLN, PLP and NLP kink. It seems that there is no obvious relationship between the left kinks. However, we are still able to establish the linkage between left kinks scrutinizing the detailed differential displacement maps in Figure 5-13. Figures 5-12(F) and (G) strongly suggest the existence of the N-P flip in the formation region of the NLN, PLP and NLP kink. Thus, the PLN kink is the basic left kink. All other left kinks are the combinations of the PLN kink and one or two N-P flips as indicated in the following equations.

$$\text{NLN} = \text{N-P} + \text{PLN}, \tag{8a}$$

$$\text{PLP} = \text{PLN} + \text{N-P}, \tag{8b}$$

$$\text{NLP} = \text{N-P} + \text{PLN} + \text{N-P}, \tag{8c}$$

The formation energy of an isolated N-P flip is 0.572 eV. The above equations explain the difference of 0.50 eV in the formation energies of the PLN (0.139 eV), PLP (or NLN, 0.632 eV) and NLP (1.153 eV) kink.

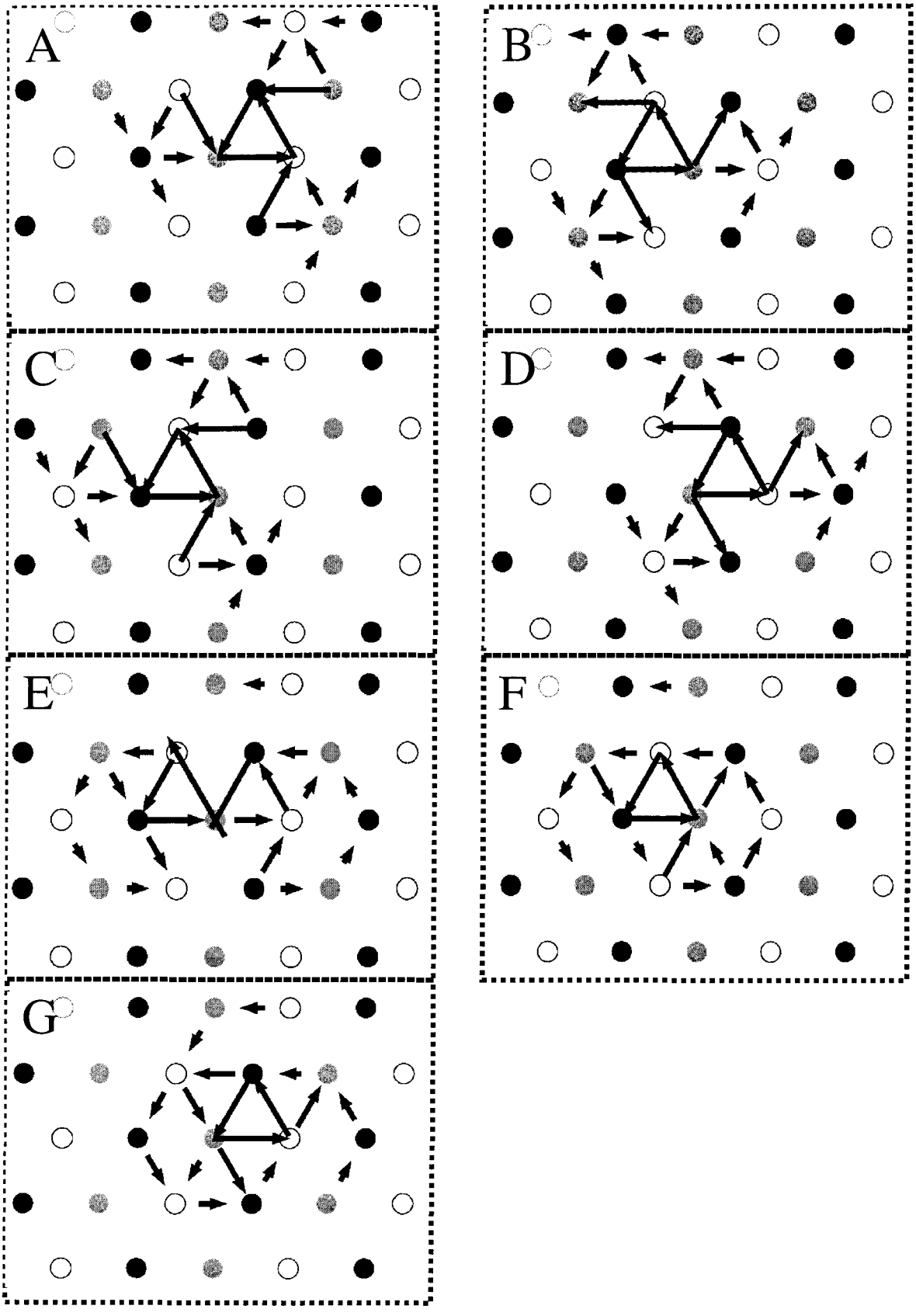
A
B
C
D
E
F
G

Figure 5-13. The differential displacement maps of dislocation core at different regions marked in Figure 5-12 along the 1/2a[111] screw dislocation. The figures (A), (B), (C), and (D) show the equilibrium dislocation cores; the figure (E) shows the atomic relative displacements at the center of the kink formation region; while the figures (F) and (G) indicate the flips in the kink formation region.

Besides the relation of the kink formation energy, the relation of the kink mobility in Eq. (6) can also be accounted by Eq. (7) and Eq. (8). The existence of flips in the kink will decrease its mobility. Thus the NRP kink and the PLN kink have the highest mobility in the right and left kinks.

B. Discussion

The kink relationship in Eq. (7) and Eq. (8) provides the first such connection in the atomistic level simulations. Although these relations were obtained using a qEAM FF for Ta, they provide a universal pattern for all bcc metals. To prove this point, we compared all available data of the kink formation energies in bcc metals[9,17,19,32].

A direct corollary of Eq. (7) is that the kink formation energy differences ΔE^{NRN}-ΔE^{NRP}, ΔE^{PRN}-ΔE^{NRN} and (ΔE^{PRN}-ΔE^{NRP})/2 should be nearly equal and close to $\Delta E^{P\text{-}N}$, which is the formation energy of the isolated P-N flip. Based on Eq. (8), the kink formation energy differences ΔE^{NLN}-ΔE^{PLN}, ΔE^{NLP}-ΔE^{NLN} and (ΔE^{NLP}-ΔE^{PLN})/2 should be similarly close to the formation energy of the N-P flip ($\Delta E^{N\text{-}P}$). It should be addressed that the flip in the composite kinks (NRN, PRP, PRN, NLN, PLN, and NLP) is under the different environments from the isolated flip. The close interaction between the flip and

the kink might relax the total strain energy, such that the kink formation energy differences could be smaller than the corresponding flip formation energy.

Table 5-3. Comparison of the formation energies (in eV) of the flips under different environments.

Materials	K [a] (Duesbery)	α-Fe [a] (Duesbery)	Mo [b] (Rao *et al.*)	Ta [c] (Yang *et al.*)	Ta (present work)
P-N flip					
$\Delta E^{P\text{-}N}$	0.048	0.300	0.00	0.03	0.005
ΔE^{NRN}-ΔE^{NRP}	0.043	0.267	-0.16	-0.11	-0.021
ΔE^{PRN}-ΔE^{NRN}	-0.022	-0.085	-0.15	0.20	-0.023
$1/2(\Delta E^{PRN}$-$\Delta E^{NRP})$	0.011	0.091	-0.16	0.05	-0.022
N-P flip					
$\Delta E^{N\text{-}P}$	0.018	0.408	0.21	0.23	0.572
ΔE^{NLN}-ΔE^{PLN}	0.028	-0.322	0.18	0.19	0.493
ΔE^{NLP}-ΔE^{NLN}	0.045	0.126	0.21	0.08	0.521
$1/2(\Delta E^{NLP}$-$\Delta E^{PLN})$	0.037	-0.098	0.20	0.14	0.507

[a] Reference 17, using a first-principle interatomic potential for potassium and an empirical interatomic potential for iron.

[b] Reference 19, using the MGPT FF.

[c] Reference 9, using the MGPT FF.

Table 5-3 compares the formation energy of the isolated flips and the flips in the composite kinks. Both present results for Ta, and calculations by Rao *et al.*[19] for Mo show the similar regularity of the flip formation energies as discussed above. Furthermore, the plot of differential energy between the kinked dislocation and an unkinked configuration for the PRP kink (denoted as p-pf kink in Figure 6 of Ref. 19) resembles the Figure 5-10(c) showing the strain energy distribution for the PRP kink in present work. We believe that the energy minima in both figures indicate the existence of a P-N flip in the PRP kink formation region. We used the qEAM FF for Ta as well as the periodic boundaries in the [11-2] and [1-10] direction and the fixed boundary in the [111] direction in our study. While the MGPT FF for Mo and Green's function boundary conditions were employed in Ref. 19. The agreement between these two simulations indicates that the relation of kinks in Eq. (7) and Eq. (8) is independent of the employed force field and boundary conditions.

However, the results by Yang *et al.*[9] using the MGPT FF for Ta and Green's function boundary conditions (also in Table 5-3) did not show a similar regularity of the flip formation energies. Neither did the even older calculations by Duesbery[17] for K and α-Fe. There are two possible reasons for this discrepancy. First, the equilibrium dislocation core in our study has a large polarization (~ 0.09 b) whereas the dislocation polarization is small (~ 0.0007 b) in Ref. 9. A smaller polarization of the dislocation implies a smaller difference among the kinks in the same category (Left or Right). The composite kinks might not dissociate into a flip and an elementary kink to decrease the strain energy when the dislocation core is symmetric and only weakly polarized. The second reason could be the incomplete relaxation of the atomistic structures. Duesbery

used the fixed boundaries where atoms are fixed at the positions determined by anisotropic elasticity theory in the simulation. These fixed boundaries could introduce bias in the atomistic relaxation if the simulation cells were not sufficiently large in three dimensions.

Ref. 32 found the following order of kink pair formation energies

PLN-NRP < NLN-NRN < NLP-PRN, (9)

However, no atomistic explanation was proposed. It is easy for us to interpret Eq. (9) with the help of the relation of kinks. The kink pair NLN-NRN can be considered as the combinations of the kink pair PLN-NRP and a pair of the N-P and the P-N flips in the kink region. Similarly, the kink pair NLP-PRN can be considered as the kink pair NLN-NRN plus a pair of the N-P and P-N flips in the kinks. Such that if the pair of a N-P and P-N flips contribute a positive strain energy in the composite kinks, the increasing order in Eq. (9) would hold true. Actually, Eq. (9) is universal as demonstrated by Table 5-4. All the available kink pair formation energies, except for α-Fe in Ref.17, follow the same trend. As to the failure case, the empirical potential for iron yielded negative formation energies for two kinds of kinks discredited those results. Thus, the kink pairs formation energies in K, Mo, Ta, and α-Fe obey the rule (9), so far.

Table 5-4. Comparison of formation energies of kink pairs. In the table, "Yes/No" indicates whether the calculated kink pair formation energies do or do not obey the rule: PLN-NRP < NLN-NRN < NLP-PRN as in Eq. (9).

Materials	$\Delta E^{PLN\text{-}NRP}$ (eV)	$\Delta E^{NLN\text{-}NRN}$ (eV)	$\Delta E^{NLP\text{-}PRN}$ (eV)	Yes/No
K [a] (Duesbery)	0.076	0.147	0.170	Yes
α-Fe [a] (Duesbery)	0.241	0.186	0.227	No
Mo [b] (Rao *et al.*)	1.62	1.64	1.70	Yes
Ta [c] (Yang *et al.*)	0.96	1.04	1.32	Yes
Ta (present work)	0.794	1.266	1.764	Yes
α-Fe [d] (Wen *et al.*)	0.84	1.29	1.94	Yes

[a] Reference 17, using a first-principle interatomic potential for potassium and an empirical interatomic potential for iron.

[b] Reference 19, using the MGPT FF.

[c] Reference 9, using the MGPT FF.

[d] Reference 32, using a nudged elastic band method and an EAM potential.

5.6.4 Determination of geometrical parameters

In addition to the formation energy and the migration energy of the kinks, the geometrical parameters, such as the kink height h and kink width w, are also essential for a mesoscopic description of kink in the continuum model. In this subsection, we present our efforts to determine these parameters from the dislocation line shape and strain energy distribution. The calculated results are given in Table 5-5.

Table 5-5. The computed geometrical parameters for the kinks in the 1/2<111> screw dislocation in Ta. In Method I, the width of the kink is determined by fitting a straight line to the kink formation region and determining the distance between the intersections of this line with the two limited locations, which are two neighboring straight dislocation

centers. In Method II, the width of the kink is determined to be the length of the region at whose boundary the strain energy deviates by 0.2% from the equilibrium dislocation strain energy.

Configuration	Height (Å)	Width (b) [Method I]	Width (b) [Method II]
NRP (right kink)	2.77	10.7	18
NRN (right kink)	2.71	10.4	34
PRP (right kink)	2.71	10.4	34
PRN (right kink)	2.65	10.2	42
NLP (left kink)	2.65	8.9	17
NLN (left kink)	2.71	9.1	15
PLP (left kink)	2.71	9.1	15
PLN (left kink)	2.77	9.3	14

Figure 5-14 shows a line representing the dislocation with the (a) NRP, (b) NRN, (c) PRP, (d) PRN, (e) PLN, (f) PLP, (g) NLN, and (h) NLP kink. Every point in the line is determined by calculating the atomistic strain energy weighted center for those 12 atoms with the highest strain energy in a 1b slice of the dislocation. The figures show that the dislocation is in its equilibrium position in the regions far away from the kink formation region. The average distance between two equilibrium positions on two sides of kink is the kink height. As indicated in Figure 5-14, the heights of the kinks are not equal for different combinations of dislocation core configurations.

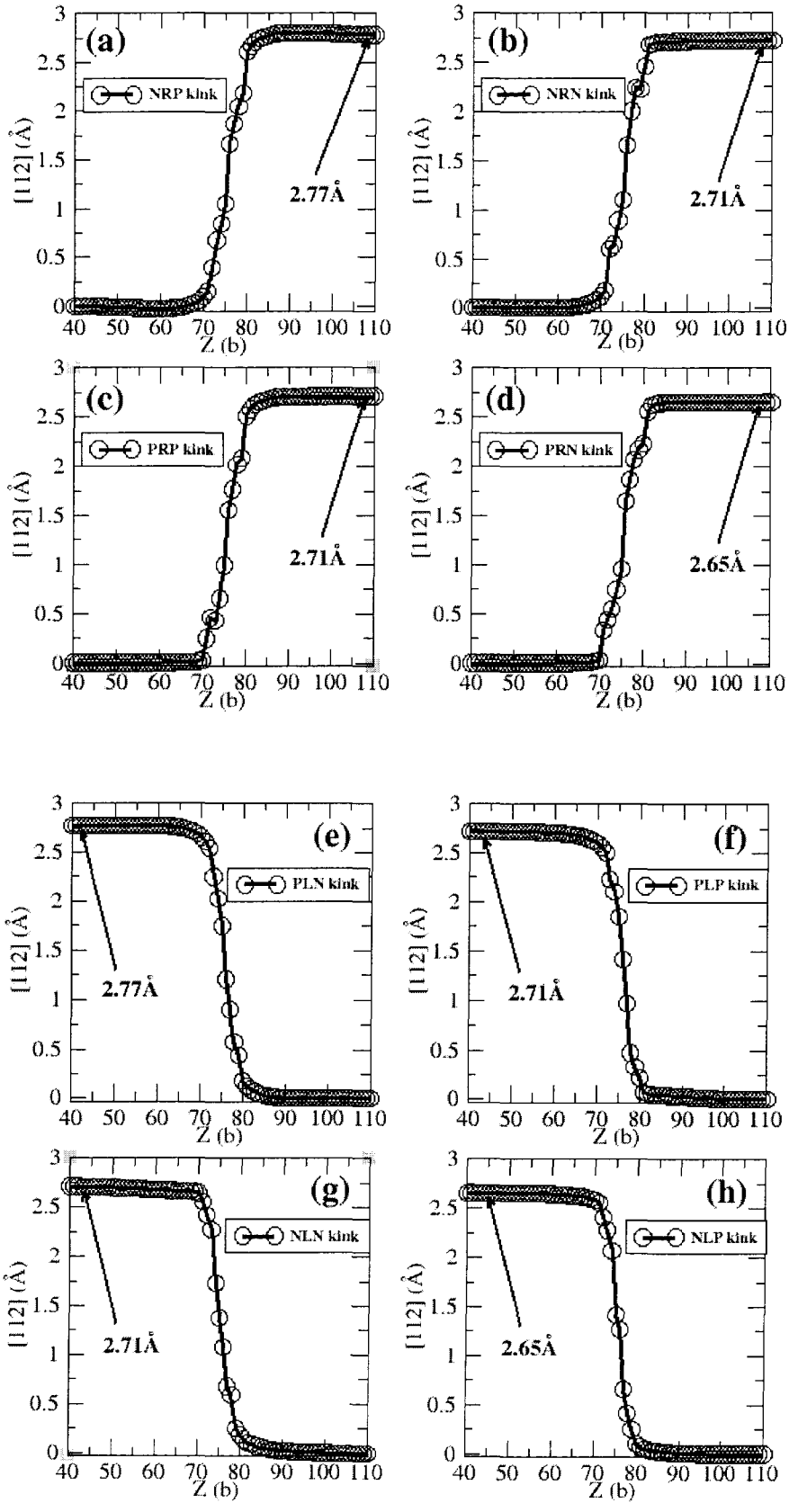
(a)
NRP kink
2.77Å
(b)
NRN kink
2.71Å
(c)
PRP kink
2.71Å
(d)
PRN kink
2.65Å
(e)
PLN kink
2.77Å
(f)
PLP kink
2.71Å
(g)
NLN kink
2.71Å
(h)
NLP kink
2.65Å
[112] (Å)
Z (b)

Figure 5-14. The profile of the dislocation lines in the kink formation regions. (a) NRP, (b) NRN, (c) PRP, (d) PRN, (e) PLN, (f) PLP, (g) NLN, and (h) NLP kink.

The kink width w can be estimated in two ways. (I) The part of the dislocation line in the kink formation region ($70b \leq Z \leq 80b$ shown in Figure 5-14) was fitted into a straight line. The kink width is the distance in the [111] direction (the abscissa in Figure 5-14) between two intersections of this line with two equilibrium dislocation lines separated by the kink height. (II) The kink width is the length of the region bounded by two points, where the strain energy deviates from the strain energy of the equilibrium dislocation by 0.2%, in the dislocation.

Determining the kink width by the line shape of the dislocation in Method I and the strain energy distribution in Method II is suitable for different applications. The kink width from Method I is the geometrical description of the kink and was used to compute the kink-kink interaction energy in Section 5.3. In the mesoscale model[4], the minimum stable distance between a left kink and a right kink is required. Instead of carrying out simulations checking the stability of the kink pair positioned at various separations, we can estimate the minimum stable distance between kinks using the kink width determined in Method II. The strain energy distributions of a pair of kinks do not overlap each other at their minimum stable distance, so the minimum stable separation of this pair of kinks is one half of the summation of two component kink widths determined in Method II. The choice of 0.2% in the calculation is somehow arbitrary. However, the attained minimum stable distance of the NRP-PLN kink pair is 16 b, which is close to the 13 b obtained by an empirical fit[4]. So, 0.2 % is a reasonable choice.

5.7 Conclusion

In this paper, we report calculations on the kink formation energies and the equilibrium kink structures using the first principle qEAM FF. The formation energies of the kink pairs in 1/2a<111> screw dislocation are in the range of 0.794-1.894 eV, which agrees with the results of the MGPT FF calculations and is in the same range of the empirical data. The PLN-NRP kink pair was found to have the lowest formation energy that is 0.794 eV compared favorably with the 0.81 eV for the zero shear stress activation enthalpy from the empirical data fitting. Our detailed structural analysis reveals that the PLN kink and the NRP kink are the elementary left and right kinks. The other kinks are the composite kinks composed of the elementary kink and the flips. This relation of kinks accounts for the observed trend of the kink formation energies and mobility.

As an atomistic simulation, our results are limited by the description capability of the force field. Our simulations yield the asymmetric and polarized (~0.09 b) dislocation cores, which cause the multiplicity of kinks and the existence of flips. However, the recent *ab initio* calculations[33,34] obtain only a symmetric screw dislocation core in Ta, also simulations using the Finnis-Sinclair type atomic interaction potential come to a symmetric core[35]. The MGPT FF calculations[9] yield an almost symmetric (slightly polarized ~0.0007 b) dislocation core in Ta. It is clear that dislocation polarization is very sensitive to the calculations. Some dislocation properties depend on whether the dislocation core is symmetric or asymmetric. For instance, the formation energy difference between the N-P flip and the P-N flip in this study (dislocation polarization is 0.09 b) is 0.567 eV. It is more than two times larger than the 0.20 eV, when the dislocation core is symmetric and polarized only by 0.0007 b. However, some other

dislocation properties would not be very sensitive to the difference of the dislocation cores. We showed in a preceding paper[22] that the discrepancy of the obtained dislocation cores did not affect the calculated core energy and Peierls stress. In this paper, our results of kink formation energies are consistent with the results from the MGPT FF, though the symmetry of dislocation core is different in two studies. On the other hand, the polarization of screw dislocation is subject to a rapid change depending on the volume and pressure conditions as pointed out by Yang *et al.*[9] The physics, such as the relation of kinks proposed in present work, should be still applicable when the dislocation is polarized under certain conditions. So, the difference of the obtained dislocation core configuration between the present work and other studies should not undermine the credibility of the present work.

5.8 References

1. V. V. Bulatov and L. P. Kubin, Curr. Opin. Solid State Mater. Sci., **3**, 558 (1998).
2. R. Phillips, D. Rodney, V. Shenoy, E. Tadmor, and M. Ortiz, Model. Simul. Mater. Sci. Eng., **7**, 769 (1999).
3. M. I. Baskes, Curr. Opin. Solid State Mater. Sci., **4**, 273 (1999).
4. A. M. Cuitino, L. Stainier, G. Wang, A. Strachan, T. Çağın, W. A. Goddard, and M. Ortiz, *A Multiscale Approach for Modeling Crystalline Solids*, J. Comput.-Aided Mater. Design, to be published.
5. V. V. Bulatov, S. Yip and A. S. Argon, Philos. Mag. A, **72**, 453 (1995).
6. J. A. Moriarty, W. Xu, P. Söderlind, J. Belak, L. H. Yang and J. Zhu, J. Eng. Mater. Tech., **121**, 120 (1999).
7. F. Louchet and L. P. Kubin, Philos. Mag. A, **39**, 433 (1979).
8. W. Xu and J. A. Moriarty, Comput. Mat. Sci., **9**, 348 (1998).
9. L. H. Yang, P. Söderlind, and J. A. Moriarty, Philos. Mag. A, **81**, 1355 (2001).
10. K. Ito and V. Vitek, Philos. Mag. A, 81, 1387 (2001).
11. G. Wang, A. Strachan, T. Çağın, and W. A. Goddard, Mater. Sci. and Eng. A, **309**, 133 (2001).
12. T. Suzuki, Y. Kamimura and H. O. K. Kirchner, Philos. Mag. A, **79**, 1629 (1999).
13. A. Seeger and P. Schiller, *Physical Acoustics*, edited by W. P. Mason (Academics, New York 1966), Vol. 3A, p. 361.
14. H. R. Kolar, J. C. H. Spence and H. Alexander, Phys. Rev. Lett., **77**, 4031 (1996).
15. A. Seeger and C. Wuthrich, Nuovo Cimento, **33B**, 38 (1976).

16. M. S. Duesbery, Acta Metall., **31**, 1747 (1983).

17. M. S. Duesbery, Acta Metall., **31**, 1759 (1983).

18. M. S. Duesbery and Z. S. Basinski, Acta Metall. Mater., **41**, 643 (1993).

19. S. I. Rao and C. Woodward, Philos. Mag. A, **81**, 1317 (2001).

20. A. Strachan, T. Çağın, O. Gülseren, S. Mukherjee, R. E. Cohen, and W. A. Goddard, *First Principles Force Field for Metallic Tantalum*, Phys. Rev. B, submitted.

21. A. Strachan, T. Çağın and W. A. Goddard, Phys. Rev. B, **63**, 060103 (2001).

22. G. Wang, A. Strachan, T. Çağın, and W. A. Goddard, *Atomistic Characterization of the Screw Dislocation in Tantalum*, Phys. Rev. B, submitted.

23. V. Vitek, Cryst. Lattice Defects, **5**, 1 (1974).

24. J. P. Hirth, Acta Mater., **48**, 93 (2000).

25. J. P. Hirth and J. Lothe, *Theory of dislocations* (Krieger, Melbourne, FL, 1982), p.242.

26. J. P. Hirth and J. Lothe, *Theory of dislocations* (Krieger, Melbourne, FL, 1982), p.162.

27. M. Tang, L. P. Kubin and G. R. Canova, Acta Mater., **46**, 3221 (1998).

28. G. Funk, Dissertation, University Stuttgart, 1985.

29. U. Rodrian and H. Schultz, Z. Metallk, **73**, 21 (1982).

30. M. Werner, Phys. Stat. Sol. (a), **104**, 63 (1987).

31. H. Mizubayashi, H. Egashira and S. Okuda, Acta Metall. Mater., **43**, 269 (1995).

32. W. Wen and A. H. W. Ngan, Acta Mater., **48**, 4255 (2000).

33. S. Ismail-Beigi and T. A. Arias, Phys. Rev. Lett., **84**, 1499 (2000).

34. C. Woodward and S. I. Rao, Philos. Mag. A, **81**, 1305 (2001).

35. M. S. Duesbery and V. Vitek, Acta Mater., **46**, 1481 (1998).

Chapter 6 A multiscale approach for modeling crystalline solids *

6.1 Overview

The proposed multiscale modeling approach for advanced materials (such as high-purity bcc single crystals) is aligned with the current *divide and conquer* paradigm in micromechanics[1-6]. This paradigm first identifies and models the controlling unit processes at microscopic scale. Then, the energetics and dynamics of these mechanisms are quantified by means of atomistic modeling. Finally, the macroscopic driving force is correlated to macroscopic response via microscopic modeling. This last step involves two stages, *localization* of the macroscopic driving force into unit-process driving forces and *averaging* of the contribution of each unit process into the macroscopic response.

We will show that the meticulous application of this paradigm renders truly predictive models of the mechanical behavior of complex systems. In particular, we predict the hardening of Ta single crystal and its dependency for a wide range of temperatures and strain rates. The feat of this approach is that predictions from these atomistically informed models recover most of the macroscopic characteristic features of the available experimental data, without a priori knowledge of such experimental tests. This approach then provides a procedure to forecast the mechanical behavior of material in extreme conditions where experimental data is simply not available or very difficult to collect.

*** This chapter is the collaborated work by different research groups. The contribution of the author of this thesis is to determine with accuracy the necessary input material parameters from atomistic simulations.**

A crucial step in this approach is the appropriate selection and modeling of the unit processes. These models supply the link between the atomic and mesoscale by identifying and correlating the relevant material properties, susceptible to atomistic determination such as energy formation for defects, with the corresponding driving forces. In this case, we specifically consider the following unit processes: double-kink formation and thermally activated motion of kinks; the close-range interactions between primary and forest dislocation, leading to the formation of jogs; the percolation motion of dislocations through a random array of forest dislocations introducing short-range obstacles of different strengths; dislocation multiplication due to breeding by double cross-slip and dislocation pair-annihilation.

A set of material parameters is then obtained from the modeling and identification stage, which is required to quantify the contribution of each of the unit processes. We compute these materials properties using a combination of *ab initio* quantum mechanics (QM) and force field (FF) calculations. QM describes the atomic interactions from first principles, i.e., with no input from experiments; unfortunately, QM methods are computationally intensive and restricted to small systems, making QM calculations impractical to study most of the materials properties governing plasticity. Force fields calculations give the total energy of a system as a potential energy function of the atomic positions and with molecular dynamics (MD) allows the simulation of systems containing millions of atoms. We used *ab initio* quantum mechanical calculations (equations of state of various crystalline phases, elastic constants, energetics of defects, etc.) to develop a many body force field (FF) (named qEAM FF) for Tantalum. Then, we use the qEAM FF with MD to calculate the core energy of the 1/2a<111> screw dislocation, that of the edge

dislocation with Burgers vector b=1/2a<111> in (110) planes. We have also calculated the formation energies and nucleation lengths of the kinks in b=1/2a<111> screw dislocations.

One of the appealing features of the present approach is the ability to incorporate additional unit mechanisms as they may be required by the physics of the problem. For example, the formation and evolution of dislocation structures are of particular interest in ductile crystals subjected to large and cyclic deformation. In recent studies, unit-mechanism-based micromechanical models have been proposed to elucidate the effective behavior of dislocation structures on the macroscopic response.

6.2 Unit processes

Plastic deformation in metallic systems is the macroscopic manifestation of dislocation activity. The resistance to the dislocation motion, therefore, engenders the hardening properties observed in this type of materials. It is then the complex interplay of microscopic mechanisms controlling **dislocation mobility, dislocation interaction and dislocation evolution,** which confers the macroscopic constitutive properties. In the present approach, these controlling processes are considered to be *orthogonal* in the sense that they are weakly coupled with each other. The interaction among them is only established through the uniqueness of the macroscopic driving force that is shared, via the localization process, by all the unit processes.

In this section, we introduce the set of controlling unit processes, which have been identified for describing the mechanical response of high-purity BCC single crystals, in

particular, for Tantalum. We also provide the final expression resulting from the modeling of each of these processes. A detailed description of the model, including comparison with experimental data, is given in Ref. 7.

6.2.1 Dislocation mobility: double-kink formation and thermally activated motion of kinks

We consider the thermally activated motion of dislocations within an *obstacle-free* slip plane. Under these conditions, the motion of dislocations is driven by an applied resolved shear stress τ and is hindered by the lattice resistance, which is weak enough that it may be overcome by thermal activation. The lattice resistance is presumed to be well described by a Peierls energy function, which assigns an energy per unit length to dislocation segments as a function of their position on the slip plane.

In bcc crystals, the core of screw dislocation segments relaxes into low-energy non-planar configurations[5,8-14]. This introduces deep valleys into the Peierls energy function aligned with the Burgers vector directions and possessing the periodicity of the lattice. At low temperatures, the dislocations tend to adopt low-energy configurations and, consequently, the dislocation population predominantly consists of long screw segments. In order to move a screw segment normal to itself, the dislocation core must first be constricted, which requires a substantial supply of energy. Thus, the energy barrier for the motion of screw segments, and the corresponding Peierls stress, may be expected to be large, and the energy barrier for the motion of edge segments to be comparatively smaller. For instance, Duesbery and Xu[15] have calculated the Peierls stress for a rigid screw dislocation in Mo to be 0.022 μ, where μ is the <111> shear modulus,

whereas the corresponding Peierls stress for a rigid edge dislocation is 0.006 μ, or about one fourth of the screw value. This suggests that the rate-limiting mechanism for dislocation motion is the thermally activated motion of kinks along screw segments[16-18].

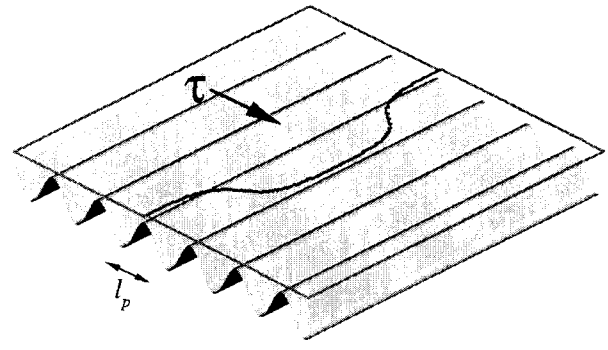

(a)

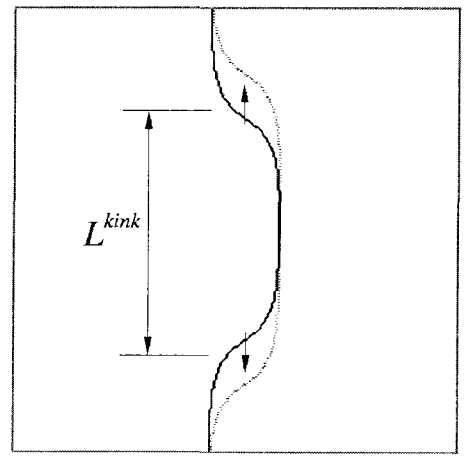

(b)

Figure 6-1. Schematic of the double-kink mechanism.

At sufficiently high temperatures and under the application of a resolved shear stress $\tau > 0$, a double-kink may be nucleated with the assistance of thermal activation[5,19,20], and the subsequent motion of the kinks causes the screw segment to effectively move forward, as shown in Figure 6-1. Under this condition the following expression for the effective temperature and strain-rate dependent Peierls τ_p is obtained:

$$\tau_p = \frac{\tau_0}{\beta E^{kink}} a \sinh\left(\frac{\dot{\gamma}}{\dot{\gamma}^{kink}} e^{\beta E^{kink}}\right), \tag{1}$$

where the effective Peierls stress is given by

$$\tau_0 = \frac{E^{kink}}{bL^{kink} l_p}, \tag{2}$$

and the reference strain is defined as

$$\dot{\gamma}_0^{kink} = 2b\rho l_P \nu_D, \tag{3}$$

In the preceding equations, b is the Burgers vector, ρ is the dislocation density, $\beta = 1/k_B T$, k_B is the Boltzmann constant, T is the absolute temperature, and ν_D is the attempt frequency, which may be identified with the Debye frequency to a first approximation. Also, l_P is the distance between two consecutive Peierls valleys. For bcc crystals, $l_P = \sqrt{2/3}\,a$ if the slip plane is {110}, $l_P = \sqrt{2}\,a$, if the slip plane is {112}, and $l_P = \sqrt{8/3}\,a$ if the slip plane is {123}, where a is the cubic lattice size[21]. Finally, E^{kink} is the energy of formation of a kink-pair and L^{kink} is the length of an incipient double kink. The formation energy E^{kink} and the length L^{kink}, which cannot be reliably estimated from elasticity since

the energy is composed mostly of core region, can, however, be accurately computed by recourse to atomistic models as shown in Chapter 5. Modeling of this first unit process renders the first 2 material properties amenable of atomistic calculations.

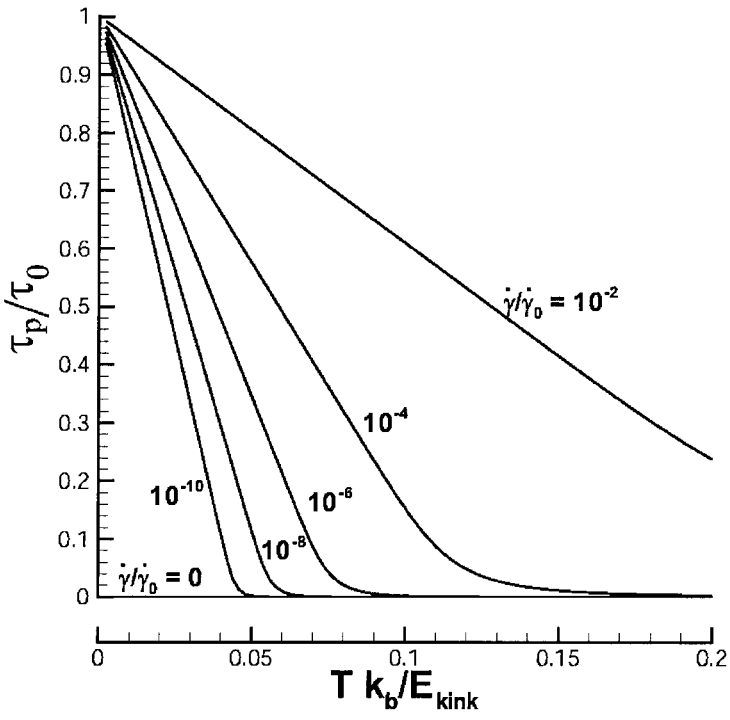

Figure 6-2. Temperature dependence of the effective Peierls stress for various strain rates. Note that the typical order of magnitude of $\dot{\gamma}_0^{kink} = 10^{-6}\ s^{-1}$.

In Figure 6-2 the dependence of the effective Peierls stress on temperature and rate of deformation is illustrated. The Peierls stress decreases ostensibly linearly up to a critical temperature T_c, beyond which it tends to zero. These trends are in agreement with the experimental observations of Wasserbäch[22] and Lachenmann and Schultz[23] The critical temperature T_c increases with the strain rate. In particular, in this model the effect of increasing (decreasing) the strain rate has an analogous effect to decreasing

(increasing) the temperature, and vice versa, as noted by Tang *et al.*[24]. In the regime of very high strain rates ($\dot{\gamma} > 10^5$ s^{-1}), effects, such as electron and phonon drag, become important and control the velocity of dislocations[25, 26].

6.2.2 Dislocation interactions: obstacle-pair strength and obstacle strength

In the forest-dislocation theory of hardening, moving dislocations could be impeded by the secondary or "forest" dislocations in their slip planes. As the moving and forest dislocations intersect, they form jogs or junctions of varying strengths[4,27-34] which, provided the junction is sufficiently short, may be idealized as point obstacles. Moving dislocations are pinned down by the forest dislocations and require a certain elevation of the applied resolved shear stress in order to bow out and bypass the pinning obstacles. For the case of infinitely strong obstacles, the resistance of the forest is provided by the strength of the obstacle pairs. This obstacle pair strength is subsequently deduced by considering that point obstacles composing the pair can only provide a finite strength. The processes imparting the pair-obstacle strength and obstacle strength are described next.

A. Obstacle-pair strength

We begin by treating the case of infinitely strong obstacles. In this case, pairs of obstacles pin down dislocation segments, which require a certain threshold resolved shear stress s in order to overcome the obstacle pair. The lowest-energy configuration of unstressed dislocation segments spanning an obstacle pair is a step of the form shown as the thin line in Figure 6-3. Under these conditions, the bow-out mechanism by which a

dislocation segment bypasses an obstacle pair may be expected to result in the configuration shown in Figure 6-3 (bold line).

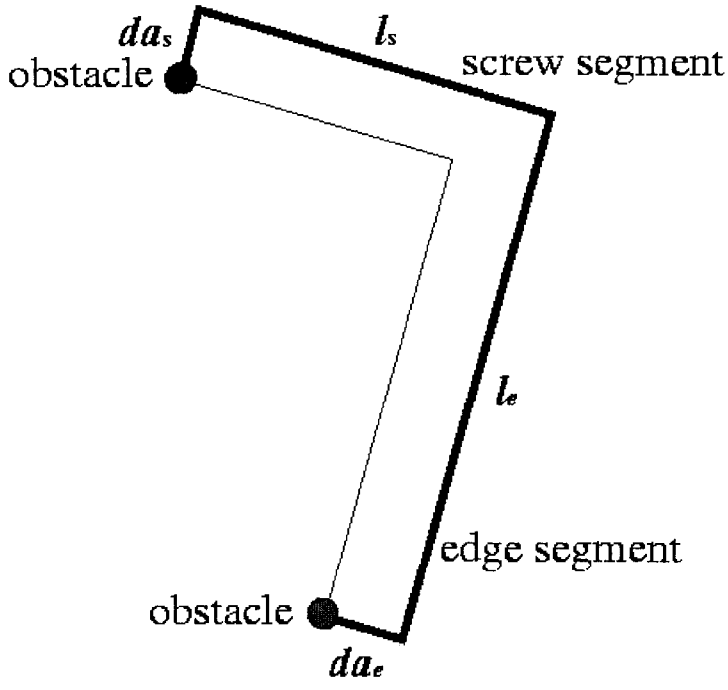

Figure 6-3. Bow-out mechanism for a dislocation segment bypassing an obstacle pair.

If the edge-segment length is l_e, a displacement da_e of the dislocation requires a supply of energy equal to $2\ U^{screw}\ da_e + b\ \tau_P^{edge}\ l_e\ da_e$ in order to overcome the Peierls resistance τ_P^{edge} and to extend the screw segments. The corresponding energy release is $b\tau\ l_e\ da_e$. Similar contributions result from a displacement da_s of the screw-segment of length l_s. Retaining dominant terms the obstacle-pair strength is

$$s = \tau_P^{screw} + \frac{2U^{edge}}{bl_s}, \tag{4}$$

The obstacle-pair strength can be therefore estimated by quantifying τ_P, l_s and U^{edge}. An expression for the Peierls stress τ_P is given in Eq. (1). The distance between obstacles along the screw direction l_s is estimated by statistics assuming a random obstacle distribution and the core energy per unit length in the edge direction U^{edge} is obtained by atomistic calculations presented in the following sections.

B. Obstacle strength

In this section we proceed to estimate the obstacle strength that reduces the obstacle-pair strength described in the previous section. The interaction between primary and secondary dislocations may result in a variety of reaction products, including jogs and junctions[4,24,27-34]. Experimental estimates of junction strengths have been given by Franciosi and Zaoui[35] for the twelve slip systems belonging to the family of {111} planes and [110] directions in fcc crystals, and by Franciosi[36] for the twenty-four systems of types {211} [111] and {110}[111] in bcc crystals. The strength of some of these interactions has recently been computed using atomistic and continuum models[4,27-29]. Tang *et al.* have numerically estimated the average strength of dislocation junctions for Nb and Ta crystals[24].

For purposes of the present theory, we specifically concern ourselves with short-range interactions between dislocations that can be idealized as point defects. For simplicity, we consider the case in which each intersecting dislocation acquires a jog. The energy of a pair of crossing dislocations is schematically shown in Figure 6-4 as a function of some convenient reaction coordinate, such as the distance between the dislocations. The interaction may be repulsive, resulting in an energy barrier, or

attractive, resulting in a binding energy (see Figure 6-4). In the spirit of an equilibrium theory, here we consider only the final reaction product, corresponding to a pair of jogged dislocations at infinite distance from each other, and neglect the intermediate states along the reaction path. In addition, we deduce the strength of the obstacles directly from the energy supply required to attain the final state, i.e., the jog-formation energy. Despite the sweeping nature of these assumptions, the predicted saturation strengths in multiple slips are in good agreement with experiment (cf. Section 6.4), which lends some empirical support to the theory.

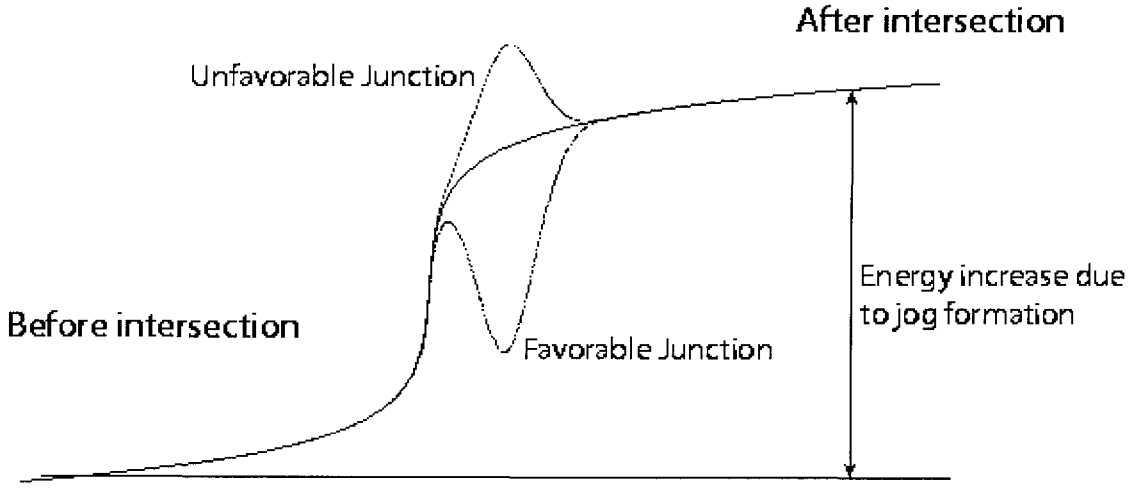

Figure 6-4. Schematic of energy variation as a function of a reaction coordinate during dislocation intersection and crossing.

We estimate the jog formation energy as follows. Based on energy and mobility considerations already discussed, we may expect the preponderance of forest dislocations to be of screw character, and the mobile dislocation segments to be predominantly of edge character. We therefore restrict our analysis to intersections between screw and edge segments. The geometry of the crossing process is schematically shown in Figure 6-5.

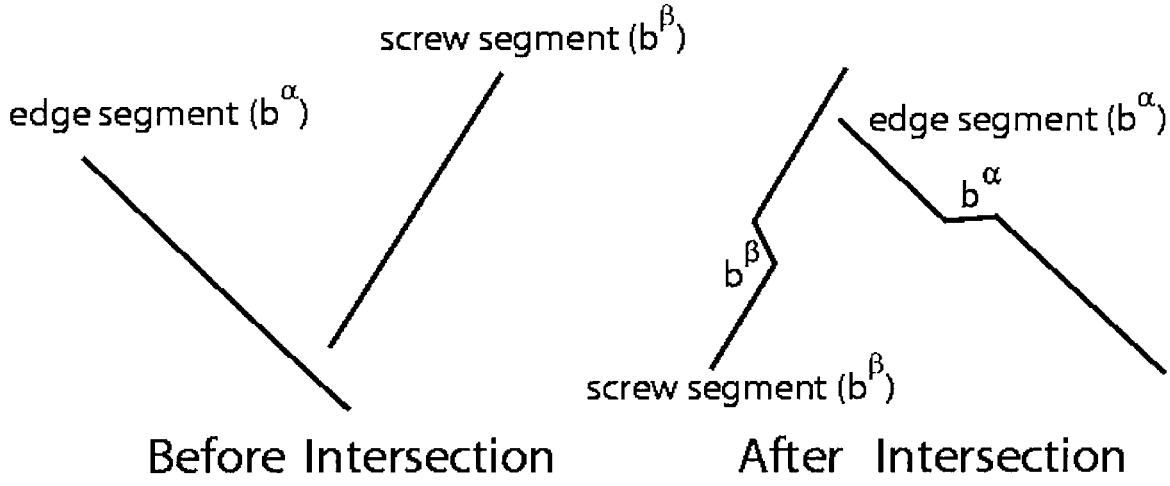

Figure 6-5. Schematic of jog formation during dislocation intersection.

Each dislocation acquires a jog equal to the Burgers vector of the remaining dislocation. The energy expended in the formation of the jogs may be estimated as

$$E_{\alpha\beta}^{jogs} = bU^{screw}[1 - r\cos\theta^{\alpha\beta}] \qquad \text{if } b^{\alpha} = b^{\beta}$$

$$E_{\alpha\beta}^{jogs} = bU^{screw}[2r - \cos\theta^{\alpha\beta} - r\cos\theta^{\alpha\beta}] \qquad \text{otherwise,} \qquad (5)$$

where $r = U^{edge}/U^{screw}$ is the ratio of screw to edge dislocation line energies. This ratio is computed by atomistic calculations presented in the next section, renders a value of r =1.77 for Ta. The resulting jog formation energies for the complete collection of pairs of {211} and {110} dislocations are tabulated in Table 6-1.

Table 6-1. Normalized jog-formation energies resulting from crossings of bcc dislocations.

	A2	A2'	A3	A3'	A6	A6'	B2	B2'	B4	B4'	B5	B5'	C1	C1'	C3	C3''	C5	C5'	D1	D1''	D4	D4''	D6	D6''
A2	—	1.0	1.0	1.0	1.0	1.0	1.5	1.5	1.5	1.5	1.5	1.5	2.4	2.4	2.4	2.4	2.4	2.4	2.4	2.4	2.4	2.4	2.4	2.4
A2'	1.0	—	1.0	1.0	1.0	1.0	3.2	3.2	3.2	3.2	3.2	3.2	1.8	1.8	1.8	1.8	1.8	1.8	1.8	1.8	1.8	1.8	1.8	1.8
A3	1.0	1.0	—	1.0	1.0	1.0	2.4	2.4	2.4	2.4	2.4	2.4	1.5	1.5	1.5	1.5	1.5	1.5	2.4	2.4	2.4	2.4	2.4	2.4
A3'	1.0	1.0	1.0	—	1.0	1.0	1.8	1.8	1.8	1.8	1.8	1.8	3.2	3.2	3.2	3.2	3.2	3.2	1.8	1.8	1.8	1.8	1.8	1.8
A6	1.0	1.0	1.0	1.0	—	1.0	2.4	2.4	2.4	2.4	2.4	2.4	2.4	2.4	2.4	2.4	2.4	2.4	1.5	1.5	1.5	1.5	1.5	1.5
A6'	1.0	1.0	1.0	1.0	1.0	—	1.8	1.8	1.8	1.8	1.8	1.8	1.8	1.8	1.8	1.8	1.8	1.8	3.2	3.2	3.2	3.2	3.2	3.2
B2	1.5	1.5	1.5	1.5	1.5	1.5	—	1.0	1.0	1.0	1.0	1.0	2.4	2.4	2.4	2.4	2.4	2.4	2.4	2.4	2.4	2.4	2.4	2.4
B2'	3.2	3.2	3.2	3.2	3.2	3.2	1.0	—	1.0	1.0	1.0	1.0	1.8	1.8	1.8	1.8	1.8	1.8	1.8	1.8	1.8	1.8	1.8	1.8
B4	2.4	2.4	2.4	2.4	2.4	2.4	1.0	1.0	—	1.0	1.0	1.0	2.4	2.4	2.4	2.4	2.4	2.4	1.5	1.5	1.5	1.5	1.5	1.5
B4'	1.8	1.8	1.8	1.8	1.8	1.8	1.0	1.0	1.0	—	1.0	1.0	1.8	1.8	1.8	1.8	1.8	1.8	3.2	3.2	3.2	3.2	3.2	3.2
B5	2.4	2.4	2.4	2.4	2.4	2.4	1.0	1.0	1.0	1.0	—	1.0	1.5	1.5	1.5	1.5	1.5	1.5	2.4	2.4	2.4	2.4	2.4	2.4
B5'	1.8	1.8	1.8	1.8	1.8	1.8	1.0	1.0	1.0	1.0	1.0	—	3.2	3.2	3.2	3.2	3.2	3.2	1.8	1.8	1.8	1.8	1.8	1.8
C1	1.8	1.8	1.8	1.8	1.8	1.8	1.8	1.8	1.8	1.8	1.8	1.8	—	1.0	1.0	1.0	1.0	1.0	3.2	3.2	3.2	3.2	3.2	3.2
C1'	1.8	1.8	1.8	1.8	1.8	1.8	1.8	1.8	1.8	1.8	1.8	1.8	1.0	—	1.0	1.0	1.0	1.0	3.2	3.2	3.2	3.2	3.2	3.2
C3	1.5	1.5	1.5	1.5	1.5	1.5	2.4	2.4	2.4	2.4	2.4	2.4	1.0	1.0	—	1.0	1.0	1.0	2.4	2.4	2.4	2.4	2.4	2.4
C3''	3.2	3.2	3.2	3.2	3.2	3.2	1.8	1.8	1.8	1.8	1.8	1.8	1.0	1.0	1.0	—	1.0	1.0	1.8	1.8	1.8	1.8	1.8	1.8
C5	2.4	2.4	2.4	2.4	2.4	2.4	1.5	1.5	1.5	1.5	1.5	1.5	1.0	1.0	1.0	1.0	—	1.0	2.4	2.4	2.4	2.4	2.4	2.4
C5''	1.8	1.8	1.8	1.8	1.8	1.8	3.2	3.2	3.2	3.2	3.2	3.2	1.0	1.0	1.0	1.0	1.0	—	1.8	1.8	1.8	1.8	1.8	1.8
D1	1.8	1.8	1.8	1.8	1.8	1.8	1.8	1.8	1.8	1.8	1.8	1.8	3.2	3.2	3.2	3.2	3.2	3.2	—	1.0	1.0	1.0	1.0	1.0
D1''	1.8	1.8	1.8	1.8	1.8	1.8	1.8	1.8	1.8	1.8	1.8	1.8	3.2	3.2	3.2	3.2	3.2	3.2	1.0	—	1.0	1.0	1.0	1.0
D4	2.4	2.4	2.4	2.4	2.4	2.4	1.5	1.5	1.5	1.5	1.5	1.5	2.4	2.4	2.4	2.4	2.4	2.4	1.0	1.0	—	1.0	1.0	1.0
D4''	1.8	1.8	1.8	1.8	1.8	1.8	3.2	3.2	3.2	3.2	3.2	3.2	1.8	1.8	1.8	1.8	1.8	1.8	1.0	1.0	1.0	—	1.0	1.0
D6	1.5	1.5	1.5	1.5	1.5	1.5	2.4	2.4	2.4	2.4	2.4	2.4	2.4	2.4	2.4	2.4	2.4	2.4	1.0	1.0	1.0	1.0	—	1.0
D6''	3.2	3.2	3.2	3.2	3.2	3.2	1.8	1.8	1.8	1.8	1.8	1.8	1.8	1.8	1.8	1.8	1.8	1.8	1.0	1.0	1.0	1.0	1.0	—

A derivation entirely analogous to that leading to Eq. (1) yields the following expression for the strength of an obstacle in the slip system α produced by a forest segment in the system β.

$$s^{\alpha\beta} = \frac{s_0^{\alpha\beta}}{\beta E_{\alpha\beta}^{jog}} a \sinh\left(\frac{\dot{\gamma}^{\alpha}}{\dot{\gamma}_0^{\alpha}} e^{(\beta E_{\alpha\beta}^{jog})}\right), \tag{6}$$

where the strength at zero temperature is given by

$$s_0^{\alpha\beta} = \frac{E_{\alpha\beta}^{jog}}{b\bar{l}^{\alpha} L^{junct}}, \tag{7}$$

and the reference strain rate by

$$\dot{\gamma}_0^{\alpha} = 2\rho^{\alpha} b \bar{l}^{\alpha} v_D, \tag{8}$$

The lengths $\bar{l}^{\alpha}$ and L^{junct} describe the geometry of the junction as illustrated in Figure 6-6. These values, which have been estimated to be of the order of few b in the present case, can also be obtained by atomistic models.

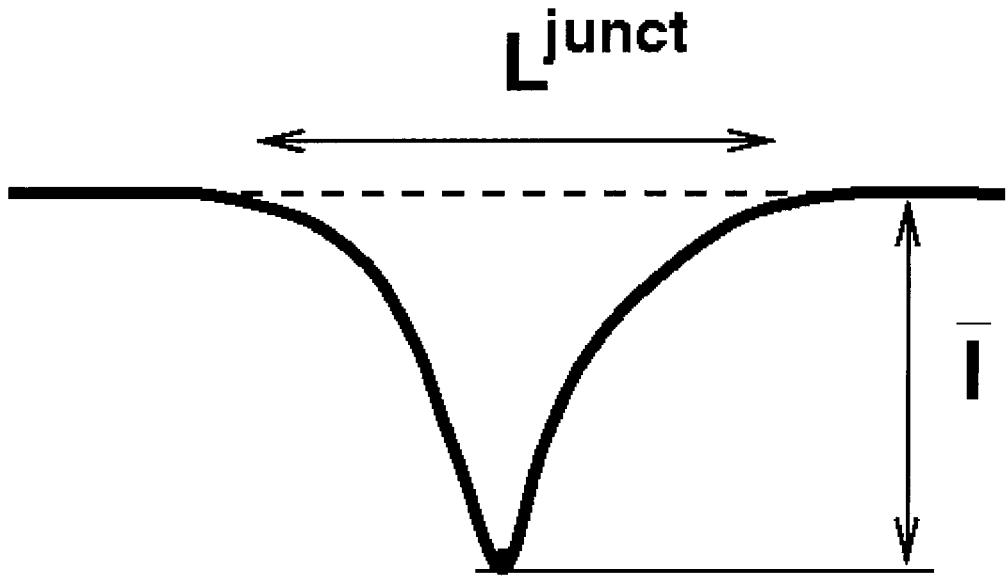

Figure 6-6. Schematic of a dislocation line overcoming a junction.

6.2.3 Dislocation evolution: multiplication and attrition

The density of forest obstacles depends directly on the dislocation densities in all slip systems of the crystal. Therefore, in order to close the model, we require an equation of evolution for the dislocation densities. Processes resulting in changes in dislocation density include production by fixed sources, such as Frank-Read sources, breeding by double cross slip and pair annihilation (see Ref. 37 for review; see also Ref. 38, 39, 40, 41, 42, 43). Although the operation of fixed Frank-Read sources is quickly eclipsed by production due to cross slip at finite temperatures, it is an important mechanism at low

temperatures. The double cross slip, fixed Frank-Read sources and pair annihilation mechanisms are considered next.

A. Dislocation multiplication: fixed Frank-Reed and breeding by cross glide

The rate of dislocation multiplication in a given slip system α produced by fixed Frank-Reed sources and by breeding by cross glide is written as

$$b\dot{\rho}^{\alpha} = \lambda_0 \sqrt{\rho^{\alpha}}\,\dot{\gamma}^{\alpha}, \tag{9}$$

where λ_0 is a constant associated with the fixed Frank-Read production; this parameter is mere topological than material dependent.

B. Attrition: pair annihilation

The rate of dislocation attrition due to pair annihilation may finally be estimated as

$$b\dot{\rho}^{\alpha} = -\kappa\rho^{\alpha}\dot{\gamma}^{\alpha}, \tag{10}$$

where κ is the effective annihilation distance. This is the maximum distance at which two screw segments with opposite direction and forced to move with a velocity $v = \dot{\gamma}/b\rho$ will annihilate. This distance can be estimated by simply equating the time required for trapping and escaping. Trapping is governed by the elastic interaction forces (attraction) while escaping by the applied strain rate. Then,

$$\frac{1}{\kappa} = \frac{1}{\kappa_c} + \frac{1}{\kappa_0 (A + \sqrt{A^2 + 1})}, \tag{11}$$

where

$$A = e^{-\beta E^{jog}} \beta E^{jog} \dot{\gamma}_0^{jog} / \dot{\gamma}^{\alpha}, \tag{12}$$

is a factor depending on the strain rate and temperature,

$$\dot{\gamma}_0^{jog} = 2b\rho l_P \nu_D, \tag{13}$$

is a reference slip-strain rate and κ_c is the cutoff value corresponding to the effective screening distance. It follows that the critical pair-annihilation distance κ decreases with increasing strain rate and decreasing temperature. Thus, at high strain rates the dislocation velocities are high and the probability of being captured by another dislocation diminishes accordingly. Additionally, an increase in temperature increases the dislocation mobility and speeds up the annihilation process, which results in an attendant increase in annihilation rates. The rate of annihilation is then modulated by the nucleation energy of a jog E^{jog}, which can be calculated from atomistic simulations.

6.3. Atomistic modeling of dislocations properties

In the previous section, we have identified the following set of *material parameters* required to estimate the contribution of each of the controlling unit processes: E^{kink}, L^{kink}, U^{edge}/U^{screw}, and E^{jog}. In this section, we briefly describe the computation of these parameters using a first principles based force field with molecular dynamics.

Quantum mechanics (QM) describes the atomic interactions from first principles, i.e., using no empirical input. Unfortunately QM methods are computationally too intensive and thus only applicable to small systems (hundreds of atoms) and short times (picoseconds). The studies of most of the unit processes that govern the plasticity of materials (such as dislocation mobility, kink energies, etc.) involve many atoms and long

simulation times. Such problems require the use of force fields, where the internal energy of the system is given by a potential energy function of the atomic positions and does not involve the solution of Schrodinger's equation. The drawback of using potentials to describe the atomic interactions is that some accuracy is lost; it is thus of great importance to use accurate force fields to describe the atomic interactions.

We developed a many body force field for Tantalum based on accurate QM calculations that can be used with molecular dynamics (MD) to simulate systems containing millions of atoms. We fitted an embedded atom model type force field (named qEAM FF) to a variety of *ab initio* calculations, including the zero temperature equation of state (EOS) for bcc, fcc, and A15 phases of Ta in a wide pressure range, elastic constants, vacancy formation energy and energetics of a shear transformation in the twinning direction. Ta is a bcc metal and no phase transition to other crystalline phase is known, but using QM we can calculate the EOS of thermodynamically unstable or metastable phases (such as A15, fcc, hcp, etc.). Including data about these high-energy phases, with different coordination numbers, in the force field training set is important to correctly describe the atomic interactions near defects, such as dislocations, grain boundaries, etc.

We have used the qEAM with MD to study a variety of materials properties[44]. We have calculated the melting curve of Ta in a wide pressure range; the calculated zero pressure melting temperature T_{melt} = 3150K is in very good agreement with the experimental result of 3290K; this is an important validation given the fact that the qEAM FF is based only on zero temperature *ab initio* data. The calculated thermal

expansion is also in good agreement with experimental results. We have also used the qEAM FF with MD to study spall failure in Ta at high strain rates[45].

We use the qEAM FF to calculate a variety of dislocation properties[14], such as core energies, Peierls stress, kink formation energies. As pointed out in previous sections, these are the fundamental quantities that govern plasticity in metals. The accuracy of the materials parameters obtained from these calculations is best assessed by their use in macroscopic models that can be directly compared with experimental results. These quantities could not be directly measured experimentally. The best validation of the accuracy of the atomistic calculations is through their use in macroscopic models that can be directly compared with experimental results. The following subsections describe some of these calculations; in subsection 6.3.1, we show the calculation of the core energy of edge and screw dislocations in Ta and in subsection 6.3.2 we calculate the double kink formation energy and nucleation length.

6.3.1. Core energy of 1/2a<111> screw and edge dislocations

In order to study static properties of the 1/2a<111> screw dislocation in Ta, such as core structure and energy, we use a dislocation quadrupole in a simulation cell with periodic boundary conditions. Two of the dislocations have Burgers vector b=1/2a<111> and the other two have b=-1/2a<-1-1-1>. Such an arrangement of dislocations minimizes the misfit of atoms on the periodic boundary due to the effects of periodic images. We build the dislocations using the atomic displacements obtained from elasticity theory and then we relax the atomic coordinates using the qEAM FF. In the bcc structure, there are two kinds of dislocation core configurations (easy core and hard core)

that can be transformed to each other by reversing the Burgers vector. In this work we focus on the lower energy easy cores. In Figure 6-7 we show the differential displacement map (DD) of our relaxed quadrupolar system. In the DD maps, atoms are represented by circles and projected on a (111) plane. The arrows represent the relative displacement in [111] direction of neighboring atoms due to the dislocation. We can see from Figure 6-7 that the equilibrium dislocation core obtained using qEAM FF has three-fold symmetry and spreads out in three <112> directions on {110} planes.

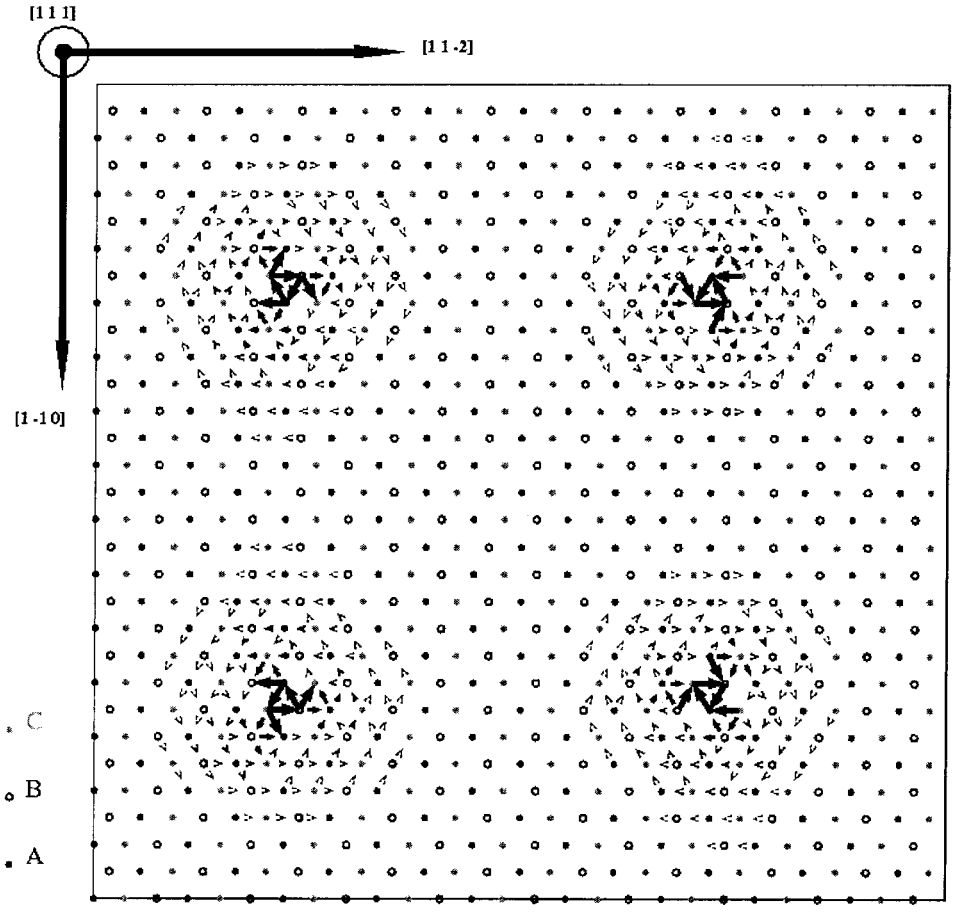

Figure 6-7. Differential displacement map of a relaxed quadrupole of screw dislocations in Ta.

Let us define strain energy as the total energy of our system once the perfect crystal energy is subtracted. The total strain energy of a system containing dislocations can be divided into two terms: core energy (E_c) and elastic energy (E_e). The latter contains the self-energy of each dislocation and their interactions and can be calculated using linear elasticity theory. The core energy is the energy contained close to the dislocation line (closer than some distance r_c called core radius), where, due to the large strains, elasticity theory is not valid and the details of the interatomic interactions are important. For our quadrupole system the total strain energy takes the form[13]

$$E = E_c(r_c) = Kb^3[\ln(\frac{d_1}{r_c}) + A(\frac{d_1}{d_2})], \quad (14)$$

where K depends on the elastic constants, d_1 and d_2 are the nearest separation of dislocations along <11-2> and <1-10> directions and $A(d_1/d_2)$ is a geometric factor which comes from the dislocation interactions.

We studied quadrupolar dislocation cells of different sizes. In Figure 6-8 we show the minimized energy as a function of $\ln(d_1/r_c)+A(d_1/d_2)$ for the different simulation cells. We took the core radius to be r_c=2.287b; this is a typical value used in previous studies[11,13]. We can see from Figure 6-8 that the total energies follow a straight line as predicted by elasticity theory [Eq. (14)], showing that the value chosen for the core radius is large enough to take account for the non elastic region near the dislocation line.

From a linear fit to our data we determine the core energy E_c=1.404 eV/b and K = 3.3497×10^{-2} eV/Å^3. The value of K can also be computed from the elastic constants giving 3.3492×10^{-2} eV/Å^3 in excellent agreement with the one obtained from the fit. Recent *ab initio* calculations of core energy (using periodic cells containing 90 atoms)

give 0.86 eV/b, lower than the value obtained with qEAM FF and the dislocation cores are compact and symmetric[13].

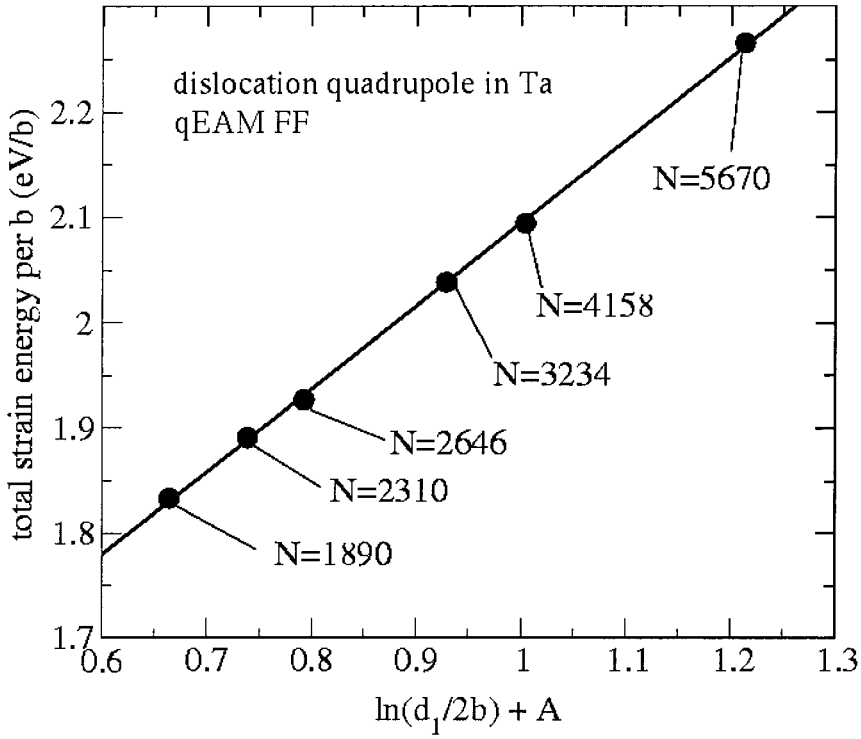

Figure 6-8. Total strain energy of the quadrupolar system as a function of $\ln(\frac{d_1}{r_c}) + A(\frac{d_1}{d_2})$; the number of atoms in each simulation is shown. The line is the linear fit to our atomistic data.

Using the qEAM we can calculate the strain energy associated with each atom. In Figure 6-9 we show the atomic energy distribution (number of atoms per dislocation per Burgers vector as a function of their strain energy) for a system containing 5670 atoms in the periodic cell. We can see that there are 6 atoms with atomic strain energy higher than 0.15 eV and another 6 atoms with energy in the range 0.06-0.08 eV. They correspond to

the 12 atoms per dislocation per Burgers vector closer to the dislocation line and their total energy is 1.400 eV/b, very similar to the core energy obtained from Eq. (14). The rest of the atoms have lower strain energy and can be considered as the elastic part of the system. We can then define the dislocation core as formed by the 12 atoms per Burgers vector with higher energy.

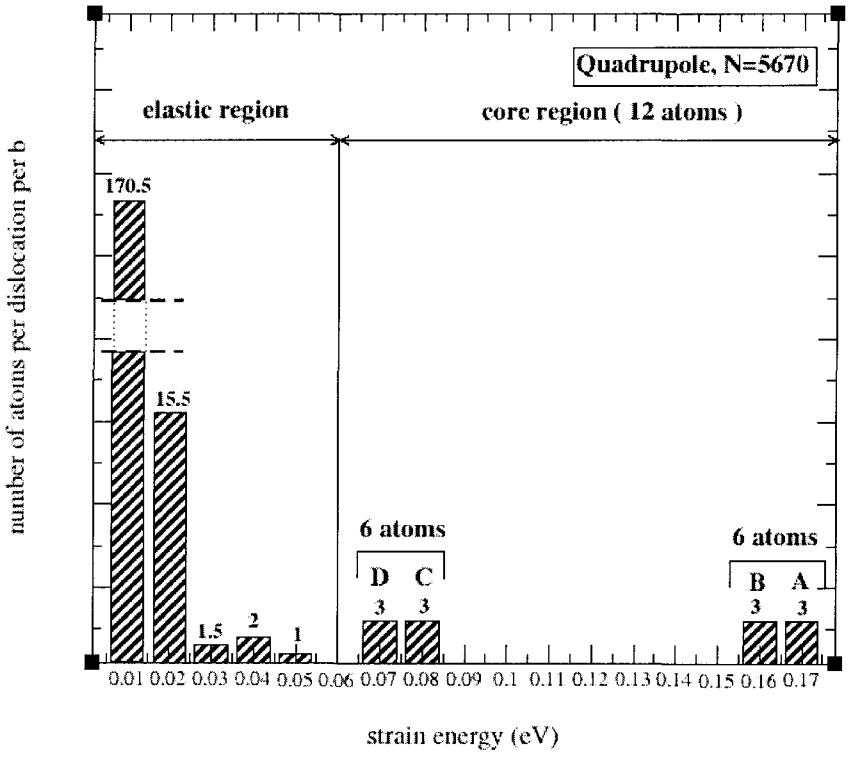

Figure 6-9. Histogram of atomistic strain energy distribution for the quadrupolar arrangement of screw dislocations. The cell contains 5670 atoms and is 7 Burgers vectors long.

We have also calculated the core energy of the edge dislocation with b=1/2a<111> on a (110) plane. We build a simulation cell with axis oriented along <112> (x axis), <110> (y axis), and 1/2a<111> (z axis); this cell contains 6 atoms. We

then replicate the cell 3 times along **X**, 16 times along **Y**, and 20 times along **Z**; the number of atoms in the cell is then N=5760. We then remove 108 atoms to form a dipole of edge dislocations. Once the system is relaxed (both atoms and cell parameters), we have a 24.3967 Å × 75.1824 Å × 56.632 Å cell. Figure 6-10 shows a snapshot of the atoms projected on a <112> plane.

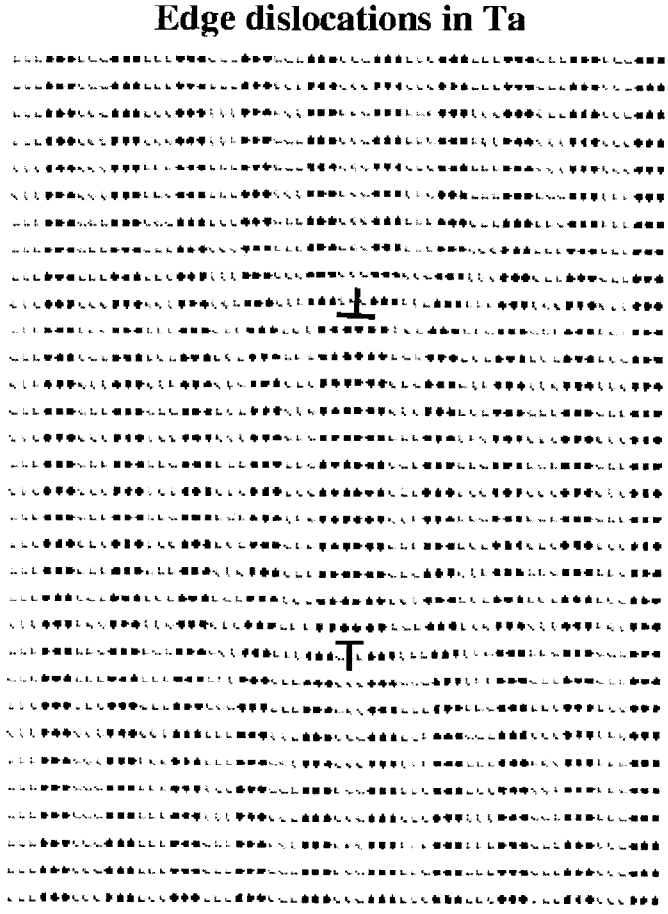

Figure 6-10. Snapshot of the relaxed edge dipole configuration. The cell contains 5652 atoms.

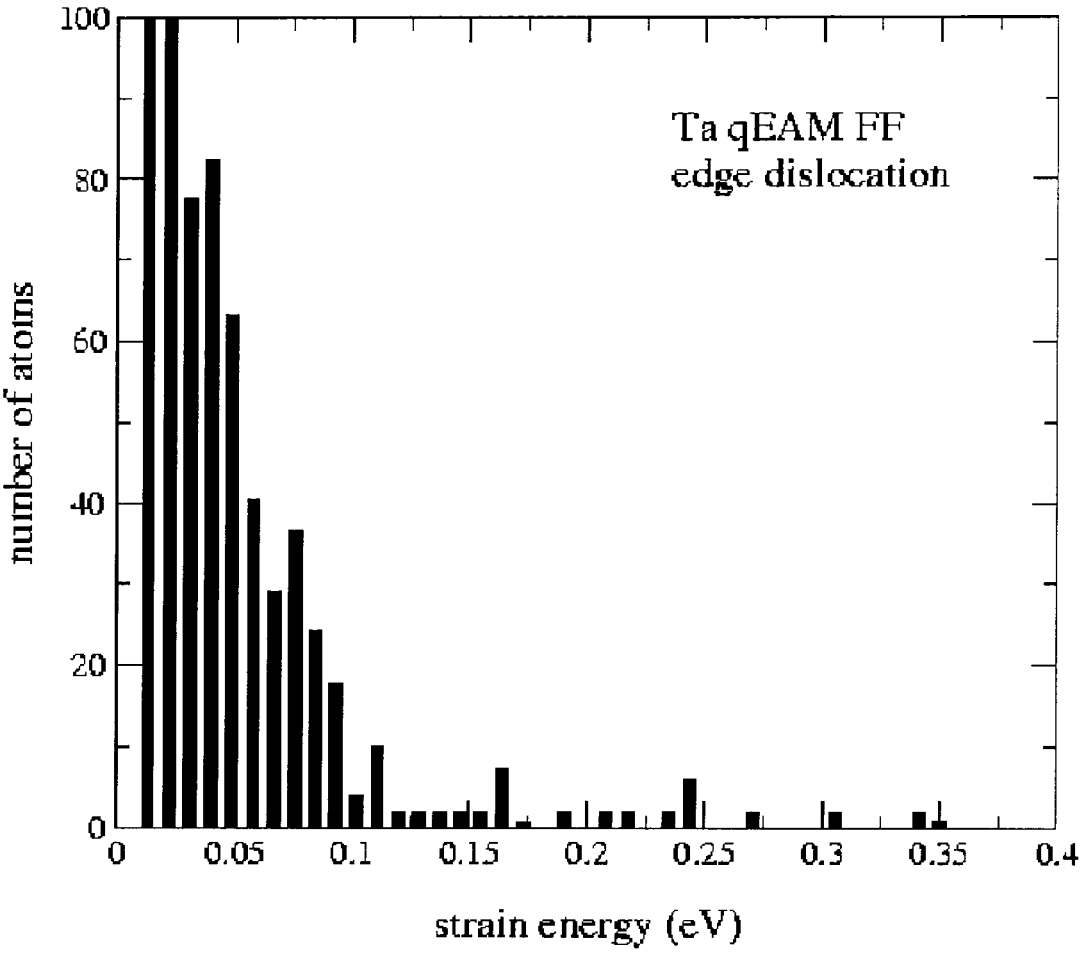

Figure 6-11. Histogram of atomistic strain energy distribution for the dipole of edge dislocations. The number of atoms is given by per dislocation per 1/2a<112> length.

In Figure 6-11 we show the energy distribution for the edge dislocation (number of atoms per dislocation and per a<112> length as a function of their energy). Figure 6-11 shows that the core of the edge dislocation contains atoms with higher energies and a broader distribution of energies as compared with the screw case (Figure 6-9). Taking into account Figure 6-11, we define the core of the edge dislocation as formed by those atoms with strain energy higher than 0.1 eV. This definition leads to 36 atoms per a<112> or ~ 4.42 atoms per Å and to a core energy of E_{core}^{edge} = 0.860 eV/Å (in the case of

the screw we had 12 atoms/b or ~ 4.17 atoms per Å). The ratio between the core energy of the edge and that of the screw is $E_{core}^{edge} / E_{core}^{screw} = 1.77$. It is important to mention that changing the number of atoms considered to belong to the core changes the core energy, but the difference is minor. Had we taken the 34 atoms per a<112> with higher energy as the core (leading to ~ 4.18 atoms / Å, a density very similar to the one obtained in the screw dislocation), we would have gotten the core energy $E_{core}^{edge} = 0.84$ eV/ Å.

6.3.2. Kink pair energy and nucleation length

As already explained, the kink pair mechanism controls the mobility of screw dislocations in bcc metals and atomistic simulations can provide the details of this mechanism.

As we can see from Figure 6-7, the core of the screw dislocation spreads in three <112> directions, this leads to two distinct, but energetically equivalent, core configurations; we name them as positive (P) and negative (N) cores. The shortest (and lowest energy) kinks possible involve the displacement of the position of the dislocation line in the (111) plane from one equilibrium position to a nearest neighbor equilibrium position; the displacement involved is 1/3 a<112>. There are six possible <112> directions but only two need to be considered by symmetry, this leads to two kink directions, which we call left (L) and right (R). The two dislocation cores (N and P) and two directions (L and R) lead to 8 different single kinks: NRP, NRN, PRP, PRN, NLP, NLN, PLP and PLN. We have studied all of them in detail; here we will concentrate on the single kinks that lead to the lowest energy kink pair. We calculated the formation

energy and length of the various kinks using quadrupole arrangements of dislocations as explained in Chapter 5. The simulation cell lengths are 40.7 Å in the [11-2] direction, 42.3 Å in the [1-10] direction and 431.8 Å in the [111] direction. The whole simulation cell contains 40,500 atoms. The details of these calculations can be found in Ref. 46. We calculate the kink energy as the difference of strain energy between the quadrupolar systems containing kinks and perfect straight dislocations. The energy difference divided by four is the formation energy for each kink. Using the qEAM FF, we find that the lowest energy kink pair is formed combining the PLN and NRP kinks. We define the kink pair nucleation energy as the sum of the formation energy of the two single kinks leading to E^{kink} = 0.730 eV. This result is comparable to that obtained by Yang *et al.* (0.96 eV) using the quantum-based multi-ion interatomic potentials derived from the model generalized pseudopotential theory (MGPT). The nucleation energy calculated in this way does not take into account the attractive interaction between the two kinks that lowers the nucleation energy. This interaction energy is very small (~ 2%) for separation of kinks larger than ~ 15 b[11, 20].

As explained above, a critical parameter for the micromechanical modeling of plasticity is, apart from the kink pair energy, its nucleation length L_{kink}. We studied both the energetics and structure of the various kinks along the dislocation line. Figure 6-12 shows the extent of the kinks both from structural and energetic points of view. We show the position of the dislocation in the direction of the kink along the dislocation line for a PLN kink [Figure 6-12(a)] and NRP kink [Figure 6-12(c)]. We also show the total strain energy of the quadrupolar system along the dislocation line for the PLN [Figure 6-12(b)] and NRP [Figure 6-12(d)] kinks. It is calculated by summing the atomic strain energies

for atoms in every 1 b slice in the [111] direction. The structural length of the PLN kinks is L_{str}^{PLN} = 8 b [Figure 6-12(a)]; while its "energetic extent" is L_{ene}^{PLN} = 14 b [Figure 6-12(b)]. For NRP kinks, we obtain L_{str}^{NRP} = 8 b [Figure 6-12(c)] and L_{ene}^{NRP} = 20 b [Figure 6-12(d)].

Going back to the definitions of the parameters entering the equation that governs the dislocation mobility [Eq. (1) and Eq. (2)]; the effective Peierls stress (τ_0) in Eq. (2) is defined as the applied stress for which the nucleation free energy for a kink pair (ΔG) is zero. ΔG is given by

$$\Delta G = E^{kink} \pm \tau l_P b L^{kink}, \tag{15}$$

where L^{kink} is the effective kink pair nucleation length and l_P is the distance advanced by the dislocations; in the kinks studied here, l_P = | 1/3 a<112> |. The second term in the right-hand side of Eq. (15) is the work done by the external stress when the kink is nucleated. Figure 6-13 shows a schematic diagram of a PLN-NRP kink pair. We can see that the work done by the external stress to nucleate the kink pair can be divided in four terms:

$$\tau b l_P L^{kink} = \tau b l_P \left(\frac{L_{str}^{PLN}}{2} + \frac{L_{ene}^{PLN} - L_{str}^{PLN}}{2} + \frac{L_{ene}^{NRP} - L_{str}^{NRP}}{2} + \frac{L_{str}^{NRP}}{2}\right), \tag{16}$$

where L^{kink} is the effective kink pair length. In Figure 6-13 we show the four terms in the right-hand side of Eq. (16). Note that Eq. (16) assumes that the kinks are straight lines connecting the two equilibrium positions of the dislocation. This way we obtain the effective kink pair nucleation length L^{kink} = 17 b.

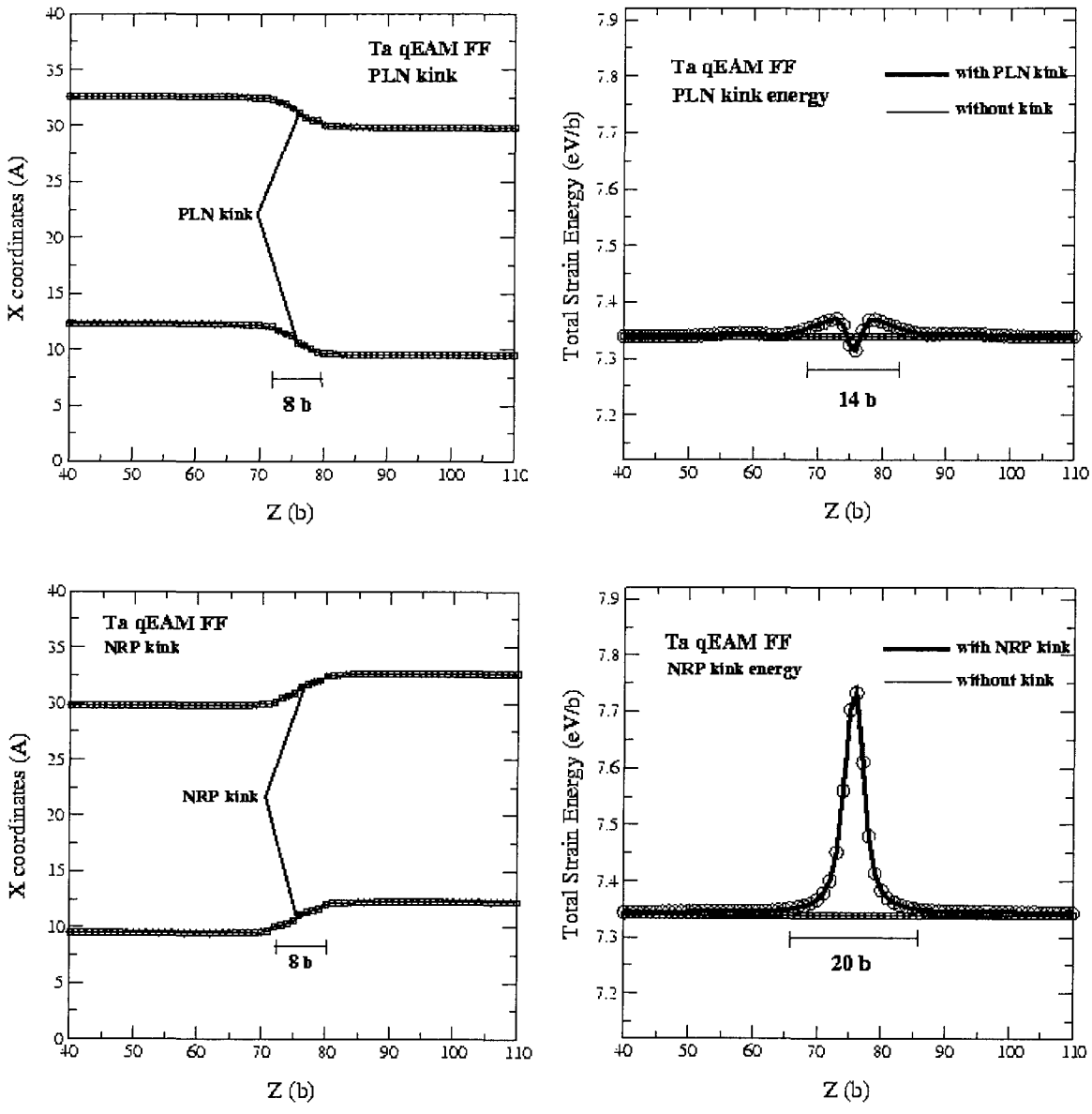

Figure 6-12. PLN and NRP kinks in Ta using the qEAM FF. (a) PLN kink: Dislocation position in the [11-2] direction along the dislocation line; we can see the dislocation moves from an equilibrium position to the next in a length of 8 Burgers vectors. (b) PLN kink: total strain energy in the quadrupolar system with four PLN kinks along the dislocation line. The system is divided in slices with thickness equal to b and the energy in each region is calculated. (c) NRP kink: Dislocation position in the [11-2] direction along the dislocation line; we can see the dislocation moves from an equilibrium position

to the next in a length of 8 Burgers vectors. (d) NRP kink: total strain energy in the quadrupolar system with four PLN kinks along the dislocation line.

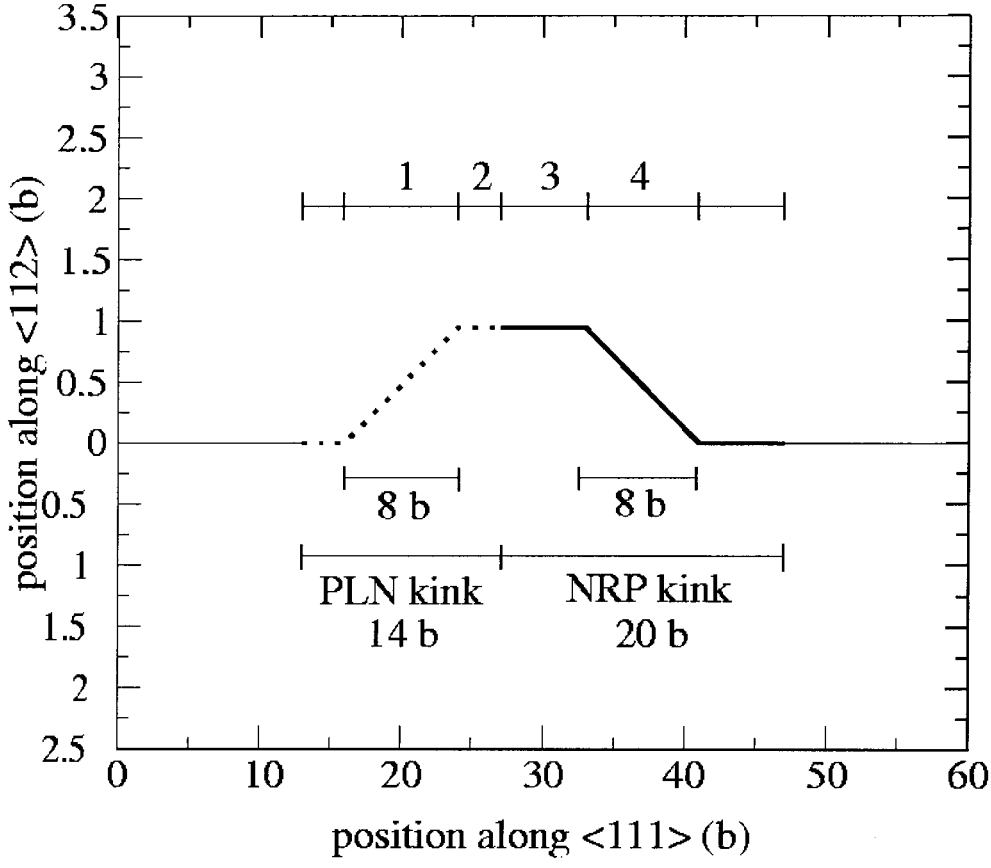

Figure 6-13. Schematic diagram of a kink pair formed by a NRP and PLN single kinks. The four terms entering in the work expression [Eq. (16)] are shown in the figure.

The remaining material parameter is the nucleation energy of a jog E^{jog}. In this work we take E^{jog} as the PLN-NRP kink pair nucleation energy.

6.4 Experiment, validation and prediction

To test the predictive capabilities of the multiscale approach, we first select a set of material parameters to best fit the experimental results, then we compare these parameters against the atomistically computed ones, and finally we *predict* the macroscopic response using the atomistic parameters. As we shall see, the agreement between the *fitted* and *computed by atomistics* material parameters is remarkable, and the predicted macroscopic response retains most of the experimental features. These facts provide confidence in the multiscale modeling approach, indicating that even in the case that experimental data would not have been available, still the macroscopic behavior could have been predicted based only on atomistic calculations.

The experiment data correspond to uniaxial tests on Ta single crystals of Mitchell and Spitzig[47]. In these tests, 99.97% pure Ta specimens were loaded in tension along the [213] crystallographic axis, at various combinations of temperature and strain rate. In particular we considered temperatures ranging from 296 K to 573 K, and strain rates ranging from 10^{-1} s^{-1} to 10^{-5} s^{-1}. The numerical procedure employed for the integration of the constitutive equations has been described elsewhere[48]. The constitutive update is fully implicit, with the active systems determined iteratively so as to minimize an incremental work function. All stress-strain curves are reported in terms of nominal stress and engineering strain.

Two different sets of material properties were used for the numerical simulations. The first set was obtained by fitting the simulation results to the experimental results.

Table 6-2 identifies the subset of parameters that are also amenable to direct calculation by atomistic-based methods. The table lists the parameter values obtained by these methods, as described in Sections 6.3, in parallel with the values obtained by the fitting approach. Thus, in the second set of properties that were used for numerical simulations, atomistic-based values replace fit-based values, when available. This is the case for the edge and screw dislocation self-energies, as well as the kink-pair formation energy and length. Clearly, those two sets do not differ by much, which strongly support the validity of the advertised multiscale paradigm. For a complete list of parameters for the model, the reader should refer to Ref. 7.

Table 6-2. Material parameters for Tantalum.

Parameter	Fitted set	Atomistic set
E^{kink} (eV)	0.70	0.730
L^{kink}/b	13	17
$U^{edge}/\mu b^2$ (*)	0.2	0.216
U^{edge}/U^{screw}	1.77 **	1.77
$\bar{l}/b$	5	5
L^{junct}/b	20	20
E^{cross} (eV)	0.67	0.730
λ_{FR}	2.3	4.5 ***
κ_c/b	1250	500 ***

* $\mu = \frac{3}{5}C_{44} + \frac{1}{5}(C_{11} - C_{12})$,

** Taken from the atomistic simulations,

*** Not computed by atomistic simulations.

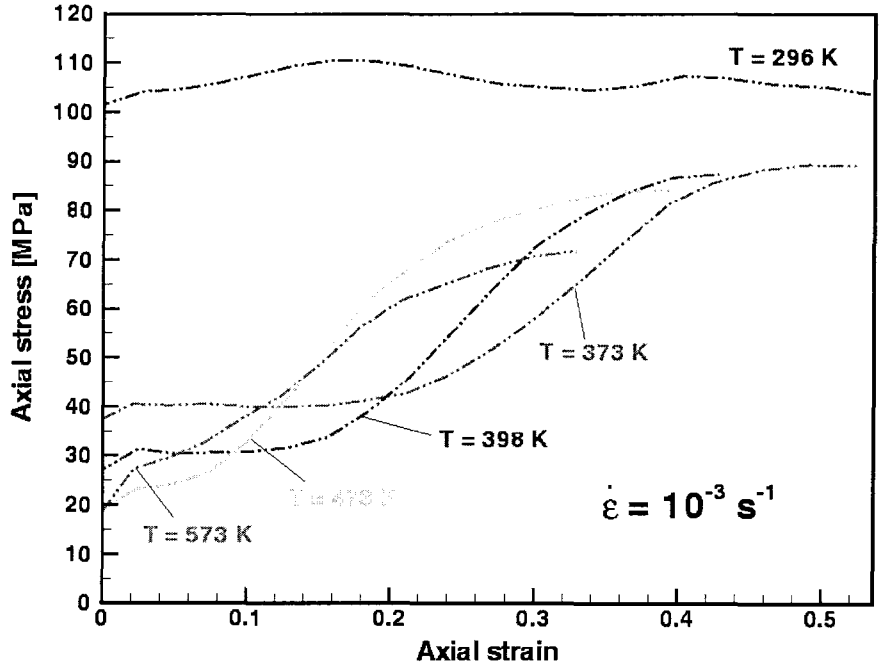

(a) Experimental data of Mitchell and Spitzig[47]

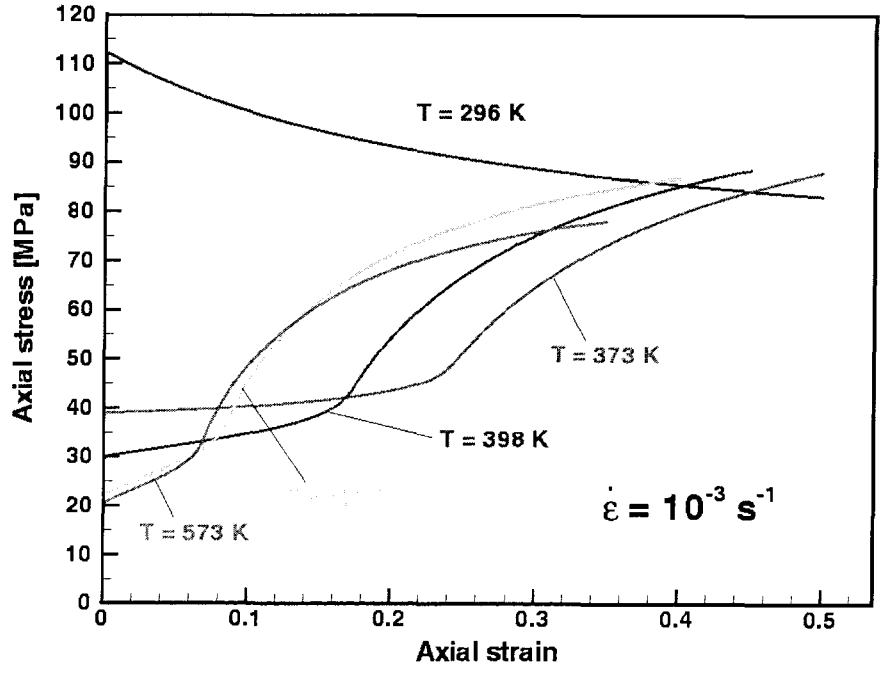

(b) Predictions of the model with fitted parameters

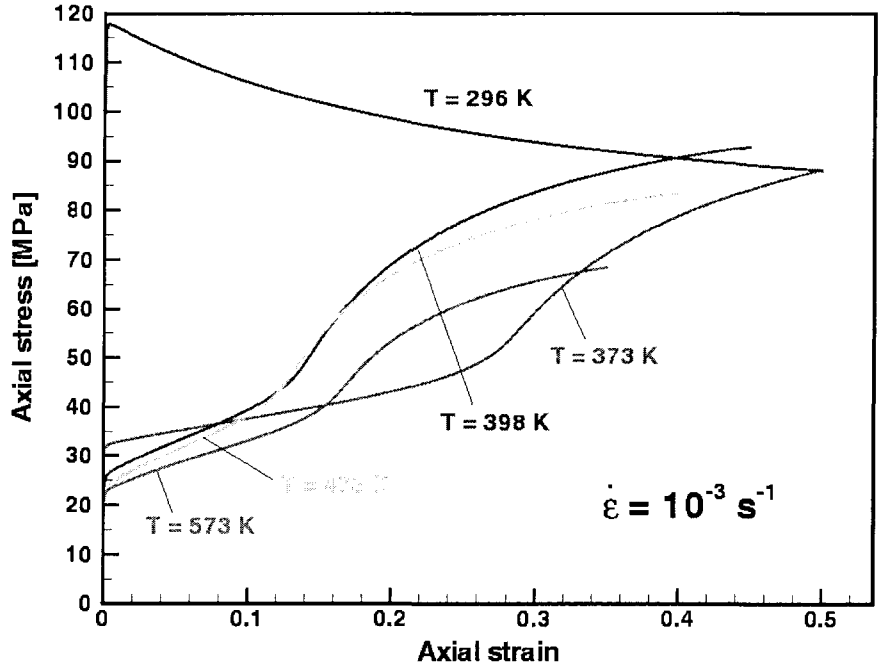

(c) Predictions of the model with atomistic parameters

Figure 6-14. Temperature dependence of stress-strain curves for [213] Ta single crystal ($\dot{\varepsilon}=10^{-3}\ s^{-1}$).

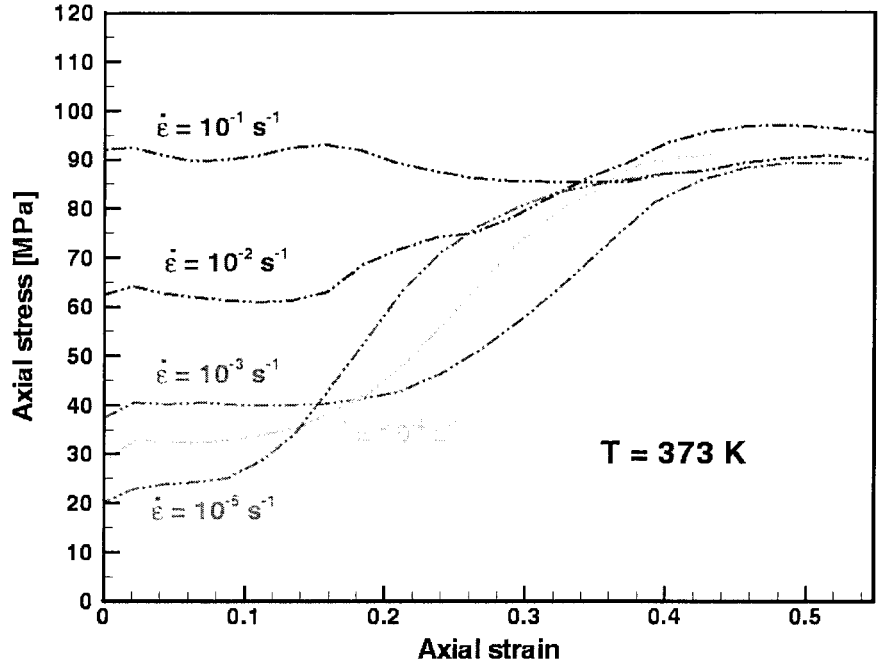

(a) Experimental data of Mitchell and Spitzig[47]

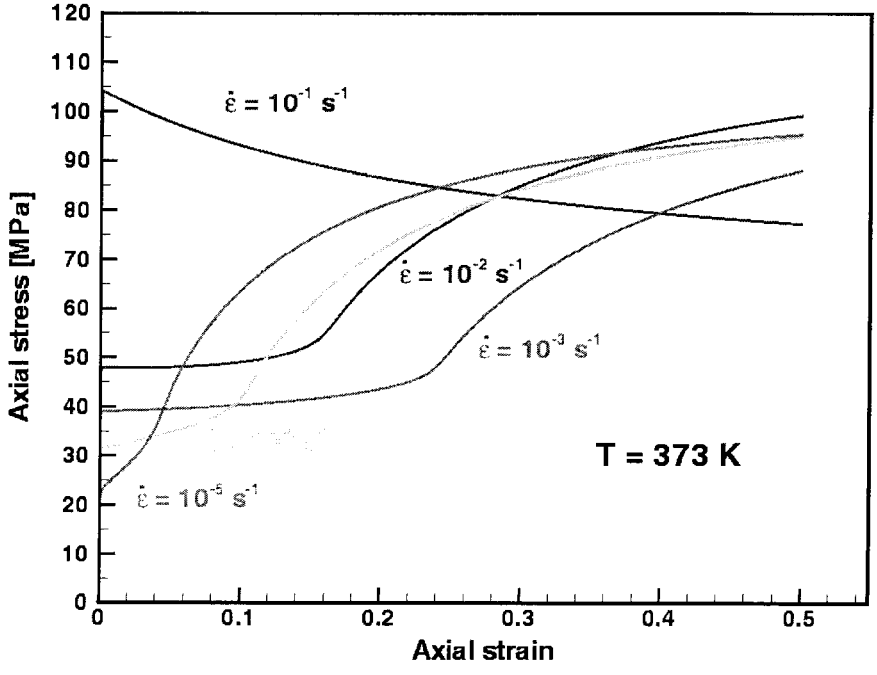

(b) Predictions of the model with fitted parameters

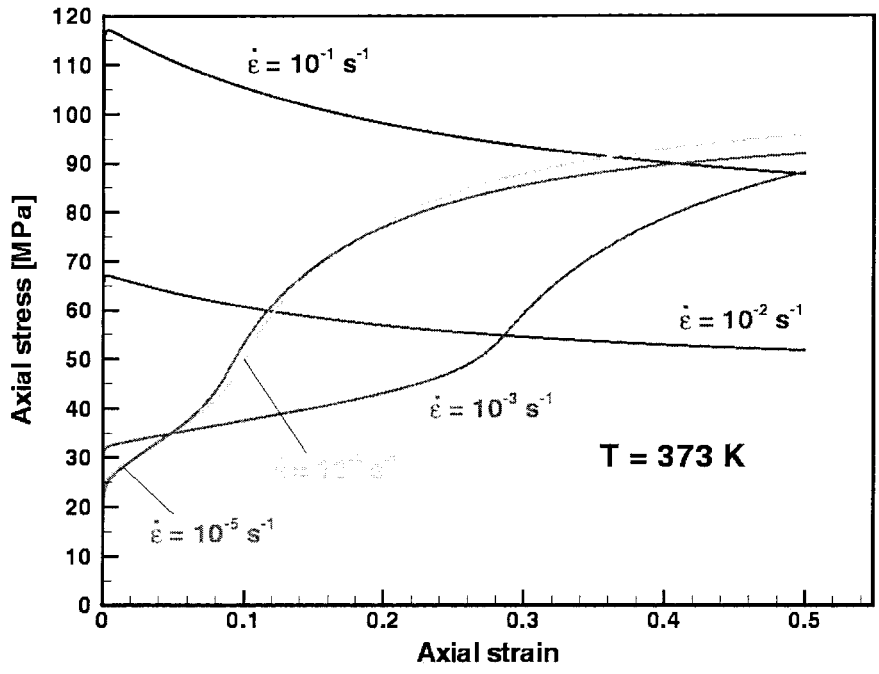

(c) Predictions of the model with atomistic parameters

Figure 6-15. Strain-rate dependence of stress-strain curves for [213] Ta single crystal (T=373 K).

Figure 6-14 and Figure 6-15 show the predicted and measured stress-strain curves for a [213] Ta crystal over a range of temperatures and strain rates. One can compare, from top to bottom: the experimental results, the results obtained after fitting the parameters, and the results obtained with atomistic-based parameters. It is evident from these figures that the model, with both sets of parameters, captures salient features of the behavior of Ta crystals such as: the dependence of the initial yield point on temperature and strain rate; the presence of a marked stage I of easy glide, specially at low temperature and high strain rates; the sharp onset of stage II hardening and its tendency to shift towards lower strains, and eventually disappear, as the temperature increases or the

strain rate increases; the parabolic stage II hardening at low strain rates or high temperatures; the stage II softening at high strain rates or low temperatures; the trend towards saturation at high strains; and the temperature and strain-rate dependence of the saturation stress. Thus, the predictive approach based on atomistic methods clearly shows its capacity to produce results matching the experimental evidence.

The theory reveals useful insights into the mechanisms underlying the plastic deformation behaviors of the single Ta crystal. For instance, since during state I the crystal deforms in single slip and the secondary dislocation densities are low, the Peierls resistance dominates and the temperature and strain-rate dependency of yield owe mainly to the thermally activated formation of kinks and crossing of forest dislocations. It is interesting to note that during this stage the effect of increasing (decreasing) temperature is similar to the effect of decreasing (increasing) strain rate, as noted by Tang *et al.*[24]. The onset of stage II is due to the activation of secondary systems. The rate at which these secondary systems harden during stage I depends on the rate of dislocation multiplication in the primary system. This rate is in turn sensitive to the saturation strain γ^{sat}, which increases with strain rate and decreases with temperature. As a result, the length of the stage I of hardening is predicted to increase with strain rate and decrease with temperature, as observed experimentally. Finally, the saturation stress is mainly governed by the forest hardening mechanism and, in particular, by the strength of the forest obstacles. This process is less thermally activated than the Peierls stress, since the corresponding energy barriers are comparatively higher. Consequently, the stress-strain curves tend to converge in this regime, in keeping with observation.

The apparent softening observed in simulation results at the lowest temperature (296 K) and the highest strain rate (10^{-1} s^{-1}) is actually an effect of the boundary conditions, allowing some level of rotation of the specimen. Since in those cases, the material hardening is relatively low (stage I only), this geometrical softening dominates in the apparent macroscopic behavior. In the other cases, the activation of several systems at high strains results in a more isotropic deformation, in turn leading to limited rotations. In order to take the exact experimental boundary conditions into account, a finite element model of the whole specimen should be used, allowing for a nonhomogeneous deformation field.

6.5 Conclusion

In this chapter, we present a modeling approach to bridge the atomistic with macroscopic scales in crystalline materials. The methodology combines identification and modeling of the controlling unit processes at microscopic level with the direct atomistic determination of fundamental material properties. These properties are computed using a many body force field derived from *ab initio* quantum-mechanical calculations. This approach is exercised to describe the mechanical response of high-purity Tantalum single crystals, including the effect of temperature and strain-rate on the hardening rate. The resulting atomistically informed model is found to capture the following salient features of the behavior of these crystals.

1. The dependence of the initial yield point on temperature and strain rate,
2. the presence of a marked stage I of easy glide, specially at low temperatures and high strain rates; The sharp onset of stage II hardening and its tendency to

shift towards lower strains, and eventually disappear, as the temperature increases or the strain rate decreases,

3. the parabolic stage II hardening at low strain rates or high temperatures,
4. the stage II softening at high strain rates or low temperatures,
5. the trend towards saturation at high strains,
6. the temperature and strain-rate dependence of the saturation stress,
7. the orientation dependence of the hardening rate.

6.6 Comment

The reported multiscale approach for modeling plasticity of Tantalum single crystal was achieved by strong collaborating among different research groups. It should be mentioned that the mesoscale simulation results were calculated by A.M. Cuitiño (Department of Mechanical and Aerosapce Engineering, Rutgers University, Piscataway, NJ 08854, USA), L. Stainier (Laboratoire de Techniques Aéronautiques et Spatiales, University of Liège, 4000 Liège, Belgium), and M. Ortiz (Graduate Aeronautical Laboratories, California Institute of Technology, Pasadena, CA 91125, USA). The contribution of the author of this thesis is to determine with accuracy the necessary input material parameters from atomistic simulations.

6.7 References

1. V. V. Bulatov and L. P. Kubin, Dislocation modeling at atomistic and mesoscopic scales, *Current Opinion in Solid State and Materials Science*, 3 (6): 558-561, 1998.
2. R. Phillips, Multiscale modeling in the mechanics of materials, *Current Opinion in Solid State and Materials Science*, 3 (6): 526-532, 1998.
3. G. H. Campbell, S. M. Foiles, H. C. Huang, D. A. Hughes, W. E. King, D. H. Lassila, D. J. Nikkel, T. D. de la Rubia, J. Y. Shu, and V. P. Smyshlyaev, Multiscale modeling of poly-crystal plasticity: a workshop report, *Materials Science and Engineering A*, 251 (1-2): 1-22, 1998.
4. R. Phillips, D. Rodney, V. Shenoy, E. Tadmor, and M. Ortiz, Hierarchical models of plasticity: dislocation nucleation and interaction, *Modeling and Simulation in Materials Science and Engineering*, 7 (5): 769-780, 1999.
5. J. A. Moriarty, W. Xu, P. Söderlind, J. Belak, L. H. Yang, and J. Zhu, Atomistic simulations for multiscale modeling in bcc metals, Journal of engineering Materials and Technology-Transactions of the ASME, 121 (2): 120-125, 1999.
6. M. I. Baskes, The status role of modeling and simulation in materials science and engineering, *Current Opinion in Solid State and Materials Science*, 4 (3): 273-277, 1999.
7. A. M. Cuitino, L. Stainer and M. Ortiz, Micromechanical modeling of hardening, rate sensitivity and thermal softening in bcc single crystals, *Journal of the Mechanics and Physics of Solids*, 2001.

8. M. S. Duesbery, V. Vitek and Bowen, *Proceedings of the royal Society of London*, A332: 85, 1973.

9. V. Vitek, *Proceedings of the royal Society of London*, A352: 109, 1976.

10. V. Vitek, Structure of dislocation cores in metallic materials and its impact on their plastic behavior, *Progress in Material Science*, 36: 1-27, 1992.

11. W. Xu and J. A. Moriarty, Atomistic simulation of ideal shear strength, point defects, and screw dislocations in bcc transition metals: Mo as a prototype, *Physical Review B - Condensed Matter*, 54 (10): 6941-6951, 1996.

12. M. S. Duesbery and V. Vitek, Plastic anisotropy in bcc transition metals, *Acta Materialia*, 46 (5): 1481-1492, 1998.

13. S. Ismail-Beigi and T. A. Arias, *Ab initio* study of screw dislocations in Mo and Ta: a new picture of plasticity in bcc transition metals, *Physical Review Letters*, 84 (7): 1499-1502, 2000.

14. G. Wang, A. Strachan, T. Cagin, and W. A. Goddard III, Molecular dynamics simulations of 1/2a<111> screw dislocation in Ta, *Materials Science and Engineering A*, 309-310: 133-137, (2001).

15. M. S. Duesbery and W. Xu, The motion of edge dislocations in body-centered cubic metals, *Scripta Materialia*, 39 (3): 283-287, 1998.

16. P. B. Hirsch, In 5^{th} *International Conference on Crystallography*, 139, Cambridge University, 1960.

17. A. Seeger and P. Schiller, *Acta Metallurgica*, 10: 348, 1962.

18. J. P. Hirth and J. Lothe, *Theory of Dislocations*, McGraw-Hill, New York, 1968.

19. J. P. Hirth and R. G. Hoagland, *Nonlinearities in the static energetics and in the kinematics of dislocations*, Physica D, 66 (1-2): 71-77, 1993.

20. W. Xu and J. A. Moriarty, Accurate atomistic simulations of the Peierls barrier and kink-pair formation energy for <111> screw dislocations in bcc Mo, *Computational Materials Science*, 9 (3-4): 348-356, 1998.

21. A. Seeger and L. Hollang, The flow-stress asymmetry of ultra-pure molybdenum single crystals, *Materials Transactions JIM*, 41 (1): 141-151, 2000.

22. W. Wasserbäch, *Philosophical Magazine A*, 53: 335, 1986.

23. R. Lachenmann and H. Schultz, *Scripta Metallurgica*, 4: 33, 1970.

24. M. Tang, B. Devincre, and L. P. Kubin, Simulation and modeling of forest hardening in body center cubic crystals at low temperature, *Modeling and Simulation in Materials Science and Engineering*, 7 (5): 893-908, 1999.

25. T. Suzuki, S. Takeuchi, and H. Yoshinaga, *Dislocation Dynamics and Plasticity*, Springer-Verlag, 1991.

26. A. D. Brailsford, Electronic component of dislocation drag in metals, *Physical Review*, 186: 959-961, 1969.

27. M. I. Baskes, R. G. Hoagland, and T. Tsuji, An atomistic study of the strength of an extended dislocation barrier, *Modeling and Simulation in Materials Science and Engineering*, 6 (1): 9-18, 1998.

28. D. Rodney and R. Phillips, Structure and strength of dislocation junctions: An atomic level analysis, *Physical Review Letters*, 82 (8): 1704-1707, 1999.

29. V. B. Shenoy, R. V. Kukta, and R. Phillips, Mesoscopic analysis of structure and strength of dislocation junctions in fcc metals, *Physical Review Letters*, 84 (7): 1491-1494, 2000.

30. G. Danna and W. Benoit, Dynamic recovery of the microstructure of screw dislocations in high-purity bcc metals, *Materials Science and Engineering A*, 164 (1-2): 191-195, 1993.

31. M. Rhee, H. M. Zbib, J. P. Hirth, H. Huang, and T. D. de la Rubia, Models for long/short range interactions and cross slip in 3-D dislocation simulation of bcc single crystals, *Modeling and Simulation in Materials Science and Engineering*, 6 (4): 467-492, 1998.

32. H. C. Huang, N. Ghoniem, T. D. de la Rubia, M. Rhee, H. Zbib, and J. Hirth, Stability of dislocation short-range reactions in bcc crystals, *Journal of Engineering Materials and Technology - Transactions of the ASME*, 121 (2): 143-150, 1999.

33. L. P. Kubin, B. Devincre, and M. Tang, *Journal of Computer Aided Material Design*, 5: 31, 1998.

34. H. M. Zbib, T. D. de la Rubia, M. Rhee, and J. P. Hirth, 3-D dislocation dynamics: stress-strain behavior and hardening mechanisms in fcc and bcc metals, *Journal of Nuclear Materials*, 276: 154-165, 2000.

35. P. Franciosi and A. Zaoui, Miltislip in fcc crystals: a theoretical approach compared with experimental data, *Acta Metallurgica*, 30: 1627, 1982.

36. P. Franciosi and A. Zaoui, Glide mechanisms in bcc crystals: an investigation of the case of α-iron through multislip and latent hardening tests, *Acta Metallurgica*, 31: 1331, 1983.

37. D. Kuhlmann-Wilsdorf, Theory of plastic deformation: properties of low energy dislocation structures, *Materials Science and Engineering A*, 113: 1, 1989.

38. W. G. Johnston and J. J. Gilman, Dislocation velocities, dislocation densities and plastic flow in lithium fluoride crystals, *Journal of Applied Physics*, 30: 129, 1959.

39. W. G. Johnston and J. J. Gilman, Dislocation multiplication in lithium fluoride crystals, *Journal of Applied Physics*, 31: 632, 1960.

40. P. P. Gillisand J. J. Gilman, Dynamical dislocation theory of crystal plasticity. II. Easy glide and strain hardening, *Journal of Applied Physics*, 36: 3380, 1965.

41. U. Essmann and M. Rapp, Slip in copper crystals following weak neutron bombardment, *Acta Metallurgica*, 21: 1305, 1973.

42. K. P. D. Lagerlof, On deformation twinning in bcc metals, *Acta Metallurgica et Materialia,* 41 (7): 2143-2151, 1993.

43. H. Dybiec, Model of the early deformation stage of bcc metals in low-temperature, *Zeitschrift für Metallurgica*, 86 (7): 512-517, 1995.

44. A. Strachan, T. Cagin, O. Gulseren, S. Mukherjee, R. E. Cohen, and W. A. Goddard III, First principles force field for metallic tantalum, *Physical Review B*, submitted.

45. A. Strachan, T. Cagin, and W. A. Goddard III, Critical behavior in spallation failure of metals, *Physical Review B*, 63: 0601034, 2001.

46. G. Wang, A. Strachan, T. Cagin, and W. A. Goddard III, Kinks in a/2<111> screw dislocation in Ta, *Journal of Computer Aided Materials Design*, in press.

47. T. E. Mitchell and W. A. Spitzig, Three-stage hardening in tantalum single crystals, *Acta Metallurgica*, 13: 1169-1179, 1965.

48. M. Ortiz and L. Stainier, The variational formulation of viscoplastic constitutive updates, Computer Methods in Applied Mechanics and Engineering, 171 (3-4): 419-444, 1999.